Universidad de Huelva

Departamento de Geología

Structural and geochemical characterization of Al and Fe minerals with low crystallinity : implication for contaminant mobility

Memoria para optar al grado de doctor
presentada por:

Sergio Carrero Romero

Fecha de lectura: 25 de julio de 2016

Bajo la dirección de los doctores:

Rafael Pérez López

Alejandro Fernández Martínez

José Miguel Nieto Liñán

Huelva, 2016

Universidad de Huelva
Facultad de Ciencias Experimentales
Departamento de Ciencias de la Tierra

“Structural and Geochemical Characterization of Al and Fe Minerals with Low Crystallinity: Implication for Contaminant Mobility”

“Caracterización Estructural y Geoquímica de los Minerales de Al y Fe con Baja Cristalinidad: Implicaciones para la Movilización de Contaminantes”

Sergio Carrero Romero

Memoria de Tesis realizada en el marco del Programa de Doctorado *Geología y Gestión Ambiental de los Recursos Minerales* para optar al grado de Doctor Internacional en Ciencias en la Universidad de Huelva

Directores:

Dr. Rafael Pérez López	**Dr. Alejandro Fernández Martínez**	**Dr. José Miguel Nieto Liñán**
Investigador Postdoctoral “Ramón y Cajal” del Dpto. de Ciencias de la Tierra de la Universidad de Huelva (España)	Investigador del Centre National de la Recherche Scientifique (CNRS) en el Insitut des Sciences de la Terre (ISTerre) de la Universidad Grenoble-Alpes (Francia)	Profesor Titular de Universidad del Área de Cristalografía y Mineralogía del Dpto. de Ciencias de la Tierra de la Universidad de Huelva (España)

Universidad de Huelva
Escuela de Doctorado

AUTORIZACIÓN PARA LA DEFENSA DE LA TESIS DOCTORAL EMITIDA POR EL DIRECTOR Y EL TUTOR Y POR LA COMISIÓN ACADÉMICA DEL PROGRAMA DE DOCTORADO

DATOS DEL DOCTORANDO:

Apellidos y nombre: Carrero Romero Sergio	NIF/NIE/Pasaporte: 49063142W	Nacionalidad: Española
Dirección a efectos de notificaciones: Calle Roque Barcia 5 8ºG, Huelva. Huelva, España		
Teléfono: 685318581	EMAIL: sergio.carrero@dgeo.uhu.es	

DATOS DE LA TESIS DOCTORAL:

Título: Structural and geochemical characterization of Al and Fe minerals with low crystallinity: Implication for contaminant mobility.

Programa Oficial de Doctorado al que se adscribe y órgano responsable: Geología y Gestión Ambiental de los Recursos Minerales

Línea de investigación a la que se adscribe y órgano responsable: Geoquímica Ambiental, Departamento de Ciencias de Tierra.

Rama de Conocimiento **(marcar casilla):**
☐ Arte y Humanidades ☒ Ciencias ☐ Ciencias de la Salud ☐ Ciencias Sociales y Jurídicas ☐ Ingeniería y Arquitectura

A CUMPLIMENTAR POR EL DIRECTOR Y POR EL TUTOR DE LA TESIS DOCTORAL: (en caso de que el Director y Tutor sean la misma persona, no es necesario cumplimentar los campos relativos al Tutor ni se precisa la firma de éste).

Director/es:	**Tutor/es:**
Dr./Dra.: Rafael Pérez López	Dr./Dra.:
Dr./Dra.: Alejandro Fernández Martínez	Dr./Dra.:
Dr./Dra.: José Miguel Nieto Liñán	Dr./Dra.:
como Director/Tutor de la Tesis Doctoral antes indicada **AUTORIZA** LA DEFENSA DE LA MISMA.	

En Huelva a, 20 de Junio De 2016

Firma del/los Director/es de la Tesis Doctoral

Fdo.: Rafael Pérez López
Fdo.: Alejandro Fernández Martínez
Fdo.: José Miguel Nieto Liñán

Firma del/los Tutor/es de la Tesis Doctoral

Fdo.:
Fdo.:
Fdo.:

A CUMPLIMENTAR POR LA COMISIÓN ACADÉMICA DEL PROGRAMA DE DOCTORADO:

Cumplidos los criterios de calidad aprobados para este Programa de Doctorado por el Comité de Dirección de la Escuela de Doctorado de la Universidad de Huelva y una vez valorada la Tesis Doctoral presentada por el Doctorando y haber incorporado éste las modificaciones y/o cambios que esta Comisión Académica le pudiera haber indicado, **se AUTORIZA** en reunión de fecha 22/06/16 **LA DEFENSA** de la misma.

En Huelva a, 22 de 06 de 2016

Firma y sello del Presidente de la Comisión Académica

Fdo. Jose M. Nieto

Universidad de Huelva

University of Huelva

ISTerre

Institut des Sciences de la Terre

Institute of Earth Sciences

Structural and Geochemical Characterization of Al and Fe Minerals with Low Crystallinity: Implication for Contaminant Mobility

Sergio Carrero Romero

Directed by:

Dr. Rafael Pérez López
Dr. Alejandro Fernández Martínez
Dr. José Miguel Nieto Liñán

A Sara,
mi hermana.

A Ildefonso y Ana María,
mis padres.

A Edu,
mi apoyo.

First and Foremost,
I urge to stay on the path you’ve chosen, and
to travel on it as far as you can.

The World needs you badly.

Edward O. Wilson.
Letters to a Young Scientist.

Financiación

La presente tesis doctoral ha sido posible gracias a la financiación recibida por parte de los proyecto EMPATIA (CGL2013-41862-C02-01, Estabilidad de metales en precipitados de drenaje ácido de mina: uso sostenible e implicaciones ambientales) concedido por el Ministerio de Economía y Competitividad, METODICA (CGL2010-21956-C02-01, El ciclo de los metales y su impacto en la calidad del agua de la cuenca del río Odiel) concedido por el Ministerio de Ciencia y Competitividad, el proyecto FO-REVER (P12-RNM-2260, Fosfoyesos: de su evaluación ambiental como residuo a su revalorización como recurso) de la Consejería de Economía, Innovación y Ciencia de la Junta de Andalucía, y al proyecto Labex OSUG@2020 (investissements d'avenir – ANR10 LABX56). Los análisis químicos y medidas en equipos convencionales se han llevado a cabo en las instalaciones del Centro de Investigación y Desarrollo de Recursos y Tecnología Agroalimentaria (CIDERTA) y los Servicios Centrales de Investigación de la Universidad de Huelva así como en los laboratorios del Instituto de Diagnóstico Ambiental y Estudios del Agua (IDAEA-CSIC) (Barcelona, España). Por otro lado, reconocer la ayuda prestada por parte del personal de Instituto Andaluz de Ciencias de la Tierra (IACT-CSIC) (Granada, España) durante la adquisición de datos en sus laboratorios. Finalmente, los análisis con luz sincrotrón fueron financiados y desarrollados en las líneas ID15B (Experimentos MA-1754 y EV-62), CRG-BM25A (Experimento 25-01-976), BM26B (Experimentos EV-62 y EV-148), ID11 (Experimentos EV-78 y EV-168) del European Synchortron Radiation Facility (ESRF) (Grenoble, Francia), en la línea XAFS (Experimentos 20140046 y 20145106) del ELETTRA Synchrotron Light Source (Trieste, Italia) y de la línea Boreas (Experimento 2013110773) del sincrotrón ALBA (Barcelona, España).

El doctorando ha sido financiado por el Ministerio de Educación Cultura y Deporte en su programa ayudas de posgrado para la Formación de Profesorado Universitario (FPU AP2010-2117, resolución en convocatoria publicada por Orden EDU/3445/2011, BOE del 20 de Diciembre de 2011). Los trabajos de investigación han sido desarrollados entre la Facultad de Ciencias Experimentales de la Universidad de Huelva y el Institut des Sciences de la Terre (ISTerre) de la Université Grenoble-Alpes (Grenoble, Francia). En el transcurso de la tesis doctoral se han realizado dos estancias en el centro ISTerre gracias a la financiación del Campus France en el programa Nano-Espagne 2013 (31415ZH, Nucleation and growth of poorly-crystalline Fe and Al oxy-hydroxysulphates in acid mine drainage) y del Ministerio de Educación, Cultura y Deporte en su subprograma de estancias breves incluido dentro del programa de ayudas de posgrado FPU.

Agradecimientos/Acknowledgments

Muchas han sido las personas que durante estos cuatro años y medio de investigación han merecido formar parte de estos agradecimientos. Por muy solo y perdido que haya podido llegar a sentirme en algunos momentos, siempre he tenido a mí alrededor a grandes amigos que no han dudado ni un segundo en dejarlo todo solo para escuchar las divagaciones y dudas que tuviera que contar, aunque estas le pudieran sonar a chino. Con estas líneas solo espero devolver, al menos, una parte del afecto y la ayuda recibida.

En primer lugar, y como no podía ser de otra manera, quiero agradecer a mis directores de tesis Rafael Pérez, Alejandro Fernández y José Miguel Nieto. Rafa, con tu paciencia a la hora de enseñar has conseguido sacar de mí a un investigador que ni yo sabía que existía, tu pasión por este mundo es contagiosa. José Miguel, con tu experiencia siempre has sabido sacar el máximo provecho de todo lo que he hecho, tu ojo crítico nunca falla. Y Alex, comenzamos a trabajar juntos por recomendación de Rafa, él me dijo que tenías mucho que enseñarme, y no se equivocaba. Tú me acogiste en Grenoble, arrojaste "luz" a la radiación sincrotrón, e hiciste que un geólogo empezara a hablar de orden local y dominio coherente. Vosotros fuisteis quienes confiasteis en mi a pesar de mi poca experiencia y me orientasteis en un camino difícil donde los primeros pasos se dan a oscuras. Gracias a los tres por guiarme, ahora toca empezar a andar solo.

Quiero agradecer a todos mis amigos de Valverde, los de toda la vida. A Miry, Carlos, Nuria, Manolo, Sandra, Guio, David, Hermes, Víctor y muy especialmente a mis ortopepinillos Juanillo, Tanke, Kinder y Luzan. Con vosotros he pasado algunos de los mejores momentos de mi vida y siempre me habéis animado a seguir adelante. Aunque ahora el trabajo nos mantiene separados, sabemos que "Nos une un vínculo que se cierra sobre sí mismo, como un **anillo**, que siempre nos recordará que, más que amigos, somos casi hermanos".

Desarrollar este trabajo me ha permitido moverme por muchos sitios. En especial, tengo un muy buen recuerdo de mis dos estancias en Grenoble. Allí conocí a grandes personas que hicieron que mí día a día fuera mucho más interesante. Mi gran grupito de españoles, Ana Pradas, Oscar, Ana Martos, Jaime, Edu, Javi, María, Laura, Carlos Falcón, Carlos Cruz, Sergio, Dery, y tantos otros que por circunstancias de esta profesión no he tenido oportunidad de conocer con más profundidad. Hemos compartido confidencias, mercados, frio, cervezas en el O'champollion (y otros muchos bares, de eso no faltó), y sobre todo muy buenos momentos, gracias a ustedes el tiempo se me pasó volando. And my lab-team, many different people from many different countries. My flat-mate Paul and Gosya, Nätalye, Elli, Maor, Franse, Lynda, Eric, Clara, Eliot,

Table of Contents

Figure Index

Table Index

ABSTRACT

The pollution of the aquatic environment by heavy metals and metalloids (from now on referred as ‘metals’) in solution can be potentially associated with acid mine drainage (AMD) or with leachates from acid sulfate soils (ASS). Both AMD and ASS derive from the exposition and oxidation of sulfide minerals contained in mineral ore bodies or in soils formed under reducing conditions, respectively. In both cases, sulfide oxidation, mainly pyrite, releases protons, sulfate, ferrous iron and other metals; reducing the pH and increasing the ionic load in the solution. This pollution is attenuated by precipitation of nanominerals such as schwertmannite and basaluminite. The schwertmannite structural framework and its affinity by metals have been previously studied in depth, whereas little is known about basaluminite. Thus, the main objective of this doctoral dissertation is to propone a structural model for basaluminite and to study its properties as scavenger of toxic elements by means of non-conventional techniques based on synchrotron radiation (*e.g.* high energy X-ray diffraction and X-ray absorption fine structure).

1) Firstly, neutralization experiments were conducted using a naturally reduced AMD with all aqueous Fe as Fe(II) under atmospheric and anoxic conditions to elucidate, individually, the sorption capacity of trace elements in solution by schwertmannite and basaluminite. Under atmospheric conditions, initial precipitation of schwertmannite led to the total removal of As, Cr, Fe and Pb in solution, masking the possible basaluminite affinity by these elements, as occurs in natural systems. However, under anoxic conditions, neutralization of the reduced solution with all Fe available in solution led first to the basaluminite precipitation, unveiling a heretofore unknown affinity of this phase for As and Cr.
2) Secondly, adsorption isotherm experiments were conducted to quantify the maximum As and Se adsorption capacities on synthetic schwertmannite and basaluminite, as well as the sulfate competitive effect for surface sorption sites. In addition, synchrotron-based techniques were used to determine the local coordination of As and Se complexes in both structural frameworks. The results showed that oxyanion exchange between structural sulfate and As or Se in solution was the main removal mechanism. Maximum As adsorption capacity

by basaluminite was twice higher than by schwertmannite and three times higher than Se by both phases. The presence of sulfate had little effect on the sorption As capacity; although it had a strong negative effect on Se removal. Synchrotron results indicated that bidentate binuclear inner-sphere was the most probable ligand for As on both phases and for Se on schwertmannite, whereas Se formed outer-sphere complexes in basaluminite.

3) Finally, synchrotron experiments and reverse Monte Carlo analysis were performed to determine the short-range structure of basaluminite. This nanomineral showed high sulfate contents with different structural coordination between natural (outer-sphere position) and synthetic (inner-sphere position) samples. Both synthetic and natural basaluminites had identical local order with 1.2 nm of coherent domain. On the other hand, Al in basaluminite showed similar features to Al_{13} Keggin ions with ~1% and 5% of tetrahedral and pentahedral coordination, respectively. According to the structural models, basaluminite revealed similar structural framework to felsöbányaite, which was formed by octahedral Al layers with vacant positions and high angular and longitudinal octahedral distortion, where sulfate and water molecules were emplace in the interlayer space.

In conclusion, this doctoral dissertation describes basaluminite as a strategic nanomineral on the metals behavior in areas affected by AMD and ASS, and its study has allowed better understand the natural attenuation processes occurring in systems affected by sulfide oxidation. This information will help also to improve the efficiency of the treatment systems and to develop new strategies focused on metal recovery with economic interest.

RESUMEN

La contaminación del medio hídrico por metales pesados y metaloides (en adelante ‘metales’) en solución puede estar asociado potencialmente al drenaje ácido de mina (AMD, de las siglas en inglés de *Acid Mine Drainage*) o a los lixiviados procedentes de suelos sulfatados ácidos (ASS, de las siglas en inglés de *Acid Sulfate Soils*). Tanto el AMD como el ASS proceden de la exposición y oxidación de los sulfuros presentes en depósitos minerales o en suelos desarrollados en condiciones reducidas, respectivamente. En ambos casos, la oxidación de sulfuros, principalmente pirita, libera protones, sulfato, hierro ferroso y otros metales, reduciendo el pH e incrementando la carga iónica en solución. Esta contaminación es atenuada por la precipitación de fases nanominerales tales como schwertmannita y basaluminita. Las características estructurales de schwertmannita y su afinidad por los contaminantes se han estudiado previamente en profundidad; sin embargo, poco se sabe aún sobre basaluminita. Así, el principal objetivo de esta tesis doctoral es proponer un modelo estructural para basaluminita y estudiar su capacidad para retener contaminantes por medio de técnicas no convencionales basadas en radiación sincrotrón (por ejemplo difracción de rayos-X de alta energía y absorción de rayos-X en estructura fina).

1) En primer lugar, se realizaron experimentos de neutralización con un agua ácida reducida en condiciones atmosféricas y anóxicas para determinar, por separado, la capacidad de retención de elementos trazas en schwertmannita y basaluminita. Bajo condiciones atmosféricas, la precipitación inicial de schwertmannita condujo a la retirada total de As, Cr, Fe y Pb de la solución, enmascarando el posible potencial de la basaluminita en los procesos de atenuación, como ocurre en condiciones naturales. Sin embargo, en condiciones anóxicas, la neutralización de la solución reducida con el hierro en solución causó la precipitación inicial de basaluminita, demostrando una elevada afinidad de esta fase, no descrita anteriormente, por As y Cr.
2) En segundo lugar, se realizaron experimentos de isotermas de adsorción para cuantificar la capacidad máxima de adsorción de As y Se en schwertmannita y basaluminita sintéticas, así como el efecto competitivo del sulfato por los sitios de adsorción superficial. Además, se emplearon técnicas basadas en radiación

sincrotrón para determinar la coordinación local de los complejos de As y Se en ambas estructuras. Los resultados mostraron que el intercambio de oxianiones entre sulfato estructural y As o Se en solución fue el mecanismo principal de retención. La capacidad máxima de adsorción de As en basaluminita fue dos veces mayor que en schwertmannita y tres veces mayor al Se en ambas fases. La presencia de sulfato en solución no afectó a la adsorción de As, pero sí tuvo un fuerte impacto en la retirada de Se. Los resultados de sincrotrón mostraron que el tipo de coordinación más probable para As en ambas fases y Se en schwertmannita fue el complejo bidentado binucleado de esfera interna, mientras que Se en basaluminita se sitúa en posición de esfera externa.

3) Finalmente, se realizaron experimentos de sincrotrón y modelos de simulación Monte Carlo para determinar la estructura de rango corto de la basaluminita. Este nanomineral mostró altos contenidos en sulfatos en diferentes posiciones estructurales entre muestras naturales (esfera externa) y sintéticas (esfera interna). Ambas muestras de basaluminita tuvieron idéntico orden local con un dominio coherente de 1.2 nm. Por otro lado, el Al en basaluminita mostró características similares a los Al_{13} con estructura Keggin, con ~1% y 5% de Al en coordinación tetraédrica y pentaédrica, respectivamente. De acuerdo con los modelos estructurales, la basaluminita presentó fuertes similitudes a la felsöbányaita, la cual estuvo formada por capas de Al octaédrico con posiciones vacantes y una alta distorsión angular y longitudinal de los octaedros, donde el sulfato y el agua se alojan en los espacios entre capas.

En conclusión, esta tesis doctoral describe la basaluminita como un nanomineral estratégico en la movilidad de metales en áreas afectadas por AMD y ASS, y su estudio ha permitido entender mejor los procesos de atenuación natural que ocurren en sistemas afectados por oxidación de sulfuros. Esta información ayudará también a mejorar la eficiencia de los sistemas de tratamiento y a plantear nuevas estrategias enfocadas a la recuperación de metales con interés económico.

CHAPTER I

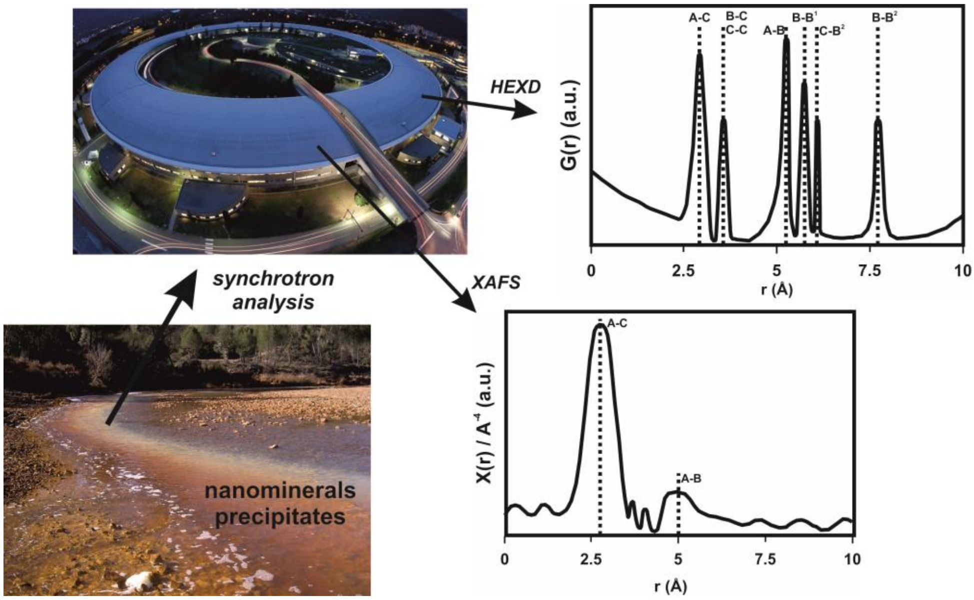

Introduction

The pollution of the hydric resources is one of the biggest environmental problems worldwide. Due to the vital human needs for water, the different cultures have developed their activity in the proximity to water resources such as rivers, lakes, coast, *etc*. Demographic and industrial growths, mainly after the industrial revolution, have contributed to the degradation of aquatic environments by generation of solid and liquid urban, industrial and mining wastes, spilling high amounts of organic compounds, heavy metals (*e.g.* Cu, Fe, Pb, Zn) and metalloids (*e.g.* Al, As, Sb, Se) (Rockström et al., 2009). Metal and metalloid (from now on referred as 'metals') pollution is especially dangerous due to: (i) the toxicity of these elements to animals and plants when they are present at high concentrations in solution (Valko et al., 2005), (ii) their longtime (bio)availability, because metals are not biodegradable (Bryan and Langston, 1992) and (iii) the metal accumulation capacity of some organisms (Clemens, 2006). Areas affected by acid mine drainage (AMD) and acid sulfate soil (ASS) show high concentration in metals and other potentially toxic elements (Nordstrom and Alpers, 1999a; Shamshuddin et al., 2014). This doctoral dissertation focuses on the geochemical and structural characterization of Al and Fe-hydroxysulfate poorly-crystalline minerals that are common in areas affected by AMD and ASS, and on their environmental implications in the mobility of metals in these areas.

1.1. SYSTEMS AFFECTED BY ACID WATER

1.1.1. Acid mine drainage

One of the main sources of metals in aquatic systems is mining activity, with AMD being one of the most serious problems due to its extension and difficult remediation (Nordstrom and Alpers, 1999b; Olías et al., 2006; Younger, 2001). AMD is generated in sulfide ore bodies, coal and porphyry copper areas by the oxidation and subsequent dissolution of sulfide minerals in presence of water and oxygen (Fig. 1.1) (Moore and Ramamoorthy, 1984; Olías et al., 2004; Younger, 1997). Sulfide oxidation is in part considered as an anthropogenic process associated with metal-mining activities; however, sulfide oxidation can occur when sulfide minerals are naturally exposed to surface by geological processes, which result in leachates known as acid rock drainage (ARD). Weathering of sulfide minerals takes place in mining waste piles, galleries, open-pits and tailing ponds, involving a set of geochemical and microbiological reactions whose result is the release to solution of high amounts of protons, sulfate and metals (Lowson, 1982; Nordstrom and Alpers, 1999a).

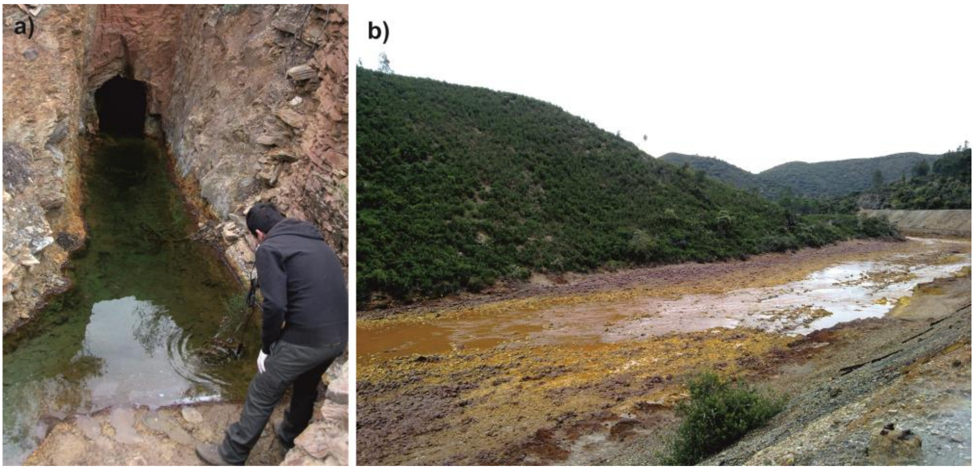

Figure 1.1: *Examples of streams affected by AMD: (a) Leachates from "Perrunal" mine gallery (Huelva, Spain) with all the iron as ferrous iron and (b) Tinto river with all the iron as ferric iron in solution.*

Many kilometers of fluvial courses are affected by AMD worldwide (Johnson and Hallberg, 2005). Although the most studied cases are located in USA and Canada, streams affected by AMD have been described in Africa, Asia, South America, Australia and Europe. Some examples of areas affected by AMD are: (i) the metal-sulfide mining districts of Cement Creek on Colorado State (USA; Schemel et al., 2000) and Sudbury mine on Ontario (Canada; Sracek et al., 2004); (ii) the coal mining districts of Pennsylvania (USA; Kairies et al., 2005), Korea (Yu and Heo, 2001) and Scotland (Woulds and Ngwenya, 2004); and (iii) the gold mining districts of Johannesburg (South Africa; Naiker et al., 2003) and Chine (Zabowski et al., 2001). In Spain, some areas are significantly affected by AMD such as the coal mines of Galicia, Asturias and Basque County (Monterroso and Macías, 1998) and the massive sulfide ore deposits of the Iberian Pyritic Belt (Leblanc et al., 2000; Sáinz et al., 2002).

1.1.2. Acid sulfate soils

The origin of ASS is the oxidation of sulfide minerals contained in the soil. This process often occurs in clayey soils of coastal plains (*e.g.* tidal swamp and marshland), but it can be also observed in wetlands, rivers and fossil-marshes (Dent and Pons, 1995). These soils may attain sulfide concentrations of up to 15%, especially in areas with low sedimentation rate and high metals and sulfate contribution (*e.g.* zones affected by AMD) (Andriesse and Mensvoort, 2005; Fanning et al., 2002). Simultaneously to unripe soil formation in coastal plains, sulfate and metals are catalytically reduced by bacterial activity during organic material degradation, precipitating metal sulfides under strongly-reduced conditions (Burton et al., 2007). Almost all coastal plains show soils composed by a variable sulfide-clay proportion, which are buried by alluvium as deltas or peats (Dent and Pons, 1995). Once these soils are exposed again to atmospheric conditions, sulfides are oxidized, releasing protons, sulfate and metals, and reducing the pH value below 3 in porewater (Andriesse and Mensvoort, 2005; Aström, 1998). The exposure and subsequent sulfide oxidation may be originated by natural processes (*e.g.* variation in the sea level and seasonal climatology) or human activity (*e.g.* marshland soils remobilization, drying of wet areas and dredging) (Åström and Spiro, 2000; Dent and Pons, 1995). ASS formation leads to large extensions of extremely acid soils with high metal and sulfate concentration (Appleyard et al., 2006; Aström, 1998), which are subsequently released to marshlands, rivers or lakes (and in some cases to crops or fishing areas) (Minh et al., 1997; Shamshuddin et al., 2014).

Large areas of unripe sulfide-clays affected by ASS are described and studied around the world (*e.g.* Finland; Åström and Björklund, 1995; Åström, 2001). However, especial attention has been paid to ASS in Queensland (Australia), where the pollution generated by these processes has important environmental implications for the Great Barrier Reef development (Powell and Martens, 2005; Preda and Cox, 2001). On the other hand, the intensive rice agriculture on soils affected by ASS in Vietnam, Indonesia, Thailand and other Southeast Asia countries has toxic effects on human health (Andriesse, 1992; Husson et al., 2000; Naruekamon and Masatomo, 2008; Nuttal et al., 2008).

1.2. GEOCHEMICAL REACTIONS

1.2.1. Pyrite oxidation and AMD/ASS generation

As stated before, AMD and ASS are the result of the oxidative dissolution of sulfides, once these minerals are exposed to atmospheric conditions. Pyrite (FeS_2) is the most abundant sulfide mineral. It commonly occurs in coal fields and metal ore bodies (Dent and Pons, 1995; Holmes and Crundwell, 2000). Its oxidation releases protons, sulfate and ferrous iron to the solution (Singer and Stumm, 1970), whereas the weathering of other minor sulfides, such as chalcopyrite ($CuFeS_2$), sphalerite (ZnS), galena (PbS) or arsenopyrite (FeAsS), releases sulfate and other metals (Aström, 1998; Evangelous and Zhang, 1995; Nordstrom and Alpers, 1999a; Nordstrom, 1982a). These oxidation processes are known as direct oxidation (see Eq. 1.1-1.5):

$$FeS_{2(s)} + 3.5O_{2(aq)} + H_2O \rightarrow Fe^{2+} + 2SO_4^{2-} + 2H^+ \qquad \text{Eq. 1.1}$$

$$CuFeS_{2(s)} + 4O_{2(aq)} \rightarrow Cu^{2+} + Fe^{2+} + 2SO_4^{2-} \qquad \text{Eq. 1.2}$$

$$ZnS_{(s)} + 2O_{2(aq)} \rightarrow Zn^{2+} + 2SO_4^{2-} \qquad \text{Eq. 1.3}$$

$$PbS_{(s)} + 2O_{2(aq)} \rightarrow Pb^{2+} + 2SO_4^{2-} \qquad \text{Eq. 1.4}$$

$$4FeAsS_{(s)} + 11O_{2(aq)} + 6H_2O \leftrightarrow 4Fe^{2+} + 4H_3AsO_3 + 4SO_4^{2-} \qquad \text{Eq. 1.5}$$

In AMD, ferrous iron from pyrite oxidation is oxidized to ferric iron according to Eq. 1.6; on the other hand, in ASS ferrous iron is kept in solution for longer times due to the typical lower Eh values. When pH is higher than 3, approximately, ferric iron is unstable in solution and precipitates as Fe hydroxide (*e.g.* schwertmannite; Eq. 1.7) (Bigham et al., 1996b, 1990). However, ferric iron is kept in solution at pH values lower than 3, acting as a pyrite indirect oxidizing agent according to the Eq. 1.8 (Singer and Stumm, 1970).

$$Fe^{2+} + 0.25O_{2(aq)} + H^+ \leftrightarrow Fe^{3+} + 0.5H_2O \qquad \text{Eq. 1.6}$$

$$8Fe^{3+} + SO_4^{2-} + 14H_2O \leftrightarrow Fe_8O_8(OH)_6SO_{4(s)} + 22H^+ \text{ (pH > 3)} \qquad \text{Eq. 1.7}$$

$$FeS_{2(s)} + 14Fe^{3+} + 8H_2O \rightarrow 15Fe^{2+} + 2SO_4^{2-} + 16H^+ \text{ (pH < 3)} \qquad \text{Eq. 1.8}$$

In acid environments, indirect oxidation (Eq. 1.8) is several times faster and releases more protons than direct oxidation (Eq. 1.1); however, the presence of oxygen in solution is even necessary in the indirect process since ferrous iron has to be previously oxidized (Eq. 1.6) and this reaction is extremely slow at low pH values (Nordstrom, 1982a). Both direct and indirect oxidations may be catalyzed by oxidizing bacteria such as *Acidithiobacillus ferrooxidans* and *Leptospirillum ferrooxidans*, increasing the oxidation rate by several orders of magnitude (Nordstrom and Alpers, 1999a). Frequently, pyrite oxidation takes place in mine galleries where the oxygen available in solution is limited. If oxygen is exhausted in these places, the reaction in Eq. 1.8 may continue until ferric iron is totally consumed and ferrous iron becomes the predominant species in solution (Younger et al., 2002).

1.2.2. Attenuation processes in AMD and ASS

Metals stability in solution is closely related to the evolution of the solution pH. When the pH value is lower than 3, metals from sulfide oxidation are stable in solution and their concentrations in AMD discharges or ASS porewaters can range from hundreds to thousands of mg L^{-1} (Burton et al., 2007; Lee, 2001; Nieto et al., 2007; Nordstrom, 2011). Whenever the pH increases, solutions start to be supersaturated with respect to different phases whose precipitation buffers the solution at specific pH intervals (Adams and Rawajfih, 1977; Bigham et al., 1994). These processes attenuate the pollution in streams and soils affected by AMD and ASS (Lee et al., 2002). The agents controlling the attenuation processes are as follow:

- Ferrous iron oxidation. Even at low pH values (around 3.0), high concentrations of sulfate and ferric iron lead to the solution supersaturation and subsequent spontaneous precipitation of Fe-oxyhydroxysulfates, mainly schwertmannite (Bigham et al., 1996b). Schwertmannite precipitation (Eq. 1.7) can remove trace elements from solution (Bigham et al., 1996a; Nordstrom and Alpers, 1999a).
- Stream confluences. Spontaneous precipitation of schwertmannite occurs until the equilibrium with the solution is reached. However, this equilibrium is disturbed in confluences between AMD-affected streams (pH > 3) and pristine or seawater (surrounding neutral pH), leading to new schwertmannite precipitation and to

proton release that buffers the pH around 2.5-3.5 (Eq. 1.7) (Olías et al., 2004). Once all iron is depleted from the solution, the pH increases up to 4.5 and the solution starts to be supersaturated with respect to Al-phases, precipitating basaluminite:

$$4Al^{3+} + SO_4^{2+} + 10H_2O \rightarrow Al_4(OH)_{10}SO_4 + 10H^+ \qquad \text{Eq. 1.9}$$

Basaluminite precipitation also releases protons that buffer the pH around 4.5-5.5 until all Al is removed from the solution (Fig. 1.2a) (Bigham and Nordstrom, 2000; Nordstrom, 1982b). Basaluminite also contributes to the sequestration of some trace elements from the solution (Nordstrom and Alpers, 1999a). Natural attenuation of pollution by circumneutral water mixing occurs by precipitation and dilution processes (Dent and Pons, 1995; Sarmiento et al., 2009b).

- Host rock dissolution. Waters affected by AMD and ASS can dissolve carbonate and silicate minerals of the host rock, mobilizing high concentrations of Al, Ca, Si and other elements. These processes are able to consume acidity, increasing the pH and decreasing the metal mobility in solution (Eq. 1.10-1.13) (Atanassova et al., 2013; Morse and Arvidson, 2002):

$$CaCO_{3(s)} + 2H^+ \rightarrow Ca^{2+} + H_2CO_3 \qquad \text{Eq. 1.10}$$

$$CaMg(CO_3)_{2(s)} + 2H^+ \rightarrow Mg^{2+} + Ca^{2+} + 2HCO_3^- \qquad \text{Eq. 1.11}$$

$$KAlSi_3O_{8(s)} + H^+ + 9/2H_2O \rightarrow K^+ + 2H_4SiO_4 + 1/2Al_2Si_2O_5(OH)_{4(s)} \qquad \text{Eq. 1.12}$$

$$NaAlSiO_{4(s)} + H^+ + 3H_2O \rightarrow Na^+ + Al^{3+} + H_4SiO_4 + 3OH^- \qquad \text{Eq. 1.13}$$

Carbonate minerals have a much higher capacity to neutralize acidity (Eq. 1.10 and 1.11), than silicates due to the slower dissolution kinetics of the latest (Bowell and Ptacek, 2003; Cama et al., 2005; Schott et al., 1989). The abundance of carbonate minerals in the area affected by AMD and ASS determines the pH of the resulting leachates and their metal concentration.

- Active/passive treatment systems. The same geochemical processes controlling natural contaminant attenuation, *i.e.* schwertmannite and basaluminite precipitation at specific pH intervals, is used in artificial treatment systems to improve the water quality in AMD-affected streams (Fig. 1.2b). These systems are only applicable to point pollution sources. The main difference between active and passive systems is the energy source. Whereas passive systems use only naturally available energy sources (*e.g.* gravity, microbial metabolic energy, photosynthesis), active systems consume high amounts of electricity (Younger et al., 2002). Therefore, passive and active systems are the common strategies for abandoned and operating mines, respectively. The procedure in both cases is similar: an initial iron oxidation is followed by reactive pools where the metal removal is induced by alkaline addition (*e.g.* limestone) and/or bio-reducing processes (*e.g.* sulfate reducing bacteria) (Caraballo et al., 2011; Macías et al., 2012; Younger et al., 2002). On the other hand, ASS treatment systems are complex to implement due to that the pollution is diffuse and it affects large soil areas and groundwater (Powell and Martens, 2005).

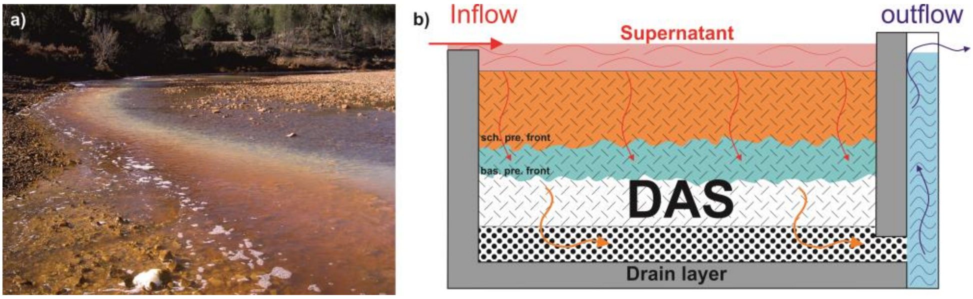

Figure 1.2: *(a) Confluent point between Odiel river (pristine water) and Agrio river (acid water) with the schwertmannite and basaluminite precipitation front (Image courtesy of Carlos Ayora, CSIC, Barcelona, Spain). (b) Schematic cross section of the dispersed alkaline substrate (DAS) reactive tank described by Rötting et al. (2008).*

1.3. NANOMINERALS IN AMD AND ASS

Contaminant attenuation processes are mainly controlled by the supersaturation and subsequent precipitation of mineral phases, which includes metal sequestration mechanisms such co-precipitation, adsorption and ion exchange (Antelo et al., 2012; Asta et al., 2010; Burton et al., 2009; Lee et al., 2002; Nordstrom, 2011). As previously mentioned, the precipitation of these phases acts as a pH buffering agent that is associated with ferric iron and aluminum hydrolysis at solution pH values between 2.5-3.5 and 4.5-5.5, respectively (Adams and Rawajfih, 1977; Bigham and Nordstrom, 2000; Bigham et al., 1996a; Burton et al., 2007; Lee, 2001; Nordstrom and Alpers, 1999a; Nordstrom, 1982a, 1982b; Schwertmann et al., 1995). Due to the higher iron, aluminum and sulfate concentrations in solution, acidic systems are mainly controlled by Fe(III)-SO_4 and Al-SO_4 hydrochemistry (Bigham and Nordstrom, 2000). As previously mentioned, during the pH-buffering region of hydrolysis of ferric iron , the watercourses are supersaturated with respect to oxyhydroxysulfates such as jarosite, goethite and schwertmannite, the latest being described as the predominant mineral phase (Bigham et al., 1990; Burton et al., 2007; Schwertmann et al., 1995). On the other hand, hydrobasaluminite/basaluminite is the main newly-formed hydroxysulfate in the aluminum buffer (Adams and Rawajfih, 1977; Bigham and Nordstrom, 2000; Nordstrom, 1982b; Sánchez-España et al., 2011).

1.3.1. Schwertmannite

Schwertmannite is a poorly-crystalline Fe-oxyhydroxysulfate that forms ochre-colored aggregates of nanoparticles with typical hedgehog morphology. The solubility products of schwertmannite show a wide range of $log\ K_{sp}$ (from 10 to 28.9; Asta et al., 2010; Regenspurg et al., 2004) and recent studies indicate that precipitation may take place at pH between 1.9 and 4.7 (Caraballo et al., 2013). The chemical composition of this mineral was initially proposed by Bigham et al. (1994) as $Fe_8O_8(OH)_{8-x}(SO_4)_x$, with x varying between 1 to 1.75. However, this formula is still object of controversy and later estimations show higher x values between 1.74 and 1.84 (Yu et al., 1999). The uncertainty on the x value may be caused by the different locations of the sulfate groups in the structure. Schwertmannite has been described as a poorly-crystalline mineral with a structure similar to a deformed akaganeite with channel-like iron oxide frameworks where sulfate molecules are located forming inner- and outer-sphere complexes (Fig. 1.3) (Bigham et al., 1990; Fernandez-Martinez et al., 2010; Wang et al., 2015).

Due to its large specific surface area and its positive charge in acidic water, schwertmannite efficiently removes metal oxyanions such as As, Cr, Mo and Se from the solutions (Antelo et al., 2012; Burton et al., 2009; Lee et al., 2002; Regenspurg et al., 2004; Waychunas et al., 1995b). Arsenic has been described as the metalloid with higher affinity by this phase. Arsenic adsorption is pH-dependent, reaching the maximum capacity (between 196 and 333 mmol$_{As}$ mol$_{Fe}^{-1}$) at pH around 3 (Antelo et al., 2012; Burton et al., 2009). Schwertmannite adsorption capacity may be questioned due to its metastable structure, which transforms into goethite and jarosite within months (Acero et al., 2006; Bigham et al., 1996a). These recrystallization processes involve the releasing of previously sorbed contaminants because the more crystalline phases show structures with less surface areas and adsorption sites and, hence, lower retention capacity (Asta et al., 2010; Loring et al., 2009).

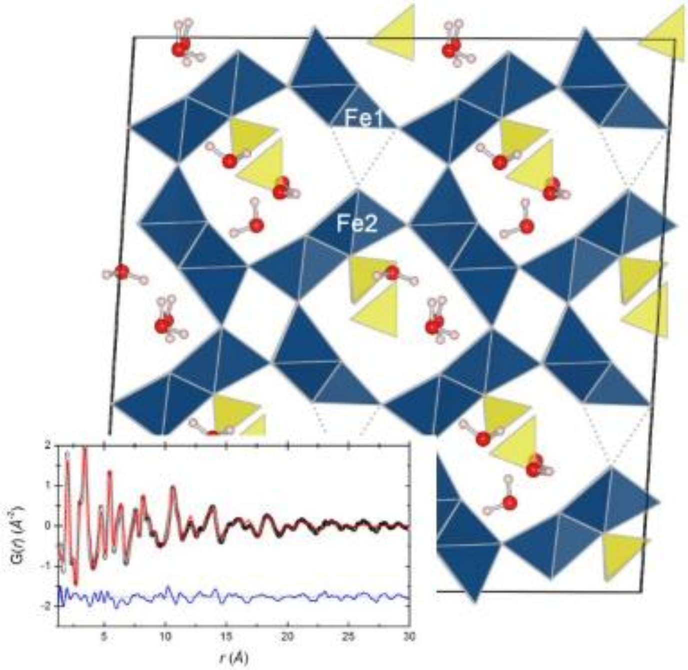

Figure 1.3: *Schwertmannite structure proposed by Fernandez-Martinez et al. (2010).*

1.3.2. Hydrobasaluminite/basaluminite

Hydrobasaluminite and basaluminite are poorly-crystalline aluminum hydroxysulfates that form plastic clay-like whitish-colored precipitates (Adams and Rawajfih, 1977; Bannister and Hollingworth, 1948). Hydrobasaluminite [$Al_4(OH)_{10}(SO_4)\cdot16\text{-}34H_2O$] is the hydrated variety of basaluminite [$Al_4(OH)_{10}(SO_4)\cdot5H_2O$]. In natural systems, hydrobasaluminite directly precipitates from solution at pH between 4.5 to 5.5 (Adams and Rawajfih, 1977; Nordstrom, 1982b). However, hydrobasaluminite is not frequently described in the literature due to its spontaneous dehydration under atmospheric conditions, yielding basaluminite in an irreversible process under natural conditions (Brydon and Singh, 1969; Hollingworth and Bannister, 1950). The structure of basaluminite has been the object of different studies. Even though it was initially considered a mineral (Hollingworth and Bannister, 1950), later studies suggested the idea that basaluminite is actually a nanoscopic version of the mineral felsobanyaite (Fig. 1.4) (Clayton, 1980; Farkas and Pertlik, 1997). Note however that hydrobasaluminite is still present in the IMA list of approved mineral species as a ‘grandfathered’ species, due to its discovery prior to the establishment of the IMA itself.

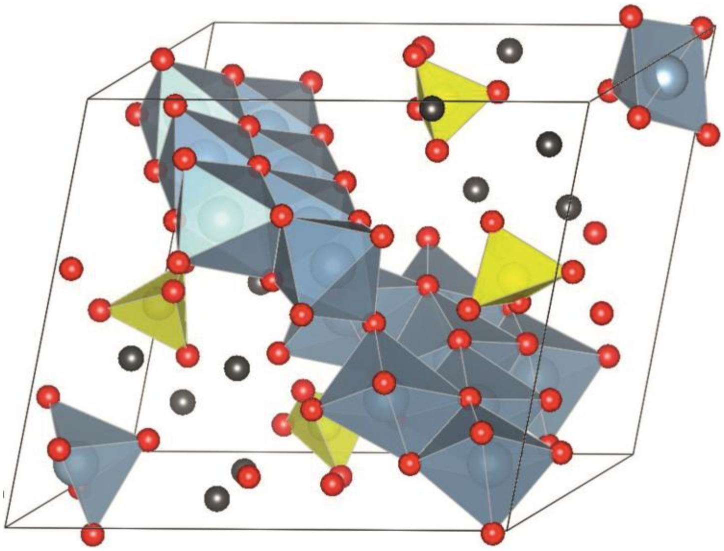

Figure 1.4: *Basaluminite structure proposed by Farkas and Pertlik (1997).*

Even though basaluminite has been less studied than schwertmannite and other iron and aluminum phases (*e.g.* jarosite, goethite and alunite), it is known that some trace elements in the acid waters, such as Cu and Si, are susceptible to be removed during basaluminite precipitation (Bigham and Nordstrom, 2000; Nordstrom, 2011; Sánchez-España et al., 2011). On the other hand, its positively-charged nature at low pH suggests that other oxyanion metals could show affinity by this phase.

1.4. EXPERIMENTAL AND THEORETICAL METHODS IN NANOSCIENCE

The disorder associated to the schwertmannite and basaluminite structures makes difficult the use of classical methods such as X-ray diffraction (XRD) for their structural characterization. Atoms at the mineral-water interface are exposed to interactions with solvents and ionic species, which cause relaxation effects and deviation from the theoretical periodic structure (*e.g*. nanocrystalline diamonds; Palosz et al., 2002). This fact is especially significant in nanocrystals due to their large proportion of surface atoms (Gilbert et al., 2004). This structural disorder makes that a non-negligible proportion of the total scattering is present as diffuse scattering in the powder X-ray patterns. Therefore, new experimental and theoretical techniques must be applied for the study of these challenging mineral nanoparticle structures.

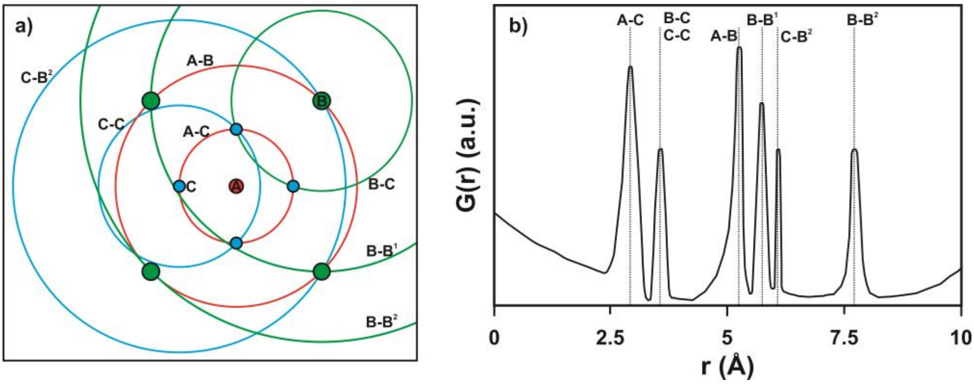

Figure 1.5: *(a) 2D view of atomic pairs such as those determined experimentally with the PDF method. The circles represent the pair interaction of A (in red), B (in green) and C (in blue) atoms with their near neighbors. (b) 1D plot of the different inter-atomic distances, a so-called pair distribution function (also called Patterson function).*

Synchrotron light sources provide intense photon beams with energies up to the hard X-ray region, which are generated by accelerating electrons in 'circular' storage rings. Electrons are injected into the storage ring, which is further equipped with electromagnets and permanent magnets devices that deviate the electrons and focus the X-ray beam generated for its use in an experimental chamber. X-ray intensities provided by synchrotron light sources are several orders of magnitude higher than in conventional laboratory sources, and the range of energies available covers a wide range from the eV to keV. Synchrotron light based techniques such as high energy X-ray diffraction (HEXD) and X-ray absorption spectroscopy (XAS) make use of these special properties of synchrotron radiation. These techniques have been previously applied to the study of poorly-crystalline minerals from AMD such as schwertmannite (Fernandez-Martinez et al., 2010; Wang et al., 2015; Waychunas et al., 1995b). In this work, basaluminite characterization using these two techniques is presented for the first time. Finally, other techniques such as nuclear magnetic resonance (NMR) and computational modeling are used to provide complementary information.

1.4.1. Pair distribution function

Pair distribution function (PDF) analysis has been used during many years to structural studies of liquids and amorphous materials and it has been recently applied to the study of natural nanoparticles (*e.g.* Fernandez-Martinez et al., 2010; Gilbert et al., 2013, 2004). PDF analysis is based on the real-space analysis of high-energy X-ray scattering (HEXS) data, obtained from a Fourier transformation of the static structure factor, *S(Q)*:

$$S(Q) = 1 + \frac{1}{N}\sum_{i,j\neq i}^{N} b_i b_j \frac{\sin(Qr_{ij})}{(Qr_{ij})} \qquad \text{Eq. 1.14}$$

Where:

$$Q = \frac{4\pi\sin(\theta)}{\lambda} \qquad \text{Eq. 1.15}$$

being N the number of atoms in the sample, b_i and b_j are the atomic scattering factor of atoms i and j, r_{ij} is the distance between atoms i and j, θ is the scattering angle and λ is the wavelength. The Debye equation (Eq. 1.14) is applicable for isotropic disordered solids. The scattering amplitude of these pairs is proportional to their atomic number. Therefore, pairs which involve heavy atoms are better represented in the *S(Q)* function. A real-space analysis of this intensity distribution can be made through a Fourier transformation, where each sinusoidal function in *S(Q)* is represented as a peak in the *G(r)* and the position of the peak represents the distance between two atoms in the structure:

$$G(r) - 1 = \frac{1}{2\pi^2 r\rho} \int_0^{\infty} Q[S(Q) - 1\,]\, sin(Qr)\, dr \qquad \text{Eq. 1.16}$$

The function *G(r)*, so-called PDF function, is not a chemical selective technique, giving a structural description of the local order around all the atoms in the structure (Fig. 1.5). More details about this technique can be found in Egami and Billinge (2003).

1.4.2. X-ray absorption spectroscopy

XAS is a probe of the local structure around selected atom species in solids, liquids and molecular gases. It is a useful complement of HEXS thanks to its chemically selectivity. This technique is commonly employed to characterize the local order of contaminants sequestered by natural nanoparticles (Peak, 2006; Randall et al., 2001; Waychunas et al., 1995a) and it has been successfully applied to study Fe and S local order in schwertmannite (Maillot et al., 2013; Waychunas et al., 1995b). XAS is based on a photoelectron excitation process, and it is based on the measurement of the absorption coefficient as a function of the incident energy. The absorption edge is observed when the incident photon has an energy equal to the binding energy of a core-level electron (*i.e.* 1s, 2s, $2p_{1/2}$, $2p_{2/2}$). When an electron from the core-level 1s, 2s, $2p_{1/2}$ or $2p_{2/2}$ is excited, the edge is called K, L1, L2 or L3, respectively. XAS is traditionally divided into two regions which give different information:

- X-ray absorption near edge structure (XANES) region. This region is within about 50-100 eV above the absorption edge. The photoelectron is strongly scattered by the atoms surrounding the studied element and the amplitude of the multiple scattering is important. The shape of the XANES is strongly sensitive to the formal oxidation state and the coordination chemistry of the element.
- Extended X-ray absorption fine structure (EXAFS) region. This region is within 80 to 1000 eV above the absorption edge. In this energy range the photoelectron has sufficient energy for exploring its surroundings, and the absorption signal can be treated with a multiple scattering approach. A Fourier transformation of the EXAFS signal provides structural information showing the distance and coordination number between studied elements and nearest neighboring atoms (Fig. 1.6). The EXAFS function [$\chi(k)$] is defined as:

$$\chi(k) = \sum_j A(r_j,k)\sin[2kr_j + \Phi_j(k,r)]e^{-2\sigma_j^2k^2}e^{-2r_j/\lambda_j(k)} \qquad \text{Eq. 1.17}$$

where k is the wave-vector of photoelectron and j involves all the coordination shells around the excited atom. $A(r_j,k)$ is the amplitude factor proportional to the number of atoms in each shell and inversely proportional to square-distance between the excited atom and the atom in the j shell (kr_j^2). $\Phi_j(k,r)$ is the phase shift originated by scattering from excited and neighboring atoms. $e^{-2\sigma_j^2k^2}$ is the thermal disorder (Debye-Waller factor) and $e^{-2r_j/\lambda_j(k)}$ describes the inelastic processes during the propagation of the photoelectron.

The determination of the X-ray absorption coefficient can be performed in so-called transmission and fluorescence modes. Transmission is the appropriate protocol for samples with high concentrations of the studied element (higher than hundreds of ppm). On the other hand, fluorescence is common in samples with low concentrations of the studied element. Further information about XANES and EXAFS can be found in Newville (2004).

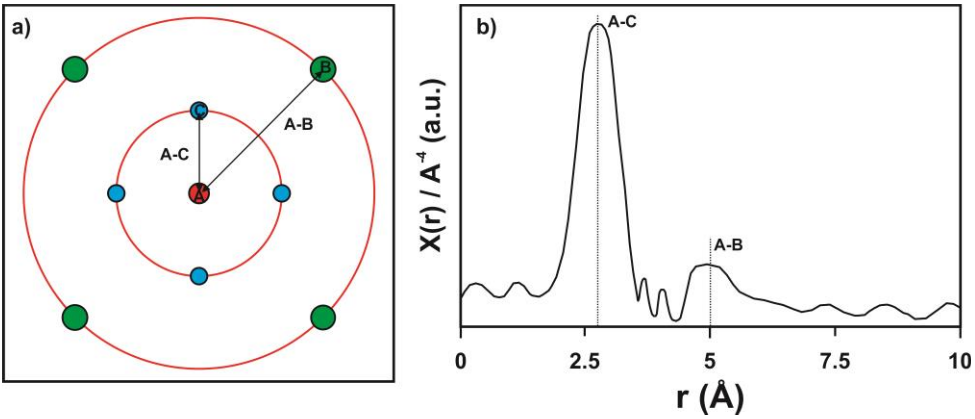

Figure 1.6: *(a) Schematic 2D atomic interaction during an X-ray absorption process, where atom A (in red) has been excited and electrons interfere with its neighbor B (in blue) and C (in green) and (b) EXAFS spectra in real space where the map of atomic neighbors is shown.*

1.4.3. Nuclear magnetic resonance

NMR spectroscopy is an energy absorption process by the nucleus in the sample, when this sample is placed in a magnetic field and it is subjected to radiofrequency (RF) radiation at the appropriate frequency. The frequency of the incident radiation necessary to induce absorption depends on three parameters: (i) the type of nucleus (*e.g.* ^{1}H, ^{27}Al), (ii) the chemical environment of the nucleus, and (iii) the strength and relative orientation of the externally-applied magnetic field. Nuclei possessing non-zero “spin”, such as ^{1}H (spin-1/2 nucleus), can be imaged as tiny bar magnets. An ensemble of these nuclei will have a random distribution of magnetic moments. When these nuclei are placed within a magnetic field, it is energetically more favorable (low-energy state) to be aligned with the magnetic field, than to be opposed to it (high-energy state). The frequency of the absorbed NMR signal is the energy difference (ΔE) between the energy states:

$$\Delta E = \gamma h B / 2\pi \qquad \text{Eq. 1.18}$$

where h is the Planck’s constant ($6.63 \cdot 10^{-34}$ m^2 kg s^{-1}), γ is the gyromagnetic ratio (constant for a particular nucleus) and B is the intensity of the experienced magnetic field (Tesla).

With the ensemble of nuclei in a magnetic field, the number of nuclei in a lower-energy state is different compared to a higher-energy state, and this difference is given by a Boltzmann distribution, according to Eq. 1.19:

$$\frac{N_{high}}{N_{low}} = e^{-\Delta E/kT} = e^{-hv/kT} \qquad \text{Eq. 1.19}$$

where N_{high} and N_{low} represent the population (in number) of nuclei in high and low-energy state, respectively, k is the Boltzmann constant, T is the absolute temperature (K) and v is the frequency. The intensity of the detected NMR signal is then related to this excess (usually very small) number of nuclei in the lower energy level. Therefore, the NMR signal depends on the type of nucleus (γ), and is larger in stronger magnetic fields and/or at lower temperatures.

Different nuclei (*e.g.* ^{1}H, ^{27}Al) will have relatively large differences in their resonance conditions (*i.e.* frequencies). However, similar nuclei (*e.g.* ^{1}H, ^{1}H) can have slight differences in their resonance frequencies, depending on their local environment. This can occur, for example, if the external magnetic field is partially canceled by an induced magnetic field originating from the motions of nearby electrons. The magnitude of this phenomenon depends then on the electron environment around the nucleus (Fig. 1.7) (*e.g.* coordination, type of bond, *etc.*). The magnetic field perceived by the nucleus

(B_{local}) will be slightly altered from the applied field B_0, so the resonance condition can be given by:

$$v = (\gamma/2\pi)B_{local} = (\gamma B_0/2\pi)(1 - \sigma) \qquad \text{Eq. 1.20}$$

where σ is a non-dimensional screening or shielding constant.

The signal measured in NMR is a time-domain signal with contributions from many different environments of the same type of nuclei. Frequency-domain NMR spectra are then obtained by Fourier transformation of the recorded time-domain data, which has usually been acquired after much signal-averaging. The difference between the signals obtained from a reference B_{ref} and the real signal obtained by B_{local} is termed the *chemical shift* (δ), which is expressed in parts per million (ppm, dimensionless number):

$$\delta = \frac{v_{ref} - v_{sample}}{v_{sample}}\, x\; 10^6 \qquad \text{Eq. 1.21}$$

where v_{ref} is the reference resonance frequency and v_{sample} is the sample resonance frequency. Further information about NMR can be found elsewhere Levitt (2008).

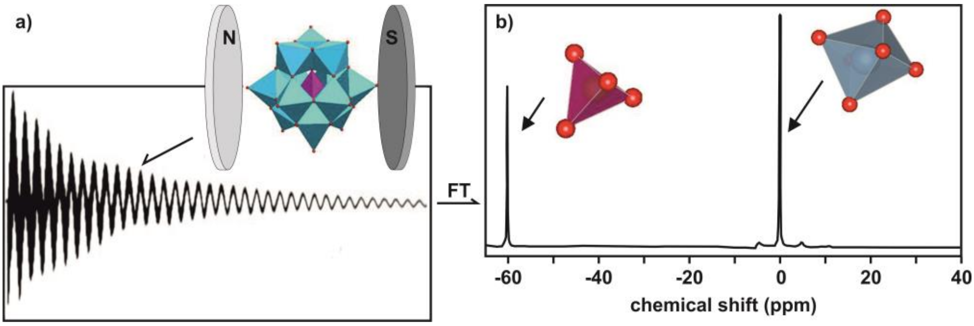

Figure 1.7: *Schematic representation of (a) a NMR measurement of an* Al_{13} *Keggin ion (where aluminum is located in tetrahedral (purple) and octahedral (blue) coordination) and (b) the Fourier transformation where each aluminum is represented by a single peak with a specific chemical shift. FT: Fourier transformation.*

1.4.4. Reverse Monte Carlo analysis

The reverse Monte Carlo (RMC) technique uses a Monte Carlo method to explore the configurational space and fit the structure factor, *S(Q)*, the PDF, *G(r)* or both. The analysis starts from a random atomistic model, and the atomic positions are updated following a Monte Carlo stochastic method driven by the minimization of:

$$\chi^2 = \sum(y_{exp} - y_{calc})^2 / \sigma^2 \qquad \text{Eq. 1.22}$$

In the RMC method an atomic displacement is accepted if the χ^2 decreases. In the opposite case, it is accepted with a probability $p = min(1, exp(-\Delta\chi^2/2))$. This allows the system to escape from local minima. More details about this technique can be found in McGreevy and Pusztail (1988) and Keen (1998). In this doctoral dissertation, the RMC analysis has been used to obtain atomistic model of basaluminite. In contrast with RMC models applied to the study of amorphous materials, this case is challenging because basaluminite is not amorphous. Therefore, a constrained RMC has been used, using constrains obtained from other experimental techniques such as ^{27}Al NMR and XAS.

1.5. AIMS AND OBJECTIVES

Despite its common occurrence in areas affected by AMD and ASS, basaluminite has been less studied than Fe-oxyhydroxysulfates due to: (i) iron concentrations are often higher than those of aluminum in these environments; (ii) pure aluminum precipitation is rare due to the fact that it occurs at higher pH than iron, making that a non-negligible part of the aluminum co-precipitates within iron phases; (iii) iron phases have been previously described as scavenger of potentially toxic elements such as As, whereas, up to our knowledge, only less hazardous elements for animals and plants (*e.g.* Si) have been reported to be strongly adsorbed by Al-phases; and (iv) aluminum is a light element difficult to characterize by conventional and synchrotron techniques. Therefore, structural and geochemical properties of basaluminite have been largely ignored in the literature, with only few works reporting their reactivity in AMD and ASS (Adams and Rawajfih, 1977; Clayton, 1980; Farkas and Pertlik, 1997; Hollingworth and Bannister, 1950; Sánchez-España et al., 2011).

The aim of this doctoral dissertation is to improve our knowledge about the environmental relevance of basaluminite, addressing its poorly-crystalline structure and its reactivity using experimental techniques based on synchrotron radiation. The following objectives were defined:

1. To simulate in the laboratory the contaminant attenuation processes occurring due to the increase of pH in natural waters and in treatment systems. These processes lead to precipitation of schwertmannite and basaluminite, in increasing order of solution pH. In natural aerated waters, this different pH makes that the reactivity of the aluminum phases is masked by the precipitation of iron phases, which retain most of the contaminants.
2. To characterize the behavior of the AMD solution when precipitated under anoxic conditions (*i.e.* preventing precipitation of iron), simulating systems where aluminum controls the solution chemistry. These experiments will give an idea of the real capacity of basaluminite for removal of contaminants, including those toxic elements (*e.g.* As and Se).

3. To quantify the maximum adsorption capacity of basaluminite for these potentially toxic elements under controlled environmental conditions. Resulting data will be compared with those previously reported for Fe-phases, allowing assessing the potential role of basaluminite in the mobility of contaminants in AMD and ASS.
4. To obtain structural information at the atomic scale about the localization of contaminants removed by basaluminite. This information can subsequently be considered in geochemical models describing the long-term fate, transport and bioavailability of contaminants in the environment.
5. To achieve a new structural and mineralogical definition of basaluminite and to review its geochemical properties by using a set of advanced high-resolution techniques available for nanoscience, including both experiments and computational modeling.

1.6. THESIS OUTLINE

The present thesis is organized in an introductory chapter, three main chapters with scientific results and a chapter with general conclusions. Each main chapter consists of a short abstract, introduction, methodology, results, discussion and conclusions. This structure has been chosen due to that each main chapter achieves its objectives through different starting hypotheses and methodological strategies. Thus, each chapter can be independently read, although some information can become redundant. The resulting structure is summarized as follows:

Chapter 1: Introduction

This chapter exposes the problem of pollution by AMD and ASS that motivated the present thesis. The most important mineral phases precipitating in these environments are explained, indicating the advances and gaps in our knowledge about these phases and their environmental implications. Finally, experimental and modeling techniques specific for characterization of poorly-crystalline mineral phases are outlined.

Chapter 2: The potential role of aluminum hydroxysulfates in the removal of contaminants in acid mine drainage (Carrero et al., 2015)

This chapter describes laboratory neutralization experiments performed using natural reduced acidic water. Mechanisms of contaminant removal were studied by correlating the chemical evolution of the experiments with the precipitation of newly-formed phases (mainly schwertmannite and basaluminite). The main processes controlling the attenuation of contamination in water courses or treatment systems were inferred, as well as the heretofore unidentified affinity of basaluminite for potentially toxic elements.

Chapter 3: Arsenic and selenium scavenging by basaluminite: Insights into the reactivity of aluminum phases in acid mine drainage

In this chapter, isotherm adsorption experiments of As and Se into basaluminite and schwertmannite were performed. Both the adsorption mechanisms and the structural coordination were determined using synchrotron-based experiments such as PDF and EXAFS. High adsorption capacities and strong retention mechanisms of As and Se into basaluminite were determined and compared with our own and previously-reported data for schwertmannite.

Chapter 4: The nanocrystalline structure of basaluminite, an aluminum hydroxide sulfate from acid mine drainage

This chapter shows the results of a structural characterization of poorly-crystalline basaluminite obtained by combining synchrotron-based analysis (HEXD-PDF and EXAFS), ^{27}Al NMR and reverse Monte Carlo modeling. Similitudes and differences between basaluminite and the structure of felsöbányaite are described.

Chapter 5: General conclusions

This final chapter presents the summarized conclusions of the performed research, including some outlooks.

CHAPTER II

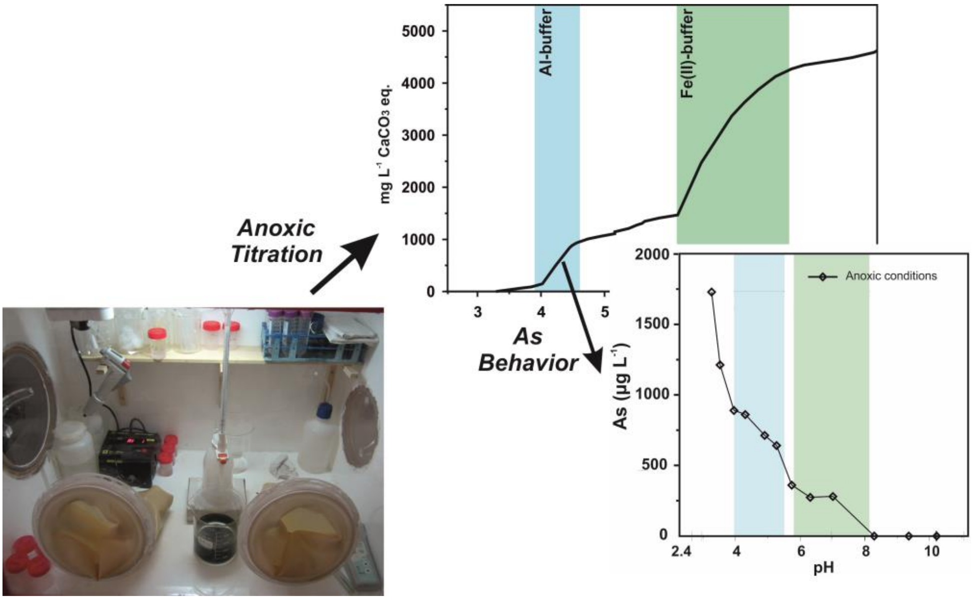

The Potential Role of Aluminum Hydroxysulfates in the Removal of Contaminants in Acid Mine Drainage

ABSTRACT

Sorption of trace elements onto poorly-crystalline Al-hydroxysulfate minerals from acid mine drainage (AMD) has received less attention compared to similar Fe(III)-phases because the former are less abundant in many mine drainage environments. In addition, Al-hydroxysulfates precipitate at a higher pH, so their sorption characteristics could be masked or less significant after sorption of trace elements to Fe minerals, which form at lower pH. In this study, oxidation and titration experiments were conducted with Fe(II)-rich AMD solutions under atmospheric and anoxic conditions to elucidate, individually, the sorption capacity of trace elements in solution by Fe and Al-hydroxysulfates. Under atmospheric conditions, precipitation of Fe(III) as schwertmannite, led to total removal of As, Cr, Fe, and Pb in solution and 50% of Al. Subsequently, contaminant-depleted solution began to be controlled by precipitation of basaluminite, which acted as an effective sink for the remaining Al, Cu and Si. On the contrary, under anoxic conditions, neutralisation of Fe(II)-rich solutions led first to the basaluminite precipitation, keeping all Fe available in solution and unveiling a heretofore unknown affinity for As and Cr. Basaluminite retains 60% of As in solution compared to 100% removal of As by schwertmannite. However, the sorption capacity of basaluminite is even more significant than that of Fe-phases, considering that Al concentrations in solution were much lower than those of Fe. These findings give new insights into the processes controlling contaminant mobility in anoxic environments (*e.g.* the bottom of AMD-affected water reservoirs) and pose new opportunities for treatment strategies.

2.1. INTRODUCTION

Contamination of receiving waters and sediments by acid mine drainage (AMD) is one of the main environmental problems associated with mining of sulfide-bearing ore deposits (Nordstrom and Alpers, 1999a; Nordstrom, 1982a). These acidic waters have high concentrations of sulfate and metals and metalloids (from now on referred as 'metals') and result from the continuous exposure of sulfide-rich mining wastes, derived mainly from coal fields or massive sulfide ores, to oxygen and water. Pollution by AMD is a serious environmental problem affecting active and abandoned mining areas around the world. Examples of contamination by AMD are described in detail in the Appalachian coalfields (USA) (Herlihy et al., 1990; Powell, 1988), in the Gangreung coalfield (Korea) (Yu and Heo, 2001; Kim and Chon, 2001) and in the Iberian Pyrite Belt (IPB; Iberian Peninsula) (Leblanc et al., 2000; Sáinz et al., 2002; Sarmiento et al., 2009a), among many others. The IPB is one of the most strongly AMD-affected areas worldwide (Nieto et al., 2013). In addition, processes that form AMD can operate within mine waste materials long after mining has stopped and AMD leachates can persist for many decades or even centuries after mine operations cease (Younger, 1997).

Acid mine drainage is characterized by high concentrations of sulfate, iron (from sulfide mineral oxidation, mainly pyrite) and aluminum (from weathering of the host rocks), in addition to the presence of other trace elements. In cases with limited oxygen renewal, such as in underground shafts, the emerging acidic water is depleted in oxygen, and thus contains high concentrations of Fe(II). In atmospheric conditions, the presence of oxygen and, mainly, the activity of extremophile microorganisms catalyze the total oxidation of Fe(II) to Fe(III) after a few meters of flow (Nordstrom and Alpers, 1999a). Under such conditions, both AMD hydrochemistry and mineralogy are controlled mainly by the SO_4-Fe(III) and SO_4-Al systems (Bigham et al., 1996b; Nordstrom and Alpers, 1999a).

In AMD-affected streams, high concentrations of ferric iron and sulfate favor the spontaneous precipitation of schwertmannite [$Fe_8O_8(OH)_{(8-2x)}(SO_4)_x \cdot nH_2O$; with x varying from 1 to 1.75], a poorly-crystalline Fe-oxyhydroxysulfate (Bigham et al., 1994, 1990; Fernandez-Martinez et al., 2010; Yu et al., 1999). Schwertmannite has a high capacity to remove trace elements, particularly As and Cr, from AMD solutions (Acero et al., 2006). The oxidation state seems to be an important factor in the removal processes. For instance, arsenic mobility may be controlled by As(V) sorption onto schwertmannite under acidic conditions (Burton et al., 2009; Maillot et al., 2013). Consequently, the spontaneous nucleation and growth of schwertmannite can lead to a natural attenuation of contamination (Courtin-Nomade et al., 2003; Fukushi et al., 2003; Schwertmann et al., 1995). The precipitation of schwertmannite is also induced by the progressive increases of pH due either to AMD mixing with pristine receiving waters or to alkali addition in AMD treatment systems. With the progressive increase of pH, after all aqueous iron has precipitated, aluminum starts precipitating as basaluminite [$Al_4(SO_4)(OH)_{10}\cdot 4\text{-}5H_2O$], a poorly-crystalline Al-hydroxysulfate (Farkas and Pertlik, 1997; Hollingworth and Bannister, 1950; Nordstrom, 1982b). Basaluminite has been less studied than schwertmannite, though it is also known that it has a strong potential to remove elements such as Cu and Si (Bigham and Nordstrom, 2000; Nordstrom and Alpers, 1999a).

The precipitation sequence of schwertmannite followed by basaluminite as the pH is increased by alkali addition, as well as their influence on the trace element mobility, has been reported in laboratory titration experiments (*e.g.* Lee et al., 2002; Sánchez-España et al., 2011) and field treatment systems (Caraballo et al., 2011; Macías et al., 2012). The alkaline neutralization of Fe(III)-Al-SO_4-rich AMD solutions exhibits two buffers at pH ranges between 2-4 and 4.5-6 that are related to Fe and Al hydrolysis, and subsequent precipitation of schwertmannite and basaluminite, respectively. In this precipitation sequence the sorption capacity of trace elements by basaluminite evidently is masked by the previous schwertmannite precipitation. No study concerning the behavior of contaminants during the exclusive precipitation of basaluminite (*i.e.* avoiding schwertmannite formation) has been reported in the scientific literature.

To help bridge this gap, the present study reports the results of AMD neutralization experiments performed in the laboratory under two different conditions: (i) under atmospheric conditions, to simulate the oxidation of Fe(II) to Fe(III) and the natural precipitation of Fe in the first instance, and the subsequent formation of Al-hydroxysulfates; and (ii) under anoxic conditions, using a Fe(II)-rich AMD solution, to precipitate first the Al-hydroxysulfates so their reactivity with the natural contaminants present in AMD can be isolated. Results from the two experiments were compared to identify the individual trace element removal capacities of poorly-crystalline Fe and Al phases. This is relevant not only for AMD-affected receiving waters, but also for other environments where poorly-crystalline precipitates as basaluminite are present, such as acid sulfate soils (ASS) (Adams and Rawajfih, 1977; Jones et al., 2011). However, understanding the geochemical processes controlling metal mobility during Al and Fe precipitation required further detailed characterization studies beyond chemical analyses. The low crystallinity of these precipitates limited the use of conventional X-ray techniques for their mineralogical characterization. In this study, high-energy X-ray diffraction (HEXD) using synchrotron-based radiation helped to overcome this obstacle.

2.2. MATERIALS AND METHODS

2.2.1. Field site and sampling description

Laboratory experiments were conducted using Fe(II)-rich acidic waters collected from an underground mine gallery at the Perrunal abandoned mining district (IPB, SW Spain). Some representative samples were collected in September 2012, during the dry season, when the stream flow was approximately 1 L s^{-1}. The pH, redox potential, electrical conductivity (EC), dissolved oxygen (DO), temperature and Fe(II)/Fe(III) speciation were measured on site. The samples were collected in airtight high density polyethylene 5 L containers, previously washed in the acid stream, and stored without exposure to air, in dark conditions and cooled to prevent Fe(II) oxidation. After collection, the samples were rapidly transported to the laboratory where the titration experiments were started immediately. An aliquot (60 mL) was filtered through a 0.45 µm nylon filter, acidified with HNO_3 to pH < 1 and stored in plastic vials at 277 K for further chemical analysis.

2.2.2. Neutralization experiments

Two neutralization experiments by alkaline titration of the Fe(II)-bearing AMD samples were conducted in the laboratory under different conditions:

- Oxygen-saturated atmosphere (atmospheric conditions): The experiment consisted firstly of a spontaneous oxidation of Fe(II) to Fe(III) (*i.e.* pre-titration oxidation), followed by a titration. To this end, a volume of 4 L of acid water was transferred to a glass beaker. The experiment was monitored using two, 20 mL aliquots that were retrieved daily; one aliquot was used to measure pH, redox potential, EC, temperature, DO and Fe speciation, and the other aliquot was used for chemical analysis after filtration and acidification. The experiment was performed at room temperature (300 K) while monitoring water loss due to evaporation. When all Fe(II) in solution was oxidized to Fe(III), an aliquot was filtered through a 0.1 µm filter and used to carry out the titration by alkaline addition, in duplicate: (i) 100 mL of Fe(III)-AMD solution were used to obtain the titration curve, and (ii) 200 mL of Fe(III)-AMD were titrated to sample the solution at desired pH values (mainly before, during and after the different buffering regions). The titration consisted of adding drop-wise a 0.01 mol L^{-1} $Ca(OH)_2$ solution while constantly stirring the sample using a magnetic bar. The pH was continuously monitored using a pH-meter. Solution samples (*ca.* 20 mL) were filtered and acidified for major and trace elements analysis.

- Oxygen-free atmosphere (anoxic conditions). This experiment was performed in such a way as to maintain the Fe in its ferrous state throughout the experiment. To this aim, the AMD solution was deaerated by continuously bubbling N_2 through the sample for 1 hour and then storing the sample inside a nitrogen-filled glove box to prevent oxidation during the experiment. The oxygen concentration in the glove box was less than 0.4% during the experiment. As in the experiment under atmospheric conditions, though without the first oxidation step, the Fe(II)-AMD solution was first filtered and then titrated using a previously deoxygenated 0.01 mol L^{-1} $Ca(OH)_2$ solution, in duplicate: (i) an aliquot of 100 mL was used to obtain the titration curve and (ii) another aliquot of 200 mL was used for sampling the solution at desired pH values during the neutralization. The solution samples (*ca.* 20 mL) were filtered for Fe speciation analysis and acidified inside the glove box for analysis of major and trace elements. After obtaining the titration curve, the final suspension of neutralized acid water and the newly-formed precipitates were exposed to atmospheric conditions without stirring to induce their spontaneous oxidation (*i.e.* post-titration oxidation). Both pH and Fe speciation were also monitored during this oxidation and solution samples (*ca.* 20 mL) were collected, filtered and acidified for major and trace elements analysis.

Several newly-formed solids were observed and collected in each pH-buffering region during the neutralization experiments. These new solids were one precipitate from the pre-titration spontaneous oxidation, three precipitates from the titration under atmospheric conditions, two precipitates from the titration under anoxic conditions and two precipitates from the post-titration spontaneous oxidation. The latter samples were examined to determine any phase transformations during the oxidation. All these solids were separated by centrifugation and then rinsed several times with ultrapure water.

2.2.3. Analytical techniques

The pH, redox potential, EC and temperature were measured with a portable multi-parameter Crison Mm40+ instrument, calibrated with different buffers for pH (4, 7 and 9.2) and standard solutions for redox potential (220 and 468 mV) and conductivity (142 and 1471 µS cm^{-1} and 12.8 mS cm^{-1}). Measured redox potentials were corrected in order to obtain the Eh with respect to the standard hydrogen electrode (Nordstrom and Wilde, 1998). The DO was measured using a Hanna DO meter HI9143. The Fe(II)/Fe(III) concentration was determined using 1,10 phenanthroline according to standard methods (Tamura et al., 1974) with a Hach DR/890 spectrophotometer. The aqueous chemistry of starting solutions and aliquots collected both during spontaneous oxidations and titration experiments was analyzed by inductively coupled plasma and atomic emission spectroscopy (ICP-AES; Jobin Yvon Ultimate 2) in the laboratories of the University of Huelva. The chemical analysis was undertaken following a custom-designed protocol specific to AMD waters (Tyler et al., 2004). Detection limits were: 140 µg L^{-1} for Al, Fe and Mg; 15 µg L^{-1} for As, Cr, Na, Ni, Pb and V; 300 µg L^{-1} for Ca and S; 60 µg L^{-1} for Co, Cu, Mn, Si and Zn; and 680 µg L^{-1} for K. The analytical error for all measurements was less than 5%.

The newly-formed precipitates were lyophilized to complete dryness using a VirTis Benchtop freeze-dryer (Hucoa-Erlöss, Spain) to avoid oxidation, mainly in those precipitates obtained under anoxic conditions. After drying, the samples were stored in plastic vials in an inert atmosphere. The HEXD measurements were conducted using the beamline ID15B at the European Synchrotron Radiation Facility (ESRF) with a monochromatic X-ray with an energy of approximately 87 keV (λ = 0.1419 Å) in transmission mode, in which the samples were loaded in polyamide (kapton) capillaries. The energy was calibrated using a CeO_2 standard (NIST 679b). The diffraction patterns were collected using a MAR345 image plate 2D detector and data were integrated using the program Fit2D (Hammersley et al., 1996). The samples were also imaged using a scanning electron microscope equipped with an energy dispersive X-ray detector to provide semi-quantitative micro-chemical analysis (SEM-EDS, JEOL JSM5410). Moreover, after acid digestion using HNO_3 the newly-formed precipitates were chemically analyzed using ICP-AES to determine the major and trace elements.

2.2.4. Geochemical modeling

Speciation-solution and reaction calculations were performed using the geochemical modeling PHREEQC code (Parkhurst and Appelo, 1999) and the Mintq.v4 thermodynamic database (Allison et al., 1998). This database was enlarged with data from Bigham et al. (1996b) and Davesne et al. (2010) to account for schwertmannite and green rust (GR) solubility, respectively. This software was used to calculate aqueous speciation of solutions and saturation indices of the solid phases [$SI = log\ (IAP/K_S)$, where SI is the saturation index, IAP is the ion activity product and K_S is the solid solubility product].

2.3. RESULTS AND DISCUSSION

The AMD solution used in the neutralization experiments contained extreme metal concentrations. In fact, this acidic leachate is one of the discharges that most profusely contributes to contamination in the Odiel River (Sarmiento et al., 2009a). The sample was collected at the exit of an underground mine gallery and exhibited acidic pH (3.29) and low DO concentration (1.30 mg L^{-1}; 15%). Its pH value matched an extremely high EC (5.98 mS cm^{-1}), and high sulfate (5990 mg L^{-1}) and iron (2040 mg L^{-1}) concentrations, in addition to other trace elements such as Al (194 mg L^{-1}), As (2 mg L^{-1}), Cu (9 mg L^{-1}), Pb (0.5 mg L^{-1}) and Zn (34 mg L^{-1}). Percentages of Fe(II) measured with respect to total Fe were higher than 98% (Table 2.1). According to the Eh-pH diagram proposed by Wagman et al. (1982), the As content in the starting AMD was presumably in the form of As(V), which was consistent with previous studies of the IPB (Sarmiento et al., 2009a).

2.3.1. Neutralization experiment under atmospheric conditions

2.3.1.1. Pre-titration spontaneous oxidation

During this experiment, an AMD sample was left at the reactor without stirring so that Fe(II) would oxidize to Fe(III) under atmospheric conditions. The spontaneous Fe(II) oxidation took 30 days to complete. During an experiment, the physic-chemical parameters of the AMD showed important variations (Table 2.1). The total Fe concentration and pH decreased from 2040 mg L^{-1} at pH 3.29 initially to 1827 mg L^{-1} at pH 2.34 when the experiment ended (Table 2.1 and Fig. 2.1a). The oxidation rate of Fe(II) to Fe(III) was calculated from the difference between the initial and final Fe(II) concentrations with respect to the time elapsed, and was found to be $1.43 \cdot 10^{-8}$ mol L^{-1} s^{-1}, in agreement with rates reported for AMD solutions from the IPB under similar conditions (Sánchez-España et al., 2007). Previous research showed significant differences between abiotic and biotic oxidation rates (*e.g.* Kirby and Elder Brady, 1998; Nordstrom and Alpers, 1999a), where the rate could vary between 10^{-12} and 10^{-7} mol L^{-1} s^{-1}, respectively. The rate obtained in the present study was congruent with a process strongly catalyzed by iron-oxidizing bacteria.

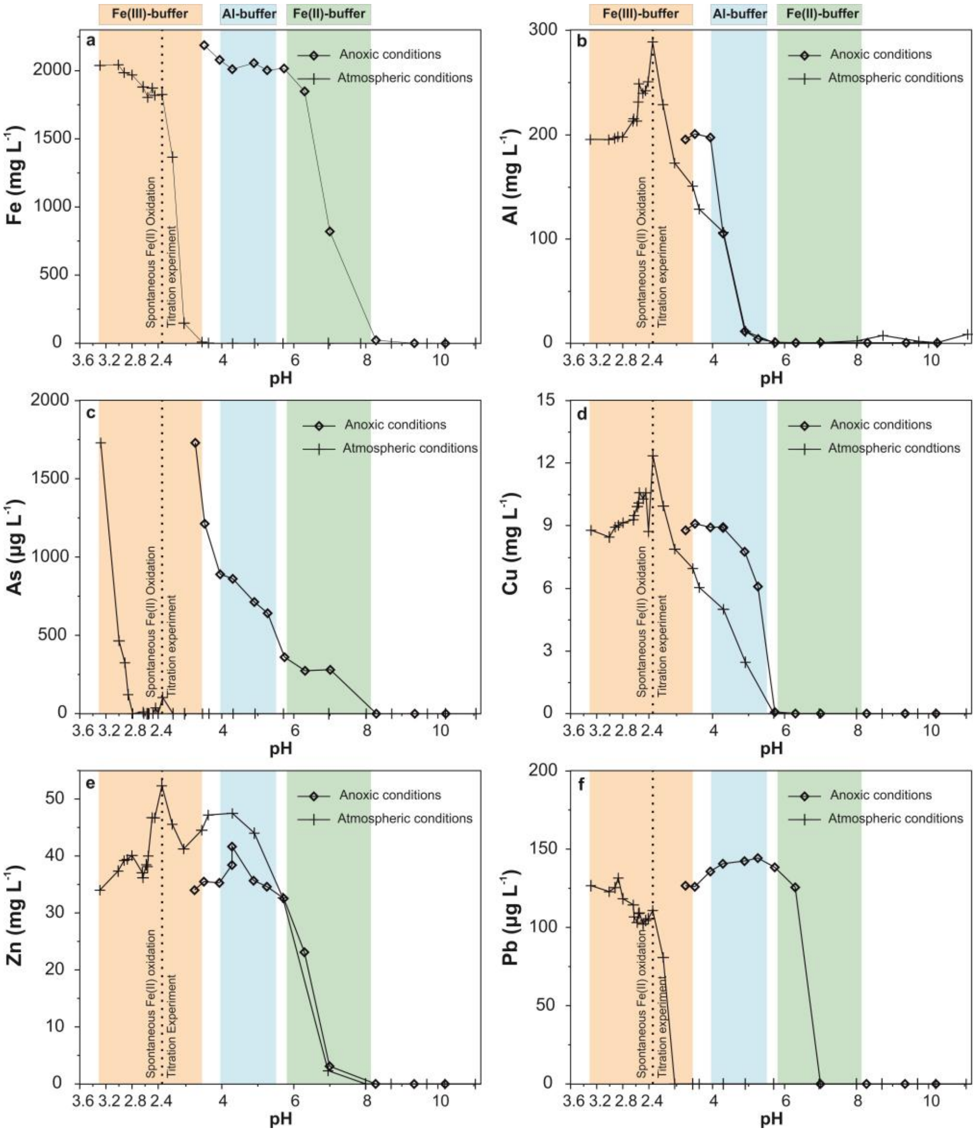

Figure 2.1: *Variation in the concentration of (a) total iron, (b) aluminum, (c) arsenic, (d) copper, (e) zinc and (f) lead as a function of pH in the pre-titration spontaneous oxidation and titration experiments under atmospheric conditions (crosses) and in the titration experiment under anoxic conditions (rhombus). Ochre, blue and green areas represent different buffers for Fe(III), Al and Fe(II), respectively.*

According to the geochemical modeling, the AMD solution was supersaturated with respect to Fe(III) phases such as ferrihydrite, jarosite, goethite, lepidocrocite and schwertmannite (Table 2.2). These calculations were congruent with visual observations of the experiment after oxidation indicating the occurrence of Fe-rich phases owing to the ochre-colored precipitates that settled to the bottom of the reactor. The hydrolysis and precipitation of Fe(III) released protons (see reactions in Table 2.2), a reaction that was consistent with the observed decreases in pH and Fe concentrations in solution.

Sample	**Date**	**time** (h)	**pH**	**Eh** (mV)	**T** (°C)	**EC** (ms cm^{-1})	**DO** (%)	**DO** (mg L^{-1})	**SO_4** (mg L^{-1})	**Fe(II)** (mg L^{-1})	**Fe(III)** (mg L^{-1})	**Fe_{tot}** (mg L^{-1})	**Fe(II)/Fe_{tot}** (%)
Field samples	11/09/2012	in flow	3.29	483	23.0	5.98	15.0	1.30	5990	2006	34	2040	98.3
Oxidation experiment	12/09/2012	24.0	3.10	561	25.8	5.99	14.1	1.22	5825	2011	33	2044	98.4
	13/09/2012	50.5	2.92	576	25.0	5.90	12.3	1.04	5897	1658	329	1987	83.4
	14/09/2012	75.0	2.87	595	24.0	5.90	9.00	0.77	5859	1972	84.7	2057	95.9
	15/09/2012	99.0	2.80	602	26.0	5.87	9.20	0.79	5786	1776	194	1970	90.1
	17/09/2012	149	2.50	617	25.5	5.82	8.90	0.78	5841	1539	306	1845	83.4
	18/09/2012	175	2.64	605	26.6	6.89	9.90	0.85	6156	1618	420	2038	79.4
	19/09/2012	197	2.63	623	26.5	6.74	9.50	0.81	6411	1346	536	1882	71.5
	20/09/2012	222	2.58	628	26.5	6.68	10.5	0.88	6607	1409	581	1990	70.8
	21/09/2012	242	2.58	635	24.0	6.73	12.9	1.13	6536	1299	650	1949	66.7
	24/09/2012	252	2.56	649	24.0	6.67	11.5	1.03	6782	941	864	1805	52.1
	26/09/2012	274	2.55	659	23.0	6.63	10.6	0.94	7136	774	1076	1850	38.4
	29/09/2012	346	2.49	670	21.0	6.68	11.2	1.05	7060	761	1112	1874	40.6
	01/10/2012	394	2.45	689	24.0	6.52	11.3	1.01	7195	364	1457	1821	20.0
	03/10/2012	444	2.41	722	25.0	6.52	13.5	1.18	7474	261	1614	1875	13.9
	05/10/2012	490	2.38	731	24.0	6.55	13.8	1.22	7310	34.0	1874	1908	1.76
	10/10/2012	616	2.34	838	23.0	7.34	67.1	6.40	8766	0.00	1827	1827	0.00

Table 2.1: *Evolution of the physical-chemical parameters and Fe speciation during the spontaneous Fe(II) oxidation experiment.*

Phases	**Reactions**	**SI Atmospheric conditions**			**SI Anoxic conditions**	
		Fe(III)-Buffer	Al-Buffer	Mg-Buffer	Al-Buffer	Fe(II)-Buffer
$Al(OH)_3$ am	$Al(OH)_3 + 3H^+ = Al^{+3} + 3H_2O$	-5.98	-1.43	-	-1.26	-
Basaluminite	$Al_4(OH)_{10}SO_4 + 10H^+ = 4Al^{+3} + SO_4^{-2} + 10H_2O$	-11.6	**1.62**	-	**3.33**	-
Boehmite	$AlOOH + 3H^+ = Al^{+3} + 2H_2O$	-3.74	**0.77**	-	**0.97**	-
Brucite	$Mg(OH)_2 + 2H^+ = Mg^{+2} + 2H_2O$	-13.5	-9.35	**0.22**	-9.64	-4.89
Calcite	$CaCO_3 = Ca^{+2} + CO_3^{-2}$	-9.27	-5.12	**3.93**	-	-
Diaspore	$AlOOH + 3H^+ = Al^{+3} + 2H_2O$	-2.04	**2.49**	-	**2.67**	-
$Fe(OH)_2$	$Fe(OH)_2 + 2H^+ = Fe^{+2} + 2H_2O$	-	-	-	-6.19	-2.22
Ferrihydrite	$Fe(OH)_3 + 3H^+ = Fe^{+3} + 3H_2O$	**0.64**	-	-	-	-
Green Rust SO_4	$Fe_6(OH)_{12}(SO_4) + 12H^+ = 4Fe^{+2} + 2Fe^{+3} + 12H_2O + SO_4^{-2}$	-	-	-	-6.52	**3.32**
Gibbsite	$Al(OH)_3 + 3H^+ = Al^{+3} + 3H_2O$	-3.47	**1.07**	-	**1.25**	-
Goethite	$FeOOH + 3H^+ = Fe^{+3} + 2H_2O$	**3.34**	-	-	-	-
Jarosite	$(H_3O)Fe_3(SO_4)_2(OH)_6 + 5H^+ = 3Fe^{+3} + 2SO_4^{-2} + 7H_2O$	**6.99**	-	-	-	-
Hausmannite	$Mn_3O_4 + 8H^+ + 2e^- = 3Mn^{+2} + 4H_2O$	-13.9	-1.06	**14.2**	-24.3	-0.61
Lepidocrocite	$FeOOH + 3H^+ = Fe^{+3} + 2H_2O$	**2.46**	-	-	-	-
Manganite	$MnOOH + 3H^+ + e^- = Mn^{+2} + 2H_2O$	-2.77	**1.52**	**6.61**	-9.95	-0.40
Schwertmannite	$Fe_8O_8(OH)_{4.5}(SO4)_{1.75} + 20.5H^+ = 8Fe^{+3} + 1.75SO_4^{-2} + 12.5H_2O$	**5.12**	-	-	-	-

Table 2.2: *Saturation indexes for supersaturated phases resulting from the neutralization experiments. All values were calculated with the PHREEQC code (Mintq.v4 database, Allison et al. 1998). Bold values represent the supersaturated phases for each pH buffer.*

During the spontaneous oxidation, the decrease with time of the Fe concentration was concomitant with a decrease in the concentration of As and Pb. The removal percentages of Fe and Pb in solution reached 15% and 20% (Fig. 2.1a and f). Arsenic concentration decreased in solution to values below the detection limit (< 15 μg L^{-1}) (Fig. 2.1c). This was in agreement with previous studies that highlighted the role of Fe(III) phases in the effective removal of As(V) at low pH (Burton et al., 2009). Due to the important evaporation observed during the experiments (approximately 30 mL d^{-1}), As, Fe and Pb concentrations increased at the end of the experiment (to approximately 0.12 mg L^{-1} for As). Evaporation was also certainly the cause of the observed increases (of up to 30%) in the concentrations of other elements such as Al, Cu and Zn (Fig. 2.1b, 2.1d and 2.1e), which appeared to be independent of the precipitation of any newly-formed phase in this range of pH.

2.3.1.2. AMD titration experiment

The titration curve of the neutralization experiment illustrates the mineral acidity distribution of the studied solution (Fig. 2.2a). As the pH increased, two main buffering regions occurred successively in the experiment, corresponding to two newly-formed precipitates (of ochre- and whitish-colored solids, respectively). The first buffering (Fe(III)-buffer) occurred at pH between approximately 2.5 and 3.2 and was concomitant with the decrease of the Fe(III) concentrations in solution, *i.e.* from 1827 mg L^{-1} initially to values below the detection limit (< 140 μg L^{-1}) (Fig. 2.1a). Geochemical modeling suggested that solutions were supersaturated with respect to Fe(III) phases such as jarosite, goethite, lepidocrocite, ferrihydrite and schwertmannite (Table 2.2). As stated in Section 2.3.1.1., the precipitation of Fe(III) released protons, counteracting alkali addition and buffering the pH of the experiment until all aqueous iron was depleted. The removal of Fe to below the detection limit (< 140 μg L^{-1}) in the Fe(III)-buffer region occurred after the addition of 1700 mg L^{-1} $CaCO_3$ equivalent (Fig. 2.3a). Moreover, As and Pb concentrations showed a similar trend to that of Fe and were depleted from the solution to below the detection limit (both < 140 μg L^{-1}) (Figs. 2.1c, f and 2.3a), completing the process that began during the spontaneous oxidation. An important point was that aluminum concentration decreased suddenly by as much as 50% (Fig. 2.3a) of its initial value, indicating a possible affinity for Fe(III)-phases. The concentrations of other elements in solution also decreased but to a much lesser extent; the final removal percentages for Cu and Zn were 35 and 20%, respectively (Fig. 2.3a).

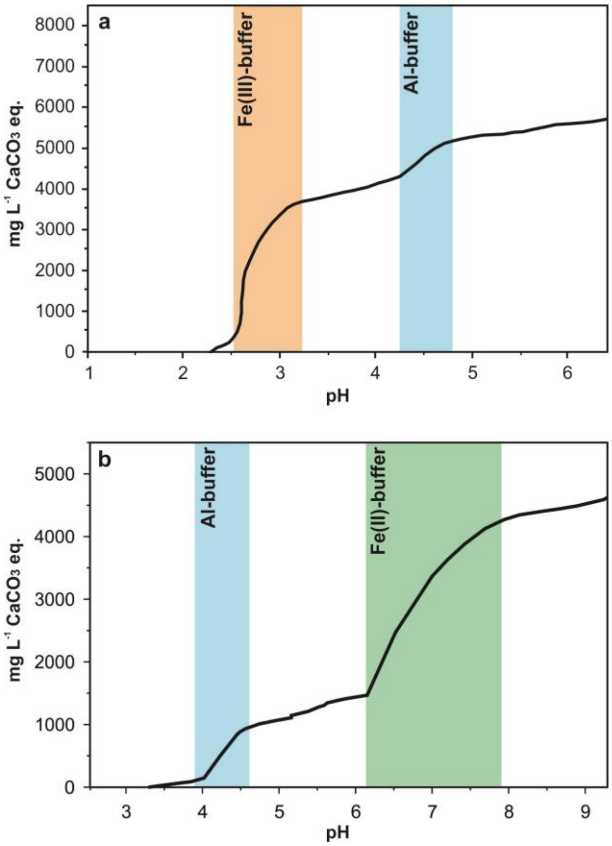

Figure 2.2: *Acid mine drainage titration curve under (a) atmospheric and (b) anoxic conditions. Ochre, blue and green areas represent different buffers for Fe(III), Al and Fe(II), respectively. Both curves were obtained without aliquot sample collection.*

The second buffer region (Al-buffer) occurred at pH values between approximately 4.2 and 4.8 (Fig. 2.2a) and matched the Al removal from the solution, *i.e.* from 152 mg L^{-1} initially to values below the detection limit (< 140 µg L^{-1}) (Fig. 2.1b). According to the geochemical calculations, these observations were consistent with the hydrolysis of Al and its subsequent precipitation. Indeed, solutions at this pH range were supersaturated with respect to Al phases such as basaluminite, boehmite, gibbsite and diaspore (Table 2.2). Complete Al removal was achieved after addition of 2250 mg L^{-1} $CaCO_3$ equivalent (Fig. 2.3a). The concentration of Cu was strongly correlated with that of Al during the AMD neutralization, and was also depleted from solution (Figs. 2.1c and 2.3a).

Finally, a third minor buffer region (Mg/Mn-buffer) occurred at pH between approximately 9.2 and 10.2 (not shown in Fig. 2.2a), and was concomitant with Mg and

Mn removal from solution, *i.e.*, from initial concentrations of 272 and 56.7 mg L^{-1}, respectively, to values below the detection limit (Mg < 140 µg L^{-1}; Mn < 60 µg L^{-1}). This buffer region was associated with the potential precipitation of brucite, hausmannite and manganite according to the geochemical modeling (Table 2.2). In addition, Zn concentrations were barely affected by Fe(III)- and Al-buffers during the neutralization. Theoretically, a different Zn-bearing precipitate could have formed in the pH range 6-8, but was not perceptible in the experiments due to low Zn concentration (< 35 mg L^{-1}) or to adsorption onto schwertmannite.

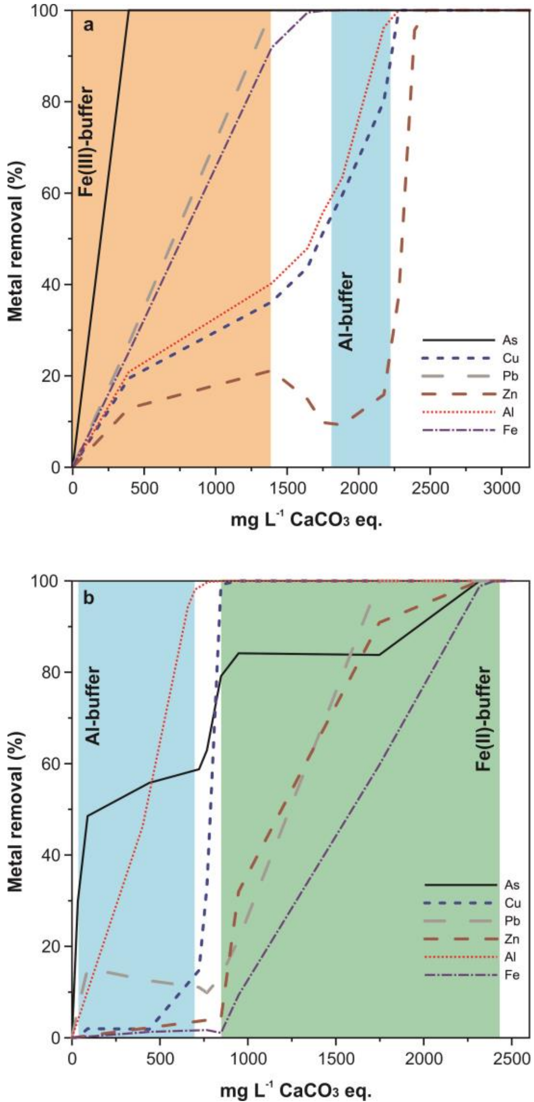

Figure 2.3: *Metal removal (%) as a function of alkaline addition (mg L^{-1} $CaCO_3$ equivalent) in the titration experiments under (a) atmospheric conditions and (b) anoxic conditions.*

The neutralization of AMD with total Fe in solution as Fe(III) consumed 8200 mg L^{-1} $CaCO_3$ equivalent for a pH variation between 2.34 to 10.2. These results were similar to those observed in previous studies (Sánchez-España et al., 2011, 2006), where AMD neutralization with Fe and Al in solution also exhibited two different buffer regions at similar pH ranges to those observed in the present study.

2.3.2. Neutralization experiment under anoxic conditions

2.3.2.1. AMD titration experiment

The neutralization experiment under anoxic conditions was performed using the naturally reduced AMD, which contained 98.4% of Fe(II) in solution (Table 2.1). In this experiment, two buffer regions were also found (Fig. 2.2b), which were associated with the successive precipitation of a whitish solid phase followed by a second solid of dark green color. The first buffer region (Al-buffer) occurred at pH values between approximately 3.9 and 4.7 and was concomitant with the decrease of Al concentration in solution, *i.e.* from 194 mg L^{-1} initially to values below the detection limit (< 140 μg L^{-1}) (Fig. 2.1b). Geochemical modeling suggested that the solutions were supersaturated with respect to Al phases such as basaluminite, boehmite, gibbsite and diaspore (Table 2.2). The removal rate for Al reached 100% in the first Al-buffer region following the addition of 700 mg L^{-1} $CaCO_3$ equivalent (Fig. 2.3b). As occurred in atmospheric conditions, Cu behavior was strongly linked to the formation of the Al precipitate (Figs. 2.1d and 2.3b), in agreement with previous studies (Bigham and Nordstrom, 2000).

The second buffer region (Fe(II)-buffer) occurred at pH between approximately 6.1 and 8.0, coinciding with the decrease of Fe concentrations in solution from 2000 mg L^{-1} initially to values below the detection limit (< 140 μg L^{-1}) (Fig. 2.1a). During the course of this experiment, the iron in solution was mainly in the Fe(II) oxidation state, with percentages of Fe(II) with respect to total Fe of approximately 90%-95%. In this case, geochemical modeling showed that the solutions were supersaturated with respect to GR phases (Table 2.2). The removal of Fe reached concentrations below the detection limit (< 140 μg L^{-1}) after addition of 1500 mg L^{-1} $CaCO_3$ equivalent (Fig. 2.3b). In this experiment, a third buffer region for Mg and Mn was not found, due to the fact that both

Mg and Mn were depleted from the reduced solutions along with the Fe(II) at the same pH range.

Arsenic was removed from the solution in both Al- and Fe(II)-buffer regions, with the Al-buffer eliminating approximately 60% of the As (Figs. 2.1c and 2.3b). Accordingly, this result seemed to indicate that the precipitates of the Al-buffer have high affinity for As. This result was masked in the titration under atmospheric conditions because As was removed below the detection limit ($< 15\ \mu g\ L^{-1}$) by precipitation with Fe(III)-phases. On the other hand, Pb concentrations sharply decreased in the Fe(II)-buffer region; and hence, its affinity for Fe seemed to be independent of the iron oxidation state, as could be deduced from comparing both experiments (Figs. 2.3a and 2.3b). Finally, Zn behaved similarly in both atmospheric and anoxic conditions (Fig. 2.1e).

This titration experiment consumed approximately 5500 mg L^{-1} $CaCO_3$ equivalent for a pH variation from 3.32 to 10.2. The first Al-buffer region in this experiment presented similar characteristics to the second Al-buffer region observed under atmospheric conditions, though with a slight change in the pH range and consumption of alkalinity. With respect to the Fe removal, both neutralization experiments presented significant differences. Under anoxic conditions, the Fe(II)-buffer required to achieve target pH values was much higher than that observed to achieve Fe(III)-buffer precipitation under atmospheric conditions. Although the alkalinity consumed in both buffers was similar, the Fe(II)-buffer included Fe(II), Mg and Mn hydrolysis, whereas the Fe(III)-buffer only implicated Fe(III) hydrolysis. This was expected due to the smaller number of protons released during the formation of Fe(II) phases (Eq. 2.1) with respect to Fe(III) precipitates (Eq. 2.2) (Table 2.2).

$$Fe_6(OH)_{12}(SO_4) + 12H^+ = 4Fe^{+2} + 2Fe^{+3} + 12H_2O + SO_4^{-2} \qquad \text{Eq. 2.1}$$

$$Fe_8O_8(OH)_{4.5}(SO4)_{1.75} + 20.5H^+ = 8Fe^{+3} + 1.75SO_4^{-2} + 12.5H_2O \qquad \text{Eq. 2.2}$$

2.3.2.2 Post-titration spontaneous oxidation

After the titration, the reactor used to obtain the titration curve was removed from the glove box and left open to the air and without stirring for four days, causing a spontaneous oxidation of the previously formed precipitates. Initial Al, As, Cu, Fe, Pb and Zn concentrations in the AMD prior to the beginning of this spontaneous oxidation were below the detection limit, whereas Mg, Mn and S concentrations were 266, 2.17 and 1830 mg L^{-1}, respectively. During the oxidation, the solution pH rapidly decreased from 10.2 to 5.65 and the precipitates that had settled to the bottom of the reactor showed a color change from dark green to ochre. This change in the nature of the solids indicated that (i) the solid phases were highly unstable in atmospheric conditions and (ii) oxidation of the solids must release protons. This proton release process has been associated with the dissolution of Fe(II) phases and their subsequent oxidation, hydrolysis and precipitation as Fe(III) phases, a very fast process at alkaline pH (Singer and Stumm, 1970). For this reason, Fe was depleted in solution before and after oxidation. On the other hand, the evolution of metallic elements in solution showed that concentrations of Mg and Mn (with final values of 921 and 79.8 mg L^{-1}, respectively) increased, but that there was no variation in concentrations of the remaining elements (Al, Cu, Fe, Pb and Zn), which remained associated with the solid phase. The metalloid As also remained in the solid phase; however, the concentration of S in solution increased (to 5520 mg L^{-1}).

2.3.3. Characterization of newly-formed phases

Identification of the different precipitates obtained during each experiment was carried out using synchrotron-based HEXD (which produced the diffraction patterns shown in Fig. 2.4). The mineralogical observations were in agreement with the thermodynamic calculations. Schwertmannite was found during the pre-titration spontaneous oxidation and the Fe(III)-buffer of the neutralization experiment under atmospheric conditions (Fig. 2.4a). The diffraction pattern was identical to that described by previous researchers (*e.g.* Fernandez-Martinez et al., 2010). Precipitates of schwertmannite occurred as micrometric aggregates composed of S and Fe with hedgehog-like morphology, as revealed by SEM-EDS (Fig. 2.5a). In addition, schwertmannite precipitate appeared to be thermodynamically the most stable phase in both spontaneous Fe(II) oxidation and Fe(III)-buffer, as suggested by the sulfur-iron Eh-pH stability diagram reported by Bigham et al. (1996b). As indicated above, in addition to Fe, 50% of the Al was removed from solution during the precipitation of schwertmannite. The fact that schwertmannite was the only phase identified in the pattern implied that Al was removed within the schwertmannite phase, or that it precipitated forming nanoparticles of such small size that they were not appreciable in the diffraction patterns.

Aluminum incorporation in Fe-oxyhydroxides is well known (Schwertmann and Wolska, 1990; Schwertmann, 1984). Previous studies on the influence of Al on the reactivity of ferrihydrite, another Fe-oxyhydroxide, have shown that the presence of Al does not alter the As binding mechanisms observed in Al-free ferrihydrites (Adra et al., 2013). However, little is known about the effect of Al in the reactivity of schwertmannite and more research is needed to determinate the precise structural location of Al in this Fe(III)-phase. In the second Al-buffer region, basaluminite occurred as the only precipitate according to the HEXD pattern, and exhibited broad diffraction peaks (Fig. 2.4a). A more exhaustive examination using SEM-EDS confirmed that the Al precipitate was present as aggregates of micrometric particles chemically composed of Al and S (Fig. 2.5b). Finally, brucite, manganite and hausmannite were the main phases found in the Mg/Mn-buffer region that was observed in this neutralization experiment, and in addition to calcite, were likely formed by dissolution of atmospheric CO_2 at high pH in the Ca-rich solutions (Fig. 2.4a).

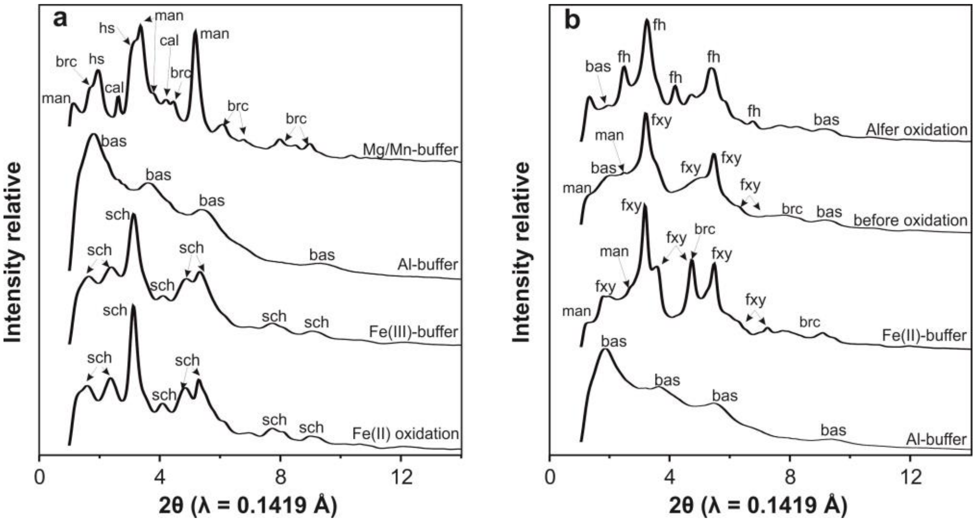

Figure 2.4: *Synchrotron-based high-energy X-ray diffraction patterns of newly-formed precipitates collected during the experiments under (a) atmospheric conditions and (b) anoxic conditions. Diffraction peaks of feroxyhyte (fxy), ferrihydrite (fh), brucite (brc), calcite (cal), manganite (man) and hausmannite (hs) match with the standard patterns (PDF) 00-013-0087, 00-046-1315, 01-088-0207, 01-086-2343, 01-074-1842, 01-080-0382, respectively, and diffraction patterns of schwertmannite (sch) and basaluminite (bas) are identical to those previously reported by Fernandez-Martinez et al. (2010) and Prietzel and Mayer (2005), respectively.*

The precipitates formed in the Al- and Fe(II)-buffer regions of the neutralization experiment under anoxic conditions were identified as, respectively, basaluminite and a complex consisting of feroxyhyte, manganite and brucite (Fig. 2.4b). During the post-titration spontaneous oxidation of the final precipitate that resulted from anoxic conditions, the phase composition changed from an initial mixture of basaluminite, manganite, brucite and feroxyhyte to a mixture of basaluminite and 6-line ferrihydrite (Fig. 2.4b). Both ferrihydrite and feroxyhyte appeared as micrometric agglomerates of globular phases chemically composed mainly of Fe (Fig. 2.5c and d).

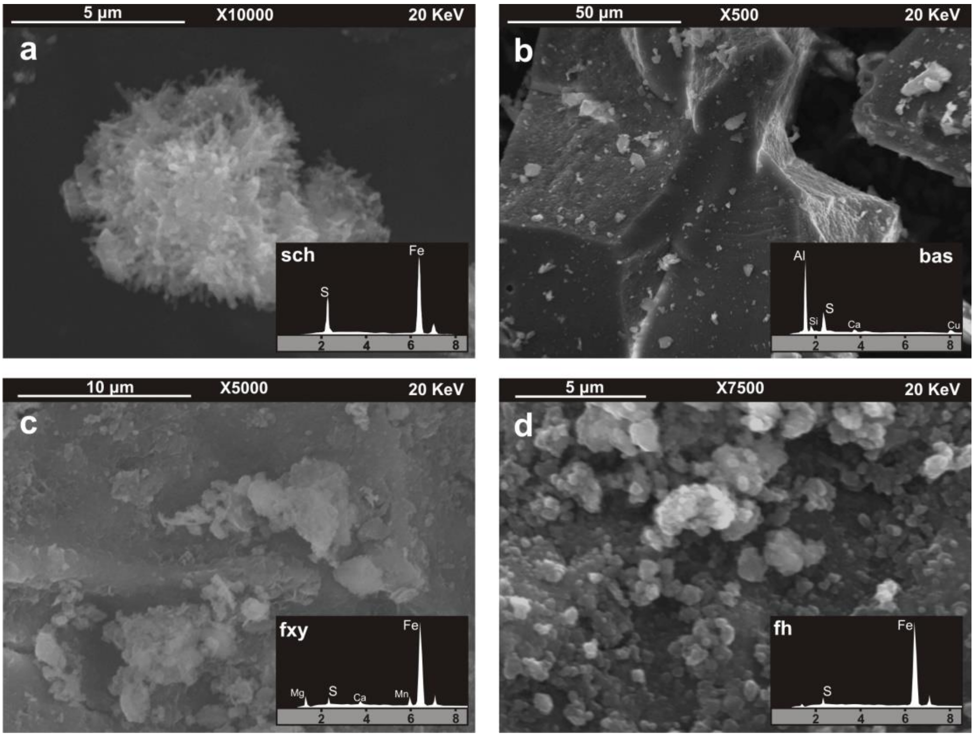

Figure 2.5: *Scanning electron microscopy images and energy dispersive spectroscopy spectra of newly-formed precipitates collected during the titration experiments under atmospheric and anoxic conditions: (a) schwertmannite (sch), (b) basaluminite (bas), (c) feroxyhyte (fxy) and (d) ferrihydrite (fh).*

The chemical and mineralogical evolution found in this study under atmospheric conditions showed similar characteristics with previous titration and oxidation experiments (Sánchez-España et al., 2011, 2006). However, the processes observed under anoxic conditions have not been described previously. The presence of feroxyhyte in the neutralization experiment under anoxic conditions was incongruent with the Fe oxidation state in solution. Feroxyhyte is a Fe(III) phase, but the Fe(III)/Fet ratio measured during the titration in anoxic conditions was variable between 5 and 10%. Two explanations are possible for this observation: (i) feroxyhyte was formed by precipitation of the 5%-10% of Fe(III) in the solution, or (ii) the pH range and the Fe(II)/Fe(III) ratio during the Fe(II)-

buffer were congruent with the formation of GR (Davesne et al., 2010; Génin et al., 1996), a phase for which the solution was supersaturated according to thermodynamic calculations (Table 2.2). Green rust has been reported to be a highly unstable intermediate phase present in the transformation of ferrous hydroxide to Fe-oxyhydroxides (Benali et al., 2001). So, GR was likely oxidized to feroxyhyte during the measurement. Green rust oxidation has been shown to be concomitant with a decrease of the solution pH, accompanied by the formation of ferrihydrite or feroxyhyte (or both), especially in systems that have arsenate or phosphate (or both) in solution (Benali et al., 2001; Refait et al., 2009). Green rust precipitation during the Fe(II)-buffer would explain the different processes observed in the neutralization experiment under anoxic conditions and the subsequent spontaneous oxidation.

Chemical compositions of the newly-formed precipitates are shown in Table 2.3. With all pollutants available in solution, spontaneous precipitation of schwertmannite under atmospheric conditions retained most of the As. Then, induced precipitation of basaluminite played a fundamental role in Cu and Si removal. Other elements such as Co, Ni and Zn were depleted from solution in the pH range of the third Mg/Mn-buffer region, probably as phases undetectable by HEXD due to their low concentrations. Under anoxic conditions, however, the initial precipitation of basaluminite retained most of the Cr and, mainly, the As. These findings suggested a high affinity of basaluminite (755 mg kg^{-1}; Table 2.3) for As, although schwertmannite affinity was higher (1550 mg kg^{-1}; Table 2.3). This fact is even more significant considering that Fe concentrations are typically higher than those of Al in AMD-affected systems. Subsequent GR precipitation removed the remaining As in solution, as well as other divalent metals. Arsenic affinity for GR has been previously reported by Bowell (1994) and Randall et al. (2001). Arsenic retention into Al-phases (*e.g.* γ-Al_2O_3 and amorphous Al-oxides) has been previously described, where Al-phases showed high adsorption capability (75 g kg^{-1} in amorphous Al-oxide at pH approximately 4) with a structural position of inner-sphere complex (Arai et al., 2001; Goldberg and Johnston, 2001). However, arsenic sorption in basaluminite seems not to have been described until now. However, this result could mean that a preferential depletion pathway for Al in solution exists under anoxic conditions. Such conditions exist in the bottom water of a stratified reservoir affected by AMD (Torres et al., 2013), or in other environments where Al-hydroxysulfates could be formed preferentially over iron oxides, as in acid sulfate soils (Adams and Rawajfih, 1977). Finally, the present study showed that AMD neutralization processes in oxygen-poor environments could have a greater efficiency than traditional remediation systems, thus highlighting the need for new research focused on the development of passive AMD treatment systems for Al-rich acid mine waters. The findings from this study corroborated those observed in the chemical evolution of the solutions, and also provided additional information for some elements not detected in solution, such as Co, Cr, Ni and V.

	Experiment	**Mineral**	**g Kg^{-1}**									**mg Kg^{-1}**							
			Al	Ca	Fe$_{tot}$	K	Mg	Mn	Na	Zn	S	As	Co	Cr	Cu	Ni	Pb	Si	V
Atmospheric	Fe(II) oxidat.	sch	0.51	0.70	462	0.80	0.21	0.04	b.l.	0.03	72.8	1550	0.82	23.0	27.6	0.72	3.17	214	138
	Fe(III)-buffer	sch	21.2	0.63	424	0.58	0.05	0.14	b.l.	0.03	68.0	32.9	0.54	23.3	294	0.80	4.30	239	11.4
	Al-Buffer	bas	226	5.30	3.36	1.18	2.06	3.13	0.36	15.1	64.5	10.9	57.5	41.1	10313	50.8	6.22	822	16.4
	Mg/Mn-Buf.	bru + man + Hs	3.20	10.8	0.25	0.62	146	28.3	0.38	17.1	14.8	4.66	520	23.3	832	323	3.79	377	9.83
Anoxic	Al-buffer	bas	197	1.33	35.5	2.50	0.68	0.05	0.52	0.49	81.9	755	3.57	112	1815	6.50	3.73	429	230
	Fe(II)-buffer	fxy	2.70	5.02	456	0.62	33.6	12.0	0.05	10.5	26.9	87.0	272	24.9	1386	164	5.13	386	12.5
	Initial Oxidat.	fxy + bas	42.9	2.23	424	1.02	9.33	10.7	0.14	8.94	44.9	397	240	45.9	2248	149	14.0	513	59.0
	Final Oxidat.	fh + bas	43.7	2.68	438	0.96	1.29	2.96	0.11	9.13	14.3	454	209	42.7	1815	129	6.63	684	58.4

Table 2.3: *Major and trace element composition of the newly-formed precipitates in both oxidation and titration experiments. Schwertmannite (sch), basaluminite (bas), feroxyhyte (fxy) ferrihydrite (fh), brucite (brc), hausmannite (hs) and manganite (man). b.l.: below detection limit*

2.4. SUMMARY AND CONCLUSIONS

In this study, several oxidation and titration experiments were conducted in the laboratory using Fe(II)-rich AMD. The reduced AMD from the abandoned Perrunal mine presented low pH values (3.29) and high concentrations of sulfate (5990 mg L^{-1}), iron (as Fe(II); up to 2040 mg L^{-1}) and other metals (*e.g.*, 194 mg L^{-1} of Al, 2 mg L^{-1} of As, 9 mg L^{-1} of Cu). The results of the study justify several conclusions.

1. Under atmospheric conditions, the spontaneous oxidation rate of Fe(II) to Fe(III) ($1.43 \cdot 10^{-8}$ mol L^{-1} s^{-1}) was congruent with a reaction catalyzed by the action of acidophilic bacteria. During the oxidation process, the solution was supersaturated in Fe(III) phases and precipitation of schwertmannite occurred, as predicted using thermodynamic calculations and confirmed using mineralogical identification. The precipitation of Fe(III) as schwertmannite was concomitant with a decrease of the As and Pb concentrations in solution.
2. Subsequently, the solutions resulting from the spontaneous oxidation were titrated by addition of a 0.01 mol L^{-1} $Ca(OH)_2$ solution to pH close to 10 under atmospheric conditions. The titration curve exhibited three Fe(III)-, Al- and Mg/Mn-buffering regions associated with the supersaturation and precipitation of, respectively, schwertmannite, basaluminite and a complex of brucite, manganite and hausmannite. These newly-formed phases seem to exert a significant mineralogical control on element mobility; in particular, schwertmannite showed high affinity for (mainly) As, whereas basaluminite selectively concentrated Cu and Si. Zinc was removed in the Mg/Mn-buffer region, probably as a single newly-formed phase that was undetectable due to the very low metal concentration in solution.
3. Under anoxic conditions, the neutralization to pH 10 by alkaline titration of the Fe(II)-rich AMD identified both an Al- and a Fe(II)-buffering region associated with the sequential precipitation of basaluminite followed by GR. As occurred under atmospheric conditions, Cu was strongly removed by basaluminite, Pb was associated with GR, and Zn probably precipitated as a single phase. Surprisingly, approximately 60% of As in solution was removed in the Al-buffer region.

4. Spontaneous oxidation under atmospheric conditions was conducted following the anoxic titration experiment. During the oxidation, the solution pH rapidly decreased and the Al, As, Cu, Fe, Pb and Zn concentrations remained below the detection limit. However, Mg, Mn and S were released to solution where their concentrations increased.
5. The precipitation of Al before Fe phases under anoxic conditions revealed that basaluminite also presents a high affinity for As and, to a lesser extent, Cr. Although As was removed by schwertmannite precipitation during the spontaneous Fe(II) oxidation, the basaluminite retention capacity for As was more significant. This was because (i) the amount of Fe phases precipitated in the AMD was ten times higher than the amount of Al phases precipitated, and (ii) the As concentration in the AMD used in the titration under anoxic conditions was several times higher than that in the titration under atmospheric conditions, because the As was previously removed during the pre-titration spontaneous oxidation in the former.

The affinity of schwertmannite for As and Cr, and the affinity of basaluminite for Cu and Si are well known. However, this results from this study describe a previously unidentified affinity of basaluminite for As and Cr, a role heretofore masked by previous precipitation of ferric phases in natural conditions. These results provide a new view on several mineral precipitation pathways that could control trace element mobility in anoxic environments, and open a new research line focusing on the optimization of treatment systems for acid mine waters.

CHAPTER III

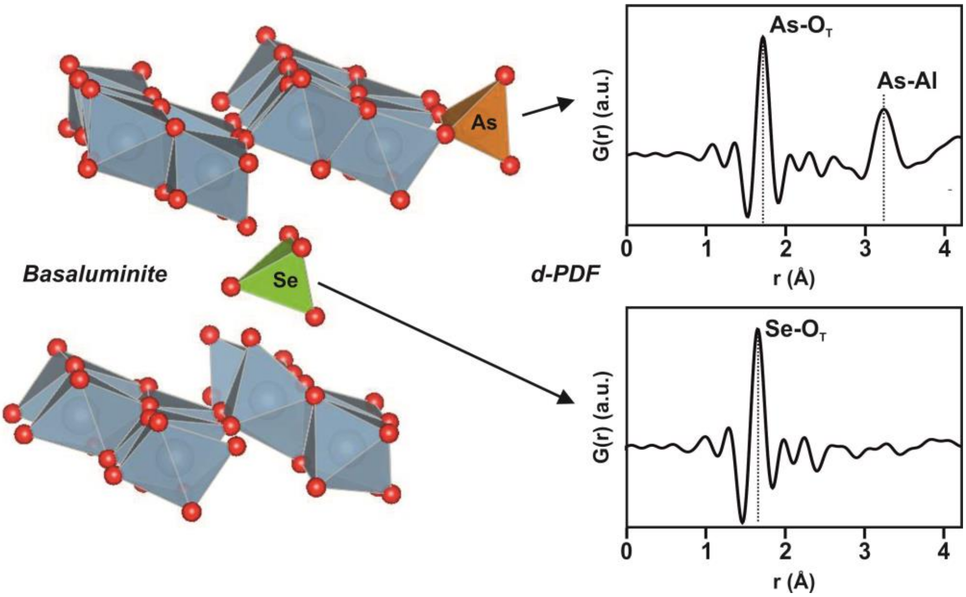

Arsenic and Selenium Scavenging by Basaluminite: Insights into the Reactivity of Aluminum Phases in Acid Mine Drainage

ABSTRACT

Basaluminite precipitation may play an important role in the behavior of trace elements in water and sediments affected by acid mine drainage and acid sulfate soils. In the present study the affinity of basaluminite and schwertmannite for arsenic and selenium is compared, and the coordination geometries of these elements in both structures are reported. Batch isotherm experiments were conducted to examine the sorption capacity of synthetic schwertmannite and basaluminite and the potential competitive effect of sulfate. In addition, synchrotron-based techniques such as differential pair distribution function (d-PDF) analysis and extended X-ray absorption fine structure (EXAFS) were used to determine the local structure of As and Se complexes. The results show that oxyanion exchange between sulfate and arsenate or selenate in solution was the main removal mechanism. Arsenate adsorption capacity by basaluminite was twice higher than in schwertmannite and three times higher than selenate in both phases. The exchange ratios were 1:2 and 1:1 sulfate with respect to arsenate and selenate, respectively. High sulfate concentrations in the solutions did not show a competitive effect for arsenate sorption capacity, but had strong impact in the selenate uptake, suggesting some kind of specific interaction for arsenate. Both d-PDF and EXAFS results indicated that bidentate binuclear inner-sphere was the most probable type of ligand for arsenate on both phases and for selenate on schwertmannite, whereas selenite forms outer-sphere complexes in the aluminum octahedral interlayer of basaluminite. Overall, these results show a strong affinity of poorly-crystalline aluminum phases such as basaluminite towards As and Se oxyanions, with adsorption capacities on the same order of magnitude as iron oxides. The results obtained in this study are relevant to the understanding of trace element behavior in environments affected by acid water, potentially opening new research lines focused on remediation by natural attenuation processes or engineered water treatment systems.

3.1. INTRODUCTION

Basaluminite [$Al_4OH_{10}(SO_4)\cdot5H_2O$] is a poorly-crystalline Al-hydroxysulfate commonly found in Al-bearing acid mine drainage (AMD) systems (Bigham and Nordstrom, 2000; Hollingworth and Bannister, 1950; Nordstrom, 1982b). Farkas and Pertlik (1997) defined basaluminite as the poorly-crystalline variety of felsöbányaite. However, although basaluminite can be found in AMD and its thermodynamic properties are broadly described in the geochemical literature and thermodynamic databases, felsöbányaite is considered a rare mineral (Farkas and Pertlik, 1997). Basaluminite precipitates from acid SO_4-Al-rich solutions with low pH values, such as water and sediments affected by (i) AMD in coalfields areas (Nordstrom, 1982b; Powell, 1988) and massive sulfide ore deposits (Leblanc et al., 2000); and (ii) acid sulfate soil (ASS) waters (Adams and Rawajfih, 1977). This precipitation releases protons and is an effective buffer for the system at a pH range from 4.5 to 5.5 (Bigham and Nordstrom, 2000; Carrero et al., 2015; Nordstrom and Alpers, 1999a). High Fe concentrations are also present in these polluted environments, which are controlled by the precipitation of another poorly-crystalline mineral, schwertmannite [$Fe_8O_8(OH)_{(8-x)}(SO4)_x\cdot nH_2O$; with x varying from 1 to 1.75]. Schwertmannite is described as a poorly-crystalline Fe-oxyhydroxysulfate (Acero et al., 2006; Bigham et al., 1994, 1990; Fernandez-Martinez et al., 2010), which precipitates at a lower pH than basaluminite (2.5-3.2) (Carrero et al., 2015).

Arsenic and selenium represent a serious environmental problem in watercourses affected by oxidation of iron sulfides ores (Dreher and Finkelman, 1992; Smedley and Kinniburgh, 2002). Both toxic elements coexist in streams, groundwater and sediments affected by AMD and ASS (Appleyard et al., 2006; Dreher and Finkelman, 1992; Smedley and Kinniburgh, 2002). The acid waters in these environments contribute to the high mobilization of both elements. Precipitation of poorly-crystalline Al- and Fe-minerals in AMD- and ASS-affected environments has a significant role in the behavior of trace elements (Bigham and Nordstrom, 2000; Bigham et al., 1994). Several laboratory experiments have reported that schwertmannite has a high affinity by As, where the sorption capacity of As(V) is higher than that of As(III) at low pH (Acero et al., 2006; Antelo et al., 2012; Burton et al., 2009), and Se (Waychunas et al., 1995b). Much less is known about the capacity of basaluminite for removing trace elements. Basaluminite has been found to be an efficient adsorbent of elements such as Cu and Si in polluted waters (Bigham and Nordstrom, 2000; Macías et al., 2012; Nordstrom and Alpers, 1999a). Recently, a significant affinity towards As has been described in systems where Fe(II)-rich AMD solutions are neutralized under reducing conditions (Carrero et al., 2015). However, the natural neutralization of acid water, typically done under oxic conditions, implies the precipitation of schwertmannite at a first stage and the concomitant removal of As and Se from solution, masking the effect of the basaluminite affinity towards these trace elements.

The high affinity by trace elements of both Al- and Fe-mineral phases seems to be related to mineral properties such as low crystallinity, small particle size (in the nanometer scale) and large specific surface areas. However, both phases have been defined as metastable minerals which can undergo mineralogical transformation during ageing processes, and thus potentially releasing previously sorbed oxyanions, and inhibiting their uptake due to the higher crystallinity of the resulting phases (Acero et al., 2006; Asta et al., 2009; Bigham et al., 1994; Farkas and Pertlik, 1997). Oxyanion sorption onto Fe-phases has been largely studied using wet chemistry and synchrotron-based techniques such as extended X-ray absorption fine structure (EXAFS) and Fourier transform of total X-ray scattering (pair distribution function; PDF) (Burton et al., 2009; Harrington et al., 2010; Sherman and Randall, 2003). While As(V) adsorption onto Fe-oxide phases present in AMD is well documented (Catalano et al., 2008; Harrington et al., 2010; Peak and Sparks, 2002; Waychunas et al., 1995a, 1993), the reactivity of poorly-crystalline Al-minerals remains less understood. To our knowledge, there are no geochemical and structural studies on the removal capacity of As and Se by basaluminite.

To fill this gap in our knowledge of the reactivity of Al-phases in acid waters, the present study examines the sorption capacity of As(V) and Se(VI) onto synthetic basaluminite and schwertmannite as a function of arsenate and selenate loadings. The solid phases resulting from these experiments were examined using high energy X-ray diffraction (HEXD) and EXAFS. These results were compared with previous values reported in scientific literature.

3.2. MATERIALS AND METHODS

3.2.1. Solid synthesis

Both As and Se adsorption experiments were carried out with synthetic basaluminite and schwertmannite. Basaluminite was synthesized by addition of 214 mL of a 0.015 mol L^{-1} $Ca(OH)_2$ solution to 30 mL of 0.05 mol L^{-1} $Al_2(SO_4)_3 \cdot 18H_2O$, according to the method described by Prietzel and Hirsch (1998). The titration was conducted by drop-by-drop addition and continuous stirring at room temperature. Synthetic schwertmannite was precipitated using the procedure described by Adams and Rawajfih (1977), where 2.506 g of $Fe_2(SO_4)_3$, previously dehydrated, was added to 1 L of Milli-Q water, preheated at 358 K, and stirred for 1 h. Both precipitates were recovered filtering the suspension through a 0.45 µm nylon membrane filter and the solids were washed several times with pure water.

3.2.2. Adsorption experiments

Adsorption isotherms were performed following the procedure previously described by Asta et al. (2009). Batch experiments were performed by the reaction of 20 mL of a As(V) or Se(VI)-doped solutions with 0.05 g of solid in high-density polyethylene plastic vials. The suspensions were continuously stirred at room temperature (300 K) and in dark during 72 h. Arsenic and selenium solutions were prepared by dissolution of sodium hydrogen arsenate ($Na_2HAsO_4 \cdot 7H_2O \geq 98\%$ of purity, from Sigma) and sodium selenate ($Na_2SeO_4 \geq 98\%$ of purity, from Acros), respectively, in Milli-Q ultrapure water, with sodium sulfate ($Na_2SO_4 \geq 99\%$ of purity, from Panreac) in sulfate-competition experiments. Arsenic and selenium uptake by basaluminite and schwertmannite was characterized by means of determining: (i) the adsorption kinetics at initial concentrations of 3.0 mmol L^{-1} of As or Se at different times (5, 15, 30 min, 1, 3, 5, 10, 24, 48 and 72 h); (ii) the adsorption capacities at different initial As and Se concentrations ($3 \cdot 10^{-2}$, $5 \cdot 10^{-2}$, 0.1, 0.4, 0.8, 1.0, 3.0, 5.0, 7.0 and 10 mmol L^{-1}) without competitive effect; and (iii) same as (ii) but in the presence of different SO_4^{2-} concentrations (5.0, 8.0, 10, 50 and 100 mmol L^{-1}) for constant As and Se concentrations (1.0 mmol L^{-1}). Finally, the pH was established at 3.5 ± 0.1 and 5.0 ± 0.1 for schwertmannite and basaluminite, respectively, by addition of HCl (36%) from Merck, and the background ionic strength was adjusted to 100 mmol L^{-1} with NaCl (≥ 99% of purity, Panreac). The pH was monitored with a portable multiparametric Crison Mm40+ equipment, previously calibrated with different buffers for pH (4, 7 and 9.2).

The amount adsorbed by the solids, $[XO_4]_s$ (mmol $mol_{Fe/Al}^{-1}$), was calculated by the difference between the initial concentration of As or Se, $[XO_4]_0$ in mmol L^{-1}, and the equilibrium concentration in solution, $[XO_4]_{eq}$ in mmol L^{-1}, normalized by the Fe or Al concentration in the solid (MC in $mol_{Fe/Al}$) to the volume (V in L), according to the equation 3.1:

$$[XO_4]_s = \left([XO_4]_0 - [XO_4]_{eq}\right) \times \frac{V}{MC} \qquad \text{Eq. 3.1}$$

After the equilibrium period, the samples were centrifuged and the supernatant was filtered through 0.2 µm nylon membrane filters, acidified with HNO_3 (65%) to pH < 1 and stored at 277 K for further chemical analysis. Solid composition was calculated by acid digestion of 0.05 g of solid in HNO_3 (65%) and recovered with 50 mL of Milli-Q ultrapure water for further chemical analysis. After adsorption experiments each solid was washed several times with Milli-Q ultrapure water and dried at 308 K for 48 h for subsequent PDF and EXAFS analysis.

3.2.3. Analytical techniques

Both As and Se solutions, before and after each adsorption experiment, and solid digestions were analyzed for Al, As, Fe, S and Se by inductively coupled plasma atomic emission spectrometry (ICP-AES Thermo Jarrel-Ash) in the laboratories of the IDAEA (CSIC) in Barcelona. Three blanks and three duplicates were analyzed every 20 samples to check the analytical accuracy. Detection limits were: 140 µg L^{-1} for Al and Fe; 15 µg L^{-1} for As and Se; 300 µg L^{-1} for S; and the analytical error was lower than 5%. In addition, the saturation index (SI) of the solid phases and aqueous speciation of solutions was calculated by using the PHREEQC code (Parkhurst and Appelo, 1999) with the Mintq.v4 thermodynamic database (Allison et al., 1998), which was enlarged with data from Bigham et al (1996b) to account for schwertmannite solubility.

Schwertmannite and basaluminite precipitates were lyophilized using a VirTis Benchtop freeze-dryer (Hucoa-Erlöss, Spain) in order to obtain a dry powder. The water proportion in both phases was calculated by thermogravimetric analysis (TGA) using a TGA92-12 SETARAM, with a N_2 flow of 1.8 l/h. The BET-determined surface area of schwertmannite and basaluminite was measured using 5-point N_2 adsorption isotherms with a Micromeritics ASAP 2000 surface area analyzer. HEXD and PDF were performed at the beamline ID31 at the European Synchrotron Radiation Facility (ESRF) using a monochromatic X-ray beam with energy of ~87.5 keV (λ = 0.1411 Å) in Debye-Scherrer geometry. The energy was calibrated using a CeO_2 standard (NIST 679b). Samples were loaded in polyamide (kapton) capillaries. The diffraction patterns were collected using a Perkin-Elmer flat-panel detector and were integrated using the program Fit2D (Hammersley et al., 1996). PDFs were obtained by Fourier transformation of the structure factor, $S(Q)$ (Q_{max} = 24.5 Å^{-1}), with the background scattering corrected using PDFgetX3 (Juhás et al., 2013). Finally, differential pair distribution functions (d-PDF) were obtained by subtracting a reference PDF of the pure material (synthetic As- or Se-free basaluminite and schwertmannite) from the PDFs of the samples recovered after adsorption experiments. Structural models of arsenate and selenite adsorbed onto both structures were constructed from the structure proposed by Fernandez-Martinez et al. (2010) and Farkas and Pertlik (1997) for schwertmannite and basaluminite, respectively. Partial pair distribution functions of arsenate and selenate located in different structural positions were calculated using PDFgui software (Farrow et al., 2009).

EXAFS data were collected at the Spanish CRG beamline BM25 at the ESRF. the BM25A beamline was equipped with a -200 K ethanol cooled double Si(111) crystal, which gives an energy resolution of $\Delta E/E = 1.5\cdot 10^{-4}$. The experiment was carried out at 50 K of temperature using a continuous liquid helium flow cryostat Optistat CF provided by Oxford Instruments. X-ray absorption spectroscopy measurements were performed both in transmission and fluorescence mode. For fluorescence mode Sirius liquid nitrogen cooled multi-element solid state X-Ray detector from e2v was employed. The detector accounts with 13 Si(Li) crystal sensors mounted on a low noise electrically restored FETs. Three high-precision low-noises home designed ionization chambers were used for transmission mode measurements. A mix of gases was selected to be introduced in the ionization chambers at 0.90 bar in order to get the rate of absorption required for each chamber. Samples were prepared in pellets using a BN matrix, and measured in transmission mode at 50 K. The necessary amount of sample in each pellet was calculated with Absorbix v3.02 (Michalowicz et al., 2009). EXAFS data were scanned in a range from 11.8 to 12.8 keV for As and 12.6 to 13.6 keV for Se, with a 0.2 eV step size in the edge region. EXAFS data reduction was performed using the Athena and Artemis software from the IFFEFIT package (Ravel and Newville, 2005). Same structural models used for PDF analyses were refined in the EXAFS data analysis. Debye-Waller factors, interatomic distances, coordination numbers and Fermi energy levels were fitted using a least square refinement algorithm. Statistical F-tests (Joyner et al., 1987; Michalowicz et al., 1999) were applied to determine the statistical significance of different tested hypothesis involving different number of shells added to the models. Only those models which improved the fit between theory and experimental EXAFS at the 90% level of confidence were selected.

3.3. RESULTS AND DISCUSSION

3.3.1. Phase characterization

The HEXD analysis of the starting solids confirmed the nature of schwertmannite and basaluminite (Fig. 3.1). The diffraction pattern of schwertmannite was identical to that described in previous studies (*e.g.* Fernandez-Martinez et al., 2010). Also, the basaluminite pattern presented broad diffraction peaks at 1.80º, 3.58º and 5.5º 2θ angle, as those described by (Farkas and Pertlik, 1997). Surface areas for schwertmannite and basaluminite were of 42.3 and 80.6 m^2 g^{-1} respectively. The value for schwertmannite was within the values reported by Burton et al. (2009), Paikaray et al. (2011) and Antelo et al. (2012). The value for basaluminite matches values found for similar Al-hydroxysulfates (Du et al., 2014).

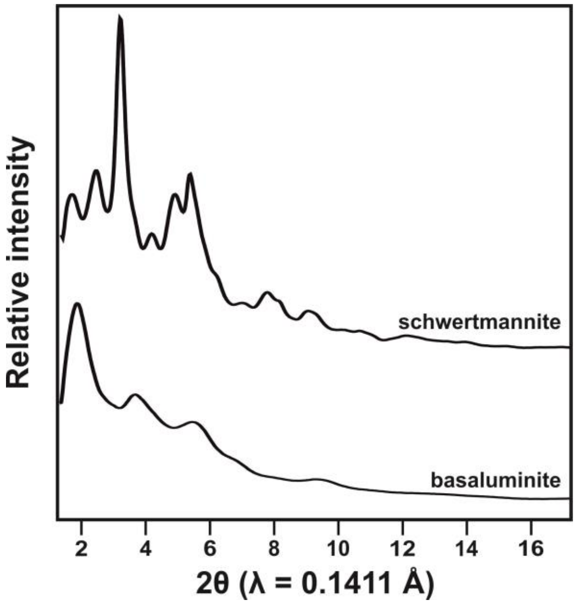

Figure 3.1: *Synchrotron-based HEXD of synthetic schwertmannite and basaluminite. Diffraction peaks are identical to those previously described by Farkas and Pertlik (1997) and Fernandez-Martinez et al. (2010) for basaluminite and schwertmannite, respectively.*

Chemical analysis and TGA data reveal a unit cell formula of schwertmannite of $Fe_8O_8(OH)_{4.15}(SO_4)_{1.92}$-$8.95H_2O$ and $Al_4(OH)_{9.02}(SO_4)_{1.49}$-$4.56H_2O$ for basaluminite. In both cases, sulfate concentration was higher than in previously reported chemical formulas of schwertmannite ($Fe_8O_8(OH)_{8-2x}(SO_4)_x$, with *x* ranging from 1 to 1.75, Bigham et al., 1996b) and basaluminite ($Al_4OH_{10}SO_4$-$5H_2O$, Hollingworth and Bannister, 1950). High sulfate concentration in schwertmannite have been related to a significant amount of outer-sphere complexes (Fernandez-Martinez et al., 2010). Although less is known about basaluminite, this phase has been described as a poorly-crystalline variety of felsöbányaite, where all the sulfate is located in the interlayer, in an outer-sphere position (*i.e.* keeping its surrounding hydration layer) (Farkas and Pertlik, 1997).

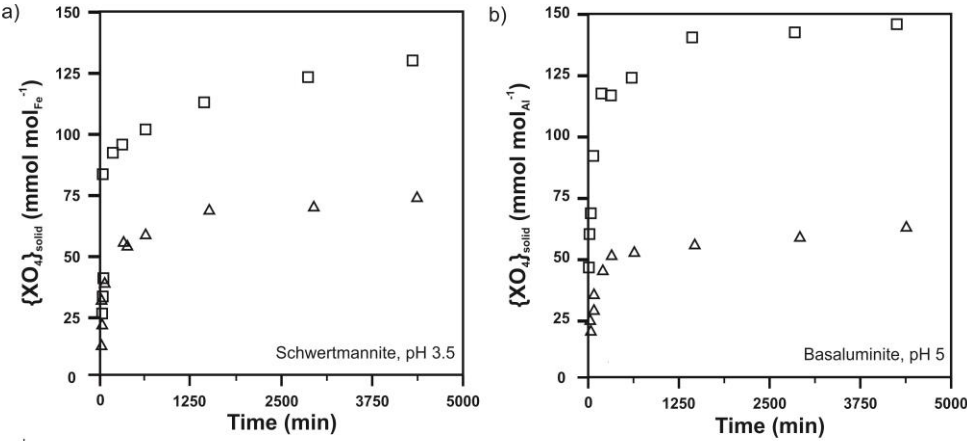

Figure 3.2: *Adsorption of arsenic (□) and selenium (Δ) (mmol$_{XO4}$ mol$_{Fe/Al}$$^{-1}$) at different time intervals (h) onto (a) schwertmannite and (b) basaluminite. The experiment was conducted at an ionic strength of 100 mmol L^{-1}, 3.0 mmol L^{-1} oxyanion concentration and 2.5 g L^{-1} of solid phase.*

3.3.2. Sorption kinetics

Speciation analyses with the PHREEQC code result in $H_2AsO_4^-$ (arsenate) and SeO_4^{2-} (selenate) as the dominant species with proportions higher than 90% within the 3-5 pH range. The time necessary to reach equilibrium between the solid phases and As- or Se-rich solutions is shown in Figure 3.2. The adsorption kinetics of both oxyanion onto schwertmannite and basaluminite show that, in all cases, the equilibrium was reached before 72 h. In addition, Al and Fe concentrations in solution during equilibrium were always lower than 0.99 mmol L^{-1} and 0.15 mmol L^{-1}, respectively, indicating a maximum dissolution of solid phases of 2% and 4.5% for schwertmannite and basaluminite, respectively. Accordingly, a reaction time of 72 h was considered enough to reach the equilibrium between solid and liquid phases without excessive solid dissolution, in agreement with other kinetic studies previously reported by Burton et al. (2009) and Antelo et al. (2012).

To check for possible dissolution of the two solids and precipitation of other phases, SI of solutions with respect to Al, As, Fe and Se-bearing phases were determined by using the PHREEQC code (Table 3.1). The results show that the solutions were undersaturated with respect to all As and Se-bearing phases and supersaturated with respect to schwertmannite and basaluminite. High-energy X-ray diffraction patterns confirmed the purity of the systems under study (Fig. 3.1), with no noticeable peaks from other phases.

Phases	**Formulas**	**As solution**	**Se solution**	**Phases**	**Formulas**	**As solution**	**Se solution**
As_2O_5(cr)	As_2O_5	-12.8	-	$Al(OH)_3$ am	$Al(OH)_3$	-1.43	-1.44
$Fe(OH)_{2.7}Cl_{0.3}$	$Fe(OH)_{2.7}Cl_{0.3}$	**5.21**	**5.54**	Al_2O_3	Al_2O_3	-0.93	-0.92
$Fe_2(SO_4)_3$	$Fe_2(SO_4)_3$	-18.0	-16.8	$AlOH(SO_4)$	$AlOH(SO_4)$	**0.22**	**0.17**
Ferrihydrite	$Fe(OH)_3$	**0.28**	**0.62**	As_2O_5(cr)	As_2O_5(cr)	-16.5	-
Goethite	FeOOH	**2.98**	**3.32**	Basaluminite	$Al_4(OH)_{10}SO_4$	**2.32**	**2.34**
Hematite	Fe_2O_3	**8.36**	**9.04**	Boehmite	AlOOH	**0.77**	**0.79**
H-Jarosite	$(H_3O)Fe_3(SO_4)_2(OH)_6$	**3.36**	**4.75**	Diaspore	AlOOH	**2.47**	**2.49**
Lepidocrocite	FeOOH	**2.10**	**2.44**	Gibbsite	$Al(OH)_3$	**1.06**	**1.07**
Mahemite	Fe_2O_3	**0.55**	**1.24**	Mansfieldite	$AlAsO_4{:}2H_2O$	-0.37	-
Na-Jarosite	$NaFe_3(SO_4)_2(OH)_6$	**4.12**	**5.49**	Na_2SeO_4	Na_2SeO_4	-	-6.54
Na_2SeO_4	Na_2SeO_4	-	-6.56	SeO_3	SeO_3	-	-32.6
Schwertmannite	$Fe_8O_8(OH)_{4.32}(SO4)_{1.84}$	**2.14**	**5.21**				
Scorodite	$FeAsO_4{:}2H_2O$	-0.21	-				
SeO_3	SeO_3	-	-29.6				

Table 3.1: *Calculated saturation index for supersaturated Fe-As-Se-S and Al-As-Se-S mineral phases of reacted solution using the PHREEQC code (Mintq.v4 database, Allison et al., 1998). Bold values represent the supersaturated phases for each adsorption experiment.*

3.3.3. Oxyanion uptake from solution

Adsorption isotherms for arsenate and selenate in schwertmannite and basaluminite are shown in Figure 3.3. The experimental data were fitted using a non-competitive Langmuir isotherm following the expression:

$$\Gamma = \Gamma_{max} \frac{K_L[XO_4]_{eq}}{1+K_L[XO_4]_{eq}} \qquad \text{Eq. 3.2}$$

where Γ ($mmol_{XO4}$ $mol_{Fe/Al}^{-1}$) is the quantity of arsenate or selenate sorbed on the solid, Γ_{max} ($mmol_{XO4}$ $mol_{Fe/Al}^{-1}$) is the maximum oxyanion sorption, K_L (mmol L^{-1}) is the Langmuir constant and $[XO_4]_{eq}$ (mmol L^{-1}) is the oxyanion concentration in equilibrium. Sulfate concentrations in equilibrium can be related to the substitution of structural sulfate by both oxyanions and OH^- ions. Given that anion exchange was considered as a possible scenario in the adsorption processes (Burton et al., 2009), As- and Se-free blank solutions were also prepared in order to account for sulfate substitution by OH^- ions. The ion exchange isotherm is described by the molar fraction of charge $\ddot{E}_{XO4}$ of the anion XO_4 adsorbed onto the solid [(mmol Kg^{-1})·(mmol Kg^{-1})$^{-1}$] against the molar fraction of charge E_{XO4} of the XO_4 anion remaining in solution [(mmol L^{-1})·(mmol L^{-1})$^{-1}$]. The molar fraction of charge, E_{XO4}, is defined as:

$$E_{XO4} = \frac{N_{XO4}}{N_{Total}} \qquad \text{Eq. 3.3}$$

with N_{XO4} being the normality of ion XO_4 and N_{total} the total normality of both exchanged ions. The exchange isotherm and the correlation between corrected sulfates concentration in solution with respect to oxyanion adsorbed on the solid are shown in Figures 3.4 and 3.5, respectively.

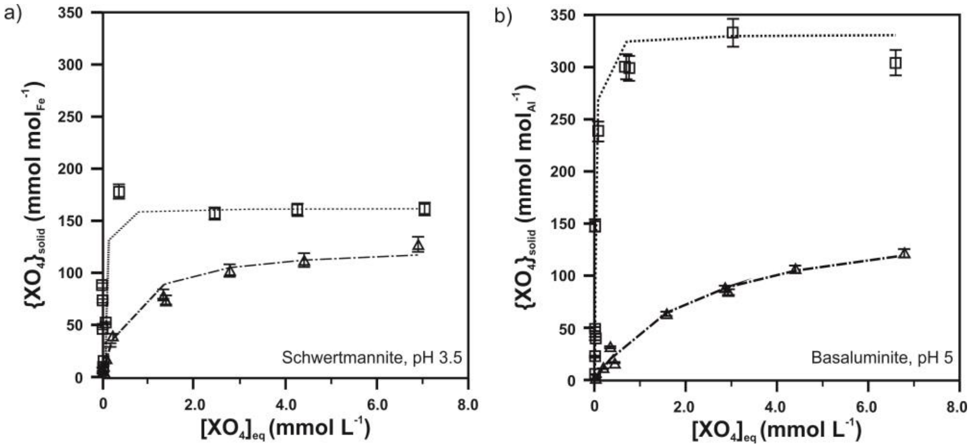

Figure 3.3: *Adsorption isotherm of arsenic (□) and selenium (Δ) (mmol$_{XO4}$ mol$_{Fe/Al}^{-1}$) onto (a) schwertmannite and (b) basaluminite. Curves obtained using the Langmuir equations are drawn for comparison with the experimental data. The experiment was conducted at ionic strength of 100 mmol L^{-1}, $3 \cdot 10^{-2}$ to 10 mmol L^{-1} oxyanion concentration and 2.5 g L^{-1} of solid phase.*

3.3.3.1. Arsenate adsorption onto solid phases

The adsorption isotherm of arsenate in both phases was perfectly fitted by a Langmuir model, with higher arsenate concentrations in basaluminite (326 mmol $_{H2AsO4}$ mol$_{Al}^{-1}$) than in schwertmannite (128 mmol$_{H2AsO4}$ mol$_{Fe}^{-1}$) (Fig. 3.3). The values obtained in this study for arsenate adsorbed onto schwertmannite were within the range previously reported for this phase (Antelo et al., 2012; Burton et al., 2009), and were higher than values reported for Fe-phases such as hydrous ferric oxide, magnetite (Dixit and Hering, 2003), goethite, jarosite (Asta et al., 2009), and Al-phases such as ɣ-alumina (Li et al., 2011).

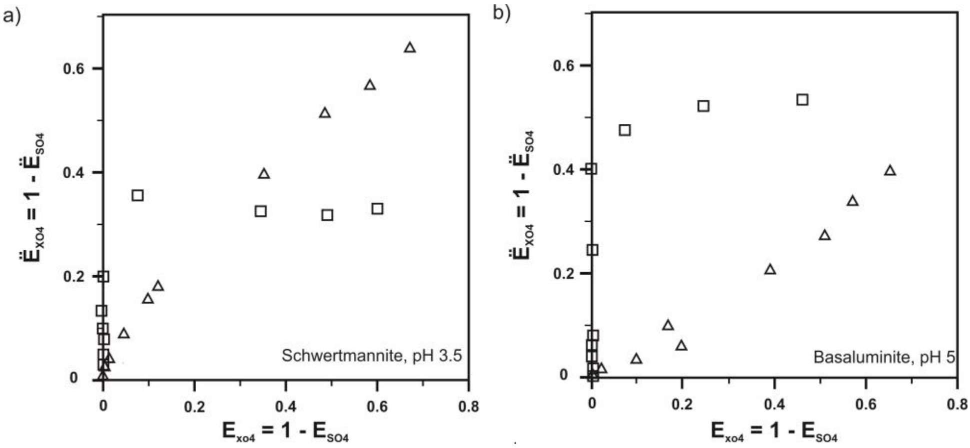

Figure 3.4: *Ion exchange isotherm: exchange between As(□)/Se(Δ) with sulfate onto (a) schwertmannite and (b) basaluminite. The experiment was conducted at ionic strength of 100 mmol* L^{-1}*,* $3 \cdot 10^{-2}$ *to 10 mmol* L^{-1} *oxyanion concentration and 2.5 g* L^{-1} *of solid phase.*

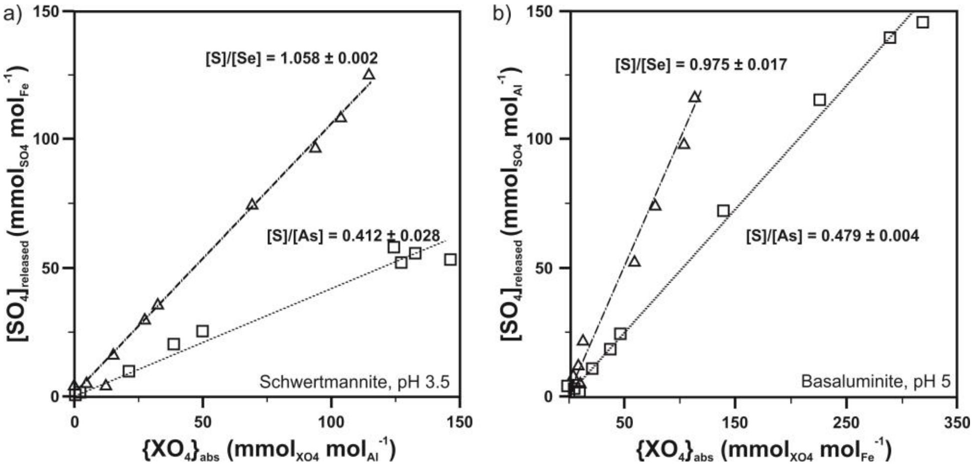

Figure 3.5: *Relationship between sulfate release from the solid phases (mmol*$_{SO4}$ *mol*$_{Fe/Al}^{-1}$*) and adsorbed arsenic (□) or selenium (Δ) from the solution (mmol*$_{XO4}$ *mol*$_{Fe/Al}^{-1}$*).*

Ion exchange seems to be one of the main processes controlling the oxyanion adsorption in both solid phases. Exchange isotherms show that, at equilibrium, around 35% and 50% of initial structural sulfate in schwertmannite and basaluminite, respectively, was substituted by arsenate (Fig. 3.4). In addition, exchange coefficients (R_{ex})

were obtained as the slope of the linear regression of the relation between desorbed sulfate ($mmol_{SO4}$ $mol_{Fe/Al}^{-1}$) and adsorbed arsenate ($mmol_{H2AsO4}$ $mol_{Fe/Al}^{-1}$) (Fig. 3.5). A value of R_{ex} close to 1 $mmol_{SO4}$ $mmol_{XO4}^{-1}$ can be interpreted as complete substitution of the structural sulfate by an equivalent charged oxyanion through an ion exchange mechanism. Values lower than 1 $mmol_{SO4}$ $mmol_{XO4}^{-1}$ would indicate only a partial substitution. The R_{ex} values for arsenate were 0.48 and 0.41 in schwertmannite and basaluminite, respectively. These R_{ex} values are in agreement with the anion charge: arsenate ($H_2AsO_4^-$) has exactly half the negative charge than sulfate (SO_4^{2-}), therefore, two arsenates were adsorbed per every sulfate removed from the solid phases.

3.3.3.2. Selenate adsorption onto solid phases

Equilibrium selenate concentrations removed by both solid phases were lower than for arsenate (Fig. 3.3). The Langmuir model shows a good agreement with the experimental data and maximum selenate adsorption capacity in basaluminite (122 $mmol_{SeO4}$ mol_{Al}^{-1}) was lower than in schwertmannite (153 $mmol_{SeO4}$ mol_{Fe}^{-1}). Sorption capacity of selenate onto schwertmannite was higher than previous values reported for other iron phases for both selenite and selenate (Jang et al., 2015; Peak and Sparks, 2002; Rovira et al., 2008). Furthermore, basaluminite shows also higher affinity for selenate than other Al-oxyhydroxides (Peak, 2006).

The exchange isotherm revealed that structural sulfate was replaced by selenate up to a 65% and 45% in schwertmannite and basaluminite, respectively, without reaching a steady state in the maximum exchange percent for the concentration range used in this experiment (Fig. 3.4). Moreover, the R_{ex} value was around 1 $mmol_{SO4}$ $mmol_{SeO4}^{-1}$ in both phases, indicating that all selenate adsorbed from the solution was removed by ionic exchange mechanisms in a stoichiometric proportion (Fig. 3.5). Synthetic schwertmannite and basaluminite precipitated in this experiment were representative of solid phases with high sulfate concentrations. Relative high sulfate content in the mineral structure has been associated with a greater presence of outer-sphere complexes onto the structure of schwertmannite (Fernandez-Martinez et al., 2010) and basaluminite (Farkas and Pertlik, 1997), where sulfate could be easily removed due to its low energetic stability.

3.3.4. Sulfate competition

Percentages of arsenate and selenate adsorbed on both solid phases at different solution initial sulfate concentrations are given in Table 3.2. Arsenate sorption on both solids was complete regardless of the sulfate concentration. On the other hand, selenate sorption onto both phases decreased as sulfate concentration increased in solution (Table 3.2). These results indicate that both phases present higher affinity for arsenate than for selenate. A similar competitive effect for arsenate on schwertmannite has been reported by Paikaray et al. (2011) and Song et al. (2015), where arsenate removal from the solution showed a weak dependence with the sulfate concentration in solution. On the contrary, other studies have shown that when arsenate and sulfate containing solutions are put in contact with minerals with exchangeable structural sulfate groups (*e.g.* jarosite), the total adsorption was lower than in minerals without structural sulfate groups (*e.g.* goethite). This is due to sulfate in solution competing with the exchangeable sites of jarosite, and to the high affinity of arsenate to specific binding sites on goethite surface sites (Asta et al., 2009; Loring et al., 2009; Sherman and Randall, 2003). Nevertheless, the isotherm adsorption carried out in this study indicated that arsenate could enter in the structure by two different mechanisms, where the ion exchange accounted for the 50% of the total arsenate removed. On the other hand, the isotherms showed that selenate uptake can be explained by just an ion exchange process.

Phases	**[SO_4^{2-}] (mol L^{-1})**	**% As sorbed**	**% Se sorbed**
Schwertmannite	-	100	75
	0.005	100	49
	0.008	100	41
	0.01	100	37
	0.05	100	20
	0.1	99	6.5
Basaluminite	-	100	65
	0.005	100	30
	0.008	100	35
	0.01	100	25
	0.05	100	15
	0.1	100	13

Table 3.2: *Comparison of the As and Se (%) adsorbed in the presence of several sulfate concentrations at constant As and Se concentration of 1 mmol* L^{-1}.

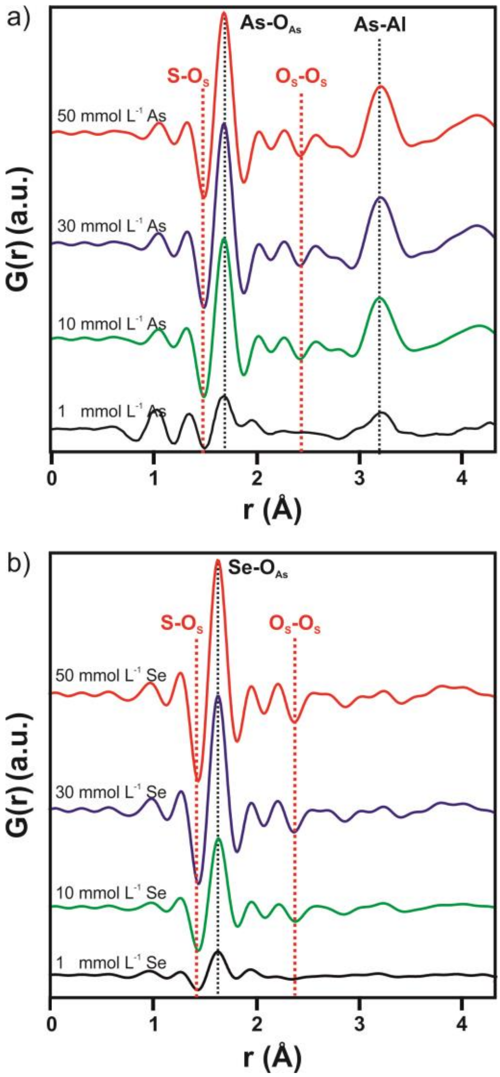

Figure 3.6: *The d-PDF of (a) arsenate and (b) selenate onto basaluminite in the sample loaded with 1, 10, 30, 50 mmol L^{-1} of As and Se. The signal intensity was normalized by the maximum of Al-O distance.*

3.3.5. Oxyanion adsorption mechanisms

3.3.5.1. Differential PDF

Differential PDFs (d-PDFs) showing the short-range order around both oxyanions on basaluminite and schwertmannite are shown in Figures 3.6 and 3.7, respectively. Semi-quantitative structural models were carried out for arsenate and selenate in the nanostructure proposed by Farkas and Pertlik (1997) for felsöbányaite, described as a microcrystalline mineral version of basaluminite (Fig. 3.8), and by Fernandez-Martinez et al. (2010) for schwertmannite (Fig. 3.9). Experimental d-PDFs were compared with modeled ones generated from different molecular models, including surface complexes with (i) a monodentate ligand, (ii) a bidentate binuclear ligand, (iii) a bidentate mononuclear ligand, and (iv) electrostatic complex in outer-sphere position (Figs. 3.8a and 3.9a).

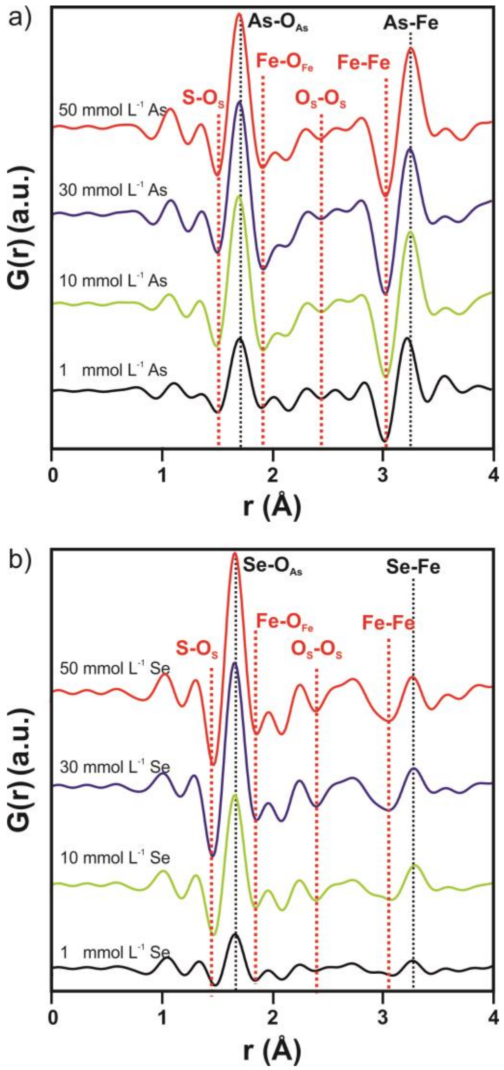

Figure 3.7: *The d-PDF of (a) arsenate and (b) selenate onto schwertmannite in the sample loaded with 1, 10, 30, 50 mmol L^{-1} of As and Se. The signal intensity was normalized by the maximum of Fe-O distance.*

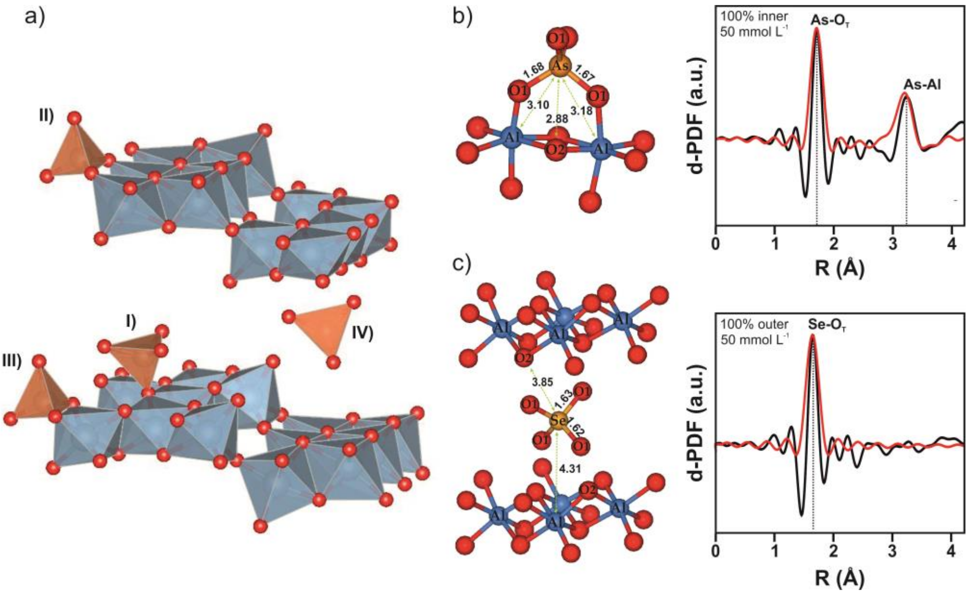

Figure 3.8: *(a) Basaluminite structure reported by Farkas and Pertlik (1997) doped with arsenate or selenate located in: I) monodentate inner-sphere, II) bidentate binuclear inner-sphere, III) bidentate mononuclear inner-sphere and VI) outer-sphere theoretical position; and the most probable structural location of (b) arsenate and (c) selenate onto basaluminite. The theoretical d-PDF models were drawn for comparison with the experimental data. The signal intensity was normalized by the maximum of Al-O distance.*

Basaluminite As d-PDF showed a peak at 1.67 Å corresponding to As-O distances in As(V) (Sherman and Randall, 2003; Harrington et al., 2010) (Fig. 3.6a). In addition, a second shell at 3.15 Å was observed, which is in agreement with previous As-Al distances described in adsorption experiments on Al-phases (Arai et al., 2001; Li et al., 2011) (Fig. 3.6a). This second neighbor was less clear, with a background close to the signal intensity, due to the low atomic number of Al. The agreement between the relative intensities of As-O and As-Al distances indicates that arsenate was bound through a bidentate binuclear inner-sphere ligand (Fig. 3.8b). On the other hand, the Se d-PDF showed only a clear first shell at 1.63 Å. (Fig. 3.6b). This was attributed to the formation of electrostatically bound outer-sphere complexes. A weak peak at 4 Å was associated with the Se-O distance with O located in the octahedral layer (Fig. 3.8c). Finally, both As and Se on basaluminite d-PDFs showed two negative peaks at 1.46 Å and 2.38 Å, whose intensities increased concomitantly with the oxyanion concentration into the solids. These peaks can be attributed to S-O and O-O distances of sulfate tetrahedra, confirming that oxyanion retention into the structure is done through an anion exchange process.

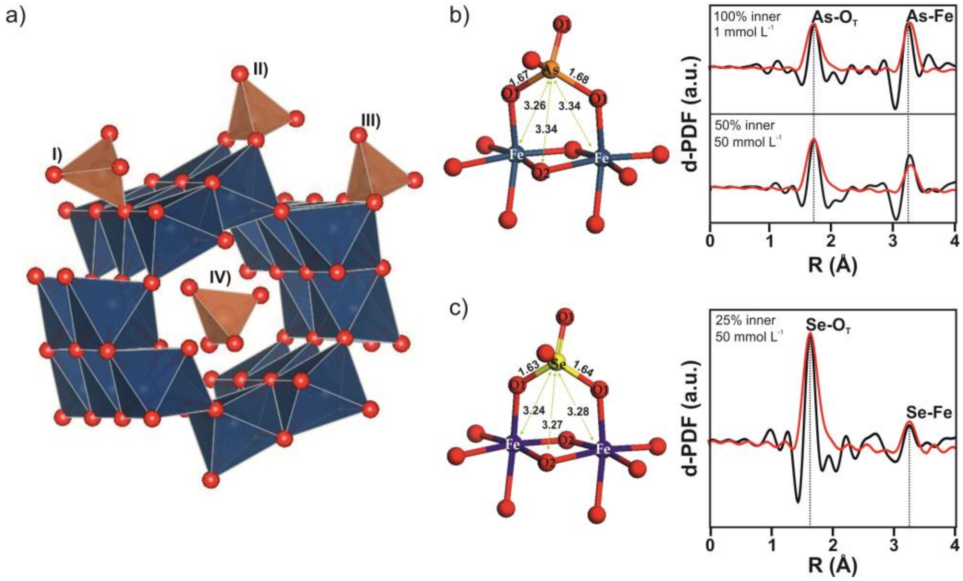

Figure 3.9: *(a) Schwertmannite structure by Fernandez-Martinez et al. (2010) doped with arsenate or selenate located in I) monodentate inner-sphere, II) bidentate binuclear inner-sphere, III) bidentate mononuclear inner-sphere and VI) outer-sphere theoretical position; and the most probable structural location of (b) arsenate and (c) selenate onto schwertmannite. The theoretical d-PDF models were drawn for comparison with the experimental data. The signal intensity was normalized by the maximum of Fe-O distance.*

Two main peaks can be observed in the As on schwertmannite d-PDF at 1.67 Å and 3.28 Å (Fig. 3.7a). The first As correlation can be assigned to the As-O distance. The second As peak was at similar distance to the As-Fe pair found in previous d-PDF experiments of As sorption onto Fe-phases (Harrington et al., 2010), and it matches As-Fe interatomic distances obtained from EXAFS studies of As sorption onto Fe-oxyhydroxides (Loring et al., 2009; Sherman and Randall, 2003; Waychunas et al., 1993). The relative intensity between As-O and As-Fe peaks indicated that, at low As concentration in solution, arsenate formed bidentate binuclear inner-sphere ligands, whereas at concentration higher than 10 mmol L^{-1}, 50% of oxyanions were located in bidentate binuclear inner-sphere and 50% in outer sphere position (Fig. 3.9b). In the case of Se, two peaks at 1.63 Å and 3.25 Å relative to the Se-O and Se-Fe pairs respectively can be observed (Fig. 3.7b) (Peak and Sparks, 2002; Waychunas et al., 1995b). Analysis of the relative peak intensities of the modeled and experimental d-PDFs yield a 25% of selenate with a bidentate binuclear inner-sphere ligand and a 75% in outer-sphere position (Fig. 3.9c). Similarly to basaluminite, the oxyanion adsorption was concomitant to sulfate desorption (negative peaks at 1.46 Å and 2.38 Å). In addition, d-PDFs from schwertmannite showed negatives peaks at 1.98 Å, 3 Å (Fig. 3.7), 4.73 Å, 5.4 Å and 6.35Å (not show in Fig. 3.7), mainly in the case of arsenate adsorption. These peaks are coincident with interatomic distances of Fe-O (first shell), Fe-Fe (first shell), Fe-O (second shell), Fe-Fe (second shell) and Fe-Fe (third shell), respectively (Fernandez-Martinez et al., 2010). The presence of these peaks indicates that structural changes are present in schwertmannite during oxyanion adsorption.

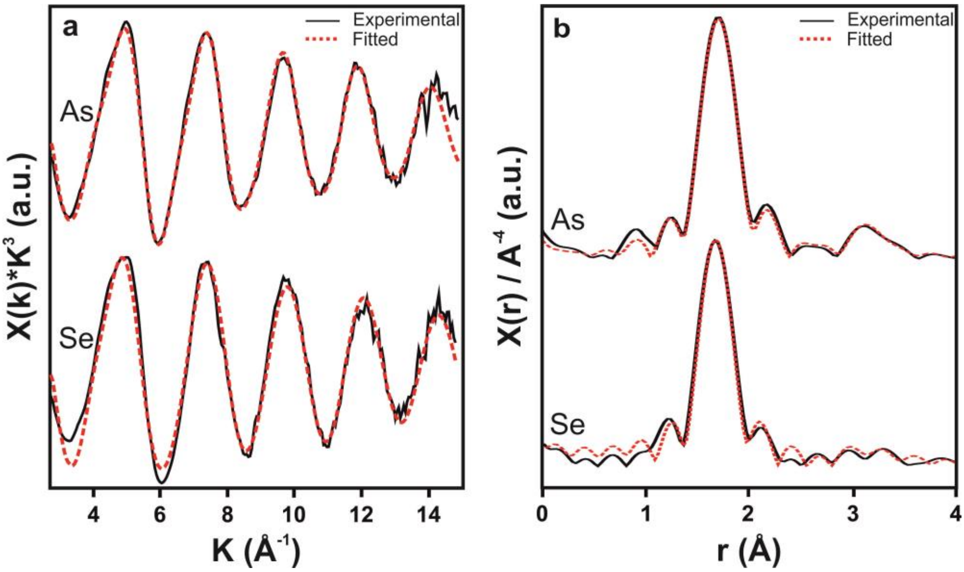

Figure 3.10: *(a) K^3-weighted and (b) Fourier transform amplitude of EXAFS spectra at the As and Se K-edge adsorbed onto basaluminite. Experimental and fit curves are displayed in black and red colors, respectively.*

As K-edge EXAFS models in basaluminite.

Model	**Path**	**Neighbor**	**N**	**σ^2**	**R**	**ΔE_0**	**V**	**$\Delta\chi^2$**
1	As-O$_T$	One shell	4.096 ± 0.053	0.0023 ± 0.0007	1.689 ± 0.003	6.918 ± 1.991	13	7355.2
2	As-O$_T$	Shell 1	4.050 ± 0.019	0.0024 ± 0.0001	1.689 ± 0.001	7.239 ± 0.294	13	940.9
	As-O$_O$	Shell 2	5.380 ± 1.946	0.0184 ± 0.0028	2.768 ± 0.015	7.239 ± 0.294		
	As-Al	Shell 3	1 (fixed)	0.0064 ± 0.0010	3.184 ± 0.032	7.239 ± 0.294		
3*	As-O$_T$	Shell 1	4.050 ± 0.018	0.0024 ± 0.0001	1.689 ± 0.001	7.239 ± 0.294	12	537.9
	As-O$_O$	Shell 2	5.380 ± 1.946	0.0065 ± 0.0023	2.768 ± 0.015	7.239 ± 0.294		
	As-Al	Shell 3	2.021 ± 0.550	0.0196 ± 0.0023	3.184 ± 0.006	7.239 ± 0.294		

Se K-edge EXAFS models in basaluminite.

Model	**Path**	**Neighbor**	**N**	**σ^2**	**R**	**ΔE_0**	**V**	**$\Delta\chi^2$**
1*	Se-O$_T$	One shell	4.004 ± 0.032	0.0019 ± 0.0002	1.648 ± 0.036	8.061 ± 0.614	13	1273.9
2	Se-O$_T$	Shell 1	3.996 ± 0.038	0.0018 ± 0.0003	1.648 ± 0.030	7.782 ± 0.699	13	1676.2
	Se-Al	Shell 2	1 (fixed)	0.0022 ± 0.0094	3.184 ± 0.032	7.782 ± 0.699		

Table 3.3: *Modeling parameter for As K-edge EXAFS in (1) 100% outer-sphere ligand, (2) 50% bidentate binuclear inner-sphere ligand, and (3) 100% bidentate binuclear inner-sphere ligand and Se K-edge EXAFS in (1) 100% outer-sphere ligand and (2) 50% bidentar binucleate inner-sphere ligand in basaluminite. *best fit according to F-test.*

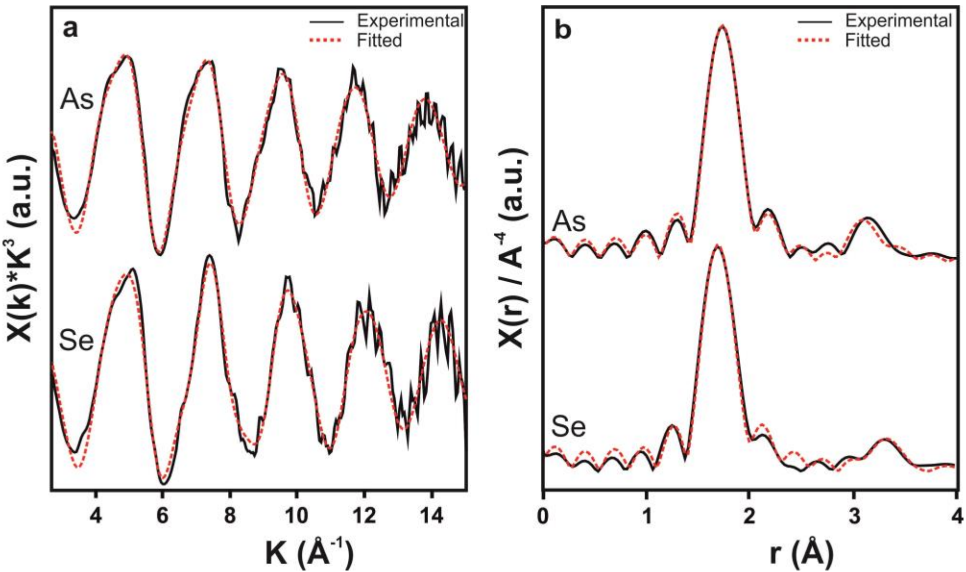

Figure 3.11: *(a) K^3-weighted and (b) Fourier transform amplitude of EXAFS spectra at the As and Se K-edge adsorbed onto schwertmannite. Experimental and fit curves are displayed in black and red colors, respectively.*

As k-edge EXAFS models in schwertmannite.

Model	**Path**	**Neighbor**	**N**	**σ^2**	**R**	**ΔE_0**	**V**	**$\Delta\chi^2$**
1	As-O_T	One shell	3.448 ± 0.048	0.0010 ± 0.0008	1.684 ± 0.003	6.938 ± 0.944	12	1248.1
2*	As-O_O	Shell 1	3.900 ± 0.068	0.0019 ± 0.0002	1.694 ± 0.002	6.747 ± 1.038	10	484.0
	As-Fe_{bi}	Shell 2	2 (fixed)	0.0082 ± 0.0019	3.295 ± 0.002	6.747 ± 1.038		
3*	As-O_T	Shell 1	3.916 ± 0.071	0.0019 ± 0.0002	1.678 ± 0.002	8.711 ± 1.262	10	471.4
	As-Fe_{mo}	Shell 2	1 (fixed)	0.0092 ± 0.0023	2.743 ± 0.023	8.711 ± 1.262		
	As-Fe_{bi}	Shell 3	2 (fixed)	0.0092 ± 0.0023	2.919 ± 0.019	8.711 ± 1.262		

Se k-edge EXAFS models in schwertmannite.

Model	**Path**	**Neighbor**	**N**	**σ^2**	**R**	**ΔE_0**	**V**	**$\Delta\chi^2$**
1	Se-O_T	One shell	3.712 ± 0.039	0.0017 ± 0.0005	1.648 ± 0.002	8.057 ± 0.927	11	828.9
2*	Se-O_O	Shell 1	3.704 ± 0.031	0.0017 ± 0.0002	1.648 ± 0.002	8.114 ± 0.677	10	442.3
	Se-Fe_{bi}	Shell 2	2 (fixed)	0.0098 ± 0.0026	3.341 ± 0.024	8.114 ± 0.677		
3	Se-O_T	Shell 1	3.776 ± 0.076	0.0018 ± 0.0003	1.648 ± 0.003	8.498 ± 0.977	10	508.5
	Se-Fe_{mo}	Shell 2	1 (fixed)	0.0128 ± 0.0052	2.696 ± 0.044	8.498 ± 0.977		
	Se-Fe_{bi}	Shell 3	2 (fixed)	0.0128 ± 0.0052	2.891 ± 0.046	8.498 ± 0.977		

Table 3.4: *Modeling parameter for As K-edge EXAFS in (1) 100% outer-sphere ligand, (2) 100% bidentate binucleate inner-sphere ligand, and (3) 100% bidentate mononuclear inner-sphere ligand and Se K-edge EXAFS in (1) 100% outer-sphere ligand, (2) 100% bidentate binuclear inner-sphere ligand, and (3) 100% bidentate mononuclear inner-sphere ligand in basaluminite. *best fit according to F-test.*

3.3.5.2. As and Se K-edge EXAFS

Arsenic and selenium K-edge EXAFS, and the parameters of the different structural models tested are shown in Figures 3.10 and 3.11 and Tables 3.3 and 3.4 for basaluminite and schwertmannite, respectively. Arsenic EXAFS in basaluminite was characterized by the presence of two shells at 1.69 ± 0.01 Å and 3.18 ± 0.01 Å, that are attributed to As-O and As-Al distances (Fig. 3.10a). Peaks attributed to As-O distance were consistent with undistorted arsenate tetrahedron with coordination number of 4.05 ± 0.02. Three different models were considered during the fitting process: (i) an arsenate in outer-sphere position (just one shell); (ii) a surface complex with a monodentate ligand; and (iii) a surface complex with a bidentate binuclear ligand. This third model, with an As-Al coordination number of 2.02 ± 0.55 (bidentate binuclear) yields the best fit, and a 99.9% of confidence in the F-test (Table 3.3). On the other hand, Se EXAFS in basaluminite was best described as an outer sphere complex, where only a peak at 1.65 ± 0.04 Å was observed and associated to the Se-O distance with coordination number of 4.01 ± 0.03 (Fig. 3.10b). None of the complexes involving inner-sphere ligands gave F-test values that were above the confidence level (Table 3.3). These results agree with the d-PDF data. It is worth noting that a broad, medium-range correlation can be observed in the d-PDF data of selenate in basaluminite at d ~ 4 Å, which matches with the distance from the center of the interlayer to the Al-hydroxide layer (distance not visible in EXAFS). This reinforces the conclusion that sulfate is exchanged by selenate occupying the same structural position.

Arsenic EXAFS in schwertmannite shows similar results to the d-PDF: A first interatomic distance corresponding to an As-O shell at 1.69 ± 0.01 Å with a coordination number of 3.90 ± 0.07 and a second shell corresponding to an As-Fe distance at 3.29 ± 0.01 Å (Fig. 3.11a). Again, three different structural models were considered, including one in outer-sphere position, a complex with a bidentate binuclear inner-sphere ligand, and another one with mononuclear bidentate inner sphere ligand. In this case, the F-test yields similar values of statistical significance for the second neighbor shells, meaning that both the binuclear and the bidentate mononuclear ligands are equally significant (Fig 3.11b) (Table 3.4). In view of past investigations, the formation of binuclear complexes is privileged (Waychunas et al., 1993), although the possibility that a monodentate ligand is present (Loring et al., 2009) or even that different types of complexes (inner- and outer-sphere) are present simultaneously cannot be ruled out. Finally, selenate absorbed in schwertmannite shows a similar distribution of interatomic distances in both EXAFS and d-PDF data, with two shells centered at 1.65 ± 0.01 Å and 3.34 ± 0.02 Å, related to the pairs Se-O and Se-Fe, respectively. A coordination number for the Se-Fe shell of 2 (fixed value), was found, indicating that selenate is covalently bonded through an inner-sphere ligand. Results from d-PDF and EXAFS models of arsenate and selenate in schwertmannite were coincident in their structural location. In addition, the relative intensities of the peaks from the d-PDFs give information about the proportion of complexes with inner and outer-sphere ligands. As d-PDF and EXFAS models have shown, schwertmannite present different sorption position where inner-sphere was filled in first place and, once it was completely occupied, oxyanions started to be placed in outer-sphere position.

3.4. CONCLUSIONS

This study reports on the basaluminite capacity as scavenger of toxic metals present in AMD-affected systems such as Se and As. It also provides new details about schwertmannite adsorption mechanisms of these elements. Basaluminite showed higher sorption capacities of arsenic and selenium than schwertmannite, controlled by two mechanisms: (i) ionic exchange with structural sulfate in both mineral structures and (ii) surface complexation forming inner- and outer-sphere complexes. Arsenate and selenate retention in schwertmannite were controlled by a combination of bidentate binuclear inner-sphere and outer-sphere ligands, whereas in basaluminite arsenate and selenate formed bidentate binuclear inner-sphere and outer-sphere complexes, respectively. The formation of inner-sphere complexes with strong covalent bonds has important environmental implications. Both basaluminite and schwertmannite are metastable solid phases which are exposed to changes in field conditions and aging towards more stables phases with less retention capability. Covalent bonding results in an increase stability of the oxyanion complexes, retarding release and enhancing colloidal transport in streams affected by AMD and ASS, as well as delaying the solid transformation into more stable phases.

Basaluminite played an important role as scavenger of arsenic and selenium, showing higher retention values and proportion of inner-sphere ligands than schwertmannite, especially for As. Schwertmannite has been considered the solid phases with highest capacity to remove trace elements from environments affected by acid waters. However, the fact that it precipitates at a more acidic pH than basaluminite has masked the basaluminite adsorption capacity. It is expected that a deeper understanding of the adsorption mechanisms and of the basaluminite structure will ensure better prediction of the transport and retention of adsorbed elements during the aging of this still relatively unknown mineral.

CHAPTER IV

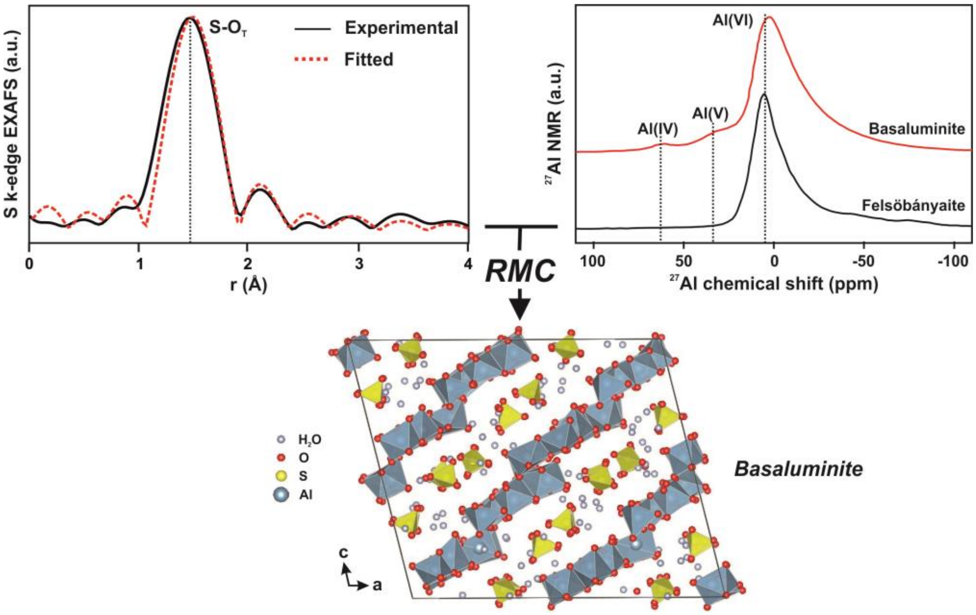

The Nanocrystalline Structure of Basaluminite, an Aluminum Hydroxide Sulfate from Acid Mine Drainage

ABSTRACT

Basaluminite is a poorly-crystalline aluminum hydroxysulfate that precipitates in waters affected by acid mine drainage (AMD) and in acid sulfate soils (ASS). Its ability to sequester potentially toxic elements, such as Cu and As, makes it an important component of AMD systems, with strong environmental implications. Although it was initially described as a mineral, basaluminite is now considered a nanoscale variety of felsöbányaite, a rare mineral. In the present study, chemical analyses of natural and synthetic basaluminites are combined with data from advanced nanoscale characterization techniques such as high-energy X-ray diffraction (HEXD) and pair distribution function (PDF) analyses, extended X-ray adsorption fine structure (EXAFS) and nuclear magnetic resonance (NMR). X-ray scattering data are analyzed with reverse Monte Carlo (RMC) modeling in order to obtain an atomistic representation of the disordered present in this nanomineral. Sulfur K-edge EXAFS results show that sulfate is coordinated to the aluminum-octahedral framework of basaluminite mainly through an outer-sphere ligand, though the existence of inner-sphere ligands seems to be slightly significant in synthetic samples. PDF analyses show that both synthetic and natural basaluminites have identical short-range order, with ~1.2 nm coherent domain size, and share structural characteristics with felsöbányaite. Interestingly, ^{27}Al NMR shows the presence of, respectively, ~1% and 5% of tetrahedral and pentahedral coordinations. RMC models of basaluminite highlight the presence of structural point defects. The understanding of this nanocrystalline character has important implications in terms of the reactivity of this nanomineral in AMD and ASS. The lack of correlation between the spatial and temporal occurrence of basaluminite and felsöbányaite suggests that the similarities between both mineral structures could be fortuitous, and highlights the need for a re-evaluation of the status of basaluminite as a nanomineral.

4.1. INTRODUCTION

Hydrobasaluminite $[Al_4(OH)_{10}(SO_4)\cdot 34H_2O]$ and basaluminite $[Al_4(OH)_{10}(SO_4)\cdot 5H_2O]$ are the names given to the white precipitates formed in streams affected by acid mine drainage (AMD) and in acid sulfate soils (ASS) with high aluminum and sulfate concentrations, when the solution pH values are around 4.5 (Adams and Rawajfih, 1977; Bannister and Hollingworth, 1948; Bigham and Nordstrom, 2000; Hollingworth and Bannister, 1950; Nordstrom, 1982b). The progressive pH increase due either to AMD mixing with pristine water or to alkaline addition in AMD treatment systems leads to solution oversaturation with respect to Al-hydroxysulfate phases, and to the formation of this poorly-crystalline precipitate. Jurbanite and alunite are other observed Al-phases in the 3-7 pH range, depending on the sulfate activity, although its metastable character kinetically favors hydrobasaluminite precipitation (Caraballo et al., 2011; Nordstrom, 1982b; Sánchez-España et al., 2011). These phases have important environmental implications because their precipitation supposes the main mechanisms of Al and S removal from AMD. In parallel, their high surface area and positive charge in acid waters provide high affinity to potentially hazardous elements (*e.g.* As and Cu) present in basins impacted by AMD and in ASS (Bigham and Nordstrom, 2000; Carrero et al., 2015; Nordstrom and Alpers, 1999a). Aluminum phases have been less studied than Fe-phases (*i.e.* schwertmannite, jarosite and goethite) in these environments due to: (i) Fe-bearing phases precipitate at lower pH value, removing As and other toxic elements previously to the formation of Al-phases (Bigham and Nordstrom, 2000; Sánchez-España et al., 2006), and (ii) Al-phases show low crystallinity, which makes difficult their structural characterization (Adams and Rawajfih, 1977; Bigham and Nordstrom, 2000; Caraballo et al., 2015).

Both hydrobasaluminite and basaluminite were first described by Bannister and Hollingworth (1948) as a white plastic clay-like mineral with a variable water content. In that study, both phases were characterized with conventional X-ray techniques, showing well-defined crystalline diffraction patterns that are not congruent with a nanomineral phase. The chemical composition reported was similar to the stoichiometry of felsöbányaite, $[Al_4(OH)_{10}(SO_4)\cdot 5H_2O]$. Later, Brydon and Singh (1969) observed that hydrobasaluminite irreversibly re-crystallizes to basaluminite in few days under atmospheric conditions, indicating that hydrobasaluminite was a less stable phase, being only preserved as a suspension in water. In addition, that study showed that basaluminite precipitated in presence of clay minerals displayed a more crystalline structure. The fact that these early studies reported patterns of well-crystallized materials that were always present as a mixture with clay minerals could suggest that the early identification of basaluminite was not precise enough, and that a mixture of basaluminite and clay mineral was really the observed mineral. More recent studies of basaluminite have reported diffraction patterns with very broad oscillations that are difficult to identify if they are present as a physical mixture with other crystalline phases (Bigham and Nordstrom, 2000; Carrero et al., 2015; Nordstrom, 1982b; Sánchez-España et al., 2011). Adams and Rawajfih (1977) showed that an Al-bearing amorphous precipitate with similar composition to basaluminite occurred in streams affected by acid waters, which aged to alunite and to ‘crystalline basaluminite’ depending upon the aging conditions. The unit cell parameters of an aged precipitate were reported by Clayton (1980) from indexed X-ray powder patterns, and a first structure was proposed containing octahedral Al layers with sulfate ions and variable water content in the interlayer space. More recently, Farkas and Pertlik (1997) reported a structure for both basaluminite and felsöbányaite, defining basaluminite as a nanoparticle of the mineral felsöbányaite. However, as mentioned above, basaluminite present in streams affected by AMD and in ASS shows an amorphous-like X-ray pattern (Bigham and Nordstrom, 2000; Carrero et al., 2015; Nordstrom, 1982b; Sánchez-España et al., 2011). Therefore the amorphous aluminum precipitate described by Adams and Rawajfih (1977) matches well with the description of basaluminite as a non-crystalline material, whereas the re-crystallized phase studied by earlier authors could be felsöbányaite. This fact led to the International Mineralogical Association (IMA) to discredit basaluminite as a mineral, although, interestingly, hydrobasaluminite is still considered as a valid mineral species (a status ‘grandfathered’ from earlier works before the instauration of the IMA). This historical confusion about the nature of basaluminite and hydrobasaluminite, and their (lack of) relation with felsöbányaite clearly deserves a thorough study. To our knowledge, felsöbányaite has never been reported in AMD or ASS systems, and it is actually considered as a rare mineral. Here, we aim to shed some light onto the nanoscale characteristics of basaluminite formed in AMD with the hope to clarify its nature and eventual re-classification as a nanomineral species.

Caraballo et al. (2015) discussed in a recent paper the difficulties related to the identification of poorly-crystalline precipitates as minerals. As described above, the case of basaluminite is paradigmatic: even though it was described as a mineral earlier after its discovery, its diffraction pattern lacks clearly defined peaks (Fig. 4.1). Usually, this would have been enough to classify it as an amorphous material. However, as discussed by Caraballo et al. (2015), the use of advanced characterization techniques for the study of a priori amorphous precipitates could facilitate the identification of nanocrystalline structural motifs that are not detectable using conventional techniques. In particular, the use of high-resolution transmission electron microscopy or of pair distribution function (PDF) analyses of the short-range order have allowed to identify nanocrystallinity as well as amorphous regions in complex natural phases such as schwertmannite, and to propose periodic crystal structures for disordered phases such as ferrihydrite (Drits et al., 1993; Fernandez-Martinez et al., 2010; French et al., 2012; Michel et al., 2007). Here, we show using a combination of spectroscopic and scattering techniques that, in spite of its amorphous diffraction pattern, basaluminite can be described as a disordered, defective version of nanocrystalline felsöbányaite. Because basaluminite plays an important role in the metals behavior in areas affected by AMD and in ASS, these results are necessary for a better understanding of contaminant pathways in these systems.

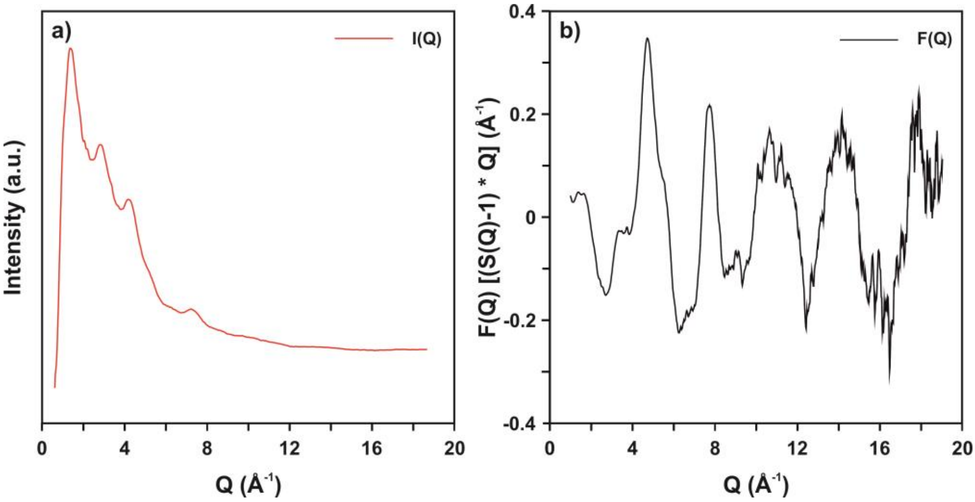

Figure 4.1: *(a) Diffraction pattern in the Q space and (b) reduced structure factor [F(Q)] of natural basaluminite sample.*

4.2. MATERIALS AND METHODS

4.2.1. Solid samples

Three types of aluminum-bearing samples were studied: natural felsöbányaite, and synthetic and natural basaluminites. A sample of natural felsöbányaite from Felsöbánya (Romania) was obtained from a private collection. Natural basaluminite was obtained by slow titration under continuous stirring of an AMD solution from the Perrunal abandoned mine (Iberian Pyrite Belt, SW Spain) using a 0.01 mol L^{-1} $Ca(OH)_2$ solution, as described by Carrero et al. (2015). The precipitate was washed several times with deionized water to dissolve the co-precipitated gypsum. Synthetic basaluminite was prepared by drop-by-drop addition of 214 mL of a 0.015 mol L^{-1} $Ca(OH)_2$ solution to 30 mL of 0.05 mol L^{-1} $Al_2(SO_4)_3 \cdot 18H_2O$ in continuous stirring, according to the method described by Prietzel and Hirsch (1998). Each solid sample was freeze-dried to complete dryness using a VirTis Benchtop freeze-dryer (Hucoa-Erlöss, Spain). After drying, the samples were digested in aqua regia and stored in plastic vials for further chemical analysis.

4.2.2. Analytical techniques

The samples from solid digestions were analyzed for Al and S by inductively coupled plasma atomic emission spectrometry (ICP-AES Thermo Jarrel-Ash) in the laboratories of the IDAEA (CSIC) in Barcelona. Detection limits were $2.6 \cdot 10^{-3}$ mmol L^{-1} for Al and $1.6 \cdot 10^{-2}$ mmol L^{-1} for S, and the analytical error was lower than 5%. Thermo-gravimetric analyses (TGA) were performed to determine the water content of basaluminite and felsöbányaite samples from weight loss *vs*. temperature curves using a TGA92-12 SETARAM, with a N_2 flow of 1.8 l/h, between room temperature and 960 K, with a rate of temperature increase of 9.8 K min^{-1} under nitrogen flow.

High energy X-ray diffraction (HEXD) experiments were performed at the ID31 beamline of the European Synchrotron Radiation Facility (ESRF, Grenoble, France). Powder samples were loaded into polyimide (Kapton) capillaries. Sample and background measurements were carried out at room temperature in a Q-range of 0-25 $Å^{-1}$. Incident X-rays had an energy of 69.5 keV ($\lambda = 0.1784$ Å) that was calibrated using a CeO_2 standard

(NIST 679b). The 2D-images collected by the flat panel Perkin Elmer 2D detector were corrected and integrated using Fit2D (Hammersley et al., 1996). Structure factors [*S(Q)*] and PDF were obtained using the PDFGetX3 software (Farrow et al., 2009).

Sulfur K-edge extended X-ray absorption fine structure (EXAFS) data for natural and synthetic basaluminite was collected at the XAFS (11.1) beamline of the ELETTRA Synchrotron Light Source (Trieste, Italy). The beamline was equipped with a harmonic rejecting double flat Si(111) and Si(311) crystal double cam Kohzu apparatus. Spectra were collected at the sulfur K-edge (2485 eV) in fluorescence mode at a temperature of 100 K. The necessary sample amount was weighted, ground and suspended under ultrasonic vibration in 30 mL of cyclohexane. Immediately, the suspension was filtered through a 0.1 µm cellulose membrane filter and dried at room temperature. EXAFS data were taken in a range from 2300 to 3220 eV with 0.2 eV step size at the edge region. EXAFS data reduction and fitting were performed using the Athena and Artemis software of the IFFEFIT package (Ravel and Newville, 2005). Structural models of sulfate in basaluminite were constructed using the felsöbányaite structure proposed by Farkas and Pertlik (1997). Debye-Waller factors, interatomic distances, coordination numbers and Fermi energy levels were fitted using a least-square refinement algorithm. Statistical F-tests (Joyner et al., 1987; Michalowicz et al., 1999) were applied to determine the statistical significance of different tested hypotheses involving different numbers of shells added to the models. Only those models that improved the fit between theory and experimental EXAFS at the 90% level of confidence were selected.

Solid-state nuclear magnetic resonance (NMR) spectra were recorded using a Bruker Avance II spectrometer operating at 9.4 T, corresponding to a ^{1}H Larmor frequency of 399.9 MHz and a ^{27}Al Larmor frequency of 104.2 MHz, equipped with a triple-resonance 3.2 mm magic-angle spinning (MAS) probe. ^{27}Al MAS NMR experiments were recorded at approximately 300 K, using a hard and short (0.5 µs) radiofrequency pulse (ensuring uniform excitation), a MAS rate of 20 kHz, an experimental repetition delay of 5 s and required approximately only 20 min of cumulative acquisition. The spectral width was 100 kHz and the free induction decay (FID) was measured for 3.2 ms, during which 100 kHz SPINAL-64 heteronuclear decoupling (Fung et al., 2000) was applied. ^{27}Al *z*-filtered multi-quantum magic-angle spinning (MQMAS) spectra (Amoureux et al., 1996) were recorded under the same experimental conditions as for the ^{27}Al MAS NMR experiments except 792 co-added transients were acquired for each of 64 indirect dimension points, using an experimental repetition delay of 0.5 s, resulting in a total experimental time of ~14 h. The spectral width in the indirect dimension was 60 kHz, triple quantum excitation and reconversion were achieved using pulses of 6.0 and 1.6 µs, respectively, and a central-transition-selective "read"-pulse of 8 µs was applied before signal detection.

4.2.3. Rietveld refinement and reverse Monte Carlo structural models

Basaluminite structural models were constructed from reverse Monte-Carlo simulations, using different modified felsöbányaite (Farkas and Pertlik, 1997) as starting structures. Prior to that, the crystal structure of felsöbányaite was refined by the Rietveld method using the FullProf suite programs (Rodríguez-Carvajal, 1993) using a powder X-ray diffraction pattern of natural felsöbányaite. The diffraction pattern was collected on a Siemens D5000 diffractometer in Bragg-Brentano geometry, equipped with a theta-theta goniometer with a rotating sample holder. The patterns were collected using Cu kα_1 ($\lambda_{k\alpha1}$ = 1.5406 Å) and kα_2 ($\lambda_{k\alpha2}$ = 1.5444 Å) radiation in the range 2θ = 0-70° with a step size of 0.04° and a counting time of 6 s per step. Specific constraints were applied during the Rietveld refinement to consider the sulfate molecule as a rigid body.

Three different starting structures were used in the RMC. All of them were built from the previously Rietveld refined felsöbányaite structure, which was modified in some cases by adding Al vacancies or SO_4^{2-} molecules to the structure to match the measured Al/S ratio from the ICP-AES. These structures were: (i) a modified-felsöbányaite with the nominal Al/S = 4 (*fels1*); (ii) a modified-felsöbányaite including Al vacancies to reach an Al/S = 2.7 (*fels2*); and (iii) a modified-felsöbányaite including extra sulfate groups to reach Al/S = 2.7 (*fels3*). In the structure containing Al vacancies (*fels2*), all aluminum sites were fully coordinated by oxygen atoms. Different supercells were used in the refinements with sizes *1×1×1*, *2×2×2* and *3×3×3*. RMC modeling (Keen, 1998; McGreevy and Pusztail, 1988) was performed using the RMCprofile software (Tucker et al., 2014).

Prior to the RMC runs, the partial PDFs of felsöbányaite were calculated using the PDFGui software (Farrow et al., 2009) in order to ascertain what are the atomic pairs that contribute more to the total PDF. This allows simplifying the RMC simulation boxes by not including the atoms with atomic correlations with low weight factors, *i.e.*, those whose correlations are not well represented in the data. Partial PDFs between atoms i and j are weighted in the total PDF with a weight factor, $w_{ij}(r)$ (Egami and Billinge, 2003):

$$w_{ij} = c_i c_j \frac{f_i f_j}{\langle f \rangle^2} \qquad \text{Eq. 4.1}$$

where c_i and c_j are the concentrations of elements i and j, f_i and f_j their atomic form factors evaluated at $Q = 0$, and

$$\langle f \rangle^2 = (\Sigma_i c_i f_i)^2 \qquad \text{Eq. 4.2}$$

A single RMC move involves the random displacement of a number of atoms, which modifies the calculated $S(Q)$ and the PDF of the model structure. Then, a χ^2 is calculated for all the points i of the $S(Q)$ and $G(r)$:

$$\chi^2 = \left\{\Sigma_i \left[S(Q_i)_{exp} - S(Q_i)_{calc}\right]^2 + \Sigma_i \left[G(r_i)_{exp} - G(r_i)_{calc}\right]^2\right\}/\sigma^2 \qquad \text{Eq. 4.3}$$

where σ is a weight factor. RMC moves are automatically accepted when χ^2 is decreased, and are accepted with a probability $p = exp\ (-\Delta\chi^2/2)$ when χ^2 increases. Atom displacements are rejected if they violate the close-contact distances between atoms (see Table 4.1). Bond lengths (S-O) and angles (O-S-O) of the sulfate molecules were constrained to restrict their deformation to less than 20%.

Pair	**O-O**	**O-Al**	**O-S**	**Al-Al**	**Al-S**	**S-S**
Distance	1.3	1.75	1.4	2.7	2.9	2.2

Table 4.1: *Close-contact distances used in the RMC runs for the different structures.*

4.3. RESULTS

4.3.1. Chemical characterization

The stoichiometry of both natural basaluminite [$Al_4(OH)_{9.20}(SO_4)_{1.40}\cdot4.77H_2O$] and synthetic basaluminite [$Al_4(OH)_{9.02}(SO_4)_{1.49}\cdot4.56H_2O$] was characterized by a higher sulfate content than the chemical formula reported by Hollingworth and Bannister (1950) and Farkas and Pertlik (1997), with only one sulfate per four aluminum atoms.

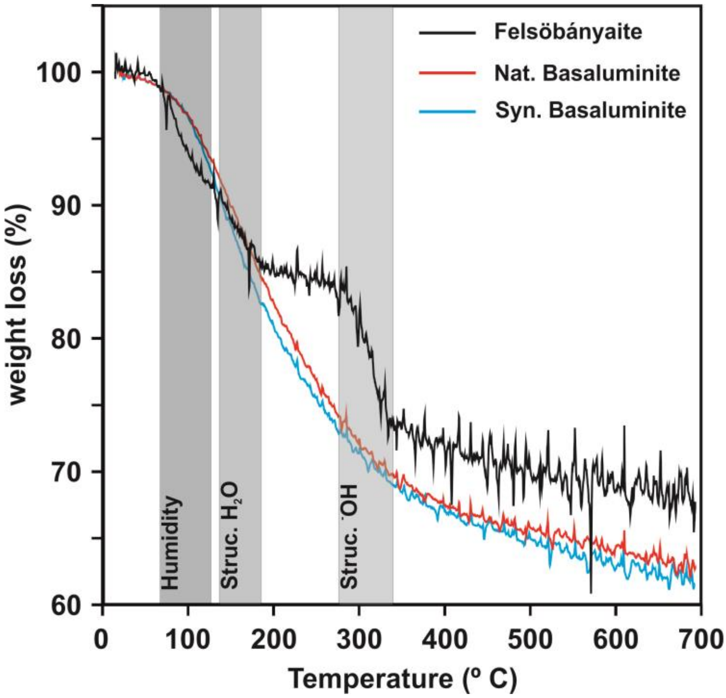

Figure 4.2: *Thermo-gravimetric spectra of felsöbányaite (black), natural (red) and synthetic (blue) basaluminite. The shaded regions represent the different dehydration steps in felsöbányaite.*

TGA analysis of natural felsöbányaite, natural and synthetic basaluminites are shown in Figure 4.2. TGA data of felsöbányaite showed three different weight losses of 8.21 wt.%, 6.30 wt.% and 17.2 wt.% between 320 K and 390 K, 400 K and 455 K, and 540 K and 610 K, respectively (Fig. 4.2). The first and second steps (~14.5 wt.%) are interpreted as corresponding to loosely bound physisorbed and structural H_2O (Brydon and Singh, 1969) (~19.4 wt.%, according to the structure reported by Farkas and Pertlik (1997). The third step (~17.2 wt.%) was associated with the release of structural OH (~19.4 wt.%, according to the structure reported by Farkas and Pertlik (1997). In contrast, TGA data of both natural and synthetic basaluminites produced a unique large sigmoidal-like water desorption and decomposition step between 360 K and 570 K, with associated weight losses of 34.5 wt.% and 34.4 wt.%, respectively. Following this period, the sample weight was constant with a slight decreasing tendency between 570 K to 870 K (Fig. 4.2). The weight loss observed in both solids was associated with the vaporization of physisorbed H_2O and of structural OH/H_2O. Dehydration reactions can be described by Eq. 4.4 and 4.5 for natural and synthetic basaluminites, respectively:

$$Al_4(OH)_{9.20}(SO_4)_{1.40}\cdot 4.77H_2O \rightarrow Al_4O_{4.60}(SO_4)_{1.40} + 9.37H_2O \qquad \text{Eq. 4.4}$$

$$Al_4(OH)_{9.02}(SO_4)_{1.49}\cdot 4.56H_2O \rightarrow Al_4O_{4.51}(SO_4)_{1.49} + 9.07H_2O \qquad \text{Eq. 4.5}$$

The fact that felsöbányaite reveals three well-differenced weight loss areas and basaluminite shows just one is interpreted as due to the structural disorder present in basaluminite. Moreover, the similarity between the curves of natural and synthetic basaluminites suggests that, even though the basaluminite structure is disordered, water in both structures shares similar positions.

4.3.2. Structural characterization

4.3.2.1. High-energy X-ray diffraction

Structure factors obtained from the diffraction patterns of the three samples are shown in Figure 4.3. *S(Q)*s of natural and synthetic basaluminites presented similar characteristics, with the regions of maximum peak intensity and diffuse scattering distributed along *Q* in a similar way to felsöbányaite, suggesting similar structural characteristics. As expected, the structure factor of both basaluminite samples lacks any well-defined diffraction ‘peak’, suggesting an amorphous material (Fig. 4.3).

PDFs of natural and synthetic basaluminites, natural felsöbányaite and calculated partial PDFs of felsöbányaite (Farkas and Pertlik, 1997) (Al-Al, Al-O, Al-S, S-S, S-O and O-O atom pairs) are shown in Figure 4.4. PDFs of synthetic and natural basaluminites revealed that the synthesis process yields nanoparticles with local order similar to that of natural samples. The intensity decay along *r* was fitted with an envelope function reproducing particles of spherical shape (Gilbert, 2008), considering as well the instrumental resolution effect determined previously with the CeO_2 standard (Toby and Egami, 1992). Natural and synthetic samples of basaluminite showed an identical coherent domain size of about 1.2 nm, while the coherent domain size obtained for the felsöbányaite sample was in the range of 4-5 nm. PDFs of both felsöbányaite and basaluminite exhibited similar structural features in the region between 1 and 6 Å, with significant variations in peak intensities and width (Fig. 4.4). Both basaluminite and felsöbányaite PDFs were compared in order to identify similarities and to associate individual peaks to interatomic distances using the calculated partial PDFs of felsöbányaite. The position of the first peak at 1.45 Å corresponded to the S-O distance in the sulfate tetrahedron, whereas the second peak at 1.88 Å was attributed to the Al-O distance in the aluminum octahedron. The peak at 3 Å corresponded to the superposition of Al-Al and O-O distances, where the Al-Al distance corresponded to edge-sharing aluminum octahedra and the O-O distance was related to consecutive oxygen atoms in the octahedra. The next three peaks (at 4, 4.8 and 6 Å) are mainly due to Al-O distances. Subsequent peaks at $r > 6$ Å presented low intensities, making it impossible to identify the corresponding atom pairs.

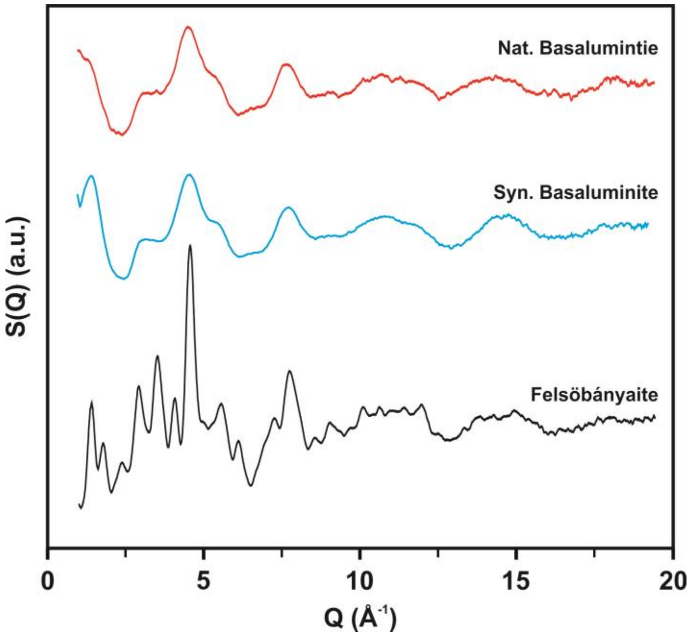

Figure 4.3: *X-ray diffraction structure factor [S(Q)] of felsöbányaite (black), natural (red) and synthetic (blue) basaluminite.*

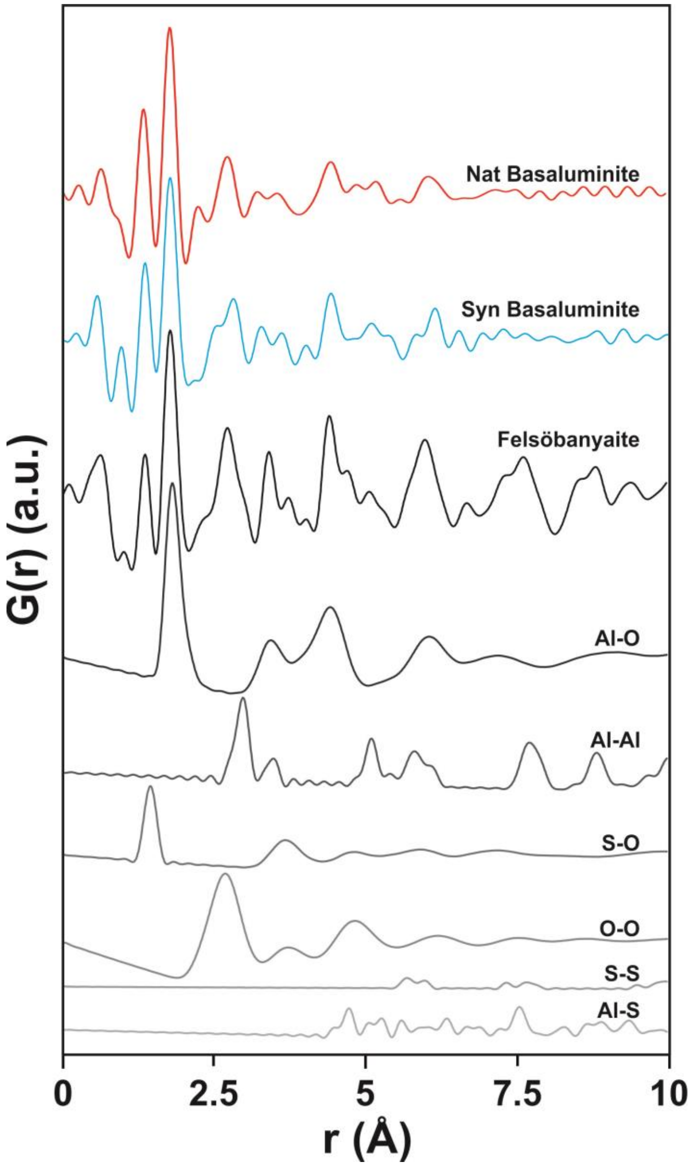

Figure 4.4: *PDF of natural felsöbányaite (black), and natural (red) and synthetic (blue) basaluminite. Calculated partial PDFs of felsöbányaite from the structure proposed by Farkas and Pertlik (1997) are showed in grayscale.*

4.3.2.2. Nuclear magnetic resonance

^{27}Al MAS and ^{27}Al MQMAS NMR spectra are shown in Figures 4.5 and 4.6, respectively. Aluminum in amorphous and mineral phases has been observed in 4-, 5- and 6-coordination states [Al(IV), Al(V) and Al(VI)], where Al(IV), Al(V) and Al(VI) are represented by ^{27}Al MAS NMR peaks between +55 and +85 ppm, +30 and +41 ppm, and

+0 and +15 ppm, respectively (Kirkpatrick and Phillips, 1993). Both natural and synthetic basaluminites showed similar Al-coordination, where Al(VI) was the most abundant coordination, characterized by a broad peak, highlighting the presence of a range of Al-O-Al bond angles (*i.e.* high degree of structural disorder). Interestingly, Al(V) and Al(IV) are also present in the structure but to a much lesser extent, about 5% and 1% respectively (Fig. 4.5). These Al-coordination states have been previously reported in white precipitates collected in systems affected by acid water (Kim, 2015). ^{1}H NMR data (not shown) indicated the presence of physisorbed H_2O as well as Al-OH hydroxyl groups. There is no evidence of Al(IV) or Al(V) coordination in felsöbányaite (Figs. 4.5 and 4.6b). The high-resolution ^{27}Al MQMAS NMR spectra (Fig. 4.6) better reveal the differences between the samples. Although felsöbányaite contains only Al(VI) coordination like gibbsite, it is evidently less well ordered. Moreover, the Al(VI) coordination of both natural and synthetic basaluminites are even less ordered, with the synthetic sample being the most amorphous. It is also interesting to note that there seems to be two different Al(IV) coordinations in the natural basaluminite, one of them being quite crystalline while the other is very similar to that in the synthetic version.

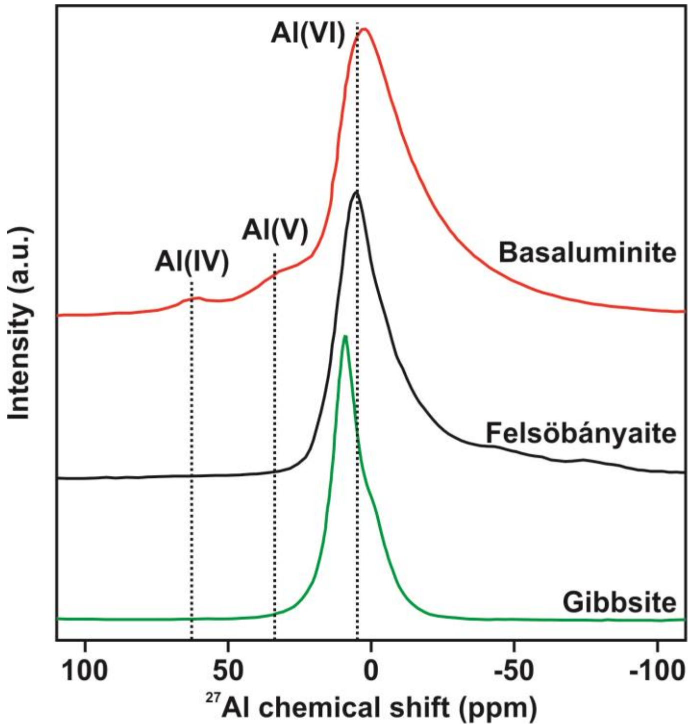

Figure 4.5: *^{27}Al MQMAS NMR spectra of basaluminite, felsöbányaite and gibbsite (standard). The three bands represent Al(IV)-, Al(V)- and Al(VI)-coordination.*

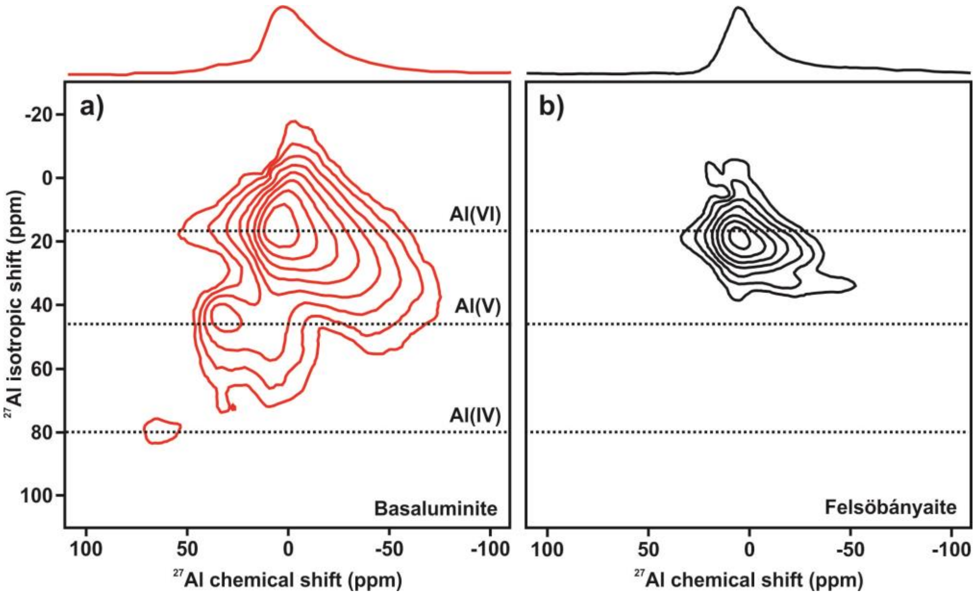

Figure 4.6: *2D ^{27}Al MQMAS-^{27}Al MAS NMD spectra of (a) basaluminite and (b) felsöbányaite.*

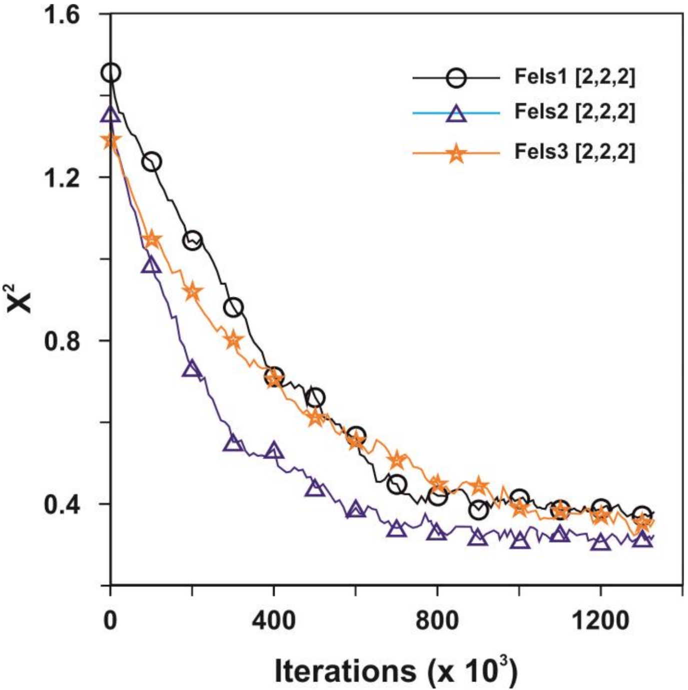

Figure 4.7: *χ^2 evolution during RMC runs of fels1[2,2,2], fels2[2,2,2] and fels3[2,2,2] supercells.*

4.3.2.3. Reverse Monte Carlo models

The qualitative analysis of the PDF data and the similarities in the Al(VI) coordination found by NMR suggest that the basaluminite structure seems to have similar features to that of felsöbányaite, though with non-negligible distortions, as suggested by Farkas and Pertlik (1997). Based on this observation, and in order to develop an atomistic structural model of basaluminite that matches the diffraction and PDF data, a RMC refinement strategy was followed.

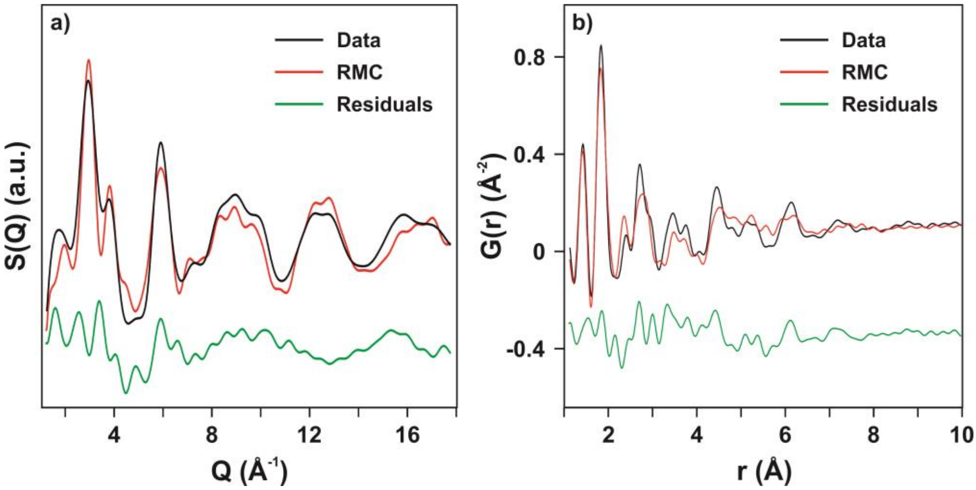

Figure 4.8: *(a) Experimental structure factor and (b) pair distribution function of synthetic basaluminite (black) compared with those obtained from RMC with the fels2 [2,2,2] structure (red), and difference (green).*

The evolution of the χ^2 agreement parameter for the $2\times2\times2$ supercells of the three models used (*fels1*, *fels2* and *fels3*) is shown in Figure 4.7. The three structures show similar final χ^2 values, indicating that the three of them provide equally good representation of the scattering data. Even though longer simulations provided better agreement, a choice was made to stop RMC simulations once the χ^2 started to show a plateau; RMC simulations that were run for a longer time (larger number of steps), provided similar χ^2 values, but showed higher structural disorder.

Differences between experimental and modeled *S(Q)* and *G(r)*, different views of the atomistic structure and a Al-O bond distances of the structure *fels2 [2,2,2]* are displayed in Figures 4.8, 4.9 and 4.10, respectively. The *fels2 [2,2,2]* model kept the octahedral-layer structure, with only slight distortions. Sulfate and oxygen from water molecules placed in the interlayer space were slightly displaced from their original positions (Fig. 4.7). However, the contribution of these molecules to the total PDF and to the scattering was negligible (Figs. 4.4 and 4.6), and therefore no sensible information about their positions can be reported.

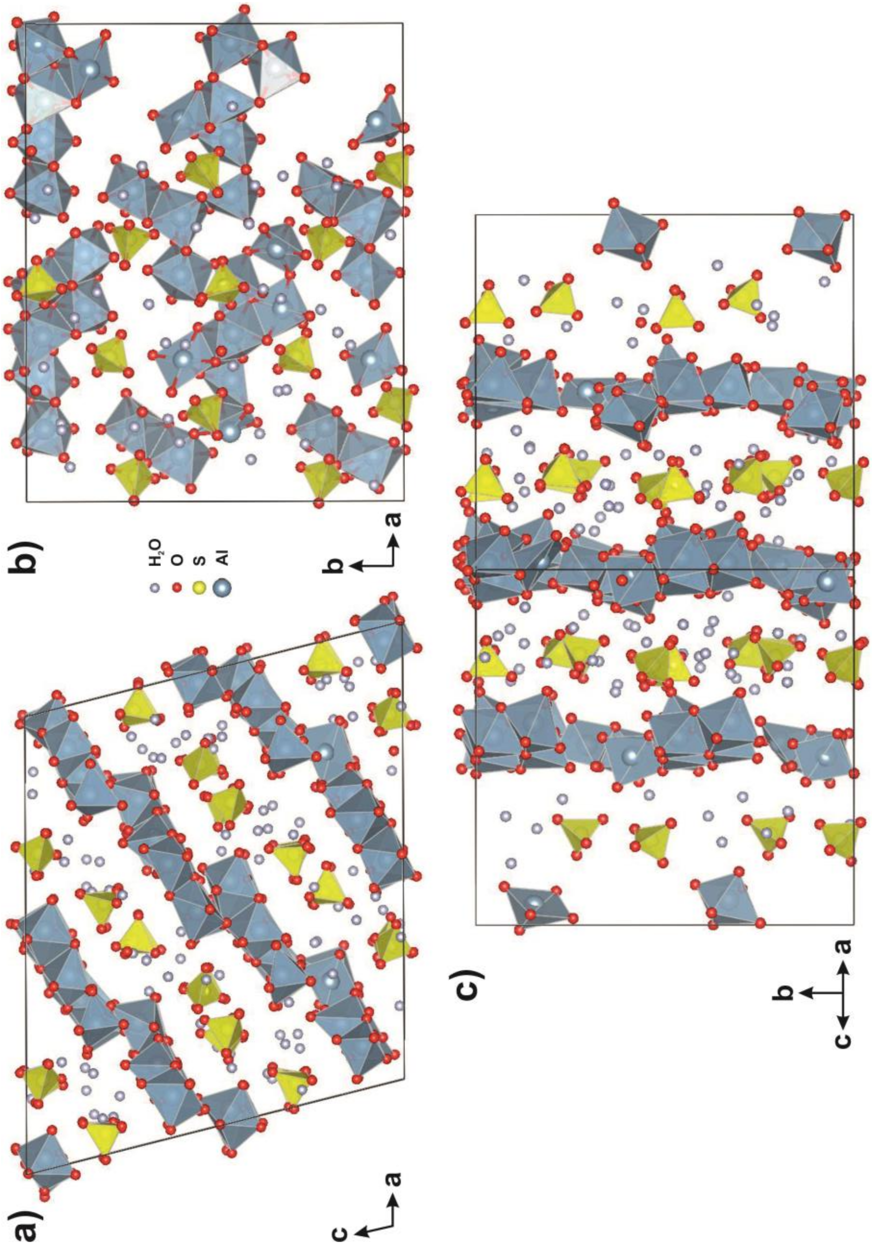

Figure 4.9: *Different views of the final basaluminite structure, from (a) plane a-c, (b) plane a-b, and (c) b-edge of the fels2 [2,2,2] structural model after RMC refinement. The section (a) and (c) reveal the octahedral-layer deformation and (b) shows the vacancies in Al-octahedral position imposed previously to RMC model by reach [Al]/[S] proportion in natural samples.*

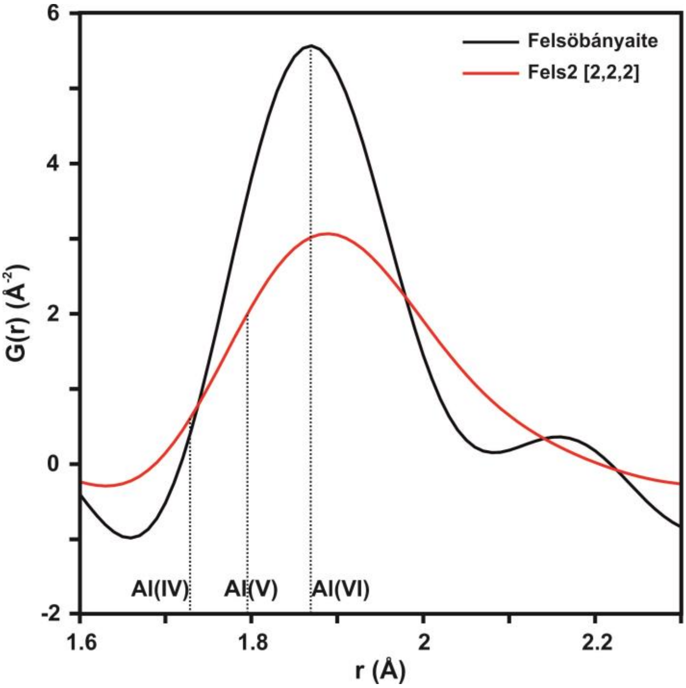

Figure 4.10: *Al-O partial pair distribution function of a Rietveld refined felsöbányaite (black) and the fels2 [2,2,2] RMC refined structure (red). The vertical lines indicate the Al-O distance for Al(IV), Al(V) and Al(VI).*

4.3.2.4. Sulfur K-edge EXAFS

Sulfur K-edge EXAFS from synthetic and natural basaluminites, and the parameters of the different structural models tested are shown in Figure 4.11 and Tables 4.2 and 4.3. Results from natural basaluminite were characterized by the presence of one shell at 1.45 ± 0.01 Å which is attributed to the S-O distance (Fig. 4.11). This peak was consistent with an undistorted sulfate tetrahedron with coordination number of 4.80 (fixed) Å. Three different models were considered during the fitting process: (i) a sulfate in outer-sphere position (just one shell); (ii) a surface complex with a monodentate inner-sphere ligand; and (iii) a surface complex with a bidentate binuclear inner-sphere ligand on aluminum octahedral layers. A model where sulfate is forming an outer-sphere location yielded the best fit and a 75% of confidence in the F-test, which is in agreement with the localization of sulfate in felsöbányaite (Farkas and Pertlik, 1997) (Table 4.2). On the other hand, S K-edge EXAFS in synthetic basaluminite showed that sulfate was also retained by bidentate binucleate inner-sphere covalent ligands, where a double shell was identified with peaks located at 1.46 ± 0.01 Å and 3.02 ± 0.03 Å. These peaks were associated to S-O and S-Al distances with coordination number of 4.58 ± 0.05 and 2.00 (fixed value), respectively (Fig. 4.11) (Table 4.3). The F-test values obtained for these models indicated that the bidentate binuclear inner-sphere was the best fit, where the confidence level was 60% (Table 4.3). The confidence levels obtained in both F-test studies were close or less to the minimum necessary, indicating that both models were possible and that the second shell is near the limit of detection.

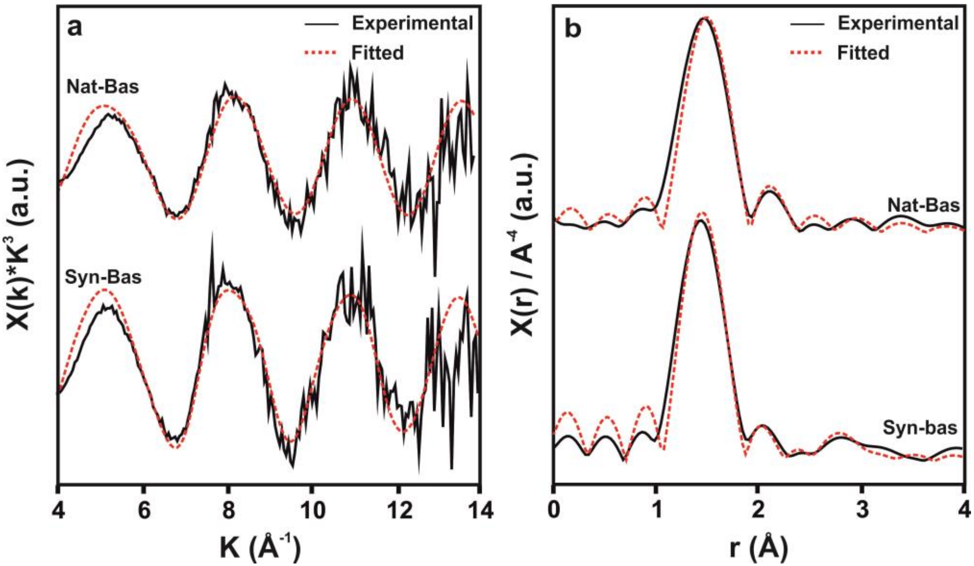

Figure 4.11: *(a) EXAFS spectra and (b) its Fourier transform* k^3*-weighted S K-edge EXAFS data of natural and synthetic basaluminite. Experimental and fitted curves are displayed in black and red color respectively.*

Model	**Path**	**Neighbor**	**N**	σ^2	**R**	ΔE_0	**V**	$\Delta\chi^2$
1*	S-O_T	One shell	4.800 (fixed)	0.0001 ± 0.0002	1.454 ± 0.002	0.213 ± 1.342	4	16.3
2	S-O_T	Shell 1	5.172 ± 00783	0.0004 ± 0.0003	1.454 ± 0.003	0.354 ± 1.736	4	32.0
	S-Al	Shell 2	2.000 (fixed)	0.0009 (fixed)	3.119 ± 0.029	0.354 ± 1.736		
3	S-O_T	Shell 1	5.208 ± 0.083	0.0003 ± 0.0003	1.453 ± 0.004	1.453 ± 1.771	4	33.3
	S-Al	Shell 2	1.000 (fixed)	0.0009 (fixed)	2.109 ± 0.023	1.453 ± 1.771		

Table 4.2: *Modeling parameters for S K-edge EXAFS in natural basaluminite with 1) 100% outer-sphere ligand, 2) 100%, and 3) 50% bidentate binucleate inner-sphere ligand. * best fit according to F-test.*

Model	**Path**	**Neighbor**	**N**	σ^2	**R**	ΔE_0	**V**	$\Delta\chi^2$
1	S-O_T	One shell	4.023 ± 0.057	0.0003 ± 0.0003	1.459 ± 0.002	3.022 ± 1.402	3	36.0
2*	S-O_T	Shell 1	4.583 ± 0.051	0.0009 ± 0.0003	1.458 ± 0.003	2.049 ± 1.201	5	17.9
	S-Al	Shell 2	2.000 (fixed)	0.0057 ± 0.0037	3.017 ± 0.033	2.049 ± 1.201		
3	S-O_T	Shell 1	4.532 ± 0.057	0.0009 ± 0.0003	1.458 ± 0.003	2.323 ± 1.350	5	21.8
	S-Al	Shell 2	1 (fixed)	0.0091 ± 0.0069	2.188 ± 0.057	2.323 ± 1.350		

Table 4.3: *Modeling parameters for S K-edge EXAFS in synthetic basaluminite with 1) 100% outer-sphere ligand, 2) 100%, and 3) 50% bidentate binucleate inner-sphere ligand. * best fit according to F-test.*

4.4. DISCUSSION

4.4.1. Sulfate and water environments in basaluminite

The higher sulfate contents observed in both natural and synthetic basaluminites with respect to the chemical composition reported for felsöbányaite (Farkas and Pertlik, 1997; Hollingworth and Bannister, 1950) could be related to the nanocrystalline, defective structure of basaluminite and its larger surface area. This difference in oxyanion content by nanomineral phases have been reported in other precipitates present in AMD and ASS (*e.g.* schwertmannite; Bigham et al., 1994). The different sulfate structural positions observed in natural and synthetic basaluminites could be associated with the higher sulfate concentration in solution during the synthesis of basaluminite, resulting in a higher proportion of adsorbed sulfate. In fact, the sulfate content is slightly higher in synthetic than in natural basaluminite (Al/S = 2.86 and 2.68 in natural and synthetic basaluminites respectively). EXAFS results and statistical F-test analysis indicated that sulfate shows a bidentate coordination with the Al-framework in synthetic basaluminite, though the statistical significance of this result is near the limit of acceptable confidence. Actually, both spectra are very similar, with mainly one frequency associated to the S-O distance. The presence of inner-sphere sulfate in synthetic basaluminite could be explained by the higher sulfate concentration in these samples, and therefore the higher probability that some sulfate can adopt different bonding environments. Most sulfate is retained in basaluminite by outer-sphere ligands, such as those present in the felsöbányaite structure (Farkas and Pertlik, 1997).

Finally, the unique large sigmoidal-like water desorption step observed in TGA data indicates that the physisorbed and hydroxyl groups in both natural and synthetic basaluminites presented a similar disorder environment with non-well-defined structural positions with respect to felsöbányaite (Fig. 4.2). However, no further information about the water positions in the structure could be obtained due to their very low X-ray scattering weight factor, resulting in a negligible contribution to the total PDF.

4.4.2. Aluminum framework

The high structural correlation observed between basaluminite and felsöbányaite in the first 6 Å of the PDF and the good fit obtained with RMC with only slight distortions of the felsöbányaite structure indicate that basaluminite can be described as a mineral nanoparticle. Two structural models were considered to explain the origin of this disorder that match well the observed Al/S ratio: (i) a structure formed by an identical Al-framework to that of felsöbányaite, where excess sulfate was due to formation of surface complexes (*fels1*) on the external surface, and (ii) a structure where aluminum point defects (vacancies) are present in the Al layers (*fels2*). RMC simulations of these two models yielded similar χ^2 values (Fig. 4.7) indicating that both are equally plausible. An atomistic model obtained from the RMC modeling is shown in Figure 4.8. The level of distortion is represented in Figure 4.10, where the Al-O first neighbor distance in *fels2* is shown. The asymmetric shape can be partially due to the presence of Al(IV) and Al(V) coordinations in basaluminite; Al(IV)-O and Al(V)-O distances in oxyhydroxide phases are in the order of 1.76 Å and 1.80 Å , respectively (Kubicki, 1998).

The presence of tetrahedral and pentahedral Al-coordinations in basaluminite found by NMR spectroscopy is an important difference between felsöbányaite and basaluminite. Different reasons can explain the presence of tetrahedral Al: (i) Al(IV) is a structural component in silicate minerals, such as feldspars and phyllosilicates (^{27}Al NMR peaks at 70 ppm, Kirkpatrick and Phillips, 1993), and basaluminite precipitation in streams affected by AMD and ASS is associated with the removal of Si from the solution (Bigham and Nordstrom, 2000). *A priori*, HEXD results found no evidence of crystalline silicate minerals, with basaluminite being the only phase present in the samples (Figs. 4.1 and 4.3). However, the presence in small proportions of a disordered aluminosilicate phase cannot be ruled out from these experiments. (ii) Al_{13} Keggin ions (^{27}Al NMR peaks at 60 ppm, Jolivet et al., 2011), which contain one Al in tetrahedral coordination, have been proposed as structural building motifs for many Al-oxyhydroxide phases (such as gibbsite, boehmite and bayerite; Jolivet et al., 2011), and it could be possible that they also participate in the precipitation process of basaluminite. Indeed, the NMR chemical shift of 60 ppm found for Al(IV) in basaluminite matches the value found for sulfate-bearing phases formed from Al_{13} Keggin ions (Kirkpatrick and Phillips, 1993) (Figs. 4.5 and 4.6a). On the other hand, the presence of Al(V) in basaluminite (~5%) is characteristic of materials with large surface areas (Kirkpatrick and Phillips, 1993), where water molecules are coordinated to surface Al(IV) atoms.

4.4.3. Is basaluminite a single nanomineral species?

The lack of clearly defined peaks in the diffraction pattern, due to small coherent domain size and to the accumulation of structural defects, prevents us from defining a unit cell to describe the basaluminite structure. However, the use of the PDF method clearly shows that the average local order is not far from that of a disordered felsöbányaite nanoparticle. Following recent discussions in the mineralogical literature (Caraballo et al., 2015), this could then just be interpreted as a case where the use of advanced characterization techniques allows revealing the nature of a mineral nanoparticle that would have been otherwise classified as an amorphous material. However, the different geological occurrences of felsöbányaite and basaluminite make that more careful analyses need to be performed on the structure of the aged basaluminite. A couple of studies (Adams and Rawajfih, 1977 and Brydon and Singh, 1968) reported the formation of a so-called 'crystalline basaluminite' when aged in the presence of Ca-bearing solutions at 320 K. Interestingly, these conditions are similar to the ones that could be found in alkaline 'chalky' sedimentary environments where some of the first basaluminite occurrences were described (Bannister and Hollingworth, 1948; Brydon and Singh, 1969; Clayton, 1980). But, to the best of our knowledge, felsöbányaite or 'crystalline basaluminite' have never been reported in AMD or ASS environments. More studies need to be undertaken to better understand the relationship between these two phases and the aging mechanisms. Performing these studies would help clarifying the status of basaluminite as a single nanomineral species or as a felsöbányaite mineral nanoparticle.

The description of the sulfate retention mechanisms reported here allows for a better description of the basaluminite-mediated anionic exchange processes that could be at play in AMD-affected streams and in ASS. Basaluminite is a nanocrystalline phase, but still it shows a strong anion exchange capacity (Carrero et al. Submitted). This is in agreement with the idea that basaluminite keeps the layered structure present in felsöbányaite, where sulfate atoms are placed in the interlayer and are exchangeable. This fact has strong environmental implications, making basaluminite an important phase controlling anionic pollutant concentrations in the environments where it occurs.

CHAPTER V

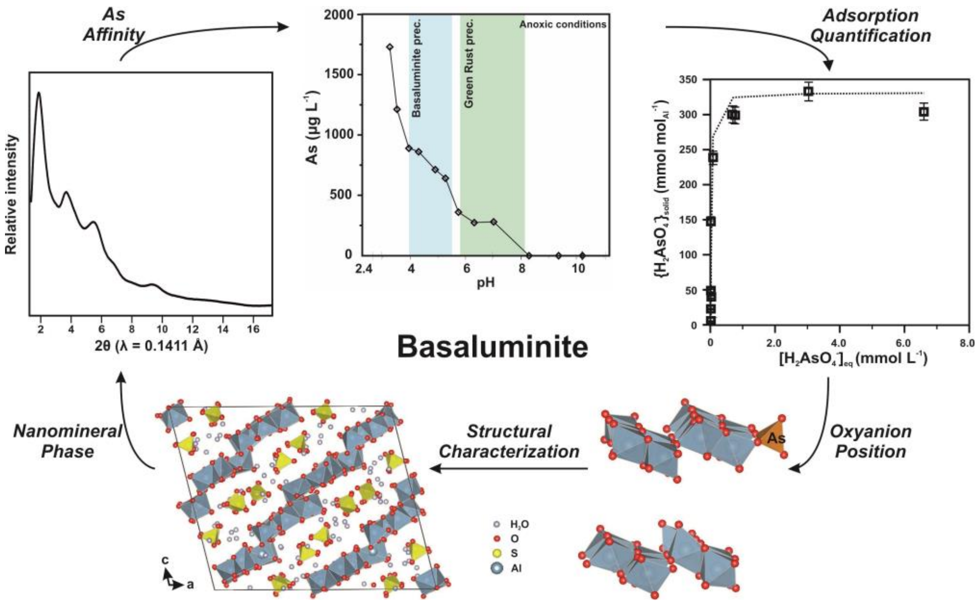

General Conclusions

The research carried out during this doctoral work is aimed to study the precipitation of basaluminite, a nanocrystalline Al-hydroxysulfate found in systems affected by AMD (*Acid Mine Drainage*) and ASS (*Acid Sulfate Soils*). The main objectives were: (i) to explore its affinity for metals and metalloids (from now on referred as 'metals') under laboratory conditions, (ii) to quantify its maximum adsorption capacity for As and Se and (iii) to build an atomistic model taking into account its short-range order. Following the results of the different experiments carried out in this doctoral dissertation, it is possible to summarize the following general conclusions:

- Schwertmannite (a nanocrystalline Fe-oxyhydroxysulfate) precipitation under atmospheric conditions occurs prior to basaluminite precipitation and removes 100% of As, Cr, Fe and Pb from the solution along with 50% of Al. Aluminum removed from the solution could either be adsorbed and/or co-precipitated by schwertmannite, which could affect its removal capacity of other elements, or form individual nanoparticles.
- Metal removal capacity of basaluminite depends significantly on precipitation conditions. During the neutralization under atmospheric conditions, basaluminite precipitates after schwertmannite and only shows affinity for Cu and Si, besides removing the remaining Al from the solution. However, under anoxic conditions with all the Fe as Fe(II) in solution, basaluminite precipitation occurs first, removing 60% and 100% of As and Cr, respectively. Hence, the previous schwertmannite precipitation under atmospheric conditions masks the high basaluminite affinity for some contaminants such as As and Cr.
- Under anoxic conditions, Fe(II) in solution precipitates after basaluminite likely as green rust according to thermodynamic modeling, which removes the remaining As and 100% of Pb. However, these phases are highly unstable under atmospheric conditions and rapidly transform into ferrihydrite or feroxyhyte, although this process does not release the previously retained contaminants. The use of X-ray diffraction based on synchrotron light was necessary to identify schwertmannite, basaluminite, ferrihydrite and feroxyhyte in the newly-formed precipitates.
- Neutralization of AMD sources of underground galleries under anoxic condition with all Fe as Fe(II) in solution involves a lower alkalinity consumption than neutralization under atmospheric condition after Fe oxidation. Therefore, the

implementation of treatment systems in punctual sources of reducing AMD could be more sustainable as passive treatment strategies.

- Once identified the strong affinity of contaminants by basaluminite, masked by schwertmannite, a comparative study of the removal capacity of As and Se in both phases was performed by adsorption isotherm experiments. Basaluminite shows almost three times higher affinity for As (326 $mmol_{H2AsO4}$ mol_{Al}^{-1}) than schwertmannite (128 $mmol_{H2AsO4}$ mol_{Fe}^{-1}), whereas schwertmannite slightly removes more Se (122 $mmol_{SeO4}$ mol_{Al}^{-1} *vs.* 153 $mmol_{SeO4}$ mol_{Fe}^{-1}).
- In both nanominerals, As is removed from the solution and retained in the solid by a combination of mechanisms of oxyanion exchange with structural sulfate and formation of surface complexes in the same proportion. Due to the necessity to compensate the difference of charge between the most abundant As specie in solution ($H_2AsO_4^-$) and sulfate (SO_4^{2-}), the rate of adsorbed As to released sulfate is 2:1. On the other hand, the main Se adsorption mechanism in both phases is the oxyanion exchange, where each sulfate group released from the structure is replaced by a single Se molecule (SeO_4^{2-}), indicating a 1:1 ratio that is expected due to that both species have equal charge.
- The presence of sulfate in solution has a competitive negative effect in the Se removal, since both oxyanions share the same structural position, replacing the structural sulfate. However, As is little affected by the sulfate presence in solution due to that this oxyanion can be also removed by formation of strong surface complexes.
- The pair distribution function analysis of high-energy X-ray diffraction patterns and X-ray absorption fine structure analysis, both based on synchrotron radiation, reveal that As is retained in both phases by a variable proportion of bidentate binuclear inner-sphere. Schwertmannite shows all As with this coordination at low initial As concentrations in solution. However, at high initial concentrations only 50% is located in inner-sphere position, whereas the remaining 50% is in outer-sphere coordination. On the other hand, basaluminite shows all As in bidentate binuclear inner-sphere coordination, regardless of initial As concentration in solution. This fact indicates that basaluminite is a more efficient As scavenger than schwertmannite because basaluminite removes more As from the solution and metal-complexes are bound to the structure by stronger ligands.

- The Se sorbed onto schwertmannite and basaluminite forms weaker ligands than As in both structures. Basaluminite shows all Se in outer-sphere position, likely in the interlayer space by replacing the sulfate groups. However, schwertmannite shows approximately 25% of Se in bidentate binuclear inner-sphere position. Therefore, schwertmannite is a slightly more efficient Se scavenger than basaluminite, with higher adsorption capacity and stronger removal complexes.
- The high adsorption capacity of basaluminite evidences the need of in-depth studies about the structure and its comparison with that previously described for the most crystalline Al-hydroxysulfate (felsöbányaite). The water content in basaluminite is similar between synthetic and natural samples, and slightly lower than the stoichiometric content. The physisorbed water and hydroxyl groups show similar coordination in both basaluminite and felsöbányaite, although the structural position in felsöbányaite is better defined.
- Basaluminite precipitation mechanism shows a significant effect in sulfate environment. In both cases, synthetic and natural basaluminite samples are characterized by higher sulfate content with respect to the stoichiometric composition. However, natural basaluminite shows all sulfates in outer-sphere coordination, whereas synthetic basaluminite exhibits inner-sphere ligands. This fact can be due to a higher sulfate concentration in solution during the synthesis procedure with respect to natural solutions, inducing to formation of these complexes on the surface of synthetic basaluminite.
- Aluminum in both basaluminite and felsöbányaite is found in different coordination. Al_{13} Keggin ion clusters could be the mineral precursor of basaluminite due to that both phases display Al in tetrahedral coordination [Al(IV)], although basaluminite also shows pentacoordinate Al [Al(V)].
- Basaluminite has a coherent domain size of ~1.2 nm. PDF data show that both felsöbányaite and basaluminite have similar structural features in the region between 1 and 6 Å. This lead us to interpret basaluminite as a felsöbányaite nanoparticle. However, the fact that felsöbányaite geological occurrence is disconnected from that of basaluminite suggests that the latest could be interpreted as a different nanomineral.
- Structural models performed with reverse Monte Carlo simulations indicate that basaluminite is effectively formed by Al-octahedral layers with vacant positions and high angular and length distortions in the octahedra. The excess sulfate is

related to a relative increase of the vacant Al positions in the structure. Finally, basaluminite cannot be described by a unique unit cell and this phase has to be understood as an extended net with high amount of structural defects that avoid the development of periodicity further than 1.2 nm.

In this doctoral dissertation, basaluminite has been described as a strategic nanomineral on the metals behavior in areas affected by AMD and ASS. However, the research presented here is only the first step in the understanding of this phase and its properties. Further and deeper research needs to be performed to ascertain nucleation and growth processes, the relationship between Al_{13} Keggin ion and basaluminite, and the fate of the adsorbed elements during the basaluminite recrystallization to more stable Al-phases due to its metastable character.

CAPÍTULO V

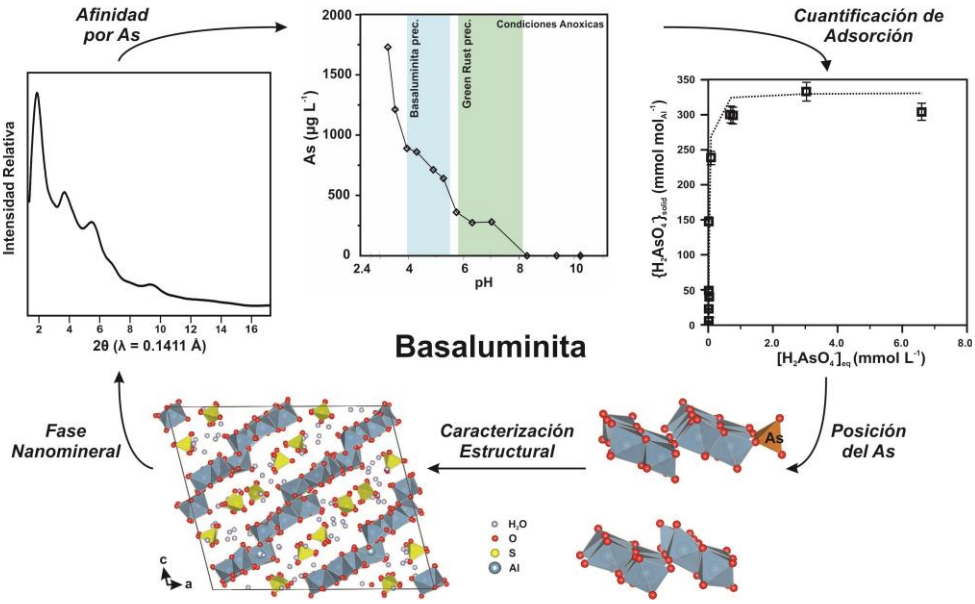

Conclusiones Generales

El trabajo de investigación desarrollado en el marco de la presente Tesis Doctoral pretende caracterizar los precipitados de basaluminita, un hidroxisulfato de aluminio nanocristalino que se forma en sistemas afectados por AMD (*Acid Mine Drainage*) y ASS (*Acid Sulfate Soils*). Los objetivos principales eran: (i) determinar la afinidad por metales y metaloides (en adelante 'metales') en experimentos de laboratorio, (ii) cuantificar su máxima capacidad de adsorción para As y Se y (iii) desarrollar un modelo atomístico teniendo en cuenta su orden local. Siguiendo los resultados de los diferentes experimentos llevados a cabo en esta Tesis Doctoral, se llegan a las siguientes conclusiones generales:

- La precipitación de schwertmannita (un oxihidroxisulfato de hierro nanocristalino) en condiciones ambientales ocurre antes que la precipitación de basaluminita y retira el 100% de As, Cr, Fe y Pb en solución junto con el 50% de Al. El aluminio retirado de la solución podría estar absorbido y/o co-precipitado por schwertmannite, lo cual pudría afectar a su capacidad para retener otros elementos, o bien formar nanopartículas individuales.
- La capacidad de retención de metales por basaluminita depende significativamente de las condiciones de precipitación. Durante la neutralización en condiciones ambientales, la basaluminita precipita después de schwertmannita y sólo manifiesta afinidad por Cu y Si, además de retirar el resto de Al en solución. Sin embargo, en condiciones anóxicas con todo el Fe como Fe(II) en solución, la precipitación de basaluminita ocurre en primer lugar, retirando 60% y 100% de As y Cr disponible, respectivamente. Por tanto, la previa precipitación de schwertmannita en condiciones ambientales enmascara la elevada afinidad de basaluminita por algunos contaminantes como As y Cr.
- En condiciones anóxicas, el Fe(II) en solución precipita después de basaluminita probablemente como *green rust,* según modelos termodinámicos, retirando el As restante y el 100% de Pb. Sin embargo, estas fases son muy inestables en presencia de oxígeno y se transforman rápidamente a ferrihidrita o feroxihita, aunque este proceso no supone la liberación de los contaminantes previamente retirados. Fue necesaria la utilización de difracción de rayos X con radiación sincrotrón para la identificación de schwertmannita, basaluminita, ferrihidrita y feroxihita en los precipitados neoformados.
- La neutralización de AMD surgente de galerías subterráneas en condiciones anóxicas con todo el Fe como Fe(II) en solución supone un menor consumo de

alcalinidad que si se realiza una vez que el Fe se ha oxidado. Por tanto, la instalación de sistemas de tratamiento en focos puntuales de AMD reducidos podría ser más sostenible como estrategia de tratamiento pasivo.

- Una vez identificada la marcada afinidad de contaminantes por basaluminita, enmascarada por schwertmannita, se hizo un estudio comparativo de capacidad de retención de As y Se en ambas fases usando isotermas de adsorción. Basaluminita muestra una afinidad casi tres veces mayor por As (326 $\text{mmol}_{\text{H2AsO4}}$ $\text{mol}_{\text{Al}}^{-1}$) en solución que schwertmannita (128 $\text{mmol}_{\text{H2AsO4}}$ $\text{mol}_{\text{Fe}}^{-1}$), mientras que schwertmannita adsorbe ligeramente más Se (122 $\text{mmol}_{\text{SeO4}}$ $\text{mol}_{\text{Al}}^{-1}$ *vs.* 153 $\text{mmol}_{\text{SeO4}}$ $\text{mol}_{\text{Fe}}^{-1}$).
- En ambos nanominerales, As es retirado de la solución y retenido en el sólido por una combinación de mecanismos de intercambio iónico con el sulfato estructural y formación de complejos superficiales a partes iguales. Dado que existe una necesidad de compensar la diferencia de cargas entre la especie dominante de As en solución ($H_2AsO_4^-$) y el sulfato (SO_4^{2-}), la relación As adsorbido con respecto a sulfato liberado a la solución es de 2:1. Por otro lado, el principal mecanismo de adsorción de Se en ambas fases es el intercambio iónico, donde cada sulfato retirado de la estructura es reemplazado por una única molécula de Se (SeO_4^{2-}), indicando una relación 1:1 esperable dada la igualdad de cargas entre especies.
- La presencia de sulfato en solución muestra un efecto significativo de competencia con Se, relacionado con el hecho de que ambos oxianiones comparten la misma posición, reemplazando el sulfato estructural. Sin embargo, la presencia de sulfato afecta levemente al As dado que este oxianión también forman fuertes complejos superficiales.
- El cálculo de la función de distribución de pares del patrón de difracción de rayos X de alta energía y análisis de absorción de rayos X en estructura fina, ambos usando radiación sincrotrón, permitieron determinar que el As es retenido en ambas fases por una proporción variable de complejo bidentado binucleado de esfera interna. La schwertmannita muestra todo el As con esta coordinación a bajas concentraciones iniciales de As en solución. Sin embargo, a altas concentraciones solo el 50% del As retenido en la estructura presenta este complejo, mientras que el 50% restante ocupa posiciones de esfera externa. Por su parte, la basaluminita muestra todo el As retenido en posición bidentada binucleada de esfera interna independientemente de la concentración inicial de As en solución. Esto indica que

la basaluminita es más eficiente en la retirada de As dado que es capaz de adsorber mayor cantidad de este elemento y los complejos metálicos son enlaces más fuertes.

- El Se adsorbido en schwertmannita y basaluminita forma enlaces menos estables en la estructura de ambas fases. La basaluminita muestra todo el Se retirado en posición de esfera externa, probablemente en los espacios entre capas sustituyendo los sulfato. Sin embargo, la schwertmannita presenta un 25% del Se en posición de esfera interna. En conclusión, la schwertmannita es ligeramente más eficiente en la retirada de Se, adsorbiendo mayor concentración de este elemento y reteniéndolo en complejos más fuertes.
- La alta capacidad de adsorción de la basaluminita evidencia la necesidad de estudiar las propiedades estructurales de dicha fase y compararlas con la fase previamente descrita como el oxihidroxisulfato de Al más cristalina (felsöbányaita). El contenido en agua de basaluminita es similar entre las muestras sintéticas y naturales, y ligeramente menor a la fórmula estequiométrica. El agua fisisorbida y los grupos hidróxilos muestran una coordinación similar en basaluminita y felsöbányaita, aunque las posiciones estructurales en felsöbányaite están mejor definidas.
- El mecanismo de precipitación de basaluminita muestra un efecto significativo en el entorno del sulfato. En ambos casos, las muestras sintéticas y naturales de basaluminita se caracterizan por un mayor contenido en sulfato con respecto a la composición estequiométrica. Sin embargo, la basaluminita natural presenta todo el sulfato en posición de esfera externa, mientras que las muestras sintéticas forman enlaces de esfera interna. Esto puede deberse a una mayor concentración de sulfato en solución durante la síntesis con respecto a las soluciones naturales, induciendo al sulfato a formar este tipo de complejos en la superficie de la basaluminita sintética.
- El Al en basaluminita y felsöbányaita presenta diferentes coordinaciones. Los compuestos de Al_{13} con estructura Keggin podrían ser los precursores minerales de la basaluminita, dado que ambas fases muestran Al en coordinación tetraédrica [Al(IV)]; aunque la basaluminita también presenta Al pentacoordinado [Al(V)].
- La basaluminita tiene un dominio coherente de ~1.2 nm. Los datos de PDF muestran que felsöbányaita y basaluminita tienen unos patrones estructurales similares en la región comprendida entre 1 y 6 Å. Esto nos lleva a interpretar

basaluminita como una felsöbányaita nanoparticulada. Sin embargo, el hecho de que los ambientes geológicos de aparición de la felsöbányaita estan desconectados de los de la basaluminita sugiere que esta última podría ser interpretada como un mineral diferente.

- Los modelos estructurales realizados con simulación Monte Carlo indican que la basaluminita efectivamente está formada por capas de Al octaédrico con posiciones vacantes y un alto grado de deformación angular y longitudinal de dichos octaedros. El exceso de concentración de sulfato está relacionado a un incremento relativo por las posiciones vacantes de Al en la estructura. Finalmente, la estructura de la basaluminita no puede ser descrita por una única celda unidad, y debe de ser entendida como una red extendida con gran cantidad de defectos estructurales que impiden el desarrollo de una periodicidad más allá de 1.2 nm.

En esta Tesis Doctoral, la basaluminita ha sido descrita como un nanomineral estratégico en el comportamiento de metales en áreas afectadas por AMD y ASS. Sin embargo, este solo es el primer paso en el entendimiento de dicha fase y sus propiedades. Es necesario llevar a cabo trabajos de investigación más profundos para entender como ocurre el proceso de nucleación y crecimiento, cual es la relación entre los Al_{13} con estructura Keggin y la basaluminita, o qué ocurre con los elementos adsorbidos cuando la basaluminita recristaliza a fases de aluminio más cristalinas dado su carácter metaestable.

BIBLIOGRAPHY

Acero, P., Ayora, C., Torrentó, C., Nieto, J.-M., 2006. The behavior of trace elements during schwertmannite precipitation and subsequent transformation into goethite and jarosite. Geochim. Cosmochim. Acta 70, 4130–4139.

Adams, F., Rawajfih, Z., 1977. Basaluminite and alunite: A possible cause of sulfate retention by acid soils. Soil Sci. Soc. Am. J. 41, 686–692.

Adra, A., Morin, G., Ona-Nguema, G., Menguy, N., Maillot, F., Casiot, C., Bruneel, O., Lebrun, S., Juillot, F., Brest, J., 2013. Arsenic scavenging by aluminum-substituted ferrihydrites in a circumneutral pH river impacted by acid mine drainage. Environ. Sci. Technol. 47, 12784–12792.

Allison, J.D., Brown, D.S., Novogradac, K.J., 1998. A geochemical assessment model for environmental systems: Version 4.0 User's Manual. EPA/600/3-91/021.

Amoureux, J.-P., Fernandez, C., Steuernagel, S., 1996. Z filtering in MQMAS NMR. J. Magn. Reson. 123, 116–118.

Andriesse, W., 1992. Acid sulfate soils: Diagnosing and illness, in: Selected Papers of the Ho Chi Minh City Symposium on Acid Sulfate Soil. pp. 11–29.

Andriesse, W., Mensvoort, M.E.F., 2005. Acid sulfate soils: Distribution and extent, in: Encyclopedia of Soil Science, 2nd Edition.

Antelo, J., Fiol, S., Gondar, D., López, R., Arce, F., 2012. Comparison of arsenate, chromate and molybdate binding on schwertmannite: Surface adsorption vs anion-exchange. J. Colloid Interface Sci. 386, 338–343.

Appleyard, S.J., Angeloni, J., Watkins, R., 2006. Arsenic-rich groundwater in an urban area experiencing drought and increasing population density, Perth, Australia. Appl. Geochemistry 21, 83–97.

Arai, Y., Elzinga, E.J., Sparks, D.L., 2001. X-ray absorption spectroscopic investigation of arsenite and arsenate adsorption at the aluminum oxide-water interface. J. Colloid Interface Sci. 235, 80–88.

Asta, M.P., Ayora, C., Román-Ross, G., Cama, J., Acero, P., Gault, A.G., Charnock, J.M., Bardelli, F., 2010. Natural attenuation of arsenic in the Tinto Santa Rosa acid stream

(Iberian Pyritic Belt, SW Spain): The role of iron precipitates. Chem. Geol. 271, 1–12.

Asta, M.P., Cama, J., Martínez, M., Giménez, J., 2009. Arsenic removal by goethite and jarosite in acidic conditions and its environmental implications. J. Hazard. Mater. 171, 965–972.

Aström, M., 1998. Mobility of Al, Co, Cr, Cu, Fe, Mn, Ni and V in sulphide-bearing fine-grained sediments exposed to atmosopheric O_2: An experimental study. Environ. Geol. 36, 438–449.

Åström, M., 2001. Effect of widespread severely acidic soils on spatial features and abundance of trace elements in streams. J. Geochemical Explor. 73, 181–191.

Åström, M., Björklund, A., 1995. Impact of acid sulfate soils on stream water geochemistry in western Finland. J. Geochemical Explor. 55, 163–170.

Åström, M., Spiro, B., 2000. Impact of isostatic uplift and ditching of sulfidic sediments on the hydrochemistry of major and trace elements and sulfur isotope ratios in streams, western Finland. Environ. Sci. Technol. 34, 1182–1188.

Atanassova, R.A., Cama, J., Soler, J.M., Offeddu, F.G., Queralt, I.G., 2013. Calcite interaction with acidic sulphate solutions: A vertical scanning interferometry and energy-dispersive XRF study. Eur. J. Mineral. 25, 331–351.

Bannister, F.A., Hollingworth, S.E., 1948. Two new British minerals. Nature 162, 565.

Benali, O., Abdelmoula, M., Refait, P., Génin, J.-M.R., 2001. Effect of orthophosphate on the oxidation products of Fe(II)-Fe(III) hydroxycarbonate: The transformation of green rust to ferrihydrite. Geochim. Cosmochim. Acta 65, 1715–1726.

Bigham, J.M., Carlson, L., Murad, E., 1994. Schwertmannite, a new iron oxyhydroxysulphate from Pyhasalmi, Finland, and other localities. Mineral. Mag. 58, 641–648.

Bigham, J.M., Nordstrom, D.K., 2000. Iron and aluminum hydroxysulfates from acid sulfate waters. Rev. Mineral. Geochemistry 40, 351–403.

Bigham, J.M., Schwertmann, U., Carlson, L., Murad, E., 1990. A poorly crystallized oxyhydroxysulfate of iron formed by bacterial oxidation of Fe(II) in acid mine waters. Geochim. Cosmochim. Acta 54, 2743–2758.

Bigham, J.M., Schwertmann, U., Pfab, G., 1996a. Influence of pH on mineral speciation in a bioreactor simulating acid mine drainage. Appl. Geochemistry 11, 845–849.

Bigham, J.M., Schwertmann, U., Traina, S.J., Winland, R.L., Wolf, M., 1996b. Schwertmannite and the chemical modeling of iron in acid sulfate waters. Geochim. Cosmochim. Acta 60, 2111–2121.

Bowell, D.W., Ptacek, C.J., 2003. The geochemistry of acid mine drainage, in: Lollar, S. (Ed.), Enviromental Geochemistry, Treatise of Geochemistry 9. Toronto, Canada, pp. 149–204.

Bowell, R.J., 1994. Sorption of arsenic by iron-oxides and oxyhydroxides in soils. Appl. Geochemistry 9, 279–286.

Bryan, G.W., Langston, W.J., 1992. Bioavailability, accumulation and effects of heavy metals in sediments with special reference to United Kingdom estuaries: A review. Environ. Pollut. 76, 89–131.

Brydon, J.E., Singh, S.S., 1969. The nature of the synthetic crystalline basic aluminium sulphate as compared with basaluminite. Can. Mineral. 9, 644–654.

Burton, E.D., Bush, R.T., Johnston, S.G., Watling, K.M., Hocking, R.K., Sullivan, L.A., Parker, G.K., 2009. Sorption of arsenic(V) and arsenic(III) to schwertmannite. Environ. Sci. Technol. 43, 9202–9207.

Burton, E.D., Bush, R.T., Sullivan, L.A., Mitchell, D.R.G., 2007. Reductive transformation of iron and sulfur in schwertmannite-rich accumulations associated with acidified coastal lowlands. Geochim. Cosmochim. Acta 71, 4456–4473.

Cama, J., Ayora, C., Querol, X., Ganor, J., 2005. Dissolution kinetics of synthetic zeolite NaP1 and its implication to zeolite treatment of contaminated waters. Environ. Sci. Technol. 39, 4871–4877.

Caraballo, M.A., Macías, F., Rötting, T.S., Nieto, J.-M., Ayora, C., 2011. Long term remediation of highly polluted acid mine drainage: A sustainable approach to restore the environmental quality of the Odiel river basin. Environ. Pollut. 159, 3613–3619.

Caraballo, M.A., Michel, F.M., Hochella, M.F., 2015. The rapid expansion of environmental mineralogy in unconventional ways: Beyond the accepted definition of a mineral, the latest technology, and using nature as our guide. Am. Mineral. 100, 14–25.

Caraballo, M.A., Rimstidt, J.D., Macías, F., Nieto, J.-M., Hochella, M.F., 2013. Metastability, nanocrystallinity and pseudo-solid solution effects on the understanding of schwertmannite solubility. Chem. Geol. 360-361, 22–31.

Carrero, S., Pérez-López, R., Fernandez-Martinez, A., Cruz-Hernández, P., Ayora, C., Poulain, A., 2015. The potential role of aluminium hydroxysulphates in the removal of contaminants in acid mine drainage. Chem. Geol. 417, 414–423.

Catalano, J.G., Park, C., Fenter, P., Zhang, Z., 2008. Simultaneous inner- and outer-sphere arsenate adsorption on corundum and hematite. Geochim. Cosmochim. Acta 72, 1986–2004.

Clayton, T., 1980. Hydrobasaluminite and basaluminite from Chickerell, Dorset. Mineral. Mag. 43, 931–937.

Clemens, S., 2006. Toxic metal accumulation, responses to exposure and mechanisms of tolerance in plants. Biochimie 88, 1707–1719.

Courtin-Nomade, A., Bril, H., Neel, C., Lenain, J.-F., 2003. Arsenic in iron cements developed within tailings of a former metalliferous mine: Enguialès, Aveyron, France. Appl. geochemistry 18, 395–408.

Davesne, E., Dideriksen, K., Christiansen, B.C., Sonne, M., Ayala-Luis, K.B., Koch, C.B., Hansen, H.C.B., Stipp, S.L.S., 2010. Free energy of formation for green rust sodium sulphate ($NaFeII_6FeIII_3(OH)_{18}(SO_4)_{2(s)}$). Geochim. Cosmochim. Acta 74, 6451–6467.

Dent, D.L., Pons, L.J., 1995. A world perspective on acid sulphate soils. Geoderma 67, 263–276.

Dixit, S., Hering, J.G., 2003. Comparison of arsenic(V) and arsenic(III) sorption onto iron oxide minerals: Implications for arsenic mobility. Environ. Sci. Technol. 37, 4182–

4189.

Dreher, G.B., Finkelman, R.B., 1992. Selenium mobilization in a surface coal mine, Powder river basin, Wyoming, U.S.A. Environ. Geol. Water Sci. 19, 155–167.

Drits, V.A., Sakharov, B.A., Salyn, A.L., Manceau, A., 1993. Structural model for ferrihydrite. Clay Miner. 28, 185–207.

Du, J., Sabatini, D.A., Butler, E.C., 2014. Synthesis, characterization, and evaluation of simple aluminum-based adsorbents for fluoride removal from drinking water. Chemosphere 101, 21–27.

Egami, T., Billinge, S.J.L., 2003. Underneath the Bragg Peaks: Structural analysis of complex materials, in: Pergamon Material Series, Elsevier, Amsterdam.

Evangelous, V.P., Zhang, Y.L., 1995. A review: Pyrite oxidation mechanisms and acid mine drainage prevention. Environ. Sci ence Technol. 25, 141–199.

Fanning, D.S., Rabenhordst, M.C., Burch, S.N., Islam, K.R., Tangren, S.A., 2002. Sulfides and sulfates, in: Soil Mineralogy with Encironmental Application. pp. 229–260.

Farkas, L., Pertlik, F., 1997. Crystal structure determinations of felsöbányaite and basaluminite, $Al_4(SO_4)(OH)_{10}\cdot 4H_2O$. Acta Mineral. Szeged 38, 5–15.

Farrow, C.L., Juhás, P., Liu, J.W., Bryndin, D., Bozin, E.S., Bloch, J., Proffen, T., Billinge, S.J.L., 2009. PDFgui user guide.

Fernandez-Martinez, A., Carrero, S., Pérez-López, R., 2013. Sulfur speciation in nanocrystalline minerals of environmental relevance in Acid Mine Drainage.

Fernandez-Martinez, A., Timon, V., Román-Ross, G., Cuello, G.J., Daniels, J.E., Ayora, C., 2010. The structure of schwertmannite, a nanocrystalline iron oxyhydroxysulfate. Am. Mineral. 95, 1312–1322.

French, R.A., Caraballo, M.A., Kim, B., Rimstidt, J.D., Murayama, M., Hochella, M.F., 2012. The enigmatic iron oxyhydroxysulfate nanomineral schwertmannite: Morphology, structure, and composition. Am. Mineral. 97, 1469–1482.

Fukushi, K., Sasaki, M., Sato, T., Yanase, N., Amano, H., Ikeda, H., 2003. A natural attenuation of arsenic in drainage from an abandoned arsenic mine dump. Appl. Geochemistry 18, 1267–1278.

Fung, B.M., Khitrin, A.K., Ermolaev, K., 2000. An improved broadband decoupling sequence for liquid crystals and solids. J. Magn. Reson. 142, 97–101.

Génin, J.-M.R., Olowe, A.A., Refait, P., Simon, B.L., 1996. On the stoichiometry and pourbaix diagram of Fe(II)-Fe(III) hydroy-sulphate containing green rust 2: An electrochemical and Mössbauer spectroscopy study. Corros. Sci. 38, 1751–1762.

Gilbert, B., 2008. Finite size effects on the real-space pair distribution function of nanoparticles. J. Appl. Crystallogr. 41, 554–562.

Gilbert, B., Erbs, J.J., Penn, R.L., Petkov, V., Spagnoli, D., Waychunas, G.A., 2013. A disordered nanoparticle model for 6-line ferrihydrite. Am. Mineral. 98, 1465–1476.

Gilbert, B., Huang, F., Zhang, H., Waychunas, G.A., Banfield, J.F., 2004. Nanoparticles: Strained and stiff. Science 305, 651–654.

Goldberg, S., Johnston, C.T., 2001. Mechanisms of arsenic adsorption on amorphous oxides evaluated using macroscopic measurements, vibrational spectroscopy, and surface complexation modeling. J. Colloid Interface Sci. 234, 204–216.

Hammersley, A.P., Svensson, S.O., Hanfland, M., Fitch, A.N., Häusermann, D., 1996. Two-dimensional detector software: From real detector to idealised image or two-theta scan. High Press. Res. 14, 235–248.

Harrington, R., Hausner, D.B., Bhandari, N., Strongin, D.R., Chapman, K.W., Chupas, P.J., Middlemiss, D.S., Grey, C.P., Parise, J.B., 2010. Investigation of surface structures by powder diffraction: A differential pair distribution function study on arsenate sorption on ferrihydrite. Inorg. Chem. 49, 325–330.

Herlihy, A.T., Kaufmann, P.R., Mitch, M.E., Brown, D.D., 1990. Regional estimates of acid mine drainage impact on streams in the mid-atlantic and Southeastern United States. Water. Air. Soil Pollut. 50.

Hollingworth, S.E., Bannister, F.A., 1950. Basaliminite and hydrobasaluminite, two new minerals from Northamptonshire. J. Mineral. Soc. 29, 1–17.

Holmes, P.R., Crundwell, F.K., 2000. The kinetics of the oxidation of pyrite by ferric ions and dissolved oxigen: An electrocheical study. Geochim. Cosmochim. Acta 64, 263–274.

Husson, O., Verburg, P.H., Phung, M.T., Van Mensvoort, M.E.F., 2000. Spatial variability of acid sulphate soils in the Plain of Reeds, Mekong delta, Vietnam. Geoderma 97, 1–19.

Jang, M., Pak, S., Kim, M.-J., 2015. Comparison of adsorption characteristics of Se(IV) and Se(VI) onto hematite: Effects of reaction time, initial concentration, pH, and ionic strength. Environ. Earth Sci. 74, 1169–1173.

Johnson, D.B., Hallberg, K.B., 2005. Acid mine drainage remediation options: A review. Sci. Total Enviroment 338(1-2), 3–14.

Jolivet, J.-P., Chanéac, C., Chiche, D., Cassaignon, S., Durupthy, O., Hernandez, J., 2011. Basic concepts of the crystallization from aqueous solutions: The example of aluminum oxy(hydroxi)des and aluminosilicates. Comptes Rendus Geosci. 343, 113–122.

Jones, A.M., Collins, R.N., Waite, T.D., 2011. Mineral species control of aluminum solubility in sulfate-rich acidic waters. Geochim. Cosmochim. Acta 75, 965–977.

Joyner, R.W., Martin, K.J., Meehan, P., 1987. Some application of statistical tests in analysis of EXAFS and SEXAFS. J. Phys. C Solid State Phys. 20, 4005–4012.

Juhás, P., Davis, T., Farrow, C.L., Billinge, S.J.L., 2013. PDFgetX3: A rapid and highly automatable program for processing powder diffraction data into total scattering pair distribution functions. J. Appl. Crystallogr. 46, 560–566.

Kairies, C.L., Capo, R.C., Watzlaf, G.R., 2005. Chemicaland physical properties of iron hydroxide precipitates associated with passively treated coal mine drainage in the bituminous region of Pennsylvania and Maryland. Appl. Geochemistry 20, 1445–1460.

Keen, D.A., 1998. Dynamic light scattering - applications of photon correlation spectroscopy, in: Local Structure from Diffraction. p. 101.

Kim, J.-Y., Chon, H.-T., 2001. Pollution of a water course impacted by acid mine drainage in the Imgok Creek of the Gangreung coal field, Korea. Appl. Geochemistry 16, 1387–1396.

Kim, Y., 2015. Mineral phases and mobility of trace metals in white aluminum precipitates found in acid mine drainage. Chemosphere 119, 803–811.

Kirby, C.S., Elder Brady, J.A., 1998. Field determination of Fe^{2+} oxidation rates in acid mine drainage using a continuously-stirred tank reactor. Appl. geochemistry 13, 509–520.

Kirkpatrick, R.J., Phillips, B.L., 1993. ^{27}Al NMR spectroscopy of minerals and related materials. Appl. Magn. Reson. 4, 213–236.

Kubicki, J.D., 1998. Molecular cluster models of aluminum oxide and aluminum hydroxide surfaces. Am. Mineral. 83, 1054–1066.

Leblanc, M., Morales, J.A., Borrego, J., Elbaz-Poulichet, F., 2000. 4,500-year-old mining pollution in Southwestern Spain: Long-term implications for modern mining pollution. Econ. Geol. 95, 655–662.

Lee, G., 2001. Transport and Tate of Trace Elements in Stream Contaminated with Acid Mine-Drainage in the Ducktown Mining District, Tennessee. Ohio State University.

Lee, G., Bigham, J.M., Faure, G., 2002. Removal of trace metals by coprecipitation with Fe, Al and Mn from natural waters contaminated with acid mine drainage in the Ducktown mining district, Tennessee. Appl. Geochemistry 17, 569–581.

Levitt, M.H., 2008. Spin dynamics: Basics of nuclear magnetic resonance. Second Edition, System.

Li, W., Harrington, R., Tang, Y., Kubicki, J.D., Aryanpour, M., Reeder, R.J., Parise, J.B., Phillips, B.L., 2011. Differential pair distribution function study of the structure of arsenate adsorbed on nanocrystalline γ-alumina. Environ. Sci. Technol. 45, 9687–9692.

Loring, J.S., Sandström, M.H., Norén, K., Persson, P., 2009. Rethinking arsenate coordination at the surface of goethite. Chemistry 15, 5063–5072.

Lowson, R.T., 1982. Aqueous oxidation of pyrite by molecular oxygen. Chem. Rev. 82, 461–497.

Macías, F., Caraballo, M.A., Nieto, J.-M., Rötting, T.S., Ayora, C., 2012. Natural pretreatment and passive remediation of highly polluted acid mine drainage. J. Environ. Manage. 104, 93–100.

Maillot, F., Morin, G., Juillot, F., Bruneel, O., Casiot, C., Ona-Nguema, G., Wang, Y., Lebrun, S., Aubry, E., Vlaic, G., Brown, G.E., 2013. Structure and reactivity of As(III)- and As(V)-rich schwertmannites and amorphous ferric arsenate sulfate from the Carnoulès acid mine drainage, France: Comparison with biotic and abiotic model compounds and implications for As remediation. Geochim. Cosmochim. Acta 104, 310–329.

McGreevy, R.L., Pusztail, L., 1988. Reverse Monte Carlo simulation: A new technique for the determination of dosodered structures. Mol. Simul. 1, 357–367.

Michalowicz, A., Moscovici, J., Muller-Bouvet, D., Provost, K., 2009. MAX: Multiplatform applications for XAFS. J. Phys. Conf. Ser. 190, 12–34.

Michalowicz, A., Provost, K., Laruelle, S., Mimouni, A., Vlaic, G., 1999. F-test in EXAFS fitting of structural models. J. Synchrotron Radiat. 6, 233–235.

Michel, F.M., Ehm, L., Antao, S.M., Lee, P.L., Chupas, P.J., Liu, G., Strongin, D.R., Schoonen, M.A.A., Phillips, B.L., Parise, J.B., 2007. The structure of ferrihydrite, a nanocrystalline material. Science (80-.). 316, 1726–1729.

Minh, L.Q., Tuong, T.P., van Mensvoort, M.E.F., Bouma, J., 1997. Contamination of surface water as affected by land use in acid sulfate soils in the Mekong river delta, Vietnam. Agric. Ecosyst. Environ. 61, 19–27.

Monterroso, C., Macías, F., 1998. Drainage waters affected by pyrite oxidation in coal mine in Galicia (NW Spain): Composition and mineral stability. Sci. Total Environ. 216, 121–132.

Moore, J.W., Ramamoorthy, S., 1984. Heavy Meals in Natural Waters: Applied Monoring and Impact Assessment, Alberta Environmental centre.

Morse, J.W., Arvidson, R.S., 2002. The dissolution kinetics of major sedimentary carbonate minerals. Earth-science Rev. 58, 51–84.

Naiker, K., Cukrowska, E., McCarthy, T.S., 2003. Acid mine drainage arising from gold mining activity in Johannesburg, South Africa and enciroment. Environ. Pollut. 122, 29–40.

Naruekamon, J., Masatomo, U., 2008. Charasteristics and distribution of acid sulfate soil in the Lower Plain, Thailand., in: Prodeedings of the Joint Conference of the 6th International Acid Sulfate Soil Conference and the Acid Rock Drainage Symposium. p. 293.

Newville, M., 2004. Fundamentals of XAFS, Consortium for Advanced Radiation Sources. University of Chicago.

Nieto, J.-M., Sarmiento, A.M., Cánovas, C.R., Olías, M., Ayora, C., 2013. Acid mine drainage in the Iberian Pyrite Belt: 1. Hydrochemical characteristics and pollutant load of the Tinto and Odiel rivers. Environ. Sci. Pollut. Res. Int. 20, 7509–7519.

Nieto, J.-M., Sarmiento, A.M., Olías, M., Cánovas, C.R., Riba, I., Kalman, J., Delvalls, T.A., 2007. Acid mine drainage pollution in the Tinto and Odiel rivers (Iberian Pyrite Belt, SW Spain) and bioavailability of the transported metals to the Huelva estuary. Environ. Int. 33, 445–455.

Nordstrom, D.K., 2011. Hydrogeochemical processes governing the origin, transport and fate of major and trace elements from mine wastes and mineralized rock to surface waters. Appl. Geochemistry 26, 1777–1791.

Nordstrom, D.K., 1982a. Aqueous pyrite oxidation and the consequent formation of secondary iron minerals, in: Kittrick, J.A., Fanning, D.S., Hossner, L.R. (Eds.), Acid Sulfate Weathering. Soil Science Society of America Publication, pp. 37–56.

Nordstrom, D.K., 1982b. The effect of sulfate on aluminum concentrations in natural waters: Some stability relations in the system Al_2O_3-SO_3-H_2O at 298 K. Geochim. Cosmochim. Acta 46, 681–692.

Nordstrom, D.K., Alpers, C.N., 1999a. Geochemistry of acid mine waters. Soc. Econ. Geol. 6A, 133–160.

Nordstrom, D.K., Alpers, C.N., 1999b. Negative pH, efflorescent mineralogy, and consequences for environmental restoration at the Iron Mountain superfund site, California. Proc. Natl. Acad. Sci. U. S. A. 96, 3455–3462.

Nordstrom, D.K., Wilde, F.D., 1998. Reduction-oxidation potential (electrode method), Section 6.5, Chapter A6, in: National Field Manual for the Collection of Water-Quality Data. p. 20.

Nuttal, R.R., Castanas, E.C., Villamayor, F.P., 2008. Soils with sulfidic materials on the coastal wetlands of Leyte, Philippines, in: Proceedings of the Joint Conference of the 6th International Acid Sulfate Soil Conference and the Acid Rock Drainage Symposium. pp. 148–153.

Olías, M., Cánovas, C.R., Nieto, J.-M., Sarmiento, A.M., 2006. Evaluation of the dissolved contaminant load transported by the Tinto and Odiel rivers (South West Spain). Appl. Geochemistry 21, 1733–1749.

Olías, M., Nieto, J.-M., Sarmiento, A.M., Cerón, J.C., Cánovas, C.R., 2004. Seasonal water quality variations in a river affected by acid mine drainage: The Odiel river (South West Spain). Sci. Total Environ. 333, 267–281.

Paikaray, S., Göttlicher, J., Peiffer, S., 2011. Removal of As(III) from acidic waters using schwertmannite: Surface speciation and effect of synthesis pathway. Chem. Geol. 283, 134–142.

Palosz, B., Grzanka, E., Gierlotka, S., Stel´makh, S., Pielaszek, R., Bismayer, U., Neuefeind, J., Weber, H.-P., Proffen, T., Dreele, R. Von, Palosz, W., 2002. Analysis of short and long range atomic order in nanocrystalline diamonds with application of powder diffractometry. Zeitschrift für Krist. 217, 497–509.

Parkhurst, D.L., Appelo, C.A.. J., 1999. User´s guide to PhreeqC (version 2) A computer program for speciation, and inverse geochemical calculations, U.S. Department of the Interior, U.S. Geological Survey.

Peak, D., 2006. Adsorption mechanisms of selenium oxyanions at the aluminum oxide/water interface. J. Colloid Interface Sci. 303, 337–345.

Peak, D., Sparks, D.L., 2002. Mechanisms of selenate adsorption on iron oxides and hydroxides. Environ. Sci. Technol. 36, 1460–1466.

Powell, B., Martens, M., 2005. A review of acid sulfate soil impacts, actions and policies that impact on water quality in Great Barrier Reef catchments, including a case study on remediation at East Trinity. Mar. Pollut. Bull. 51, 149–164.

Powell, J.D., 1988. Origin and influence of coal mine drainage on streams of the United States. Environ. Geol. Water Sci. 11, 141–152.

Preda, M., Cox, M.E., 2001. Trace metals in acid sediments and waters, Pimpama catchment, Southeast Queensland, Australia. Environ. Geol. 40, 755–768.

Prietzel, J., Hirsch, C., 1998. Extractability and dissolution kinetics of pure and soil-added synthesized aluminium hydroxy sulphate minerals. Eur. J. Soil Sci.

Prietzel, J., Mayer, B., 2005. Isotopic fractionation of sulfur during formation of basaluminite, alunite, and natroalunite. Chem. Geol. 215, 525–535.

Randall, S.R., Sherman, D.M., Ragnarsdottir, K.V., 2001. Sorption of As(V) on green rust ($Fe_4(II)Fe_2(III)(OH)_{12}SO_4\cdot 3H_2O$) and lepidocrocite (gamma-FeOOH): Surface complexes from EXAFS spectroscopy. Geochim. Cosmochim. Acta 65, 1015–1023.

Ravel, B., Newville, M., 2005. ATHENA, ARTEMIS, HEPHAESTUS: Data analysis for X-ray absorption spectroscopy using IFEFFIT. J. Synchrotron Radiat. 12, 537–541.

Refait, P., Girault, P., Jeannin, M., Rose, J., 2009. Influence of arsenate species on the formation of Fe(III) oxyhydroxides and Fe(II–III) hydroxychloride. Colloids Surfaces A Physicochem. Eng. Asp. 332, 26–35.

Regenspurg, S., Brand, A., Peiffer, S., 2004. Formation and stability of schwertmannite in acidic mining lakes. Geochim. Cosmochim. Acta 68, 1185–1197.

Rockström, J., Steffen, W., Noone, K., Persson, Å., Chapin, F.S., Lambin, E.F., Lenton, T.M., Scheffer, M., Folke, C., Schellnhuber, H.J., Nykvist, B., de Wit, C.A., Hughes, T., van der Leeuw, S., Rodhe, H., Sörlin, S., Snyder, P.K., Costanza, R., Svedin, U., Falkenmark, M., Karlberg, L., Corell, R.W., Fabry, V.J., Hansen, J., Walker, B., Liverman, D., Richardson, K., Crutzen, P., Foley, J.A., 2009. A safe operating space for humanity. Nature 461, 472–475.

Rodríguez-Carvajal, J., 1993. Recent advances in magnetic structure determination by neutron powder diffraction. Phys. B Condens. Matter 192, 55–69.

Rötting, T.S., Caraballo, M.A., Serrano, J.A., Ayora, C., Carrera, J., 2008. Field application of calcite Dispersed Alkaline Substrate (calcite-DAS) for passive treatment of acid mine drainage with high Al and metal concentrations. Appl. Geochemistry 23, 1660–1674.

Rovira, M., Giménez, J., Martínez, M., Martínez-Lladó, X., de Pablo, J., Martí, V., Duro, L., 2008. Sorption of selenium(IV) and selenium(VI) onto natural iron oxides: Goethite and hematite. J. Hazard. Mater. 150, 279–284.

Sáinz, A., Grande, J.A., de la Torre, M.L., Sánchez-Rodas, D., 2002. Characterisation of sequential leachate discharges of mining waste rock dumps in the Tinto and Odiel rivers. J. Environ. Manage. 64, 345–353.

Sánchez-España, J., López Pamo, E., Santofimia Pastor, E., 2007. The oxidation of ferrous iron in acidic mine effluents from the Iberian Pyrite Belt (Odiel basin, Huelva, Spain): Field and laboratory rates. J. Geochemical Explor. 92, 120–132.

Sánchez-España, J., López Pamo, E., Santofimia Pastor, E., Reyes Andrés, J., Matín Rubí, J.A., 2006. The removal of dissolved metals by hydroxysulphate precipitates during oxidation and neutralization of acid mine waters, Iberian Pyrite Belt. Aquat. Geochemistry 12, 269–298.

Sánchez-España, J., Yusta, I., Diez-Ercilla, M., 2011. Schwertmannite and hydrobasaluminite: A re-evaluation of their solubility and control on the iron and aluminium concentration in acidic pit lakes. Appl. Geochemistry 26, 1752–1774.

Sarmiento, A.M., Nieto, J.-M., Olías, M., Cánovas, C.R., 2009a. Hydrochemical characteristics and seasonal influence on the pollution by acid mine drainage in the Odiel river basin (SW Spain). Appl. Geochemistry 24, 697–714.

Sarmiento, A.M., Olías, M., Nieto, J.-M., Cánovas, C.R., Delgado, J., 2009b. Natural attenuation processes in two water reservoirs receiving acid mine drainage. Sci. Total

Environ. 407, 2051–2062.

Schemel, L.E., Kimball, B.A., Bencala, K.E., 2000. Colloid formation and metal transport through two mixing zones affected by acid mine drainage near Silverton, Colorado. Appl. geochemistry 15, 1003–1018.

Schott, J., Brantley, S., Crerar, D., Guy, C., Borcsik, M., Williame, C., 1989. Dissolution kinetics of strained calcite. Geochim. Cosmochim. Acta 53, 373–382.

Schwertmann, U., 1984. The influence of aluminium on iron oxides: IX. Dissolution of Al-goethites in 6 M HCl. Clay Miner. 19, 9–19.

Schwertmann, U., Bigham, J.M., Murad, E., 1995. The first occurrence of schwertmannite in a natural stream environment. Eur. J. Mineral.

Schwertmann, U., Wolska, E., 1990. The influence of aluminum on iron oxides. XV. Al-for-Fe substitution in synthetic lepidocrocite. Clays Clay Miner. 38, 209–212.

Shamshuddin, J., Elisa Azura, A., Shazana, M.A.R.S., Fauziah, C.I., Panhwar, Q.A., Naher, U.A., 2014. Properties and management of acid sulfate soils in Southeast Asia for sustainable cultivation of rice, oil palm, and cocoa, in: Advances in Agronomy. Elsevier Inc., pp. 91–142.

Sherman, D.M., Randall, S.R., 2003. Surface complexation of arsenic(V) to iron(III) (hydr)oxides: Structural mechanism from ab initio molecular geometries and EXAFS spectroscopy. Geochim. Cosmochim. Acta 67, 4223–4230.

Singer, P.C., Stumm, W., 1970. Acidic mine drainage: The rate determining step. Science (80-.). 167, 1121–1123.

Smedley, P.L., Kinniburgh, D.G., 2002. A review of the source, behaviour and distribution of arsenic in natural waters. Appl. Geochemistry 17, 517–568.

Song, J., Jia, S.-Y., Ren, H.-T., Wu, S.-H., Han, X., 2015. Application of a high-surface-area schwertmannite in the removal of arsenate and arsenite. Environ. Sci. Technol. 12, 1559–1568.

Sracek, O., Choquette, M., Gelinas, P., Lefebvre, R., Nicholson, R.V., 2004. Geochemical characterization of acid mine drainage from a waste rock pile, mine Doyon, Quebec, Canada. J. Contam. Hydrol. 69, 45–71.

Tamura, H., Goto, K., Yotsuyanagi, T., Nagayana, M., 1974. Spectrophotometric determination of iron(II) with 1,10-phenanthroline in the presence of large amounts of Iron(III). Talanta 21, 314–318.

Toby, B.H., Egami, T., 1992. Accuracy of pair distribution function analysis applied to crystalline and non-crystalline materials. Acta Cristallogr. Sect. A 48, 336–346.

Torres, E., Ayora, C., Canovas, C.R., García-Robledo, E., Galván, L., Sarmiento, A.M., 2013. Metal cycling during sediment early diagenesis in a water reservoir affected by acid mine drainage. Sci. Total Enviroment 461-462, 416–429.

Tucker, M., Dove, M., Goodwin, A., Keen, D.A., Playford, H., 2014. RMCProfile User Manual. Code version 6.5.2.

Tyler, G., Carrasco, R., Nieto, J.-M., Pérez-López, R., Ruiz, M.J., Sarmiento, A.M., 2004. Optimization of major and trace element determination in acid mine drainage samples by ultrasonic nebulizer-ICP-OES (USN-ICP-OES)., in: Pittcon Conference (Chicago, USA). pp. 9000–1000.

Valko, M., Morris, H., Cronin, M., 2005. Metals, toxicity and oxidative stress. Curr. Med. Chem. 12, 1161–1208.

Wagman, D.D., Evans, H.H., Parker, V.B., Schumm, R.H., Harlow, I., Bailey, S.M., Churney, K.L., Butall, R.L., 1982. The NBS Tables of Chemical Thermodynamic Properties. Selected Values for Inorganic and Organic Substances in SI Units, Journal of Physical Chemistry.

Wang, X., Gu, C., Feng, X., Zhu, M., 2015. Sulfate local coordination environment in schwertmannite. Environ. Sci. Technol. 49, 10440–10448.

Waychunas, G.A., Davis, J.A., Fuller, C.C., 1995a. Geometry of sorbed arsenate on ferrihydrite and crystalline FeOOH : Re-evaluation of EXAFS results and topological factors in predicting sorbate geometry , and evidence for monodentate complexes. Geochim. Cosmochim. Acta 59, 3655–3661.

Waychunas, G.A., Rea, B.A., Fuller, C.C., Davis, J.A., 1993. Surface chemistry of ferrihydrite: Part 1. EXAFS studies of the geometry of coprecipitated and adsorbed arsenate. Geochim. Cosmochim. Acta 57, 2251–2269.

Waychunas, G.A., Xu, N., Fuller, C.C., Davis, J.A., Bigham, J.M., 1995b. XAS study of AsO_4^{3-} and SeO_4^{2-} substituted schwertmannites. Phys. B 209, 481–483.

Woulds, C., Ngwenya, B.T., 2004. Geochemical processes governing the performance of a contructed wetland treating acid mine drainage, Central Scotland. Appl. Geochemistry 19, 1773–1783.

Younger, P.L., 2001. Passive treatment of european mine wasters: The european commission's "Piramid" project.

Younger, P.L., 1997. The longevity of minewater pollution: A basis for decision-making. Sci. Total Environ. 194-195, 457–466.

Younger, P.L., Banwart, S.A., Hedin, R.S., 2002. Mine Xater. Hidrology, Pollution, remediation.

Yu, J.Y., Heo, B., 2001. Dilution and removal of dissolved metals from acid mine drainage along Imgok Creek, Korea. Appl. Geochemistry 16, 1041–1053.

Yu, J.Y., Heo, B., Choi, I.K., Cho, J.P., Chang, H.W., 1999. Apparent solubilities of schwertmannite and ferrihydrite in natural stream waters polluted by mine drainage. Geochim. Cosmochim. Acta 63, 3407–3416.

Zabowski, D., Henry, C.L., Zheng, Z., Zhang, X., 2001. Mining impacts on trace metal content of water, soil, and stream sediments in the Hei river basin, Chine. Water. Air. Soil Pollut. 131, 261–273.

APPENDIX

A.1. CHAPTER II SUPPLEMENTARY INFORMATION

In this appendix is displayed the physic (pH, dissolved oxygen, *etc.*) and chemical (alkalis consume, metal(loid)s concentration through ICP-OES) of the titration and oxidation experiments performed in Chapter II (Tables A.1.1 to A.1.6). In addition, pictures of experimental setup and precipitates evolution are showed as well (Figs. A.1.1 to A.1.4). The main S specie in solution in this experiment was sulfate (SO_4^{2-}), although the results showed in this appendix are expressed in elemental sulfur.

Date	time (min)	Δtime (min)	Initial V (ml)	initial pH	Add V (ml)	Total V (ml)	Total add V (ml)	$CaCO_3$ eq. (g)	$CaCO_3$ eq. (mg L^{-1})	DO (ppm)	Final pH
30/07/2012	0	0	100	3.26	6.1	106.1	6.1	0.0061	61	0.84	3.62
30/07/2012	26	26	106.1	3.63	2.8	108.9	8.9	0.0089	89	0.74	3.82
30/07/2012	70	44	108.9	3.82	5.95	114.85	14.85	0.01485	148.5	0.66	4
30/07/2012	130	60	114.85	3.99	35.4	150.25	50.25	0.05025	502.5	0.44	4.25
30/07/2012	215	85	150.25	4.2	34	184.25	84.25	0.08425	842.5	0.43	4.5
30/07/2012	320	105	184.25	4.42	9.15	193.4	93.4	0.0934	934	-	4.5
31/07/2012	465	145	193.4	4.53	7.6	201	101	0.101	1010	0.43	4.8
31/07/2012	545	80	201	4.71	5.35	206.35	106.35	0.10635	1063.5	0.34	5.01
31/07/2012	620	75	206.35	4.92	14.8	221.15	121.15	0.12115	1211.5	0.36	5.31
31/07/2012	810	190	221.15	5.35	13.6	234.75	134.75	0.13475	1347.5	1.02	5.75
31/07/2012	1310	500	234.75	5.6	6.4	241.15	141.15	0.14115	1411.5	-	6
31/07/2012	1410	100	241.15	5.83	5.8	246.95	146.95	0.14695	1469.5	-	6.28
31/07/2012	1520	110	246.95	6.12	100	346.95	246.95	0.24695	2469.5	-	6.83
31/07/2012	1675	155	346.95	6.49	90	436.95	336.95	0.33695	3369.5	1.41	7.21
31/07/2012	1810	135	436.95	6.97	26	462.95	362.95	0.36295	3629.5	-	7.33
01/08/2012	1960	150	462.95	7.17	24.75	487.7	387.7	0.3877	3877	1.38	7.5
01/08/2012	2065	105	487.7	7.39	25.05	512.75	412.75	0.41275	4127.5	1.59	7.77
01/08/2012	2170	105	512.75	7.66	14.5	527.25	427.25	0.42725	4272.5	-	8.01
01/08/2012	2260	90	527.25	7.91	7.45	534.7	434.7	0.4347	4347	-	8.25
01/08/2012	2380	120	534.7	8.11	5.7	540.4	440.4	0.4404	4404	-	8.56
01/08/2012	2480	100	540.4	8.41	3.9	544.3	444.3	0.4443	4443	1.31	8.79
01/08/2012	2580	100	544.3	8.63	4.7	549	449	0.449	4490	-	9.11
01/08/2012	2710	130	549	8.86	10	559	459	0.459	4590	0.89	9.51
01/08/2012	2830	120	559	9.21	20	579	479	0.479	4790	1.11	9.9
01/08/2012	2960	130	579	9.49	40	619	519	0.519	5190	-	10.4
01/08/2012	3065	105	619	9.85	-	-	-	-	-	-	-

Table A.1.1: *pH evolution in the titration experiment under anoxic condition since 100 ml of acid water with 2000 mg* L^{-1} *of Fe(II) in solution from Perrunal mine (Calañas, Spain). The results indicated in this table were collected after achieving pH equilibrium.*

Date	time (min)	Δtime (min)	Initial V (ml)	initial pH	Add V (ml)	Total V (ml)	Total add V (ml)	$CaCO_3$ eq. (g)	$CaCO_3$ eq. (mg L^{-1})	DO (ppm)	Final pH
22/10/2012	0	0	100	2.28	50	150	50	0.05	500	0.84	2.57
22/10/2012	60	60	150	2.56	150	300	200	0.2	2000	0.74	2.78
22/10/2012	270	210	300	2.65	97	397	297	0.297	2970	0.66	3.05
22/10/2012	330	60	397	2.87	62	459	359	0.359	3590	0.44	3.4
23/10/2012	1290	960	459	3.14	28.7	487.7	387.7	0.3877	3877	0.43	3.78
23/10/2012	1410	120	487.7	3.63	15.8	503.5	403.5	0.4035	4035	-	4.09
23/10/2012	1470	60	503.5	3.92	31.4	534.9	434.9	0.4349	4349	0.43	4.39
23/10/2012	1545	75	534.9	4.28	63	597.9	497.9	0.4979	4979	0.34	4.69
23/10/2012	1650	105	597.9	4.61	24.1	622	522	0.522	5220	0.36	5.05
23/10/2012	1710	60	622	4.92	16	638	538	0.538	5380	1.02	5.5
23/10/2012	1755	45	638	5.49	13	651	551	0.551	5510	-	6.05
23/10/2012	1940	185	651	5.77	18	669	569	0.569	5690	-	6.55
24/10/2012	2760	820	669	6.4	14.5	683.5	583.5	0.5835	5835	-	7.05
24/10/2012	2820	60	683.5	6.91	17	700.5	600.5	0.6005	6005	1.41	7.8
24/10/2012	2910	90	700.5	7.5	13.6	714.1	614.1	0.6141	6141	-	8.2
24/10/2012	2990	80	714.1	7.97	13.7	727.8	627.8	0.6278	6278	1.38	8.53
24/10/2012	3060	70	727.8	8.49	13.9	741.7	641.7	0.6417	6417	1.59	9.03
24/10/2012	3120	60	741.7	8.69	21.3	763	663	0.663	6630	-	9.43
25/10/2012	4320	1200	763	9.08	17.1	780.1	680.1	0.6801	6801	-	9.63
25/10/2012	4380	60	780.1	9.28	32	812.1	712.1	0.7121	7121	-	9.84
25/10/2012	4500	120	812.1	9.42	34.6	846.7	746.7	0.7467	7467	1.31	10.1
25/10/2012	4560	60	846.7	9.7	43	889.7	789.7	0.7897	7897	-	10.44
25/10/2012	4620	60	889.7	9.99	41	930.7	830.7	0.8307	8307	0.89	10.74
25/10/2012	4680	60	930.7	10.26	50	980.7	880.7	0.8807	8807	1.11	10.89
25/10/2012	4740	60	980.7	10.68	25.4	1006.1	906.1	0.9061	9061	-	10.96
25/10/2012	4785	45	1006.1	10.9	-	-	-	-	-	-	-

Table A.1.2: *pH evolution in the titration experiment under atmospheric condition since 100 ml of acid water from Perrunal mine (Calañas, Spain) after a complete Fe oxidation. The results indicated in this table were collected after achieving pH equilibrium.*

pH	Dilution	Al	As	Ca	Cd	Co	Cu	Fe^{2+}	Fe^{3+}	Fe_t	K	Li	Mg	Mn	Ni	Pb	S	Si	Sr	Ti	V	Zn
	%	mg L^{-1}																				
3.25	0	194	1.73	298	0.16	0.81	8.78	2006	33.9	2040	4.41	0.65	317	51.6	0.56	0.13	2000	34.9	0.11	0.02	0.19	34.0
3.51	3.2	199	1.21	316	0.18	0.83	9.09	2141	48.4	2189	8.07	0.66	323	52.8	0.59	0.13	2002	33.3	0.11	0.02	0.19	35.5
3.94	8.8	196	0.89	343	0.17	0.83	8.92	2044	37.6	2081	8.16	0.64	325	52.3	0.58	0.14	2005	34.7	0.13	0.02	0.13	35.3
4.29	67.5	104	0.76	553	0.06	0.82	8.93	1997	16.2	2013	10.9	0.53	328	53.7	0.51	0.16	1949	33.0	0.19	b.l.	b.l.	38.4
4.29	67.5	105	0.86	555	0.11	0.97	8.89	2156	18.1	2174	10.3	0.46	315	60.4	0.48	0.14	1942	36.7	0.24	b.l.	b.l.	41.7
4.89	48.6	10.9	0.71	720	0.13	0.80	7.75	2058	0.00	2058	11.5	0.59	318	51.7	0.52	0.14	1841	28.6	0.26	0.01	b.l.	35.7
5.26	49.9	3.64	0.64	774	0.09	0.79	6.09	1956	48.9	2005	11.6	0.59	311	51.4	0.52	0.14	1835	27.6	0.27	b.l.	b.l.	34.6
5.73	53.0	0.41	0.36	797	0.10	0.78	0.07	1727	292	2018	12.8	0.56	304	50.9	0.50	0.14	1802	20.9	0.28	b.l.	b.l.	32.6
6.30	56.7	b.l.	0.27	900	0.09	0.74	b.l.	1850	0.00	1850	13.8	0.58	314	50.5	0.44	0.13	1860	15.5	0.32	b.l.	b.l.	23.1
7.00	74.2	b.l.	0.28	1670	b.l.	0.09	b.l.	731	91.3	822	15.2	0.45	306	51.4	b.l.	b.l.	1800	19.7	0.58	b.l.	b.l.	3.11
8.28	80.2	b.l.	b.l.	2205	b.l.	b.l.	b.l.	23.0	0.01	23.0	28.3	0.33	291	42.7	b.l.	b.l.	1814	11.4	0.75	b.l.	b.l.	b.l.
9.35	80.9	b.l.	b.l.	2320	b.l.	b.l.	b.l.	0.94	b.l.	0.95	31.0	0.29	291	14.2	b.l.	b.l.	1846	5.54	0.84	b.l.	b.l.	b.l.
10.2	81.7	b.l.	b.l.	2391	b.l.	b.l.	b.l.	b.l.	b.l.	b.l.	39.1	0.24	266	2.17	b.l.	b.l.	1831	3.96	0.93	b.l.	b.l.	b.l.

Abbreviations: b.l., below detection limit.

Table A.1.3: *Sample dissolution and metal concentration in the aliquot collected at specific pH during the AMD titration experiment under anoxic conditions.*

pH	Dilution %	Al	As	Ca	Cd	Co	Cu	Fe^{3+}	Fe_t	K	Li	Mg	Mn	Ni	Pb	S	Si	Sr	Ti	Zn
		$mg L^{-1}$																		
2.34	0	287	0.10	401	0.22	1.28	12.3	1827	1827	5.94	0.91	469	82.5	0.75	0.11	2927	49.7	0.18	0.03	52.3
2.63	28.2	227	b.l.	617	0.15	1.05	9.94	1367	1367	5.46	0.67	368	65.6	0.66	0.08	2267	41.2	0.27	0.02	45.6
2.95	59.6	171	b.l.	1196	0.05	0.96	7.88	148	148	4.81	0.36	304	57.1	0.48	b.l.	1711	37.4	0.65	b.l.	41.3
3.45	63.8	149	b.l.	1389	0.05	1.01	6.95	9.30	9.30	4.08	0.24	300	60.2	0.44	b.l.	1708	37.6	0.84	b.l.	44.5
3.63	65.4	127	b.l.	1476	0.07	0.99	6.04	2.20	2.20	4.36	0.17	296	65.1	0.41	b.l.	1688	33.9	0.88	b.l.	47.2
4.3	67.3	105	b.l.	1543	0.05	1.02	5.00	0.16	0.16	4.92	0.20	283	57.3	0.40	b.l.	1596	36.8	0.92	b.l.	47.5
4.91	71	10.8	b.l.	1678	0.03	0.95	2.46	b.l.	b.l.	4.42	0.11	271	58.2	0.36	b.l.	1518	31.0	1.06	b.l.	44.0
5.7	72.1	b.l.	b.l.	1760	b.l.	0.91	b.l.	b.l.	b.l.	5.05	0.11	273	57.0	0.32	b.l.	1517	23.6	1.16	b.l.	32.7
6.96	73.3	b.l.	b.l.	1848	b.l.	0.41	b.l.	b.l.	b.l.	5.32	0.06	367	48.8	b.l.	b.l.	1587	7.05	1.20	b.l.	2.30
8	74.2	1.68	b.l.	1862	b.l.	b.l.	b.l.	b.l.	b.l.	5.91	0.04	361	25.8	b.l.	b.l.	1580	3.06	1.30	b.l.	b.l.
8.71	75	6.89	b.l.	1922	b.l.	b.l.	b.l.	b.l.	b.l.	7.11	b.l.	325	7.22	b.l.	b.l.	1547	2.57	1.38	b.l.	b.l.
9.7	76.6	1.26	b.l.	1988	b.l.	b.l.	b.l.	b.l.	b.l.	6.61	b.l.	159	b.l.	b.l.	b.l.	1489	2.48	1.24	b.l.	b.l.
10.2	77.7	b.l.	b.l.	2088	b.l.	b.l.	b.l.	b.l.	b.l.	6.55	b.l.	55.4	b.l.	b.l.	b.l.	1428	3.00	1.45	b.l.	b.l.
11.05	80.4	8.05	b.l.	2186	b.l.	b.l.	b.l.	b.l.	b.l.	10.3	b.l.	1.22	b.l.	b.l.	b.l.	1358	3.36	1.39	b.l.	b.l.

Abbreviations: b.l., below detection limit.

Table A.1.4: *Sample dissolution and metal concentration in the aliquot collected at specific pH during the AMD titration experiment under atmospheric conditions.*

pH	time (days)	Al	As	Ca	Cd	Co	Cu	Fe^{2+}	Fe^{3+}	Fe_t	K	Li	Mg	Mn	Ni	Pb	S	Si	Sr	Ti	Zn
												$mg\ L^{-1}$									
3.29	0	194	1.73	298	0.16	0.81	8.78	2006	34	2040	4.41	0.65	317	51.6	0.56	0.13	2000	34.9	0.11	0.02	34.0
3.01	1	194	0.47	301	0.19	0.90	8.45	2011	33	2045	4.38	0.58	315	57.0	0.56	0.12	1945	36.2	0.13	0.02	37.4
2.92	2	195	0.33	298	0.19	0.96	8.93	1658	329	1987	4.22	0.61	322	59.6	0.54	0.13	1969	37.8	0.14	0.02	39.2
2.87	3	196	0.12	301	0.19	0.97	9.01	1972	85	2057	4.09	0.62	324	59.0	0.55	0.13	1957	37.5	0.14	0.02	39.4
2.8	4	196	b.l.	302	0.18	0.96	9.14	1776	195	1970	4.33	0.62	104	62.4	0.56	0.12	1932	38.1	0.15	0.02	40.1
2.5	6	200	b.l.	309	0.15	1.06	9.46	1539	306	1845	4.21	0.55	339	65.3	0.57	0.11	1951	40.9	0.14	0.02	45.8
2.5	6	213	b.l.	317	0.14	1.01	b.l.	1758	348	2107	5.46	0.60	347	62.9	0.54	0.11	2115	40.3	0.13	0.02	43.5
2.64	7	211	0.01	316	0.16	0.86	9.28	1618	420	2038	4.88	0.67	104	53.4	0.57	0.11	2056	35.1	0.11	0.02	37.1
2.63	8	213	b.l.	330	0.15	0.87	9.49	1346	536	1882	5.12	0.72	330	52.6	0.58	0.11	2141	36.5	0.12	0.02	36.2
2.58	9	226	b.l.	338	0.18	0.88	9.94	1409	581	1990	5.31	0.70	339	56.0	0.63	0.12	2206	36.3	0.12	0.02	38.2
2.58	10	211	b.l.	332	0.15	0.89	9.92	1299	650	1949	5.37	0.73	359	56.3	0.62	0.10	2182	36.5	0.12	0.02	38.5
2.56	13	229	b.l.	345	0.16	0.92	10.1	941	865	1806	5.47	0.76	362	55.9	0.60	0.11	2264	38.8	0.12	0.02	38.2
2.55	15	247	b.l.	368	0.17	0.95	10.6	775	1242	2016	5.80	0.80	364	60.4	0.62	0.11	2383	40.1	0.13	0.02	40.0
2.49	17	238	b.l.	361	0.19	1.11	10.3	762	1112	1874	5.46	0.72	391	70.1	0.65	0.10	2357	42.4	0.16	0.02	46.7
2.45	20	240	0.04	359	0.18	1.11	10.6	364	1457	1821	5.25	0.73	385	69.9	0.66	0.10	2403	42.2	0.15	0.02	46.7
2.41	22	252	b.l.	378	0.16	1.19	10.9	261	1615	1876	5.75	0.69	1876	75.0	0.67	b.l.	2496	46.9	0.15	b.l.	50.1
2.41	22	249	b.l.	360	0.26	1.55	8.72	33.6	1874	1908	4.53	0.39	397	90.6	0.60	0.11	2441	49.8	0.23	0.01	67.4
2.34	34	287	0.10	401	0.22	1.28	12.3	b.l.	1827	1827	5.94	0.91	469	82.5	0.75	0.11	2927	49.7	0.18	0.03	52.3

Abbreviations: b.l., below detection limit.

Table A.1.5: *pH value and metal concentration in the aliquot collected during AMD pre-titration spontaneous oxidation experiment.*

pH	time (days)	Al	As	Ca	Cd	Co	Cu	Fe $^{2+}$	Fe $^{3+}$	Fe $_t$	K	Li	Mg	Mn	Ni	Pb	S	Si	Sr	Ti	V	Zn
		mg L^{-1}																				
10.2	0	b.l.	b.l.	2391	b.l.	b.l.	b.l.	b.l.	b.l.	b.l.	39.1	0.24	266	2.17	b.l.	b.l.	1831	3.96	0.93	b.l.	b.l.	b.l.
8.2	1	b.l.	b.l.	301	b.l.	b.l.	b.l.	b.l.	b.l.	b.l.	121	0.88	778	26.9	b.l.	b.l.	1945	9.89	2.62	b.l.	b.l.	b.l.
7.5	2	b.l.	b.l.	298	b.l.	b.l.	b.l.	b.l.	b.l.	b.l.	118	0.77	800	51.8	b.l.	b.l.	1969	12.3	2.63	b.l.	b.l.	b.l.
6.2	3	b.l.	b.l.	301	b.l.	b.l.	b.l.	b.l.	b.l.	b.l.	123	0.89	893	76.7	b.l.	b.l.	1957	15.7	2.84	b.l.	b.l.	b.l.
5.4	5	b.l.	b.l.	302	b.l.	b.l.	b.l.	b.l.	b.l.	b.l.	117	0.83	922	79.9	b.l.	b.l.	1932	16.8	2.91	b.l.	b.l.	b.l.

Abbreviations: b.l., below detection limit.

Table A.1.6: *pH value and metal concentration in the aliquot collected during AMD pos-titration spontaneous oxidation experiment.*

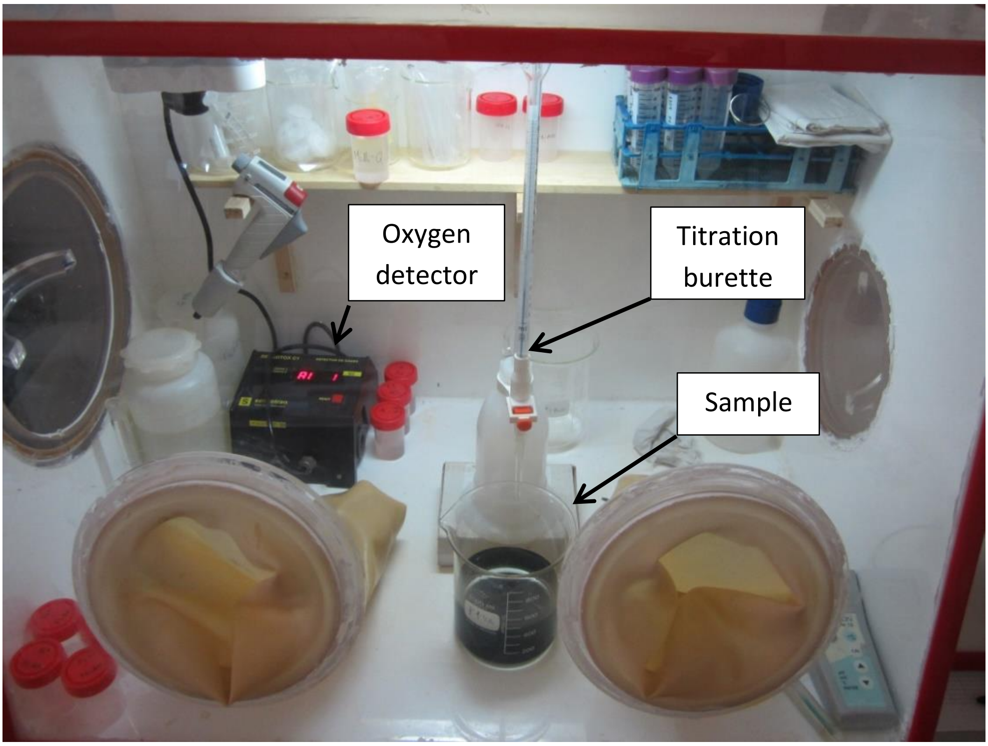

Figure A.1.1: *Experimental setup in titration under anoxic conditions preformed in globebox. The oxygen concentration was monitored throughout the experiment.*

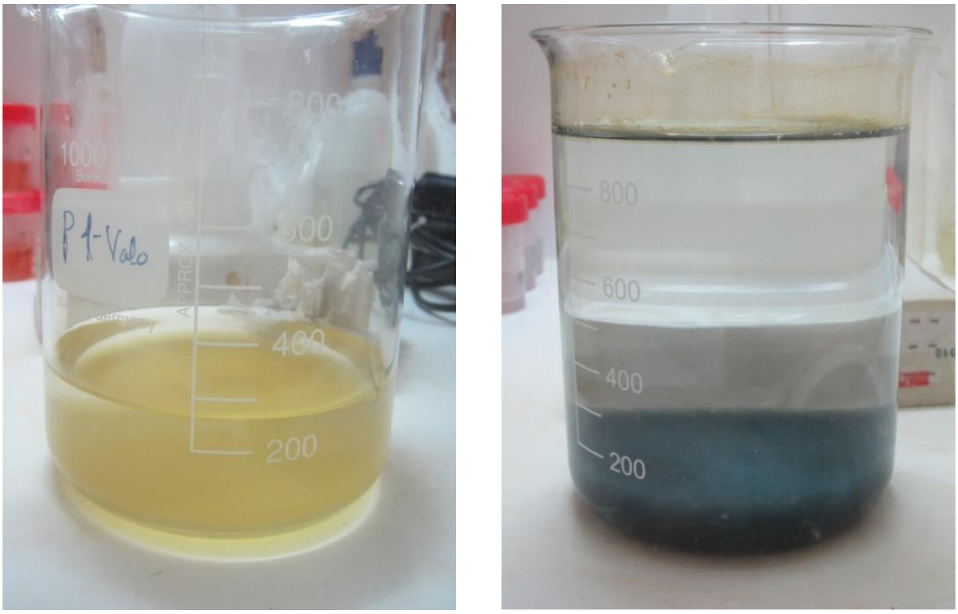

Figure A.1.2: *Basaluminite (left) and green rust (right) precipitates formed under anoxic conditions.*

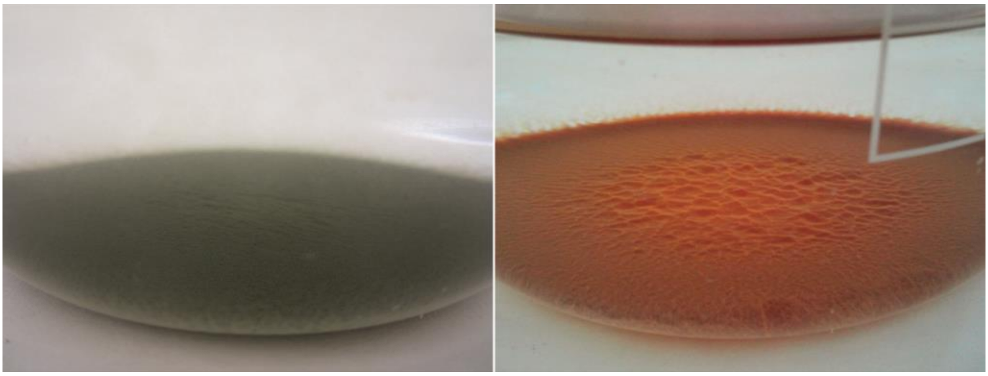

Figure A.1.3: *Final precipitates of titration under anoxic condition previous exposing to atmospheric conditions (left) and after 5 days under atmospheric conditions (right).*

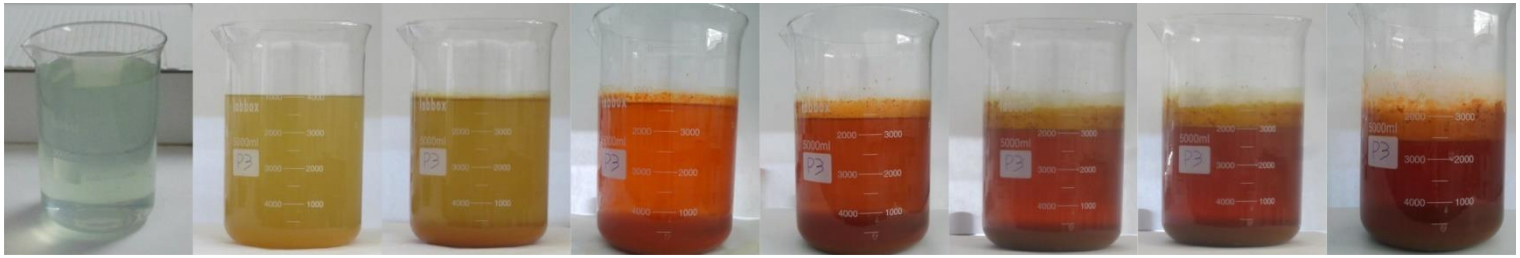

Figure A.1.4: *AMD evolution between all Fe in solution as Fe(II) (left) to Fe(III) (right). The ochre color in the first steps indicate that the solution is over saturate in schwertmannite and the red color in final steps show that the solution is equilibrate with Fe(III).*

A.2. CHAPTER III SUPPLEMENTARY INFORMATION

In this appendix is showed the chemical information (ICP-OES results, isotherm models, *etc.*) related to adsorption experiments preformed in Chapter III (Tables A.2.1 to A.2.6). On the other hand, the F-test results and d-PDF of structural models with less fit to experimental data is displayed as well (Tables A.2.7 to A.2.8 and Figures A.2.1 to A.2.4).

Sample	pH	$[As]_I$	Weight	$[As]_F$	Γ	Γ_{model}	Sample	pH	$[Se]_I$	Weight	$[Se]_F$	Γ	Γ_{model}
		(mmol)	(g)	(mmol)	$(mmol_{As}\ mol_{Fe}^{-1})$	$(mmol_{As}\ mol_{Fe}^{-1})$			(mmol)	(g)	(mmol)	$(mmol_{Se}\ mol_{Fe}^{-1})$	$(mmol_{Se}\ mol_{Fe}^{-1})$
Sch-As1	3.92	0.031	0.051	0.000	0.002	0.000	Sch-Se1	4.49	0.027	0.050	0.003	0.001	0.001
Sch-As2	3.53	0.049	0.050	0.000	0.002	0.000	Sch-Se2	4.80	0.058	0.049	0.006	0.003	0.001
Sch-As3	3.53	0.087	0.049	0.000	0.004	0.000	Sch-Se3	4.85	0.128	0.049	0.015	0.006	0.003
Sch-As3	3.53	0.087	0.050	0.002	0.004	0.016	Sch-Se4	5.10	0.395	0.050	0.067	0.016	0.013
Sch-As4	3.50	0.419	0.050	0.000	0.021	0.000	Sch-Se5	5.10	0.756	0.049	0.172	0.030	0.030
Sch-As5	3.52	0.772	0.050	0.000	0.038	0.000	Sch-Se6	5.05	0.919	0.050	0.231	0.034	0.037
Sch-As6	3.46	0.992	0.050	0.000	0.049	0.000	Sch-Se7	4.92	2.817	0.049	1.343	0.074	0.087
Sch-As7	3.58	3.305	0.050	0.358	0.146	0.124	Sch-Se7	4.92	2.817	0.049	1.401	0.071	0.089
Sch-As8	3.54	4.961	0.050	2.457	0.124	0.128	Sch-Se8	5.02	4.749	0.050	2.786	0.098	0.103
Sch-As9	3.23	6.834	0.050	4.272	0.126	0.128	Sch-Se9	4.86	6.574	0.050	4.414	0.108	0.109
Sch-As10	3.53	9.722	0.051	7.053	0.130	0.128	Sch-Se10	5.03	9.292	0.050	6.906	0.118	0.114

$[]_I$: Initial concentration

$[]_F$: Concentration after adsorption experiment

Weight: Weight of schwertmannite employed in each adsorption experiment

Γ: mmol of As or Se sorbed per mol of Fe in schwertmannite

Γ_{model}: mmol of As or Se sorbed per mol of Fe in schwertmannite calculate with Langmuir model

Table A.2.1: *Chemical and Langmuir model results of As and Se adsorption experiment onto schwertmannite. The volume of As or Se solution in each adsorption experiment was 0.02 L.*

Sample	pH	$[As]_I$	Weight	$[As]_F$	Γ	Γ_{model}	Sample	pH	$[Se]_I$	Weight	$[Se]_F$	Γ	Γ_{model}
		mmol	(g)	mmol	($mmol_{As}$ mol_{Al}^{-1})	($mmol_{As}$ mol_{Al}^{-1})			mmol	(g)	mmol	($mmol_{Se}$ mol_{Al}^{-1})	($mmol_{Se}$ mol_{Al}^{-1})
Bas-As1	3.65	0.026	0.048	0.000	0.001	0.000	Bas-Se1	5.39	0.029	0.049	0.011	0.001	0.001
Bas-As2	3.55	0.090	0.048	0.000	0.005	0.000	Bas-Se2	4.97	0.044	0.048	0.015	0.001	0.001
Bas-As3	3.50	0.102	0.048	0.000	0.005	0.000	Bas-Se3	4.90	0.083	0.048	0.033	0.003	0.002
Bas-As4	3.40	0.442	0.049	0.000	0.022	0.000	Bas-Se4	4.96	0.381	0.048	0.171	0.011	0.011
Bas-As5	3.35	0.778	0.048	0.000	0.039	0.000	Bas-Se5	4.95	0.743	0.048	0.425	0.016	0.025
Bas-As6	3.50	0.958	0.049	0.000	0.048	0.000	Bas-Se6	5.03	0.944	0.048	0.330	0.031	0.020
Bas-As7	3.90	2.877	0.048	0.006	0.146	0.089	Bas-Se7	5.43	2.801	0.048	1.563	0.062	0.065
Bas-As8	3.47	4.727	0.048	0.068	0.234	0.263	Bas-Se8	4.76	4.549	0.048	2.911	0.083	0.088
Bas-As9	3.49	6.635	0.049	0.683	0.295	0.318	Bas-Se8	4.76	4.549	0.048	2.844	0.086	0.087
Bas-As9	3.49	6.635	0.049	0.744	0.294	0.319	Bas-Se9	4.97	6.476	0.049	4.382	0.104	0.103
Bas-As10	3.51	9.583	0.049	3.022	0.327	0.324	Bas-Se10	5.02	9.140	0.048	6.770	0.119	0.117

$[]_I$: Initial concentration

$[]_F$: Concentration after adsorption experiment

Weight: Weight of basaluminite employed in each adsorption experiment

Γ: mmol of As or Se sorbed per mol of Al in basaluminite

Γ_{model}: mmol of As or Se sorbed per mol of Al in basaluminite calculate with Langmuir model

Table A.2.2: *Chemical and Langmuir model results of As and Se adsorption experiment onto basaluminite. The volume of As or Se solution in each adsorption experiment was 0.02 L.*

Sample	Weight	$[SO_4^{2-}]_{liq}$	$[H_2AsO_4^-]_{liq}$	$[SO_4^{2-}]_{sol}$	$[H_2AsO_4^-]_{sol}$	E $[SO_4]$	E $[H_2AsO_4]$	Ë $[SO_4]$	Ë $[H_2AsO_4]$	$[SO_4^{2-}]_{liq}$	$[H_2AsO_4^-]_{sol}$
	(g)	(meq L^{-1})		(meq Kg^{-1})						($mmol_{SO4}$ mol_{Fe}^{-1})	($mmol_{AsO4}$ mol_{Fe}^{-1})
Sch-As1	0.051	2.255	b.l.	2991	13.88	1.002	-0.002	0.995	0.005	1.131	1.746
Sch-As2	0.050	2.053	b.l.	3062	21.06	1.002	0.000	0.993	0.007	-3.887	2.623
Sch-As3	0.050	2.182	b.l.	2999	36.81	1.002	0.000	0.988	0.012	-0.685	4.521
Sch-As4	0.051	2.578	b.l.	2860	167.3	1.002	0.000	0.945	0.055	9.127	20.96
Sch-As5	0.051	2.999	b.l.	2692	307.3	1.001	0.000	0.898	0.102	19.57	38.48
Sch-As6	0.050	3.210	b.l.	2597	398.1	1.001	0.000	0.867	0.133	24.80	49.38
Sch-As7	0.050	4.341	0.358	2150	1174	0.924	0.078	0.647	0.353	52.84	146.1
Sch-As8	0.050	4.531	2.457	2071	1000	0.648	0.353	0.674	0.326	57.55	124.1
Sch-As9	0.050	4.284	4.272	2183	1015	0.501	0.501	0.683	0.317	51.41	127.0
Sch-As10	0.051	4.434	7.053	2141	1047	0.386	0.616	0.672	0.328	55.13	132.3

Sample	Weight	$[SO_4^{2-}]_{liq}$	$[SeO_4^{2-}]_{liq}$	$[SO_4^{2-}]_{sol}$	$[SeO_4^{2-}]_{sol}$	E $[SO_4]$	E $[SeO_4]$	Ë $[SO_4]$	Ë $[SeO_4]$	$[SO_4^{2-}]_{liq}$	$[SeO_4^{2-}]_{sol}$
	(g)	(meq L^{-1})		(meq Kg^{-1})						($mmol_{SO4}$ mol_{Fe}^{-1})	($mmol_{SeO4}$ mol_{Fe}^{-1})
Sch-Se1	0.050	1.970	0.005	3091	19.41	0.997	0.003	0.994	0.006	4.348	1.202
Sch-Se2	0.050	1.902	0.012	3112	41.89	0.993	0.007	0.987	0.013	2.639	2.574
Sch-Se3	0.049	2.031	0.030	3056	91.40	0.985	0.015	0.971	0.029	5.843	5.584
Sch-Se4	0.050	2.502	0.133	2883	261.1	0.950	0.050	0.917	0.083	17.52	16.25
Sch-Se5	0.049	3.077	0.343	2623	476.9	0.900	0.100	0.846	0.154	31.78	28.96
Sch-Se6	0.050	3.314	0.462	2550	551.0	0.878	0.122	0.822	0.178	37.66	34.05
Sch-Se7	0.049	4.930	2.682	1888	1190	0.648	0.352	0.613	0.387	77.71	72.98
Sch-Se8	0.050	5.856	5.565	1525	1577	0.513	0.487	0.492	0.508	100.7	97.19
Sch-Se9	0.050	6.345	8.816	1324	1738	0.419	0.581	0.432	0.568	112.8	107.0
Sch-Se10	0.050	7.020	13.79	1081	1900	0.337	0.663	0.363	0.637	129.5	118.1

b.l. below to detection limit.
$[]_{lig}$: Concentration in solution
$[]_{sol}$: Concentration in solid

Weight: Weight of schwertmannite employed in each adsorption experiment
E []: Portion in solution
Ë []: Portion in solid

Table A.2.3: *Results of As and Se exchange experiment with sulfate onto schwertmannite. The volume of As or Se solution in each adsorption experiment was 0.02 L.*

Sample	Weight	$[SO_4^{2-}]_{liq}$	$[H_2AsO_4^-]_{liq}$	$[SO_4^{2-}]_{sol}$	$[H_2AsO_4^-]_{sol}$	E $[SO_4]$	E $[H_2AsO_4]$	Ë $[SO_4]$	Ë $[H_2AsO_4]$	$[SO_4^{2-}]_{liq}$	$[H_2AsO_4^-]_{sol}$
	(g)	(meq L^{-1})		(meq Kg^{-1})						($mmol_{SO4}$ mol_{Al}^{-1})	($mmol_{AsO4}$ mol_{Al}^{-1})
Bas-As1	0.048	2.701	b.l.	4973	12.42	1.001	0.000	0.998	0.002	-1.929	1.449
Bas-As2	0.048	2.791	b.l.	4938	39.12	1.001	0.000	0.992	0.008	0.243	4.574
Bas-As3	0.049	2.832	b.l.	4933	43.74	1.001	0.000	0.991	0.009	1.260	5.168
Bas-As4	0.049	3.200	b.l.	4803	180.6	1.001	0.000	0.964	0.036	10.21	21.69
Bas-As5	0.049	3.528	b.l.	4653	319.9	1.001	0.001	0.936	0.064	18.19	37.98
Bas-As6	0.049	3.759	b.l.	4563	392.8	1.001	0.001	0.921	0.079	23.79	46.75
Bas-As7	0.048	5.737	0.006	3722	1189	0.999	0.003	0.758	0.242	71.93	139.7
Bas-As8	0.049	7.520	0.068	3009	1915	0.991	0.010	0.611	0.389	115.3	226.7
Bas-As9	0.049	8.508	0.683	2643	2418	0.926	0.076	0.522	0.478	139.4	289.6
Bas-As10	0.049	8.767	3.022	2512	2685	0.744	0.258	0.483	0.517	145.6	319.3

Sample	Weight	$[SO_4^{2-}]_{liq}$	$[SeO_4^{2-}]_{liq}$	$[SO_4^{2-}]_{sol}$	$[SeO_4^{2-}]_{sol}$	E $[SO_4]$	E $[SeO_4]$	Ë $[SO_4]$	Ë $[SeO_4]$	$[SO_4^{2-}]_{liq}$	$[SeO_4^{2-}]_{sol}$
	(g)	(meq L^{-1})		(meq Kg^{-1})						($mmol_{SO4}$ mol_{Al}^{-1})	($mmol_{SeO4}$ mol_{Al}^{-1})
Bas-Se1	0.049	2.768	0.022	4972	14.90	0.992	0.008	0.997	0.003	2.025	0.891
Bas-Se2	0.048	2.769	0.031	4953	23.54	0.989	0.011	0.995	0.005	2.057	1.384
Bas-Se3	0.049	2.787	0.066	4958	23.54	0.977	0.023	0.992	0.008	2.499	2.439
Bas-Se4	0.048	3.241	0.342	4759	173.3	0.905	0.095	0.965	0.035	13.53	10.19
Bas-Se5	0.048	3.622	0.848	4588	265.5	0.810	0.190	0.945	0.055	22.81	15.49
Bas-Se6	0.049	3.378	0.659	4714	502.6	0.837	0.163	0.904	0.096	16.88	29.82
Bas-Se7	0.049	4.894	3.123	4084	1018	0.610	0.390	0.800	0.200	53.74	60.15
Bas-Se8	0.048	5.797	5.814	3706	1351	0.499	0.501	0.733	0.267	75.73	79.63
Bas-Se9	0.049	6.767	8.753	3339	1706	0.436	0.564	0.662	0.338	99.33	101.8
Bas-Se10	0.048	7.524	13.52	2994	1953	0.357	0.643	0.605	0.395	117.7	115.1

b.l. below to detection limit.
$[]_{lig}$: Concentration in solution
$[_{sol}]$: Concentration in solid

Weight: Weight of basaluminite employed in each adsorption experiment
E []: Portion in solution
Ë []: Portion in solid

Table A.2.4: *Results of As and Se exchange experiment with sulfate onto basaluminite. The volume of As or Se solution in each adsorption experiment was 0.02 L.*

Sample	**time** (min)	**$[As]_I$** mmol	**Weight** (g)	**$[As]_F$** mmol	**Γ** ($mmol_{As}\ mol_{Fe}^{-1}$)	**Sample**	**time** (min)	**$[Se]_I$** mmol	**Weight** (g)	**$[Se]_F$** mmol	**Γ** ($mmol_{Se}\ mol_{Fe}^{-1}$)
Sch-As-05	5	3.305	0.050	2.736	28.39	Sch-Se-05	5	2.817	0.050	2.516	15.058
Sch-As-015	15	3.305	0.051	2.587	35.03	Sch-Se-015	15	2.817	0.049	2.354	23.298
Sch-As-030	30	3.305	0.050	2.447	42.36	Sch-Se-030	30	2.817	0.049	2.198	31.268
Sch-As-1	60	3.305	0.050	1.617	83.81	Sch-Se-1	60	2.817	0.050	2.015	40.182
Sch-As-3	180	3.305	0.051	1.389	93.27	Sch-Se-3	180	2.817	0.051	1.723	53.868
Sch-As-5	300	3.305	0.049	1.383	96.42	Sch-Se-5	300	2.817	0.051	1.649	57.491
Sch-As-10	600	3.305	0.049	1.965	67.07	Sch-Se-10	600	2.817	0.051	1.591	60.454
Sch-As-24	1440	3.305	0.051	0.985	113.7	Sch-Se-24	1440	2.817	0.051	1.416	68.582
Sch-As-48	2880	3.305	0.051	0.770	123.9	Sch-Se-48	2880	2.817	0.050	1.376	71.854
Sch-As-72	4320	3.305	0.050	0.358	130.5	Sch-Se-72	4320	2.817	0.050	1.343	73.875

$[]_I$: Initital concentration

$[]_F$: Concentration after cinetic experiment

Weight: Weight of schwertmannite employed in each adsortion experiment

Γ: mmol of As or Se sorbed per mol of Fe in schwertmannite

Table A.2.5: *Results of As and Se absorption kinetic onto schwertmannite. The volume of As or Se solution in each adsorption was 0.02 L.*

Sample	time	$[As]_I$	weght	$[As]_F$	Γ	Sample	time	$[Se]_I$	weght	$[Se]_F$	Γ
	(min)	mmol	(g)	mmol	($mmol_{As}$ mol_{Al}^{-1})		(min)	mmol	(g)	mmol	($mmol_{Se}$ mol_{Al}^{-1})
Bas-As-05	5	0.049	2.877	1.915	47.36	Bas-Se-05	5	2.801	0.049	2.387	20.49
Bas-As-015	15	0.050	2.877	1.620	61.40	Bas-Se-015	15	2.801	0.048	2.305	24.88
Bas-As-030	30	0.049	2.877	1.453	70.16	Bas-Se-030	30	2.801	0.049	2.211	29.12
Bas-As-1	60	0.049	2.877	1.007	93.49	Bas-Se-1	60	2.801	0.048	2.082	36.07
Bas-As-3	180	0.048	2.877	0.549	118.6	Bas-Se-3	180	2.801	0.048	1.872	46.53
Bas-As-5	300	0.050	2.877	0.459	118.5	Bas-Se-5	300	2.801	0.049	1.832	49.35
Bas-As-10	600	0.049	2.877	0.323	125.8	Bas-Se-10	600	2.801	0.048	1.772	51.88
Bas-As-24	1440	0.048	2.877	0.071	142.3	Bas-Se-24	1440	2.801	0.049	1.657	56.77
Bas-As-48	2880	0.048	2.877	0.022	144.5	Bas-Se-48	2880	2.801	0.049	1.610	59.95
Bas-As-72	4320	0.047	2.877	0.006	147.6	Bas-Se-72	4320	2.801	0.049	1.563	61.97

$[]_I$: Initital concentration

$[]_F$: Concentration after cinetic experiment

Weight: Weight of basaluminite employed in each adsorption experiment

Γ: mmol of As or Se sorbed per mol of Al in basaluminite

Table A.2.6: *Results of As and Se absorption kinetic onto basaluminite. The volume of As or Se solution in each adsorption was 0.02 L.*

	Fit	Coordination 1	Proportion (%)	$\chi2$	R-factor	Ind. Point	Variable	Ind. Variable	Red. $\chi2$	Model 1	Model 2	F-test	Probability (%)
Sch-As	1	b. b. inner sp.	100	484.0	0.013	15	5	10.21	47.38	Fit 2	Fit 1	1.027	52.00
	2	b. m. inner sp.	100	471.4	0.013	15	5	10.21	46.15	Fit 2	Fit 3	1.039	54.00
	3	m. inner sp.	100	489.6	0.013	15	5	10.21	47.93	Fit 2	Fit 4	8.416	99.99
	4	outer sp.	100	1248	0.034	15	3	12.21	102.2				
Sch-Se	1	b. b. inner sp.	100	442.3	0.011	15	5	10.39	42.56	Fit 1	Fit 2	1.671	78.00
	2	b. m. inner sp.	100	739.3	0.019	15	5	10.39	71.14	Fit 1	Fit 3	1.150	60.00
	3	m. inner sp.	100	508.5	0.013	15	5	10.39	48.93	Fit 1	Fit 4	9.083	99.99
	4	outer sp.	100	828.9	0.021	15	4	11.39	72.76				

b.b. inner sp.: bidentate binucleate inner-sphere
b.m. inner sp.: bidentate mononucleate inner-sphere
m. inner sp.: monodentate inner-sphere
outer sp.: outer-sphere

Table A.2.7: *Fit parameters obtained from the different structural models compared with As and Se K-edge EXAFS results in schwertmannite.*

	Fit	Coordination 1	Proportion (%)	χ2	R-factor	Ind. Point	Variable	Ind. Variable	Red. χ2	Model 1	Model 2	F-test	Probability (%)
Bas-As	1	b. b. inner sp.	100	537.9	0.003	15.42	3	12.42	43.30	Fit 1	Fit 2	1.511	82.25
	2	b. m. inner sp.	100	812.6	0.003	15.42	3	12.42	65.40	Fit 1	Fit 3	9.308	99.98
	3	m. inner sp.	100	940.9	0.004	15.42	2	13.42	70.09	Fit 1	Fit 4	157.5	99.99
	4	outer sp.	100	7355	0.035	15.42	2	13.42	547.9				
Bas-Se	1	b. b. inner sp.	50	1676	0.017	16.53	3	13.53	123.9	Fit 4	Fit 1	1.316	74.00
	2	b. m. inner sp.	50	1695	0.017	16.53	3	13.53	125.3	Fit 4	Fit 2	1.331	77.00
	3	m. inner sp.	100	1584	0.016	16.53	3	13.53	117.1	Fit 4	Fit 3	1.243	65.00
	4	outer sp.	100	1274	0.013	16.53	3	13.53	94.14				

b.b. inner sp.: bidentate binucleate inner-sphere
b.m. inner sp.: bidentate mononucleate inner-sphere
m. inner sp.: monodentate inner-sphere

Table A.2.8: *Fit parameters obtained from the different structural models compared with As and Se K-edge EXAFS results in basaluminite.*

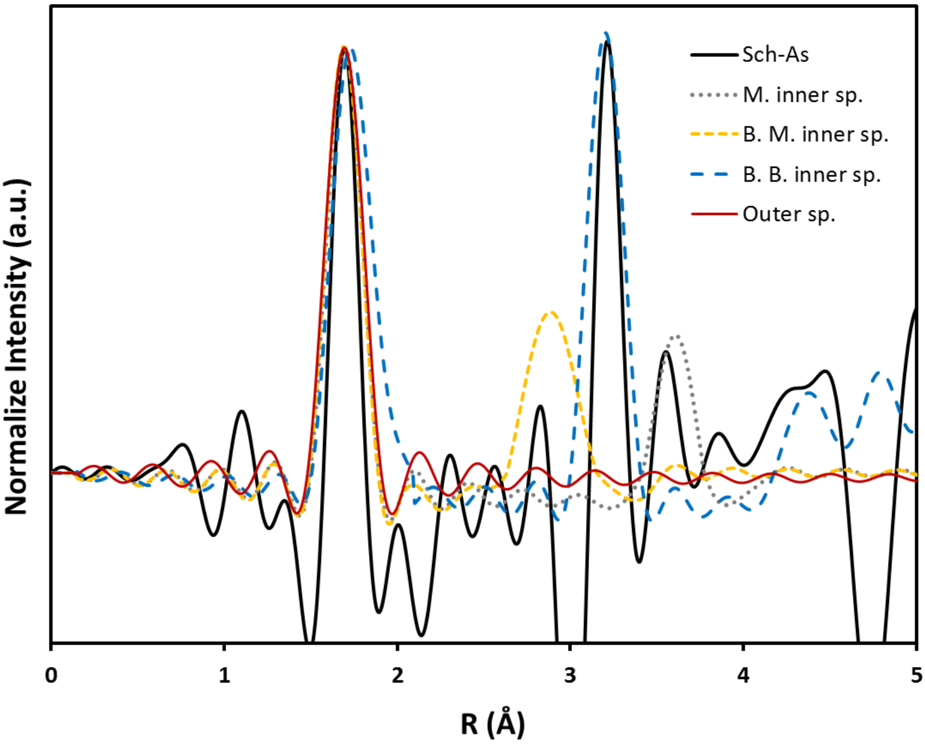

Figure A.2.1: *As oxyanion models coordinate in monodentate (M. inner sp.; grey), bidentate mononuclear (B. M. inner sp.; yellow), bidentate binuclear inner sphere (B. B. inner sp.; blue) and outer sphere (Outer sp.; red) position onto schwertmannite. Experimental result is represented with black line.*

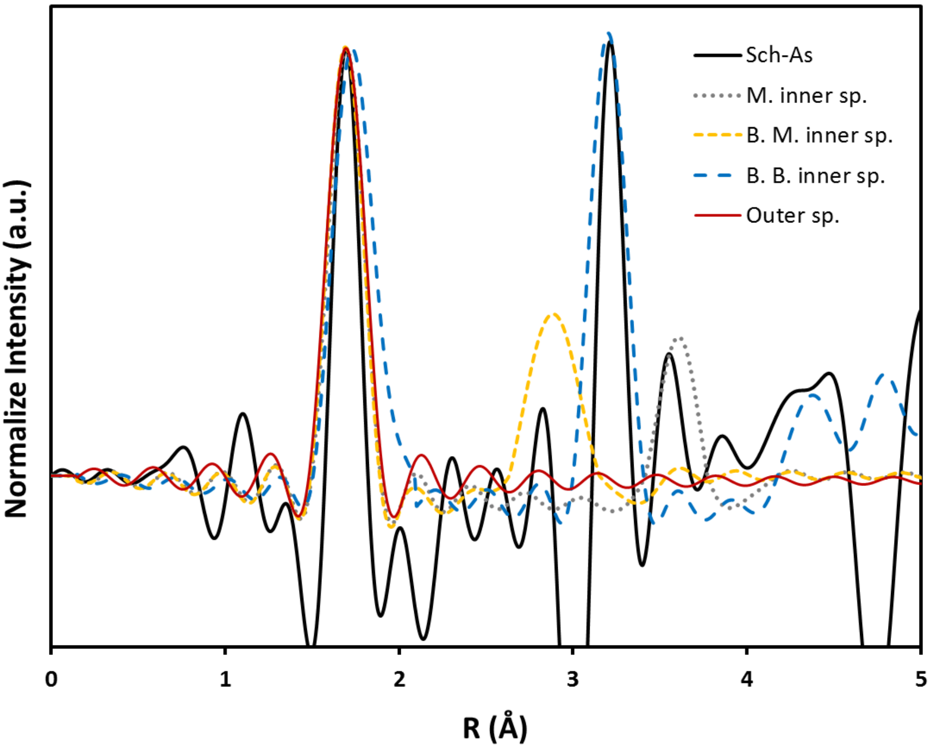

Figure A.2.2: *Se oxyanion models coordinate in monodentate (M. inner sp.; grey), bidentate mononuclear (B. M. inner sp.; yellow), bidentate binuclear inner sphere (B. B. inner sp.; blue) and outer sphere (Outer sp.; red) position onto schwertmannite. Experimental result is represented with black line.*

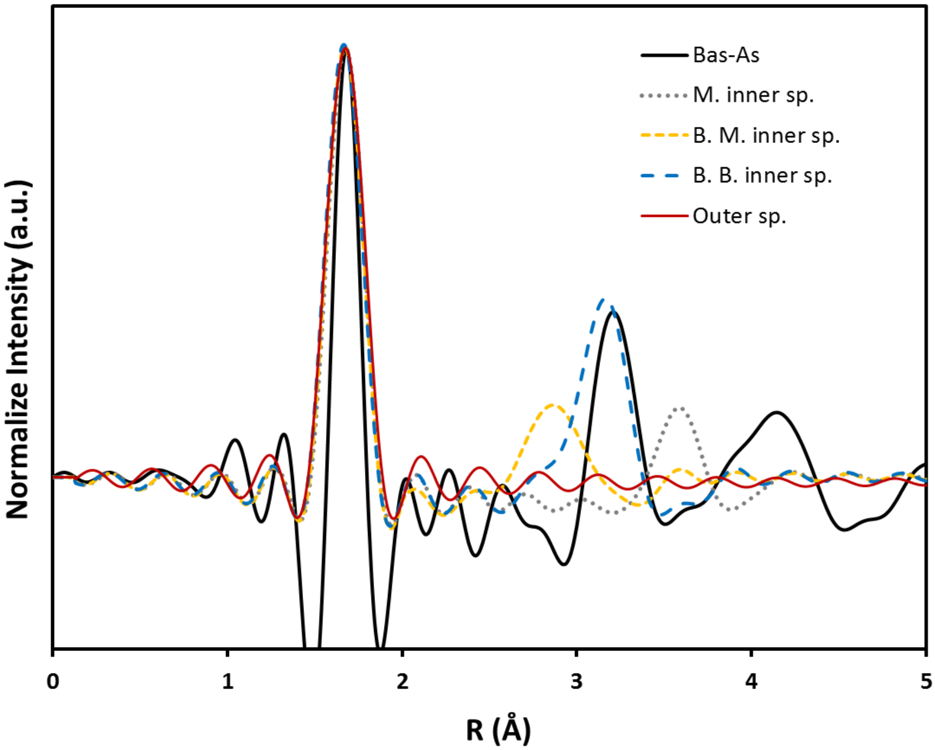

Figure A.2.3: *As oxyanion models coordinate in monodentate (M. inner sp.; grey), bidentate mononuclear (B. M. inner sp.; yellow), bidentate binuclear inner sphere (B. B. inner sp.; blue) and outer sphere (Outer sp.; red) position onto basaluminite Experimental result is represented with black line.*

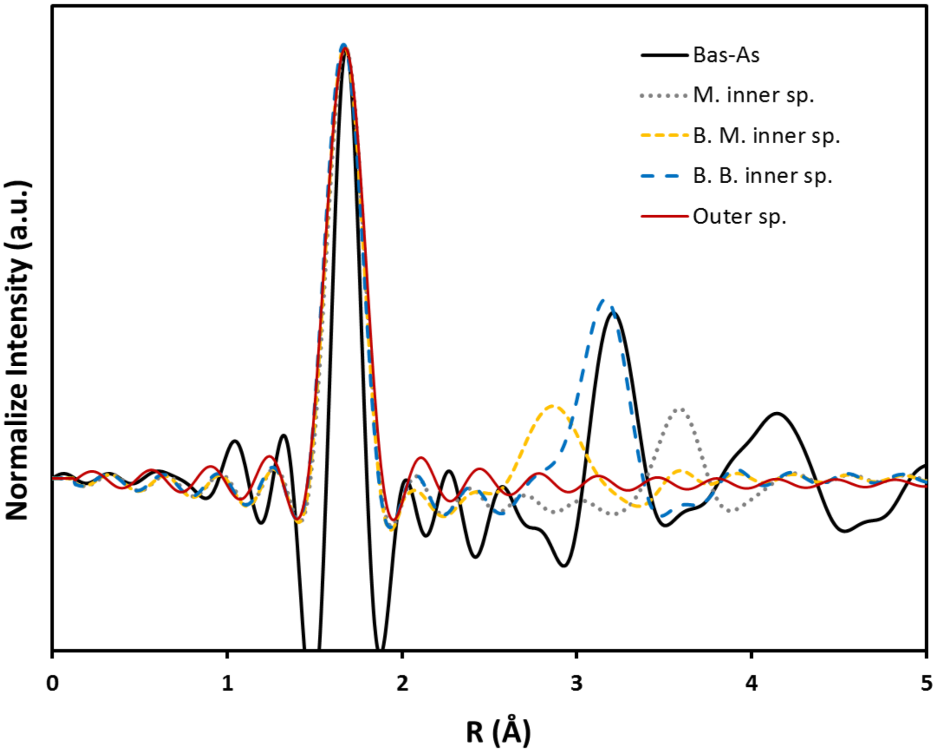

Figure A.2.4: *Se oxyanion coordinate in monodentate (M. inner sp.; grey), bidentate mononuclear (B. M. inner sp.; yellow), bidentate binuclear inner sphere (B. B. inner sp.; blue) and outer sphere (Outer sp.; red) position onto basaluminite. Experimental result is represented with black line.*

A.3. CHAPTER IV SUPPLEMENTARY INFORMATION

In this appendix is showed the chemical information of solid samples (Table A.3.1) and parameter obtained in EXAFS (Table A.3.2) and RMC (Table A.3.3) models related to structural study performed in Chapter IV. On the other hand, the χ^2 evolution, *S(Q)* and *G(r)* obtain in the different structural models run in RMC are displayed as well (Figures A.3.1 to A.3.18).

	Natural bas.			**Synthetic bas.**		
	weight	**g**	0.050	**weight**	**g**	0.051
	Volume	**L**	0.050	**Volume**	**L**	0.050
	mg L^{-1}	**mmol g^{-1}**	**ratio**	**mg L^{-1}**	**mmol g^{-1}**	**ratio**
Al	219.5	8.200	4.00	200.3	7.306	4.00
S	96.99	3.050	1.49	83.18	2.554	1.40
Ca	0.428	0.011	0.01	1.350	0.033	0.02
Mg	0.004	0.000	-	0.436	0.028	0.02
Na	0.242	0.011	0.01	0.690	0.023	0.01
Si	-0.044	-0.002	-	0.530	0.015	0.01
OH	3.120	18.49	9.02	290.4	16.04	9.20
H_2O	167.0	9.348	4.56	159.5	8.712	4.77
	$Al_4(OH)_{9.02}(SO_4)_{1.49}$-$4.56H_2O$			$Al_4(OH)_{9.2}(SO_4)_{1.4}$-$4.77H_2O$		

Table A.3.1: *Chemical results of solid samples.*

	Fit	Coordination 1	Proportion (%)	χ2	R-factor	Ind. Point	Variable	Ind. Variable	Red. Chi^2	Model 1	Model 2	F-test	Probability (%)
Bas-Nat	1	b. b. inner sp.	100	30.98	0.019	9.346	4	5.346	5.795	Fit 3	Fit 1	1.901	73.00
	2	b. m. inner sp.	100	33.28	0.020	9.346	4	5.346	6.226	Fit 3	Fit 2	2.043	75.00
	4	outer sp.	100	16.29	0.010	9.346	4	5.346	3.048				
Bas-Syn	1	b. b. inner sp.	100	17.87	0.008	9.346	5	4.346	4.112	Fit 1	Fit 2	2.206	79.00
	2	b. m. inner sp.	100	21.83	0.011	9.346	5	4.346	5.024	Fit 1	Fit 3	1.222	60.00
	4	outer sp.	100	36.01	0.017	9.346	3	6.346	5.674				

b.b. inner sp.: bidentate binucleate inner-sphere
b.m. inner sp.: bidentate mononucleate inner-sphere
outer sp.: outer-sphere

Table A.3.2: *Fit parameters obtained from the different structural models compared with S K-edge EXAFS results in natural and synthetic basaluminite.*

	Felsöbányaite **P21-C22**	**Fels1 [1,1,1]** **P1**	**Fels1 [2,2,2]** **P1**	**Fels1 [3,3,3]** **P1**	**Fels2 [1,1,1]** **P1**	**Fels2 [2,2,2]** **P1**	**Fels2 [3,3,3]** **P1**	**Fels3 [1,1,1]** **P1**	**Fels2 [2,2,2]** **P1**	**Fels3 [3,3,3]** **P1**
a (Å)	12.968	12.994	25.993	39.186	13.075	26.182	39.123	13.004	25.978	39.013
b (Å)	9.9363	9.9565	19.916	30.025	10.018	20.061	29.952	9.9637	19.905	29.893
c (Å)	11.026	11.048	22.100	33.318	11.117	22.261	33.211	11.056	22.087	33.171
β(º)	105.14	105.32	103.94	106.30	106.99	105.72	105.42	105.19	105.02	105.31
V(Å^3)	1166.0	1348.5	11103	37625	1392.6	11255	37516	1382.4	11031	37312
U	-0.2168	-	-	-	-	-	-	-	-	-
V	-0.2587	-	-	-	-	-	-	-	-	-
W	0.0461	-	-	-	-	-	-	-	-	-
X	0.8784	-	-	-	-	-	-	-	-	-
U_{al}(Å^2)	0.0052	0.0021	0.0004	0.0024	0.0013	0.0022	0.0009	0.0004	0.0003	0.0010
U_O(Å^2)	0.0176	0.0008	0.0002	0.0007	0.0032	0.0045	0.0024	0.0009	0.0008	0.0021
U_S(Å^2)	0.0003	0.0004	0.0628	0.0859	0.0223	0.0367	0.0052	0.0108	0.0063	0.0040
d(Å)	44.677	10.658	12.239	16.165	11.634	12.851	15.248	9.186	10.694	13.593
σ_q(Å^{-1})	0.0978	0.0274	0.0274	0.0274	0.0274	0.0274	0.0274	0.0274	0.0274	0.0274
R_w(%)	19.43	-	-	-	-	-	-	-	-	-

Table A.3.3: *Fit parameters obtained from the different structures employed in RMC models.*

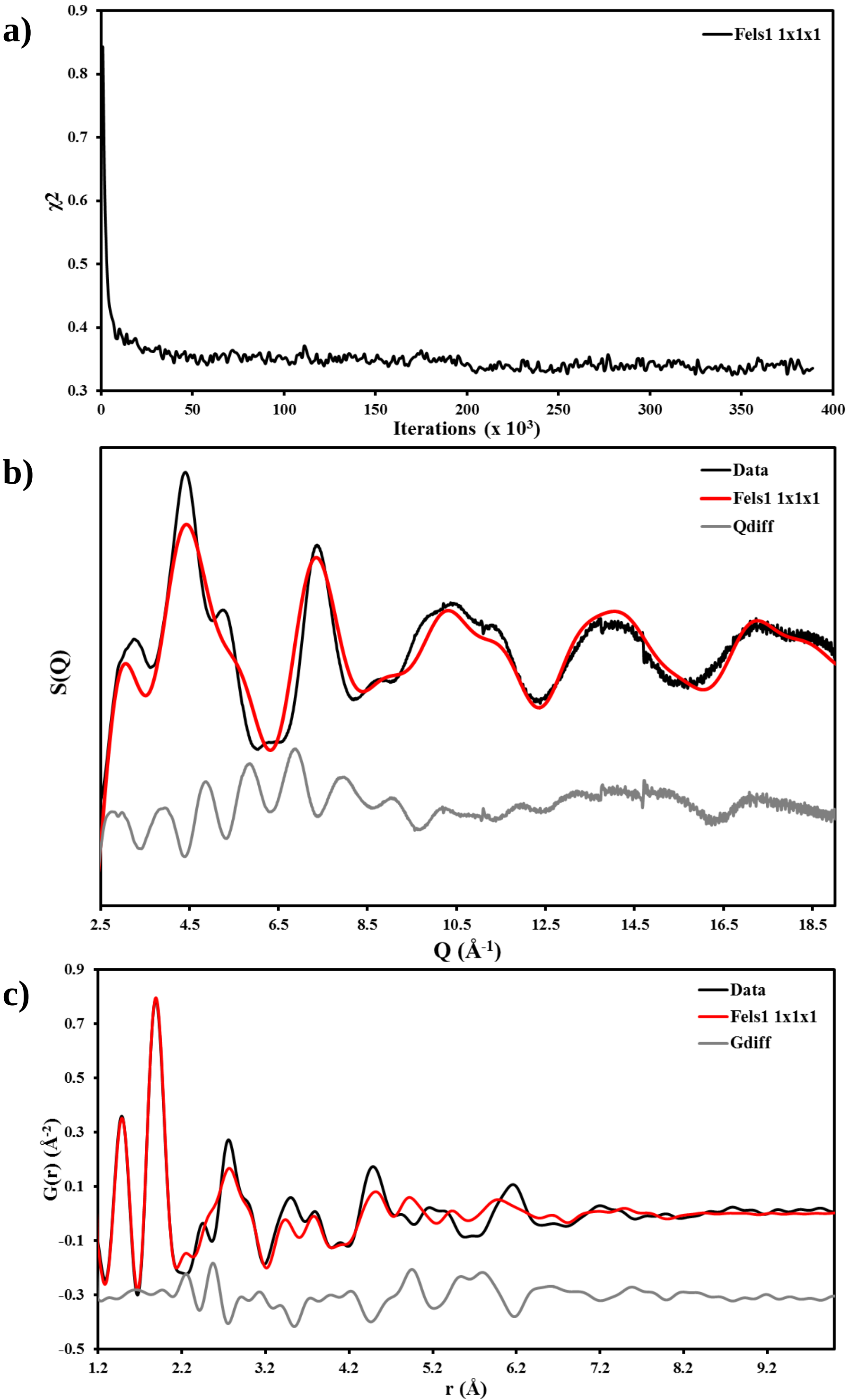

Figure A.3.1: *(a) χ^2 evolution, (b) S(Q) and (c) G(r) modeled with RMC of the Fels1 [1,1,1] final structure.*

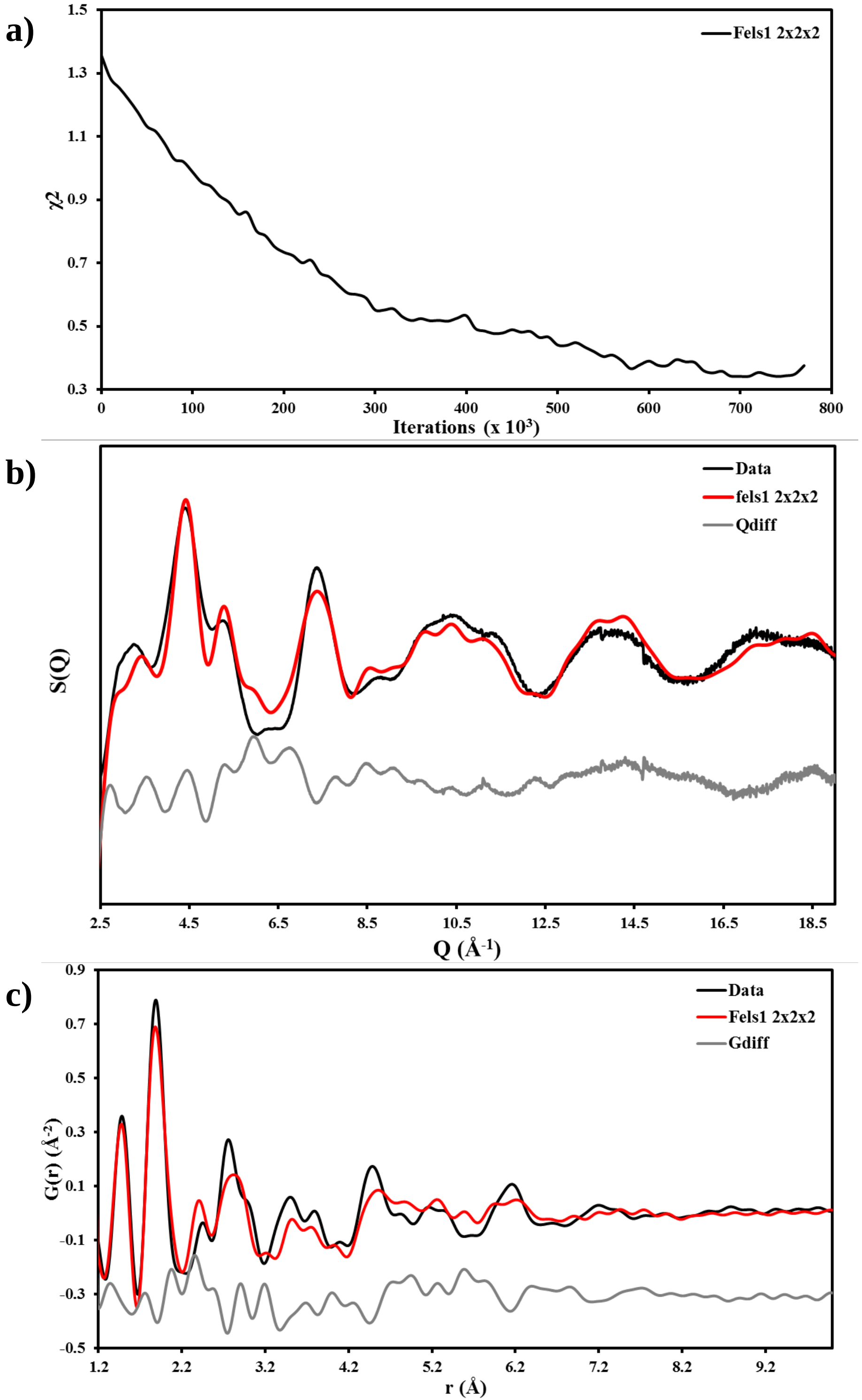

Figure A.3.2: *(a) χ^2 evolution, (b) S(Q) and (c) G(r) modeled with RMC of the Fels1 [2,2,2] final structure.*

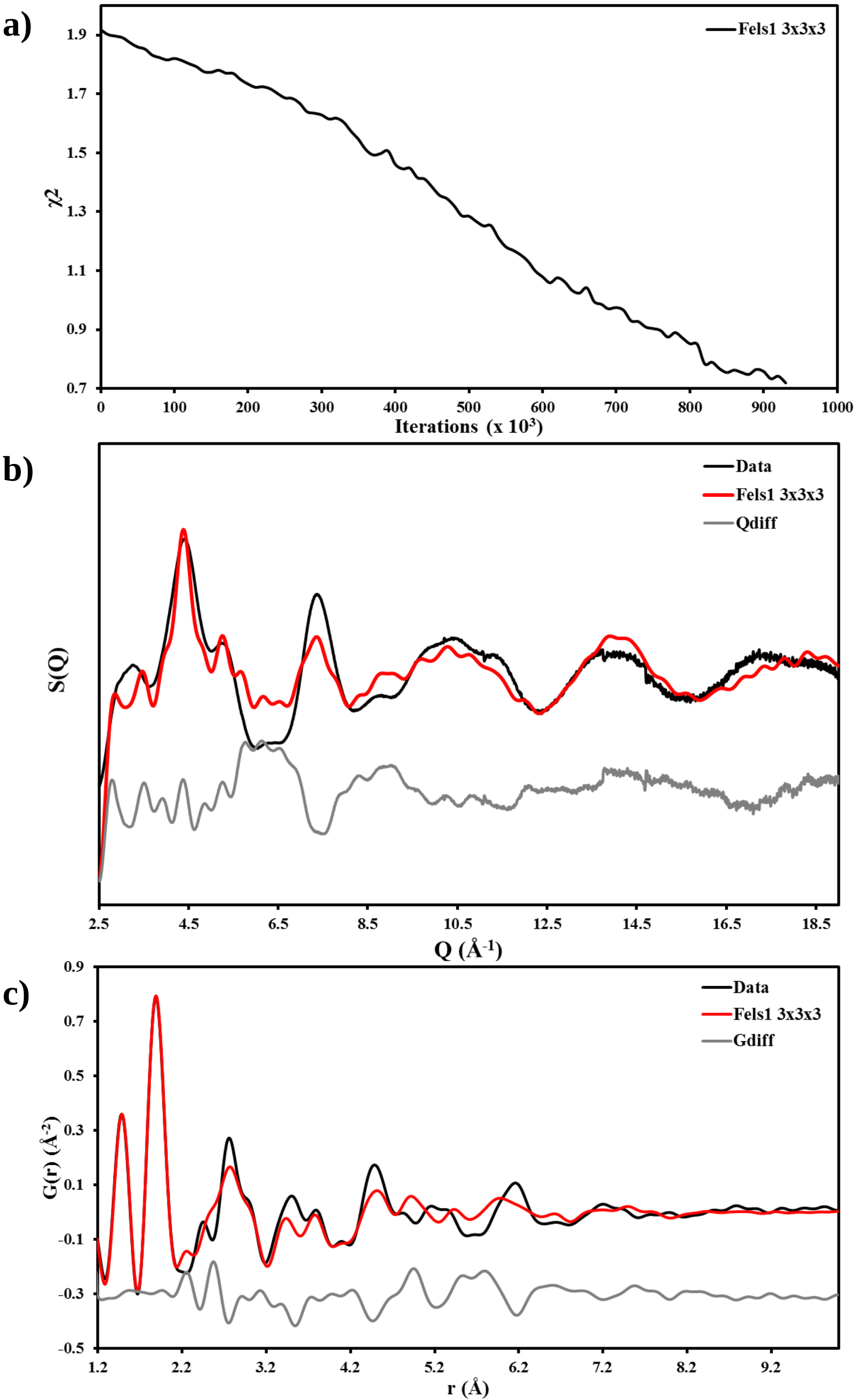

Figure A.3.3: *(a) χ^2 evolution, (b) S(Q) and (c) G(r) modeled with RMC of the Fels1 [3,3,3] final structure.*

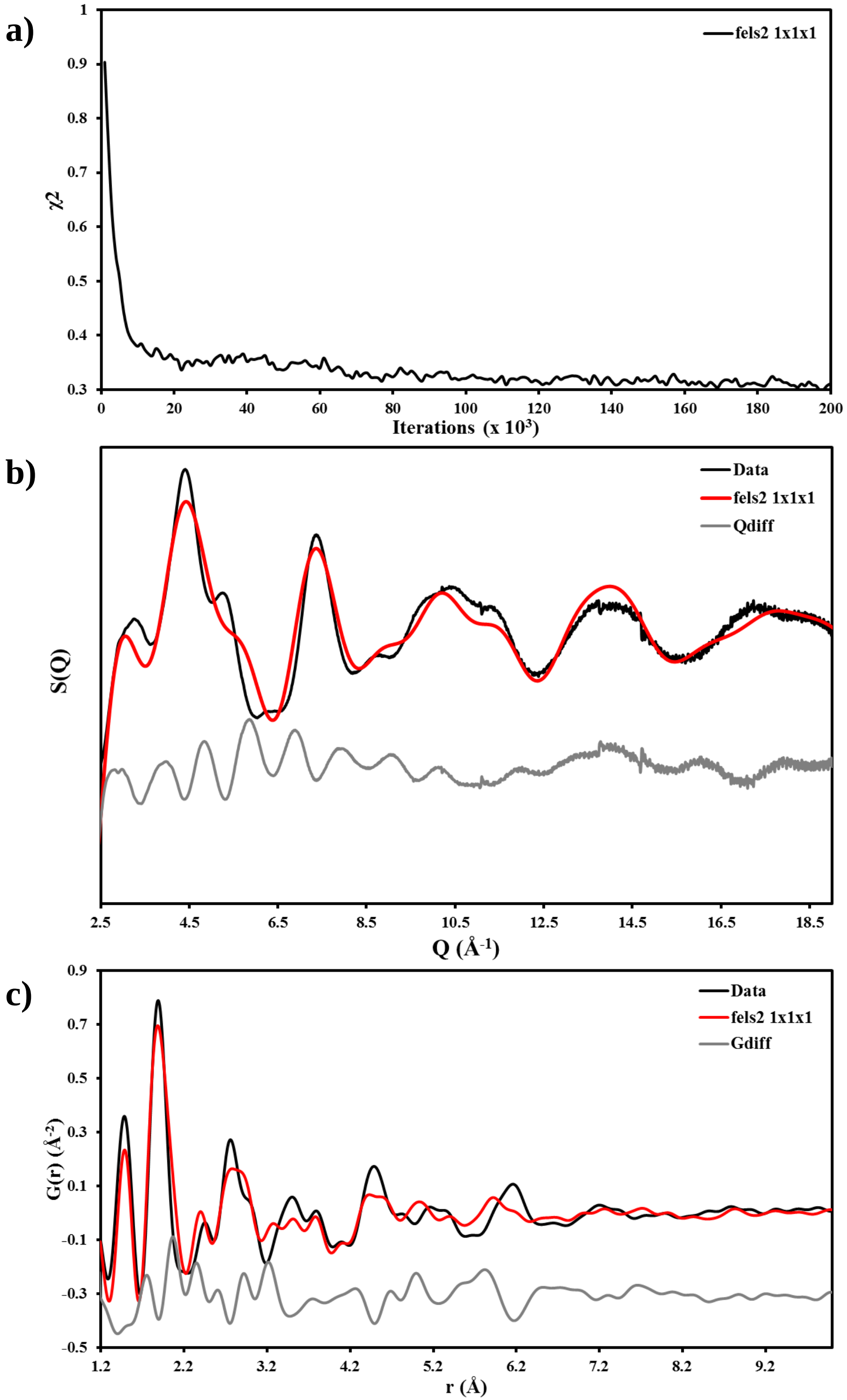

Figure A.3.4: *(a) χ^2 evolution, (b) S(Q) and (c) G(r) modeled with RMC of the Fels2 [1,1,1] final structure.*

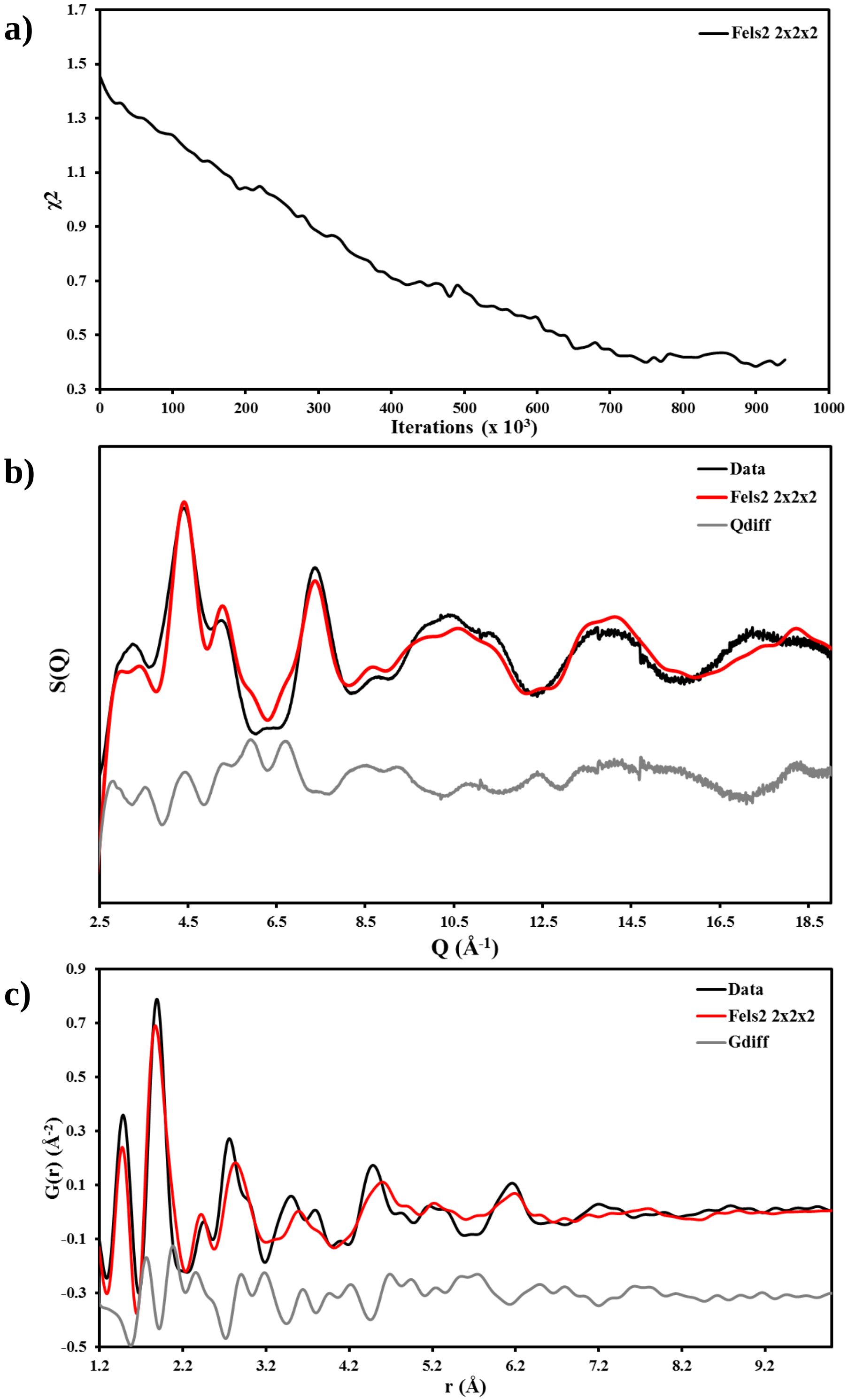

Figure A.3.5. *(a) χ^2 evolution, (b) S(Q) and (c) G(r) modeled with RMC of the Fels2 [2,2,2] final structure.*

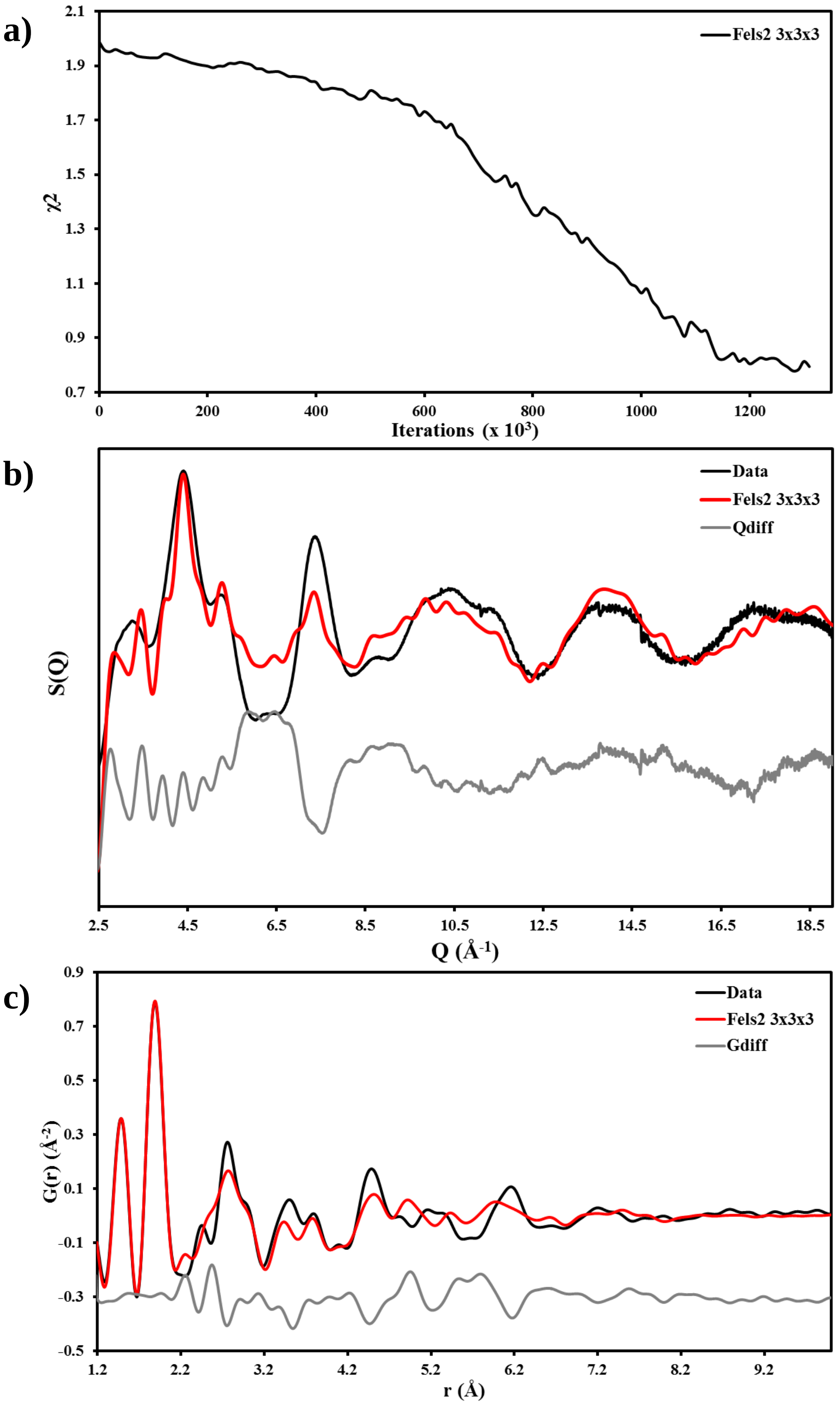

Figure A.3.6. *(a) χ^2 evolution, (b) S(Q) and (c) G(r) modeled with RMC of the Fels2 [3,3,3] final structure.*

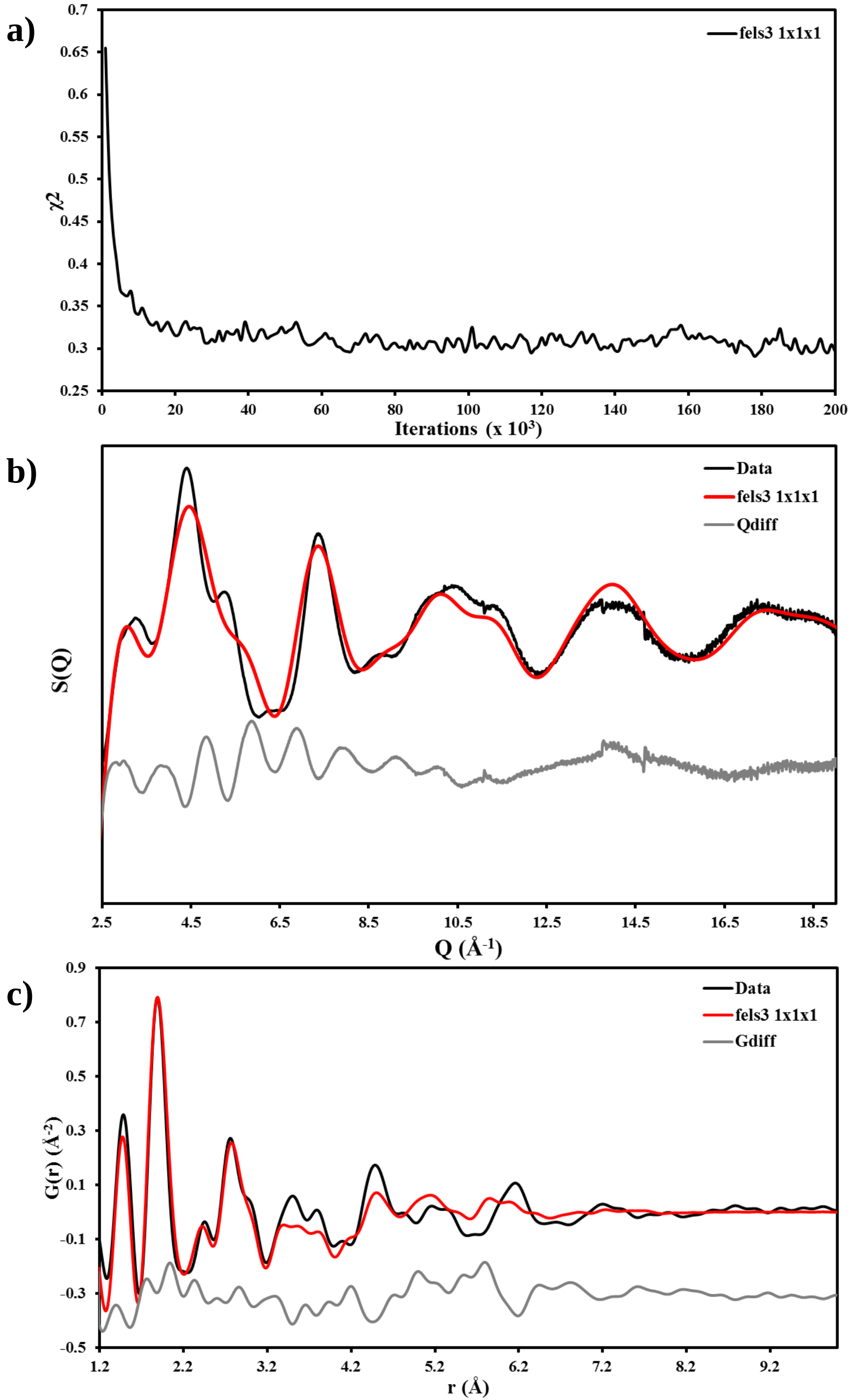

Figure A.3.7: *(a)* χ^2 *evolution, (b) S(Q) and (c) G(r) modeled with RMC of the Fels3 [1,1,1] final structure.*

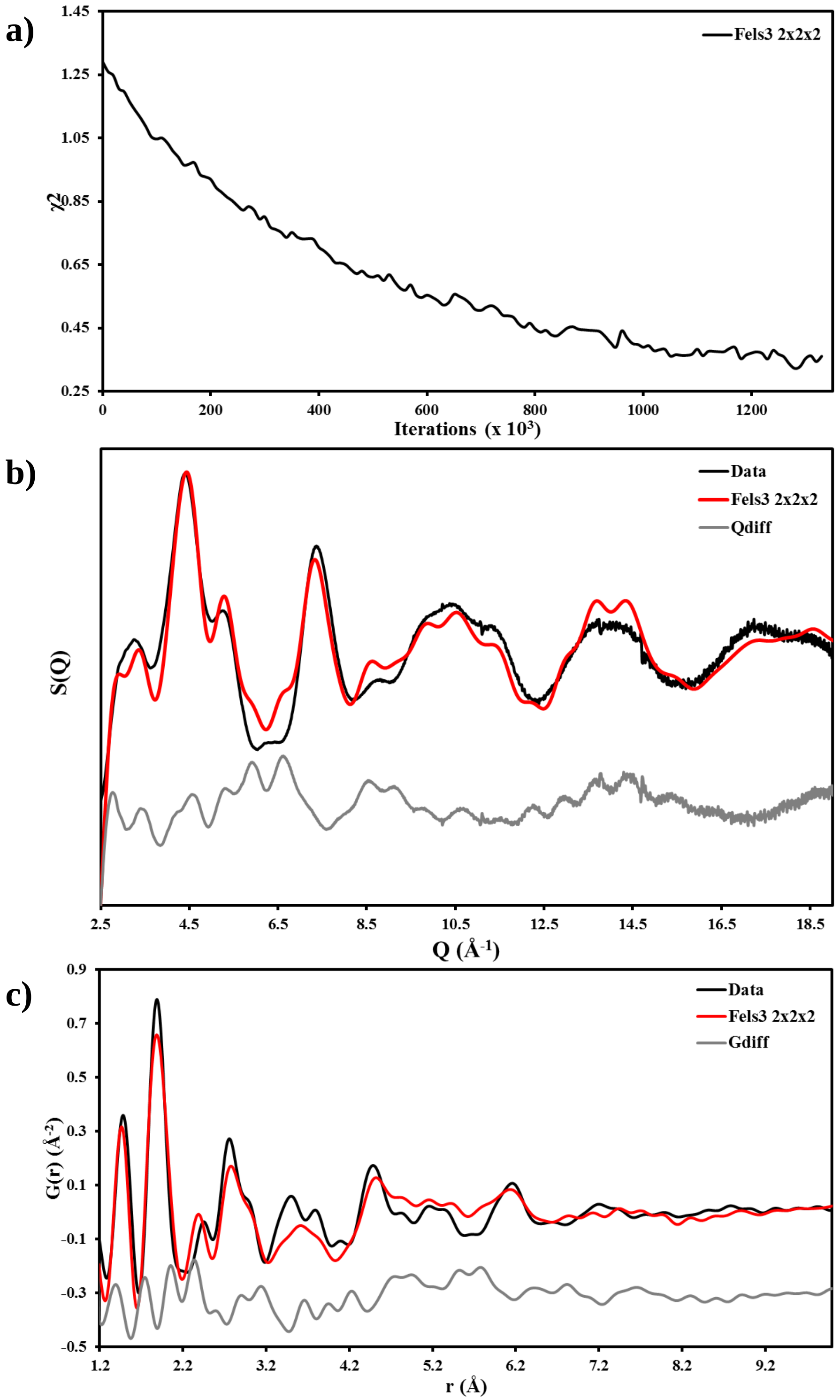

Figure A.3.8: *(a) χ^2 evolution, (b) S(Q) and (c) G(r) modeled with RMC of the Fels3 [2,2,2] final structure.*

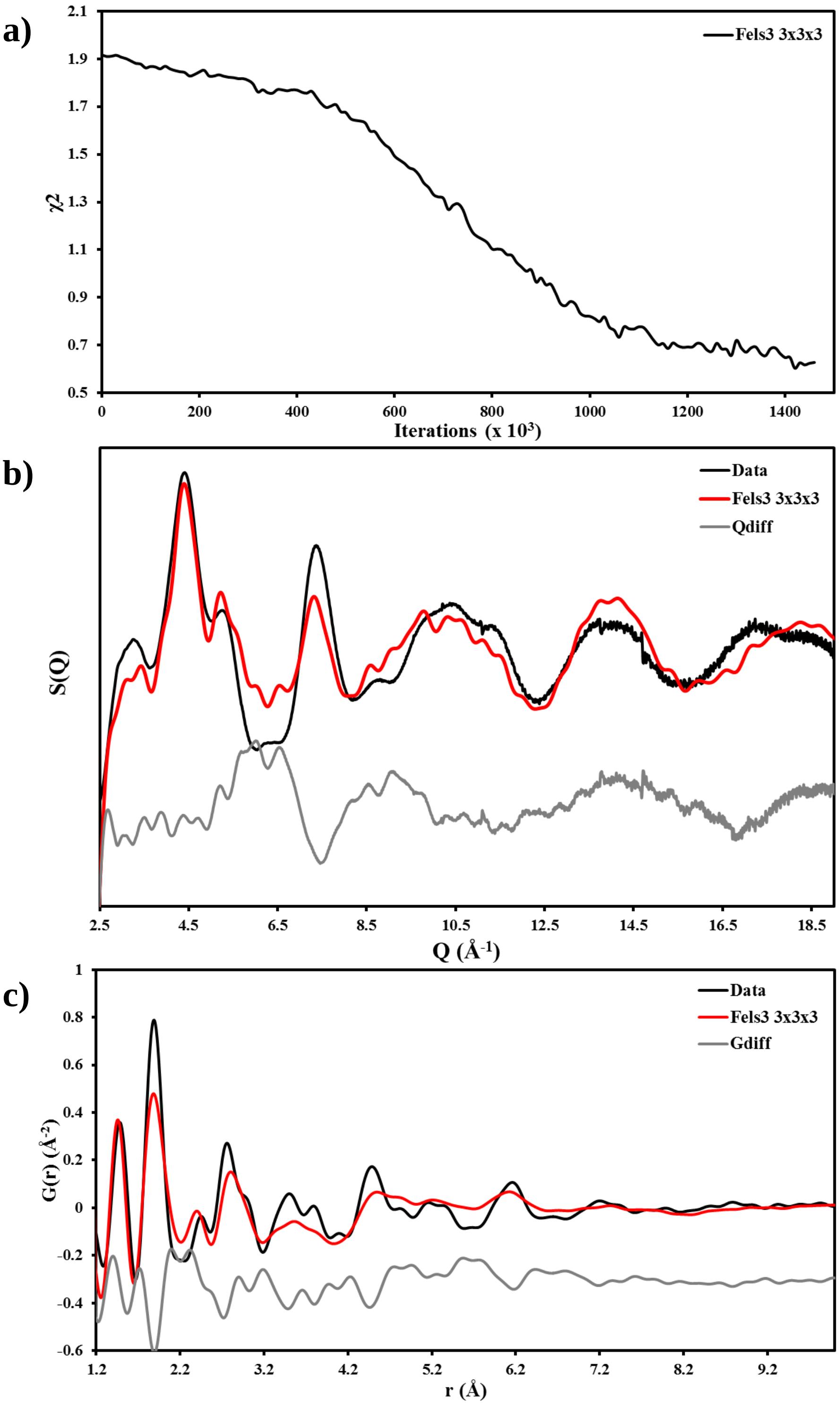

Figure A.3.9: *(a) χ^2 evolution, (b) S(Q) and (c) G(r) modeled with RMC of the Fels3 [3,3,3] final structure.*

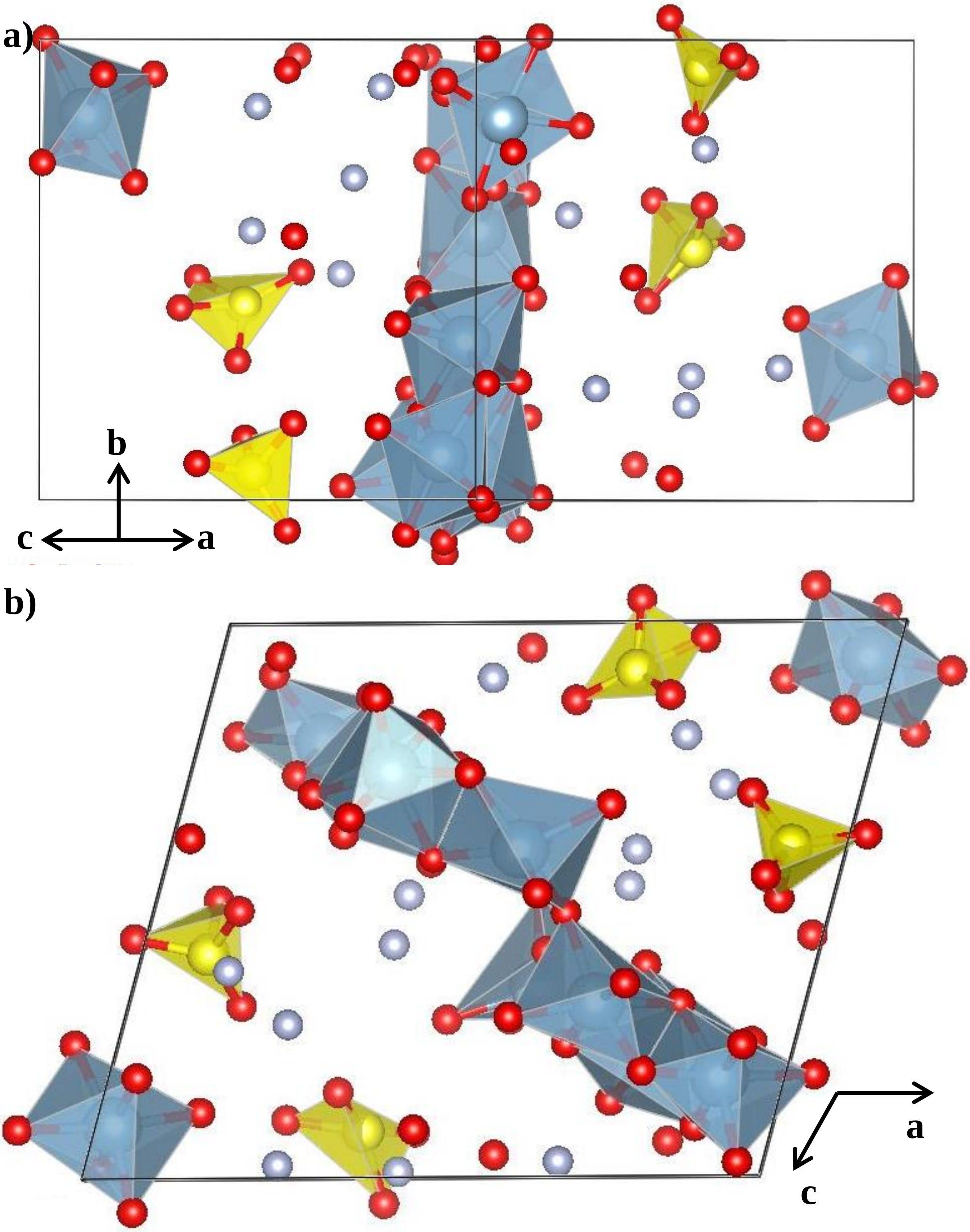

Figure A.3.10: *Cross section parallel to (a) plane a-c, and (b) b-edge of the Fels1 [1,1,1] final structure.*

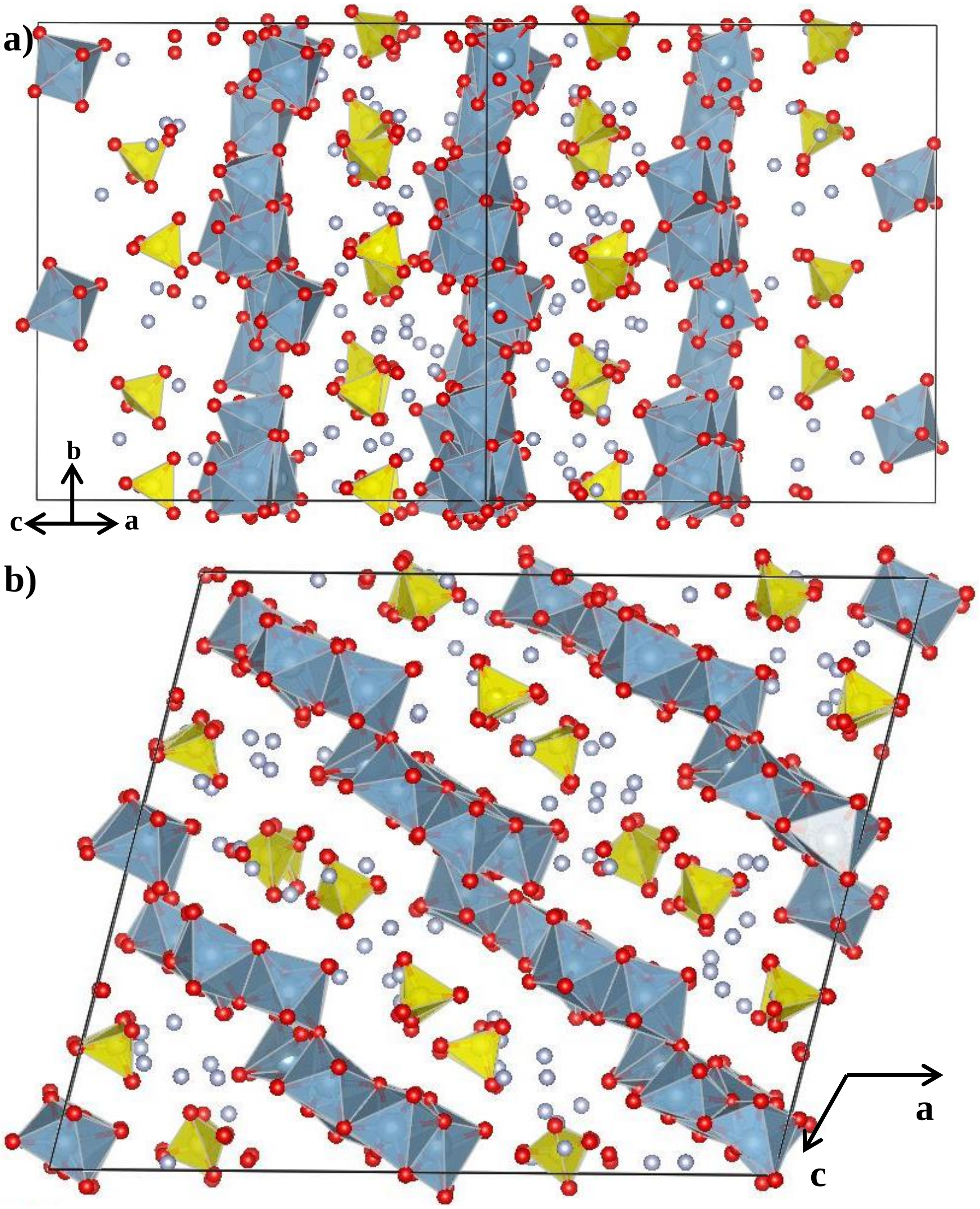

Figure A.3.11: Cross section parallel to (a) plane a-c, and (b) b-edge of the Fels1 [2,2,2] final structure.

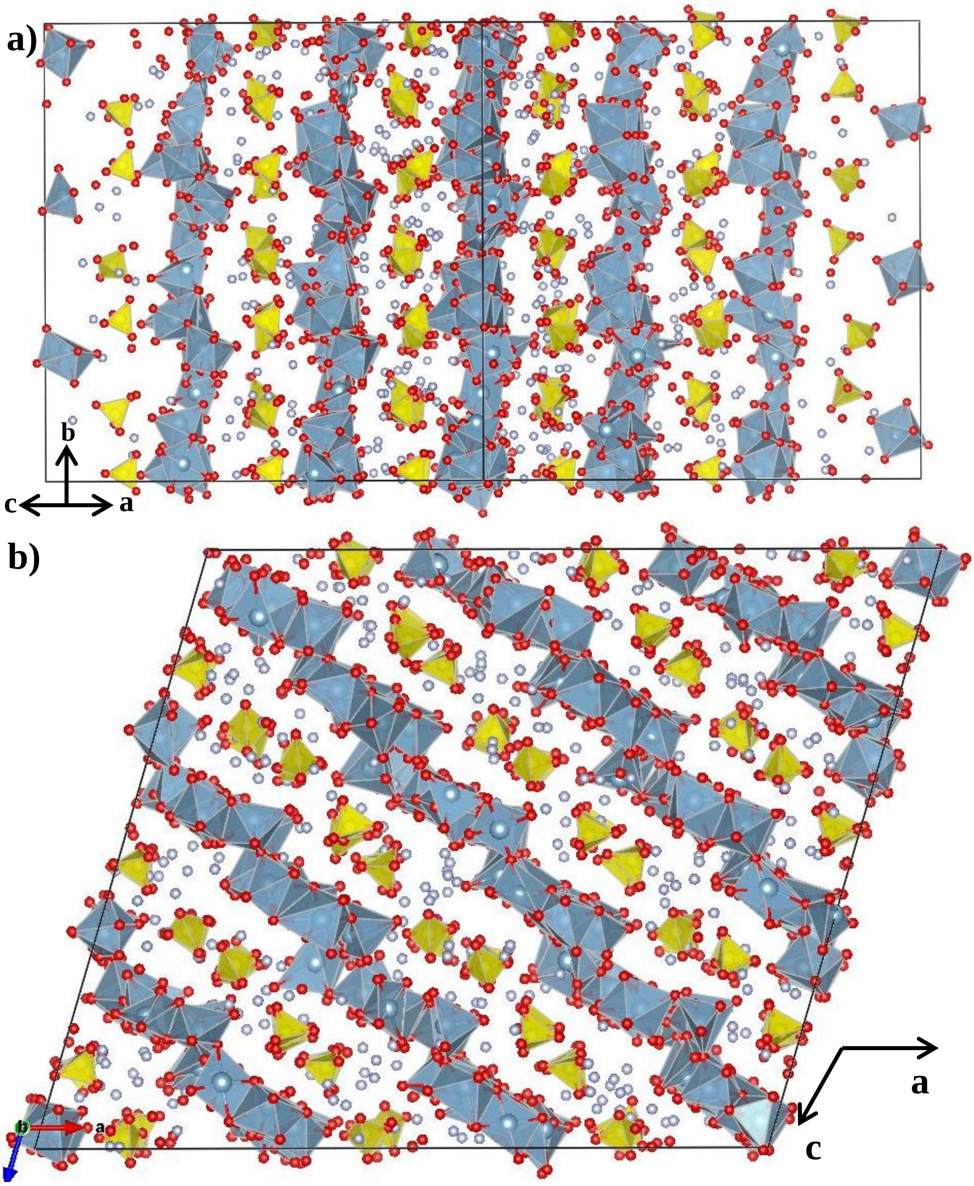

Figure A.3.12: *Cross section parallel to (a) plane a-c, and (b) b-edge of the Fels1 [3,3,3] final structure.*

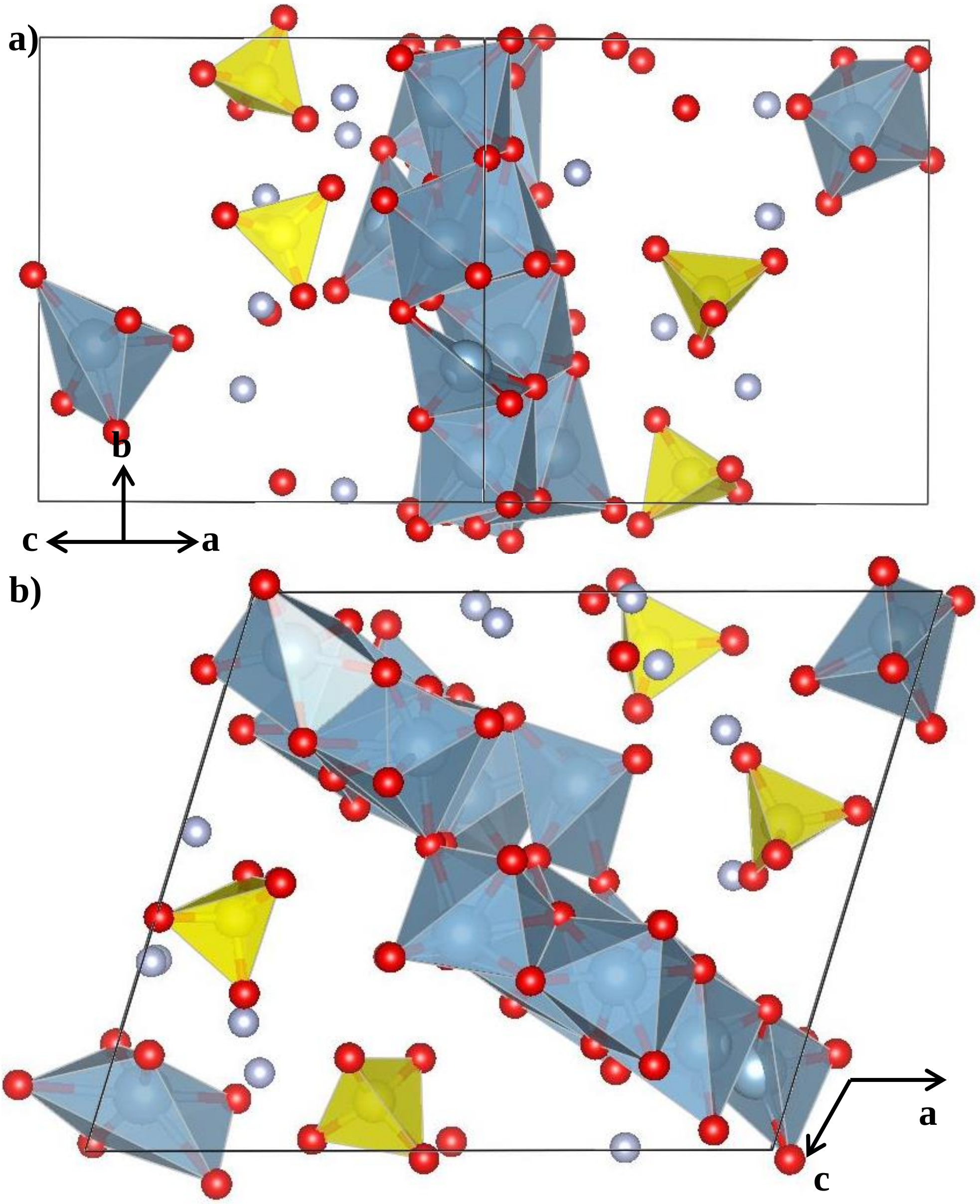

Figure A.3.13: Cross section parallel to (a) plane a-c, and (b) b-edge of the Fels2 [1,1,1] final structure.

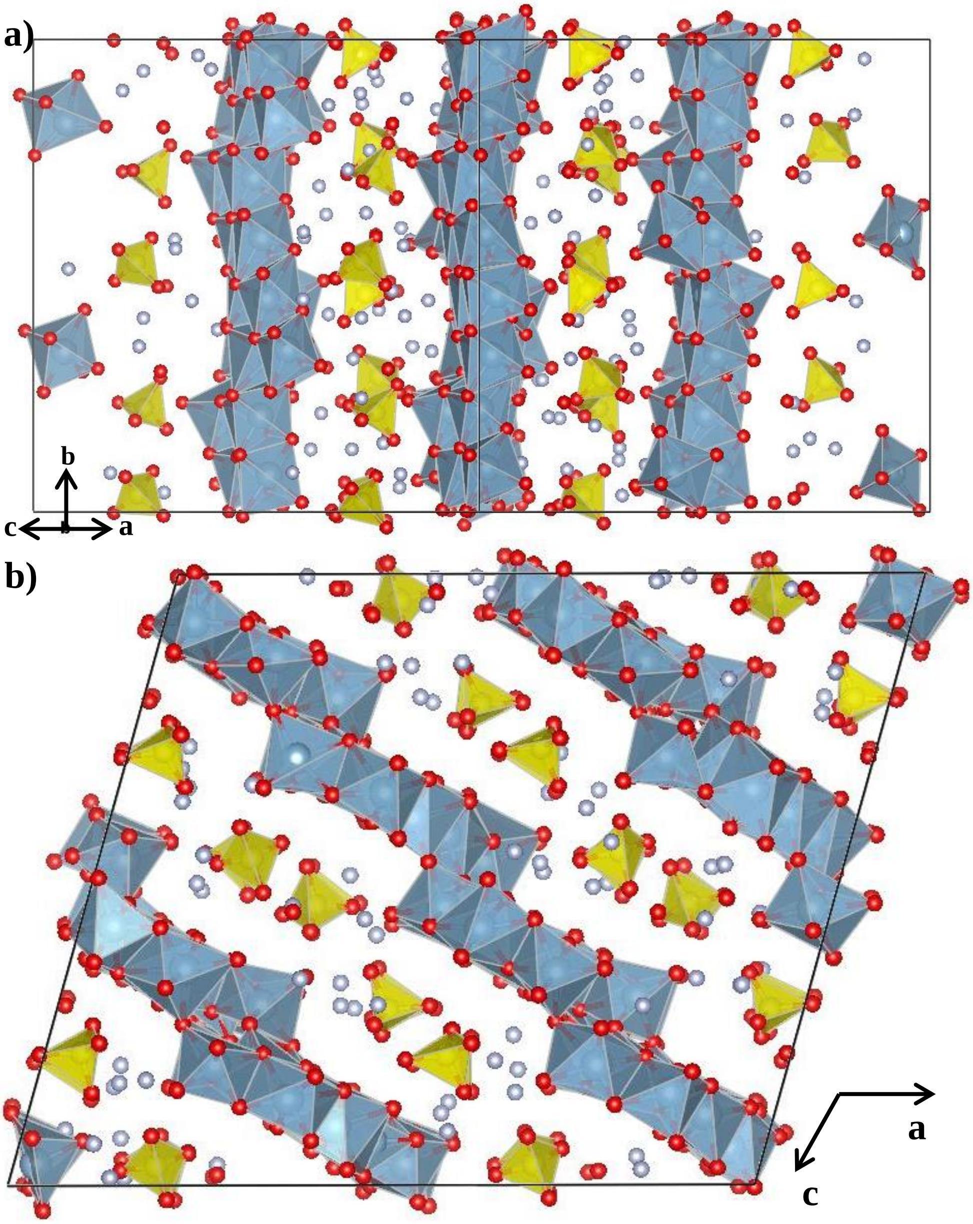

Figure A.3.14: *Cross section parallel to (a) plane a-c, and (b) b-edge of the Fels2 [2,2,2] final structure.*

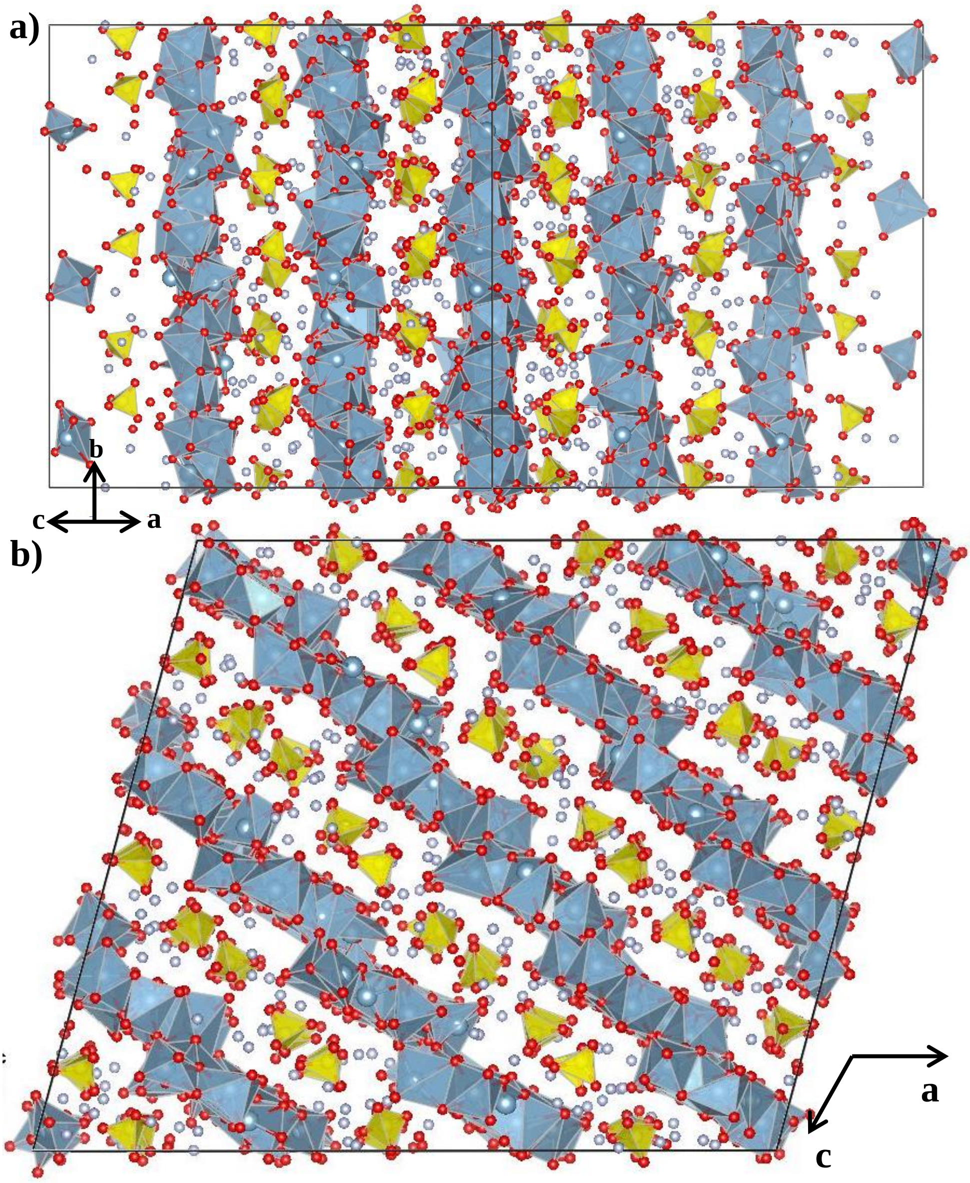

Figure A.3.15: *Cross section parallel to (a) plane a-c, and (b) b-edge of the Fels2 [3,3,3] final structure.*

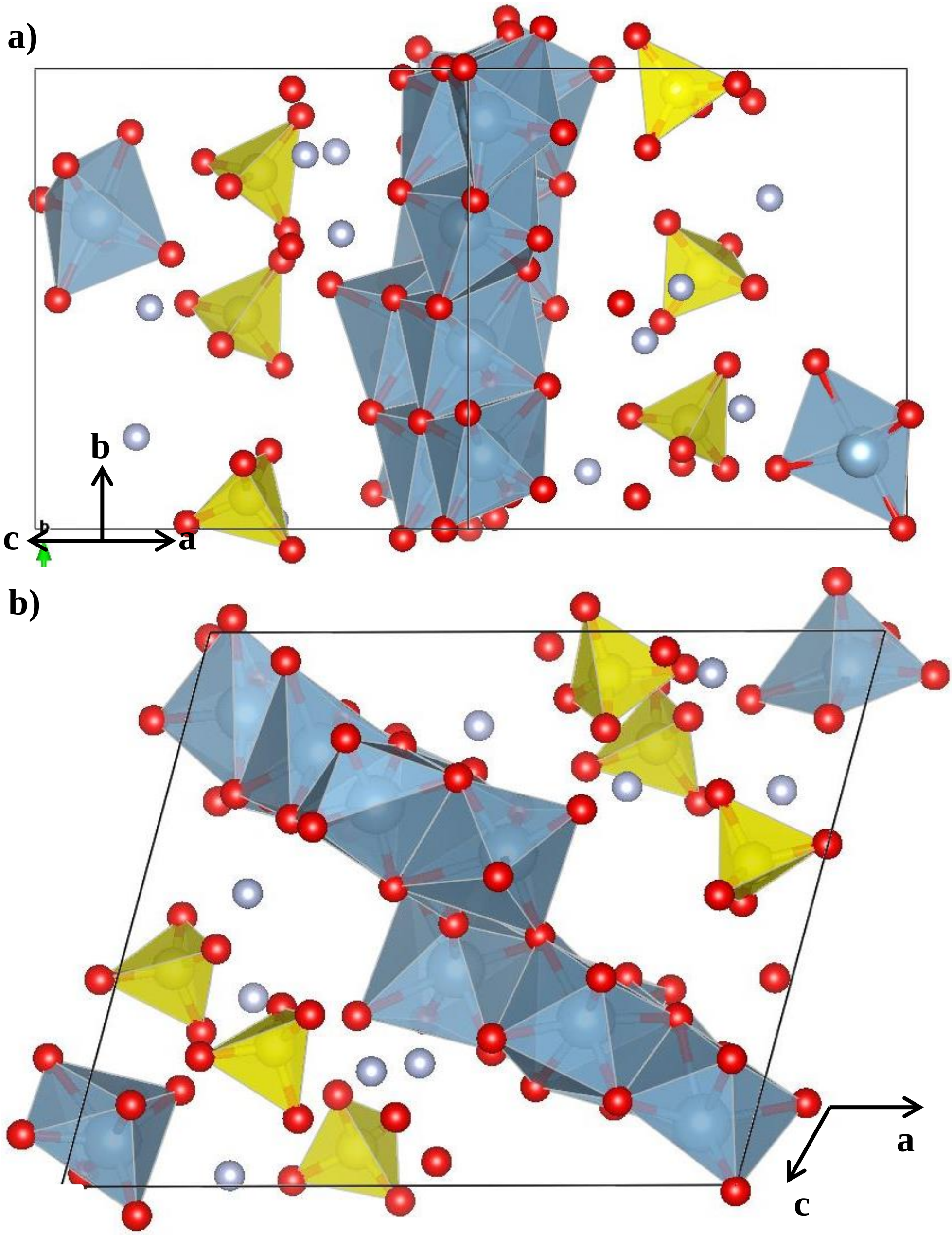

Figure A.3.16: *Cross section parallel to (a) plane a-c, and (b) b-edge of the Fels3 [1,1,1] final structure.*

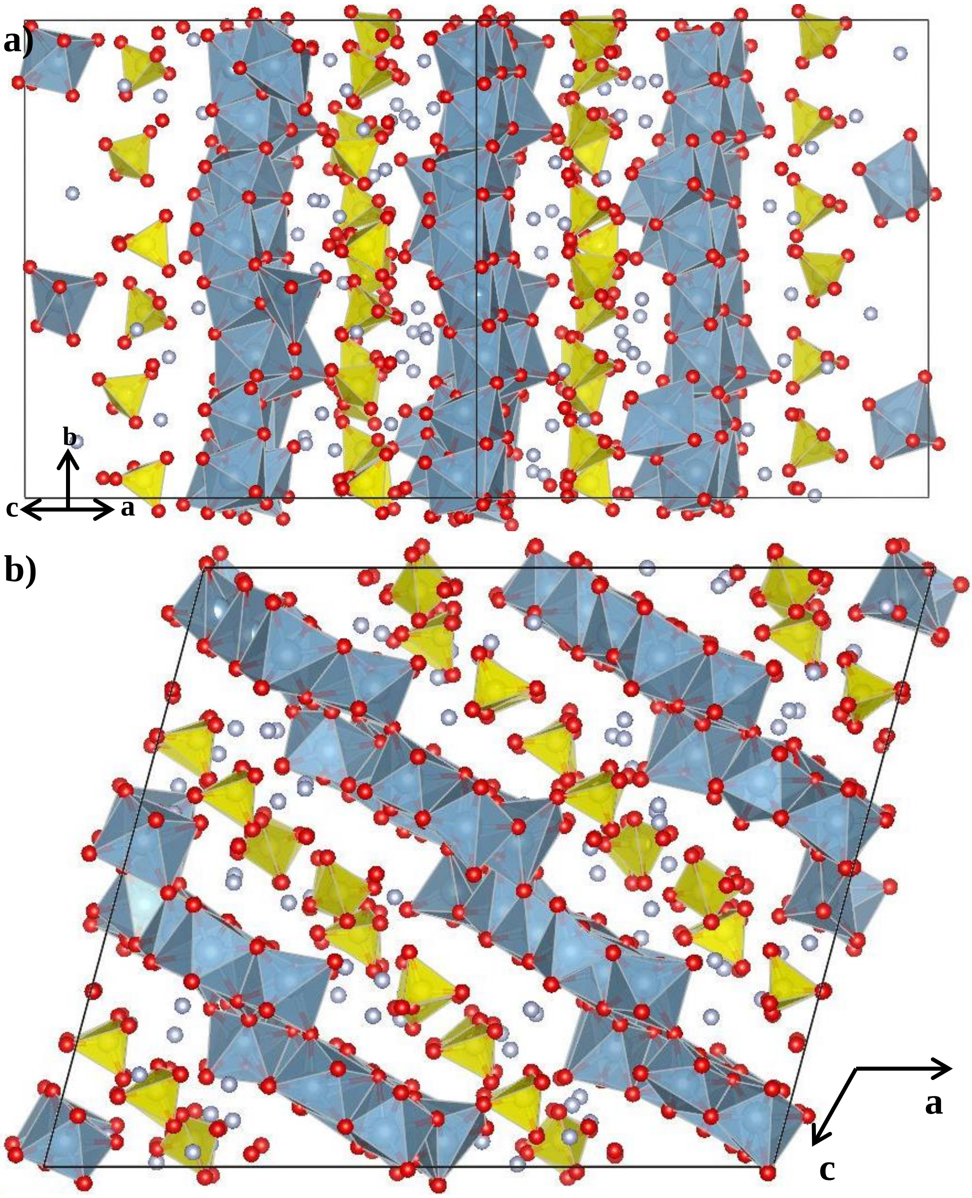

Figure A.3.17: *Cross section parallel to (a) plane a-c, and (b) b-edge of the Fels3 [2,2,2] final structure.*

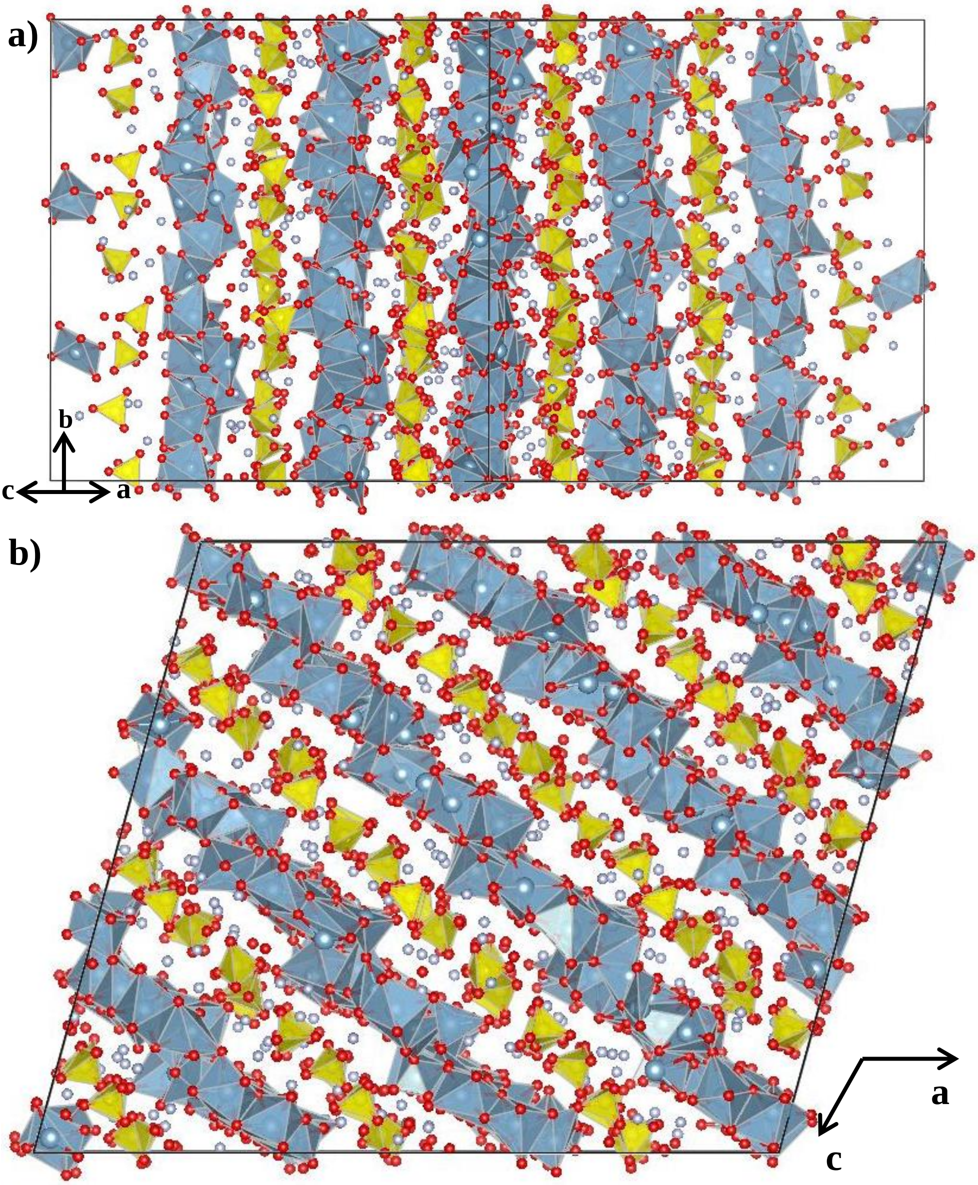

Figure A.3.18: *Cross section parallel to (a) plane a-c, and (b) b-edge of the Fels3 [3,3,3] final structure.*